NASA/TM-20210024786/PART2

9- by 15-Foot Low-Speed Wind Tunnel Acoustic Upgrade
Part 2: Improvement Comparison

David Bruce Stephens, Martin J. Krupar, and Christopher J. Miller
Glenn Research Center, Cleveland, Ohio

Steven J. Sedensky
Jacobs Technology, Brook Park, Ohio

July 2022

NASA STI Program . . . in Profile

Since its founding, NASA has been dedicated to the advancement of aeronautics and space science. The NASA Scientific and Technical Information (STI) Program plays a key part in helping NASA maintain this important role.

The NASA STI Program operates under the auspices of the Agency Chief Information Officer. It collects, organizes, provides for archiving, and disseminates NASA's STI. The NASA STI Program provides access to the NASA Technical Report Server—Registered (NTRS Reg) and NASA Technical Report Server—Public (NTRS) thus providing one of the largest collections of aeronautical and space science STI in the world. Results are published in both non-NASA channels and by NASA in the NASA STI Report Series, which includes the following report types:

- TECHNICAL PUBLICATION. Reports of completed research or a major significant phase of research that present the results of NASA programs and include extensive data or theoretical analysis. Includes compilations of significant scientific and technical data and information deemed to be of continuing reference value. NASA counter-part of peer-reviewed formal professional papers, but has less stringent limitations on manuscript length and extent of graphic presentations.

- TECHNICAL MEMORANDUM. Scientific and technical findings that are preliminary or of specialized interest, e.g., "quick-release" reports, working papers, and bibliographies that contain minimal annotation. Does not contain extensive analysis.

- CONTRACTOR REPORT. Scientific and technical findings by NASA-sponsored contractors and grantees.

- CONFERENCE PUBLICATION. Collected papers from scientific and technical conferences, symposia, seminars, or other meetings sponsored or co-sponsored by NASA.

- SPECIAL PUBLICATION. Scientific, technical, or historical information from NASA programs, projects, and missions, often concerned with subjects having substantial public interest.

- TECHNICAL TRANSLATION. English-language translations of foreign scientific and technical material pertinent to NASA's mission.

For more information about the NASA STI program, see the following:

- Access the NASA STI program home page at http://www.sti.nasa.gov

- E-mail your question to help@sti.nasa.gov

- Fax your question to the NASA STI Information Desk at 757-864-6500

- Telephone the NASA STI Information Desk at 757-864-9658

- Write to:
  NASA STI Program
  Mail Stop 148
  NASA Langley Research Center
  Hampton, VA 23681-2199

NASA/TM-20210024786/PART2

9- by 15-Foot Low-Speed Wind Tunnel Acoustic Upgrade
Part 2: Improvement Comparison

David Bruce Stephens, Martin J. Krupar, and Christopher J. Miller
Glenn Research Center, Cleveland, Ohio

Steven J. Sedensky
Jacobs Technology, Brook Park, Ohio

National Aeronautics and
Space Administration

Glenn Research Center
Cleveland, Ohio 44135

July 2022

Acknowledgments

The NASA Environmentally Responsible Aviation Project funded the 9- by 15-Foot Low-Speed Wind Tunnel (9x15 LSWT) background noise measurements conducted in 2012, along with the original study by Jacobs Engineering in 2012. The NASA Aeronautics Test Program and Aeronautics Evaluation and Test Capabilities project funded the improvement project with support from NASA Glenn Research Center. The writing of this report was funded by the NASA Advanced Air Transport Technology project. Thanks to the 9x15 LSWT facility staff for support throughout.

This work was sponsored by the Advanced Air Vehicle Program
at the NASA Glenn Research Center

Level of Review: This material has been technically reviewed by technical management.

This report is available in electronic form at http://www.sti.nasa.gov/ and http://ntrs.nasa.gov/

Contents

9- by 15-Foot Low-Speed Wind Tunnel Acoustic Upgrade
Part 2: Improvement Comparison

David Bruce Stephens, Martin J. Krupar, and Christopher J. Miller
National Aeronautics and Space Administration
Glenn Research Center
Cleveland, Ohio 44135

Steven J. Sedensky
Jacobs Technology
Brook Park, Ohio 44142

Summary

The 9- by 15-Foot Low-Speed Wind Tunnel at NASA Glenn Research Center was refurbished in a major construction project starting in June 2017 and ending in March 2019. Facility background noise and acoustical properties were documented before and after the refurbishment in order to quantify improvement. Noise throughout the tunnel loop during operation was documented before and after refurbishment. Design concepts and photographs of the tunnel modifications are described and documented. The effect of tunnel operation modes and aerodynamic instrumentation on the background noise of an empty tunnel were documented. The absorption coefficient of the acoustic boxes used in the refurbished test section was measured and statistics were compiled. The present report documents the acoustic performance of the tunnel before and after refurbishment.

1.0 Introduction

This report describes an acoustic improvement project carried out in the NASA Glenn Research Center 9- by 15-Foot Low-Speed Wind Tunnel (9×15 LSWT) and the effect on the acoustic measurement capabilities of the facility. The improvement project began in June 2017 and ended in March 2019, with some work stoppages in between. The main purpose of the project was to reduce the background noise of the facility to enable better signal-to-noise ratio measurements of quiet aircraft propulsion concepts. The term “background noise” refers to the noise measured inside the facility without a model installed. This report discusses the details of the project, the motivation for the upgrade, and the history of the facility background noise levels that motivated the upgrade. This report is one of a two-volume set documenting the 9×15 LSWT acoustic improvement. The companion report (Ref. 1) documents the “supporting studies” that were conducted as part of the improvement project, but do not relate explicitly to the 9×15 LSWT. The present report is focused specifically on studies conducted by NASA regarding the 9×15 LSWT, and thus, may be less broadly applicable to other facilities or projects.

1.1 Brief History of 9- by 15-Foot Low-Speed Wind Tunnel

The 8- by 6-Foot Supersonic Wind Tunnel (8×6 SWT) at NASA Glenn was completed in 1949 as an open loop propulsion tunnel for testing ramjets and other high-speed air-breathing engines. The operation of the tunnel and the testing of ramjet engine components was found to produce objectionable noise for miles around the facility. An immediate and comprehensive acoustic mitigation upgrade was conducted during the first half of 1950, performed by Bolt, Beranek, and Newmann, Inc. (BBN) (Ref. 2). This upgrade included the addition of a series of Helmholtz resonators tuned to reduce frequencies as low as 5 Hz, building a large muffler downstream of the 8×6 SWT diffuser and the addition of acoustic panels in various parts of the facility. The 8×6 SWT was converted into a closed loop tunnel with the addition of a return leg in 1956. The 9×15 LSWT was built in the return leg of the 8×6 SWT in 1969 (Ref. 3). By 2005, the tunnel had been upgraded with a flow conditioner, a downstream diffuser extension, and acoustic treatment. The 9×15 LSWT was designed for performance testing of vertical and short takeoff and landing (V/STOL) aircraft models, but the last 30 years has seen the tunnel used principally for testing noise and performance of aircraft propulsion systems. A schematic of the 8×6 SWT and 9×15 LSWT complex (8×6/9×15 complex) is shown in Figure 1. A number of reports overview the facility including aerodynamic test capabilities (Refs. 4 and 5).

1.2 Acoustic Studies of 9- by 15-Foot Low-Speed Wind Tunnel

The acoustic quality of the 9×15 LSWT has received considerable attention through the years. After the 1950 study to mitigate community noise mentioned previously, BBN was involved in studying a number of wind tunnels at NASA for acoustics research. Authors of these studies included many famous acousticians, including Leo Beranek, Uno Ingard, and Allan Piersol. BBN was called upon again to evaluate the first-generation acoustic treatment installed in the 9×15 LSWT in the 1970s, with a pair of reports covering the facility before and after the modification (Refs. 6 and 7). This first acoustic treatment was 2 in. of fiberglass covered with a screen for durability, and was used until 1986, when the current 13-in.-deep treatment was installed. The 1986 treatment was an unwoven Kevlar® (DuPont™) bulk absorber in two different densities, with a 40 percent open perforated plate on the flow surface and a second plate as a divider between the two densities of Kevlar®. Details about the design and testing of the acoustic treatment are given by Dahl and Woodward (Refs. 8 and 9). Background noise of the facility prior to the current improvement project has been reported by Woodward (Ref. 10) and Stephens (Ref. 11).

1.3 Motivation for Upgrades

The 9×15 LSWT has been a critical tool for testing fans used in commercial aircraft engines. Aircraft engine propulsors tested at subscale in the 9×15 LSWT include model turbofans and propellers for both NASA research projects and external customers (Refs. 12 to 14). Turbofan models are powered by the NASA Ultra-High Bypass drive rig (Ref. 15) while the NASA Open Rotor Propulsion Rig is used for testing counterrotating propeller systems (Ref. 16). The turbofan models being evaluated are advanced designs incorporating technologies such as reduced fan tip speeds, increased bypass ratios, and novel acoustic liners. Model engines utilizing these technologies in combination are significantly quieter than earlier models. In the past, most turbofan models have been tested at a tunnel speed of Mach 0.1 in order to limit the tunnel background noise level. This speed was determined to be fast enough to provide the desired aerodynamic inflow condition at the fan face, for models where the nacelle inlet was sufficiently long. Future turbofan engines are expected to feature shorter inlets to reduce weight and drag such that less flow conditioning from the nacelle is available. To achieve the desired inflow at the fan face, the tunnel must be operated at a higher free-stream velocity that more closely matches the intended flight speed. This significantly raises the background noise level in the facility, making acoustic measurements of advanced turbofans increasingly challenging.

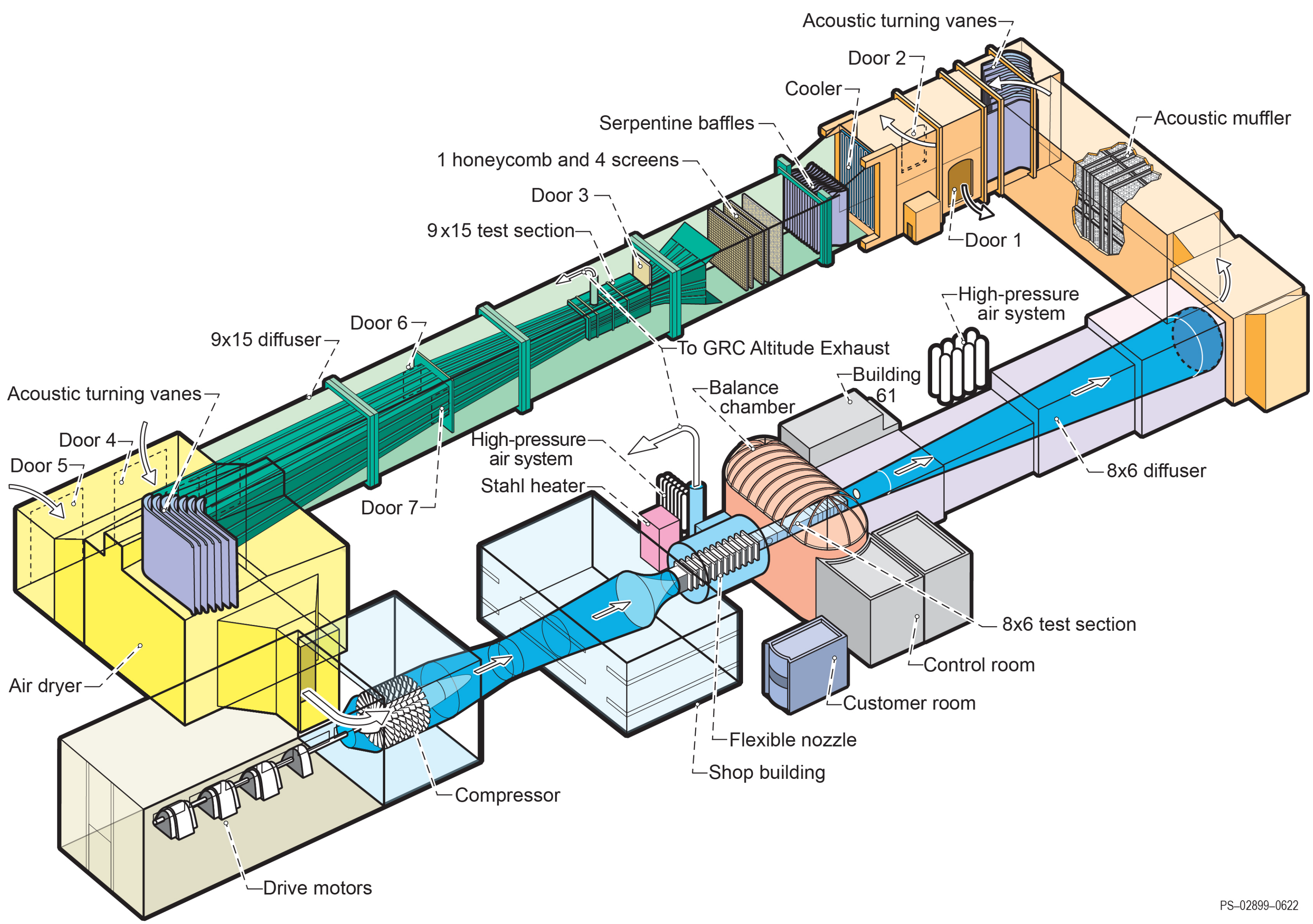

Figure 1.—Schematic of 8- by 6-Foot Supersonic Wind Tunnel and 9- by 15-Foot Low-Speed Wind Tunnel complex.

1.4 Report Structure

The present report is a compilation of studies that were conducted in support of the improvement project, either motivating the work or quantitatively documenting the improvement. The first study was conducted in early 2012 and is documented in Section 2.0. It describes a detailed set of background noise measurements that set the initial direction of the task. Section 3.0 describes the five major physical modifications made to the facility. Section 4.0 contains the main results regarding background noise reduction in the test section, with comparisons of before versus after the improvement project. Thus, Sections 2.0 to 4.0 are organized as documenting first the preconstruction condition, then describing the construction, and finally reporting on the results.

The background noise of the facility was the main focus of the task, but the acoustic quality was also considered. Smooth solid walls for the test section would have low roughness noise but would have strong reflections that would make microphone measurements problematic. A tunnel with acoustic wedges for the walls would provide a good anechoic environment but would be incompatible with airflow through the wind tunnel. The anechoic quality of the test section was measured using an impulse response method, a reverberation time analysis, and also a tone-based draw-away method. The goal of these three tests was to quantify how well the facility approximates an infinite environment where sound waves only propagate outward and there are no reflections. Sections 5.0 to 7.0 discuss the acoustic quality of the old and new test sections by use of impulse response, reverberation time, and draw-away measurements, respectively.

Section 8.0 describes the testing of the acoustic boxes that make up the wind tunnel, including the use of a specialized measurement method applicable to large samples and high frequencies. Section 9.0 describes a set of computational studies that supported the tunnel improvement project and helped guide multiple decisions.

Three appendixes are included. Appendix A describes the 2012 background noise measurements in detail, providing extra material to describe Section 2.0. Appendix B describes the 2018 background noise measurements in detail, supporting Section 4.0. Appendix C gives details about the acoustic box testing, giving expanded information relating to Section 8.0.

2.0 Preconstruction Background Noise

The NASA and GE Aviation Open Rotor test ended Jan. 19, 2012. The next customer was delayed, so there was an opportunity to take a thorough set of background noise measurements throughout the wind tunnel. Without this schedule happenstance, the improvement project might not have been undertaken.

2.1 Historical Data

As part of normal acoustic testing procedures, noise levels in the test section are periodically recorded and occasionally published (Ref. 10). Measurements taken many years apart have been found to be very similar, suggesting the background noise is largely stationary in time and dependent on the main features of the facility. Measurements of the empty tunnel taken over an 11-year period are shown in Figure 2 for the tunnel operating at Mach 0.10 and in Figure 3 for Mach 0.20. There were no major changes to the tunnel during this period, although repairs and minor modifications were frequent.

High-frequency electronic noise was recorded in 2005 (shown in blue), especially apparent at Mach 0.10 and frequencies above 20 kHz. The present author was not involved in these measurements and this problem has not been observed recently. The inflow microphones are known to be prone to a flow-induced tone at flow speeds above about Mach 0.10, and this is readily apparent in Figure 3 in the 2005 (blue) and 2011 (green) spectra at frequencies around 30 kHz. This effect can be mitigated by the use of a specially designed microphone windscreen (Ref. 17) developed at NASA Ames Research Center. The windscreen issue is discussed further by Mueller (Ref. 18), and the NASA Ames microphone design was adopted at NASA Glenn in 2011 as described in a report on acoustic testing methods used in the 9×15 LSWT (Ref. 19). It can be seen that the 2012 and 2016 measurements do not have the flow-induced tone. The 2012 test data (red) is the quietest of the four shown, especially below 1,000 Hz and at both Mach numbers. It is not known why this is the case, but it appears to be the exception compared to the other three measurements. The scaling of the measured spectra with tunnel speed was discussed by Stephens (Ref. 11) and is not repeated here.

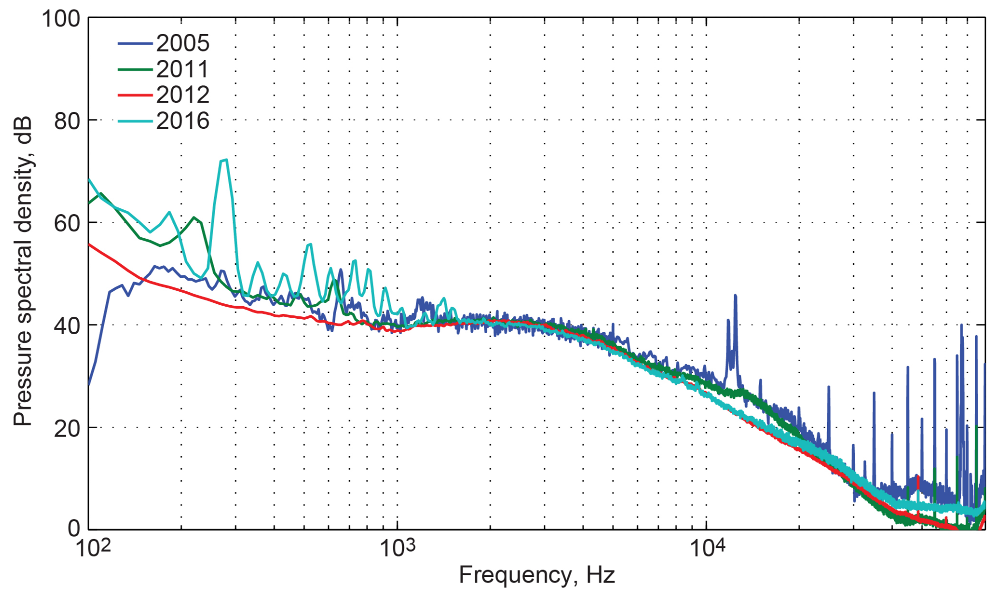

Figure 2.—Background noise level measured in 9- by 15-Foot Low-Speed Wind Tunnel over time at Mach 0.10.

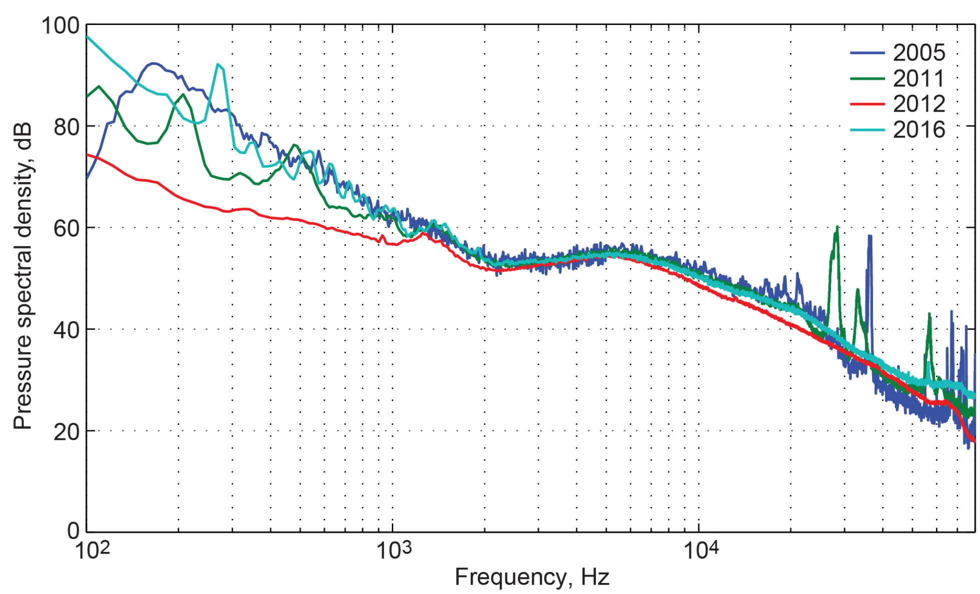

Figure 3.—Background noise level measured in 9- by 15-Foot Low-Speed Wind Tunnel over time at Mach 0.20.

2.2 2012 Background Noise Measurement

In early spring 2012, there was an opening in the tunnel schedule that permitted a set of background noise measurements to be made from Feb. 23 to Mar. 12, 2012. The objective was to acquire a comprehensive database of the noise levels around the tunnel loop that could be used to support a proposed background noise reduction task, which was not yet defined. Microphones were placed around the tunnel loop during a number of runs while the tunnel was operated in various configurations and modes. The NASA Environmentally Responsible Aviation project funded the testing and also sponsored a followup study by Jacobs Technology. The purpose of the study was to investigate whether a reduction in the background noise was possible and propose modification concepts. This section describes the testing and main findings from the study that encouraged the construction project. Figures, diagrams, tables, and other test documentation are included as Appendix A.

The 9×15 LSWT test section is shown in Figure 4, in a view looking upstream while standing in the diffuser. The test section is empty except for the three fixed microphones and the three-sensor traversing microphone rake. Other microphones were placed in the tunnel loop outside the test section to try to identify where the noise might be coming from.

The noise level was measured through the 9×15 LSWT leg and a story was found to emerge, shown in Figure 5 and Figure 6. Starting at the muffler, there is a local maximum in the spectra at about 900 Hz. Turn 2 is a highly turbulent region of the tunnel, so the next measurement shown is just upstream of the cooler. This area is where the flow control doors 1 and 2 are located, and these doors are known to leak air, whistle, etc. The third spectra, shown in Figure 5, is on the downstream side of the cooler, and a small amount of attenuation is apparent.

Moving downstream through the tunnel leg towards the test section, measurements were also made around the flow conditioner. It is apparent that the honeycomb and screens are largely benign, neither producing nor attenuating the noise. The microphone downstream of the screens is at the foot of the

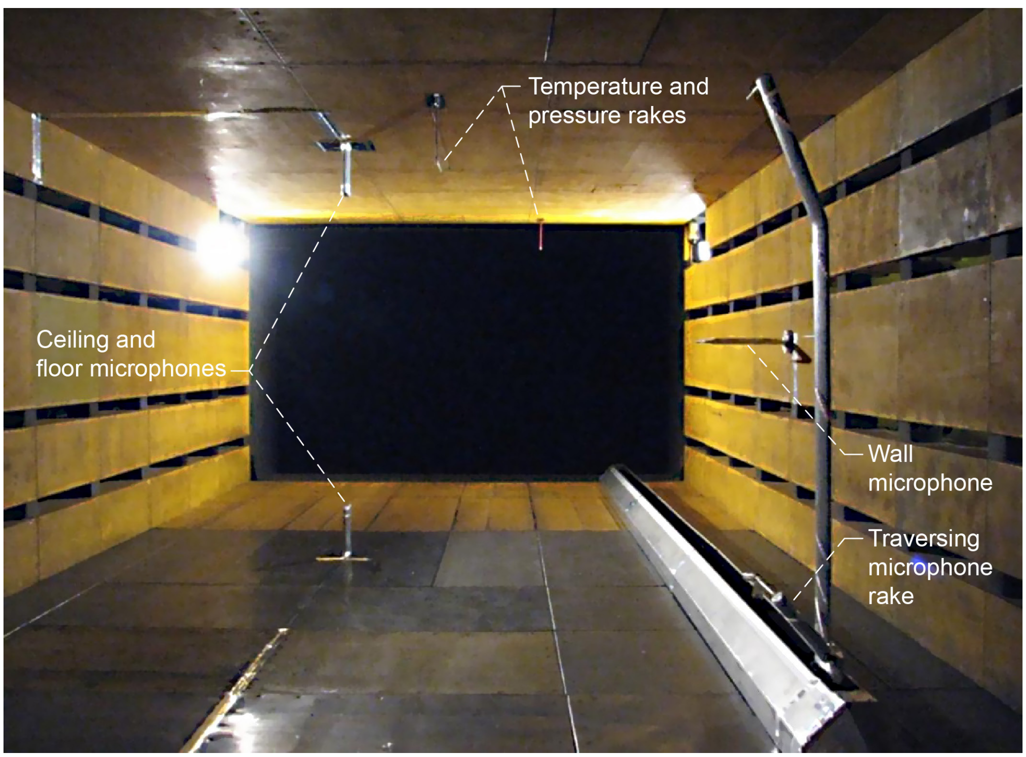

Figure 4.—Empty tunnel measurement setup used in 2012.

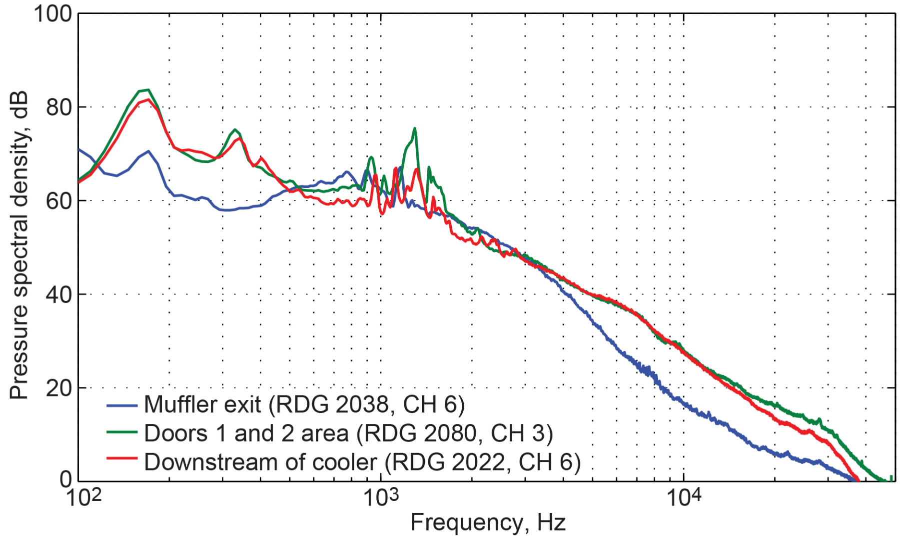

Figure 5.—Measured sound spectra in 9- by 15-Foot Low-Speed Wind Tunnel leg for noise around turn 2 at Mach 0.20. Channel (CH). Reading number (RDG).

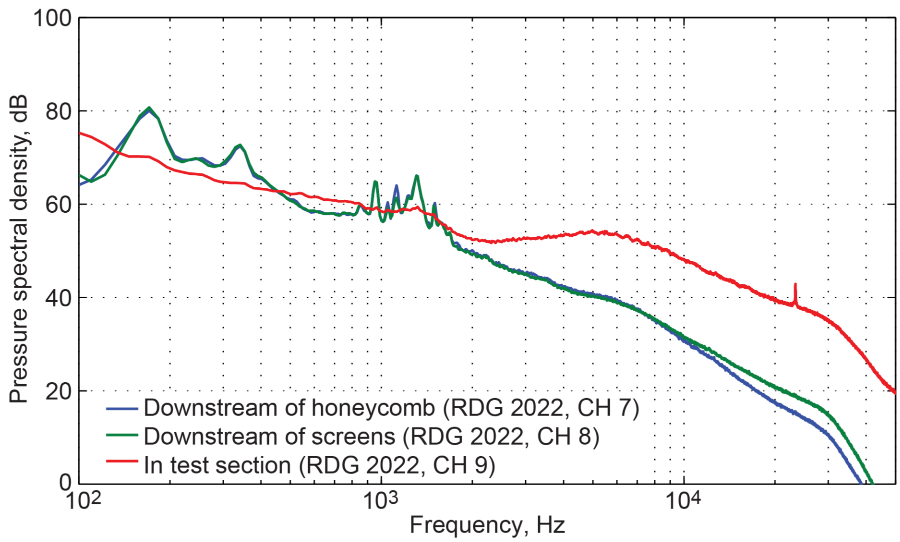

Figure 6.—Measured sound spectra in 9- by 15-Foot Low-Speed Wind Tunnel leg for noise in and near test section at Mach 0.20. Channel (CH). Reading number (RDG).

contraction. The measurement location inside the test section, however, is seen to have dramatically more noise above 2 kHz. This noise increase is 10 dB at 4 kHz, 14 dB at 6 kHz, and 16 dB at 10 kHz. Below 2 kHz, the noise levels are largely similar to each other. The test section is covered with acoustic treatment, which may explain why this noise does not radiate strongly upstream. It was our eventual conclusion, in collaboration with Jacobs Engineering, that this additional high-frequency noise was generated in or by the empty test section. The noise peak at 1,500 Hz is somewhat attenuated by the contraction and test section, and this weak local maximum is believed to be the remnants of the noise generated around doors 1 and 2.

2.3 Analysis by Jacobs Engineering

The full dataset from this preconstruction testing was delivered to Jacobs Engineering for analysis and preparation of an improvement proposal. Part of their work included modeling the noise through the tunnel loop as a number of individual sources that were calibrated to match the measurements. This allowed for noise reduction concepts to be evaluated, and their overall effectiveness determined. The main finding was that the dominant noise in the test section above 2 kHz was due to the rough perforated sheet metal flow surface in the test section. This motivated a considerable effort into studying roughness noise, as discussed in the companion report (Ref. 1). The reduction of this noise source was expected to be the most significant improvement that could be made to the background noise level in the facility.

Secondary sources included the noise from the doors 1 and 2 area, which was found to be propagating into the test section. Additionally, the diffuser angle was too wide for attached flow, and this was judged to be a likely noise source as well. Doors 1, 2, 4, and 5 were all noted as potential paths for noise leakage into the test section from nearby noise sources like cars on the Center and the Aero-Acoustic Propulsion Laboratory, as well as more distant outdoor sources like aircraft operating out of Cleveland Hopkins International Airport. Altogether, Jacobs Technology proposed five major modifications to the facility. The physical aspects of the improvement project are discussed in the following section of this report.

3.0 Tunnel Modifications

This section describes the five major modifications made to the 9×15 LSWT during the acoustic improvement effort. Figure 7 shows the 8×6/9×15 complex, with flow circulating in the counterclockwise direction. The 8×6 SWT is in the lower part of the image, while the 9×15 LSWT is in the return leg, pictured in the upper part. The five improvements are indicated, numbered from upstream to downstream. Acoustic turning vanes book end the project, while the other three modifications are between these two areas. Details of the five modifications made to the wind tunnel complex during the present project are given in the next five subsections.

The five improvements can be visualized by comparing the two parts of Figure 8, showing the preconstruction and postconstruction planform view of the 9×15 LSWT leg. The shapes of the turning vanes, baffles, and diffuser are all apparent and can be referred to as the reader reviews the rest of this section of the report.

Figure 7.—Rendering of 8- by 6-Foot Supersonic Wind Tunnel and 9- by 15-Foot Low-Speed Wind Tunnel complex showing facility improvements numbered from upstream to downstream: (1) turn 2 vanes, (2) serpentine baffles, (3) test section, (4) diffuser, and (5) turn 3 vanes.

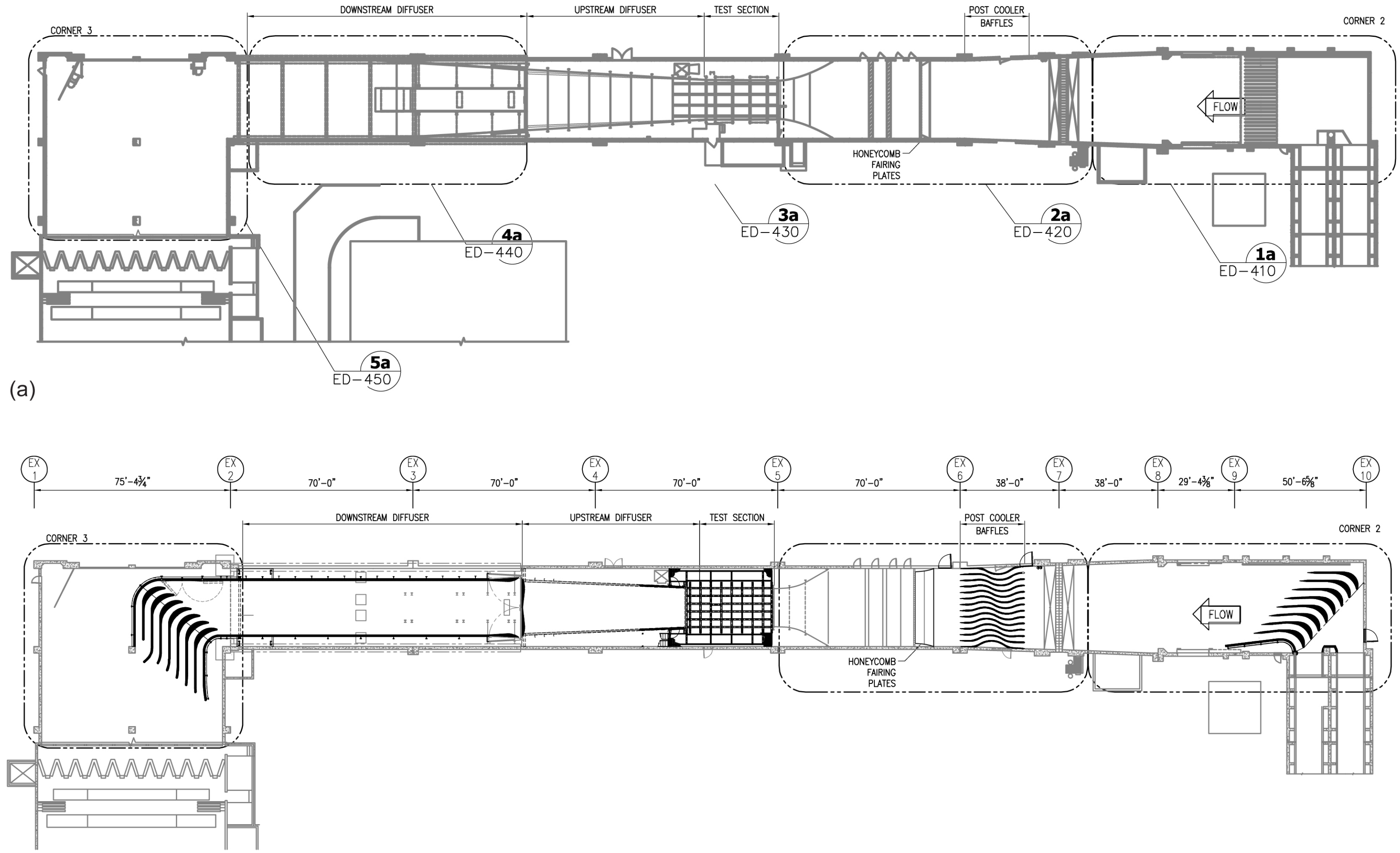

Figure 8.—9- by 15-Foot Low-Speed Wind Tunnel drawings. (a) Preconstruction, 2016. (b) Postconstruction, 2019.

3.1 Turn 2

The upstream-most modification, labeled (1) in Figure 7, was to turn 2, between the acoustic muffler and flow control doors 1 and 2. This turn was previously empty, except for acoustic treatment on the wall opposite the muffler exit and a set of parallel acoustic baffles that formed the outlet of the 8×6 SWT before the return leg was built, shown in Figure 9(a). These were installed as part of the 1950 community noise mitigation effort. Not clear in the photograph is that the wall of the tunnel opposite the muffler exit (left in the photographs) is also covered with acoustic paneling. The baffles were removed in the improvement project and replaced with acoustically treated turning vanes. The treatment on the wall was retained and an inboard fairing with acoustic treatment was added, visible in the right side of Figure 9(b). This fairing includes a pocket that the flow control door slides into when it is opened. The turning vanes were aerodynamically designed by Jacobs Engineering and constructed by their subcontractor. The downstream edges of the eight turning vanes are seen in Figure 9, from an observer standing in open door 2. The vanes are identical to one another, 12 m (40 ft) tall with structural splitters at 3-m (10-ft) vertical increments. These turning vanes were also required to be tolerant of elevated temperatures, as this area is upstream of the cooler.

3.2 Serpentine Baffles

Between the heat exchanger and the flow conditioner was a large straight and empty section of the rectangular ducting of the tunnel shell. This area was identified as a good opportunity for installing additional acoustic treatment. The cross-sectional area is very large, and thus, the flow velocity is low, and treatment could be added with relatively minor pressure drop. Also, the area is very close to the test section and so would be expected to be quite effective. Assuming the new treatment could block all upstream noise, the only remaining noise source before the test section would be the flow conditioner, which is composed of a honeycomb followed by four screens. Noise models developed by Jacobs Technology predicted only a small source from the flow conditioner, as shown in Figure 5 and Figure 6. A series of acoustic treatment concepts utilizing long straight baffles or shorter staggered baffles were explored before a final design was selected. The best performance was expected if line of sight in the streamwise direction could be eliminated, and a serpentine baffle pattern was developed to meet these criteria while creating only a small additional pressure drop. The ceiling also slopes downward during this section, as the height of the heat exchanger is more than that of the flow conditioner. Accurate measurement and fabrication were required for a successful installation. The area now containing the baffles is shown in Figure 10.

3.3 Test Section

The biggest change to the facility was a complete replacement of the test section. The original steel frame was sized for a 9- by 15-ft cross section when the flow surfaces were 12-mm- (1/2-in.-) thick aluminum plate. When the tunnel was modified with 33-cm- (13-in.-) deep acoustic treatment in 1986, the deep sections were fit between the beams and shallow 50-mm (2-in.) treatment was used over the beams. The dozens of individual boxes were a combination of flow surface and pressure shell, stuffed with acoustic absorber as discussed by Dahl and Woodward (Ref. 8). This resulted in a patchwork of acoustic impedance throughout the tunnel. The acoustic box design and original steel frame are shown in Figure 11(a) and Figure 12(a). The modification project provided the opportunity to replace the structure with a frame that was 33 cm (13 in.) larger in all interior dimensions so that acoustic boxes could be uniform depth, attaching to the frame from the back of the box and eliminating fasteners on the flow surface side. The new design kept the acoustic treatment design, as well as the one-piece flow surface, pressure shell, and acoustic absorber design. Graphics illustrating the updated designs are given in Figure 11(b) and Figure 12(b).

Figure 9.—Modification 1 of acoustic improvement task. Looking upstream at trailing edges of (a) old turn 2 baffles and (b) new turn 2 turning vanes.

Figure 10.—Modification 2 of acoustic improvement task. (a) Looking upstream towards heat exchanger. (b) Looking upstream at trailing edges of new serpentine baffles.

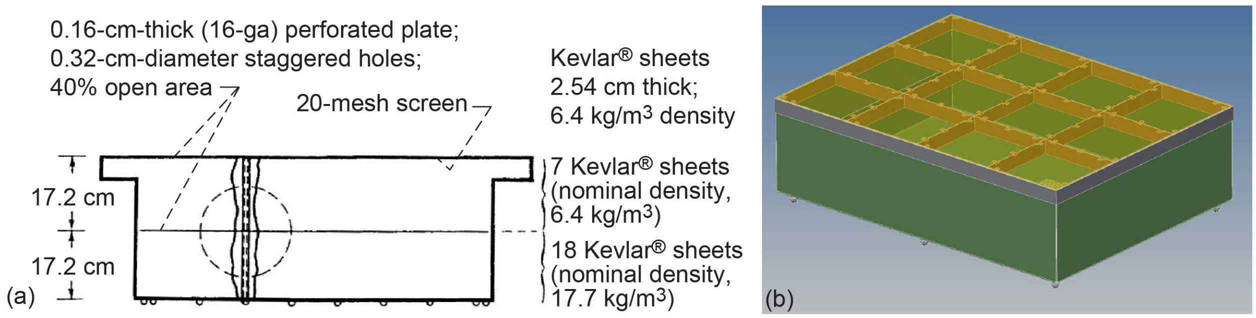

Figure 11.—Old versus new box design. (a) Acoustic box with flanges for original test section. (b) Acoustic box without flanges for new test section.

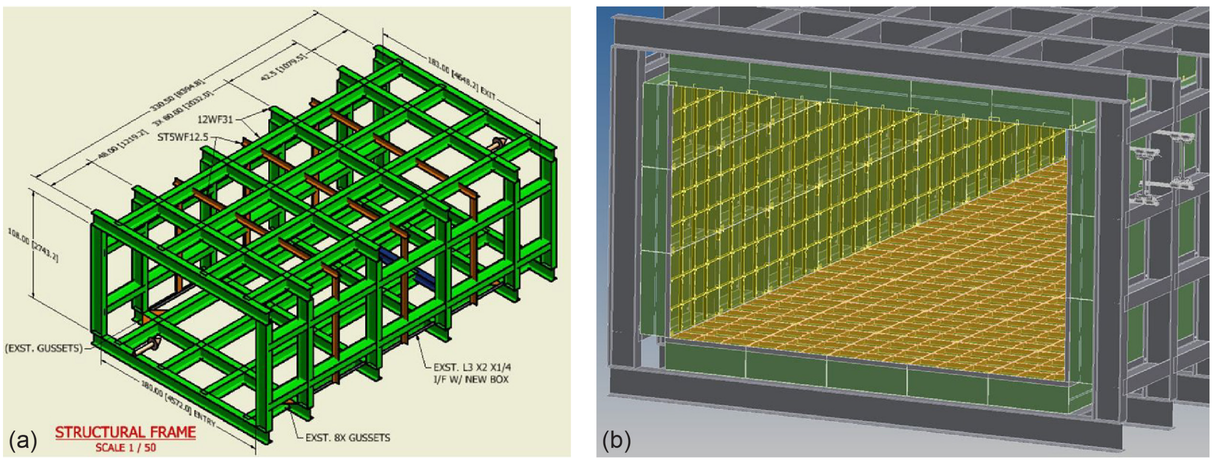

Figure 12.—Old versus new test section structural steel. (a) Original test section structural frame. (b) New test section structural frame.

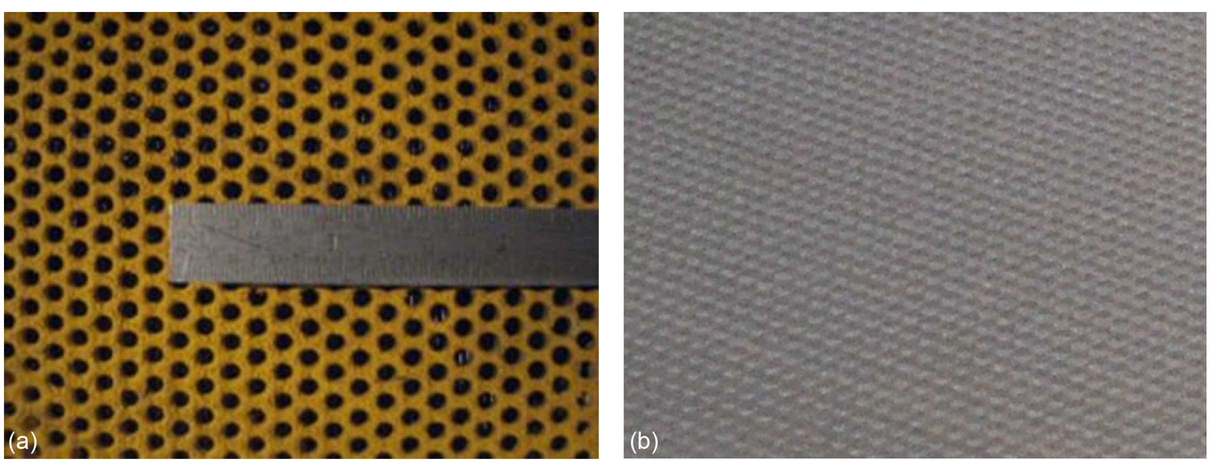

Figure 13.—Old versus new test section flow surface. (a) Original test section flow surface. (b) New test section flow surface.

The flow surface of the test section was replaced during this upgrade as the goal was to reduce noise due to flow over a rough surface. The topic is discussed extensively in Reference 1, but to summarize, the surface designed in 1986 is a 1.6-mm-thick (16-ga) perforated plate, with 3.2-mm-diameter (1/8-in.) holes at an open area ratio of 40 percent. The new panel is 63 percent open, 4-mm (5/32-in.) holes with a 200 by 600 thread per inch micronic wire cloth diffusion bonded to the flow surface. The walls and ceiling are 0.95 mm (20 ga), while the floor is 1.6 mm (16 ga). Figure 13 shows the old flow surface versus the new flow surface.

A view from inside the test section is shown in Figure 14. It is apparent that the slots have been eliminated and the test section lengthened by about 1.4 m (4.5 ft). The light and camera boxes now utilize a clear plastic flow surface instead of being open to the flow. There are also fewer boxes and correspondingly fewer seams, a design decision intended to reduce discontinuities that might be a source of noise.

Figure 14.—Test section. Looking upstream towards contraction. (a) Through old test section (b) Through new test section.

3.4 Diffuser

The old diffuser was constructed of steel and concrete and featured no acoustic treatment. It was built in two parts, with an original upstream diffuser that had a diffusion angle that was right on the edge of what might result in attached flow and a downstream diffuser expanded on this angle. The new diffuser has acoustic treatment on all surfaces, except for a loading ramp down the center. The diffuser was also lengthened as much as possible, resulting in a much narrower diffusion angle. As shown in Figure 8, the upstream diffuser was largely kept intact, but corner fillets were added to close the overall diffusion angle slightly. The downstream diffuser was replaced with a rectangular section with parallel walls, a downward sloping ceiling, and a downward sloping floor that extends all the way to turn 3. The view downstream from the test section is shown in Figure 15. In Figure 15(a), the old diffuser has already been demolished.

3.5 Turn 3

The 8×6/9×15 complex was built without any turning vanes in the corners. The 9×15 LSWT leg dumped flow into turn 3 where a large area was available for the flow to decelerate, mix, and spread out before the flow entered the air dryer. Since the exit to the 9×15 LSWT leg was now much narrower due to the longer diffuser, there was concern that the airflow would not diffuse adequately before entering the air dryer. This could result in additional pressure drop through the air dryer, and the desiccant in the dryer not being utilized uniformly. The turning vanes were customized with trailing edges spread apart to aggressively diffuse the flow in both horizontal and vertical directions. These vanes are also acoustically treated to block noise from traveling upstream into the 9×15 LSWT test section. The before and after condition of turn 3 is shown in Figure 16.

4.0 Postconstruction Background Noise

The principal objective of the improvement project was to reduce the background noise level in the facility, as was previously discussed. This section compares the noise measured in the 9×15 LSWT before and after the renovation, quantifies the amount of noise reduction achieved and discusses the implications for acoustic testing of aircraft propulsion systems. Additional information is provided in Appendix B, including noise measurements made in the loop outside of the test section, the effect of tunnel operations on the noise, and the effect of pneumatic seals for doors 1 and 2.

4.1 Test Section

The experimental setup for the background noise reduction validation measurements was a single microphone mounted to the floor of the 9×15 LSWT, as shown in Figure 17. This configuration was selected as utilizing the simplest practical experimental setup, forgoing the use of the usual microphone traverse in favor of a single floor-mounted microphone. The traversing microphone method was intended to remain the primary method for measuring radiated sound in a simulated flyover, but a new traverse was not directly part of the improvement project.

The validation testing was performed as three different tunnel runs, with the sideline microphone moved between three stations, as shown in Figure 18. A short microphone was mounted on the ceiling as a reference for both tests, visible in Figure 17(b) due to the angle the picture was taken.

Figure 15.—Diffuser. Looking downstream (a) through tunnel shell where old diffuser dumps and (b) from test section into diffuser. Observer location is same as Figure 14, just downstream of test section.

Figure 16.—Diffuser. (a) Looking upstream through turn 3 into 9- by 15-Foot Low-Speed Wind Tunnel leg. Filters to air dryer system are visible on right. Intake door 4 visible on left. (b) Looking upstream at trailing edges of turn 3 turning vanes. Intake doors 4 and 5 are visible in back of picture. Note ceiling beams and post in both images.

Figure 17.—Experimental setup for background noise validation measurements in test section. (a) Preconstruction background noise measurement, Jan. 7, 2016. (b) Postconstruction background noise measurements, June 3, 2019.

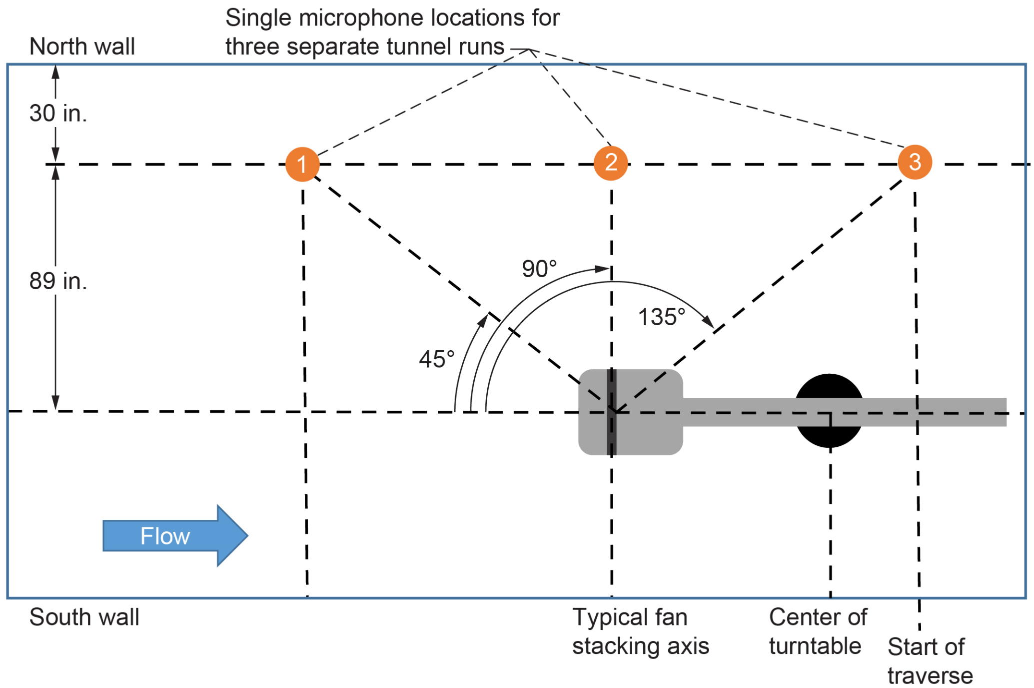

Figure 18.—Diagram showing configurations used for validation testing of background noise. Fan model shown only for reference. No model was present in tunnel during this testing.

4.1.1 Background Noise Measurement

The main result of the improvement project can be seen in Figure 19, showing the background noise in the test section before and after construction at Mach 0.20. It is shown that noise was reduced at all frequencies measured, and the amplitude reduction ranged from 5 to 20 dB, depending on the frequency.

The main focus of the task was on the one-third octave band sound pressure levels at center frequencies between 630 Hz and 50 kHz, a total of 20 frequency values. As discussed in Section 2.1, the noise in the test section was known to be broadband in nature, without strong tones, and with no measured noise from the tunnel drive. It was thus practical to consider only one-third octave band levels. At the frequencies specified, the average noise reduction was 13 dB. The noise reduction at frequencies above 2 kHz is believed to come principally from the smoother flow surface enabled by the diffusion bonded panels. The flow surface had previously been bare perforate, which was believed to be responsible for the broad hump in the spectra of Figure 19 with a peak of around 6 kHz in the 2016 measurements. A local maximum remains in the 2019 measurements but is now at a higher frequency of around 8 kHz. The narrowband features measured at 200 and 300 Hz at Mach 0.20 are believed to be caused by the inflow microphone, including perhaps the mounting mechanism. Since these stands were for temporary use while the new traversing microphone system was being finalized, they may not be present in data acquired with the new purpose-built system. Also note that these frequencies are lower than the frequency range of interest used for this renovation project.

A corresponding chart is given in Figure 20 for the tunnel at Mach 0.10. It can be seen that the overall trends are similar at the lower tunnel speed, but the specific frequency of the largest noise reduction is lower. This is because the noise source frequency scales with flow speed.

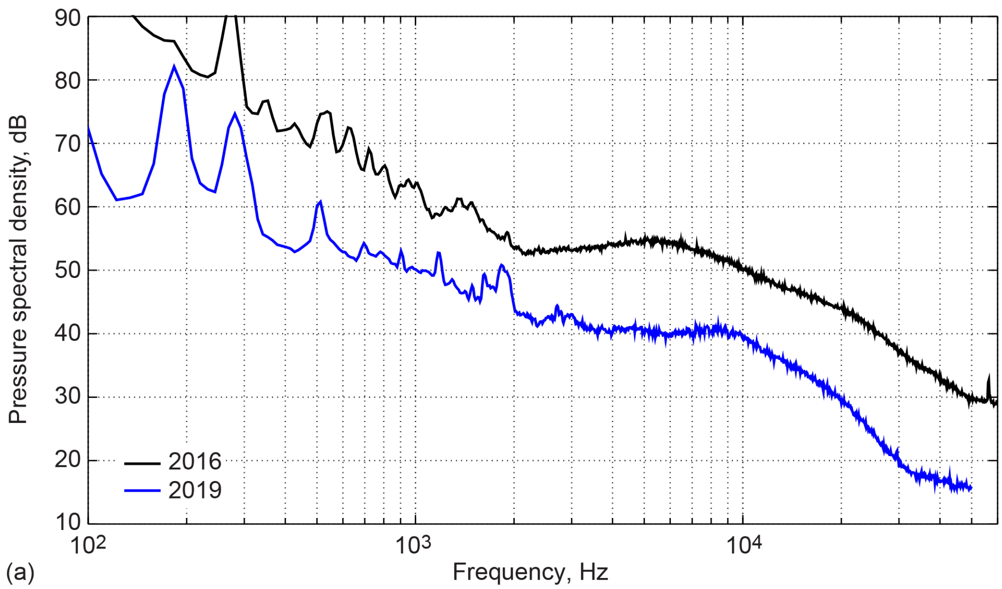

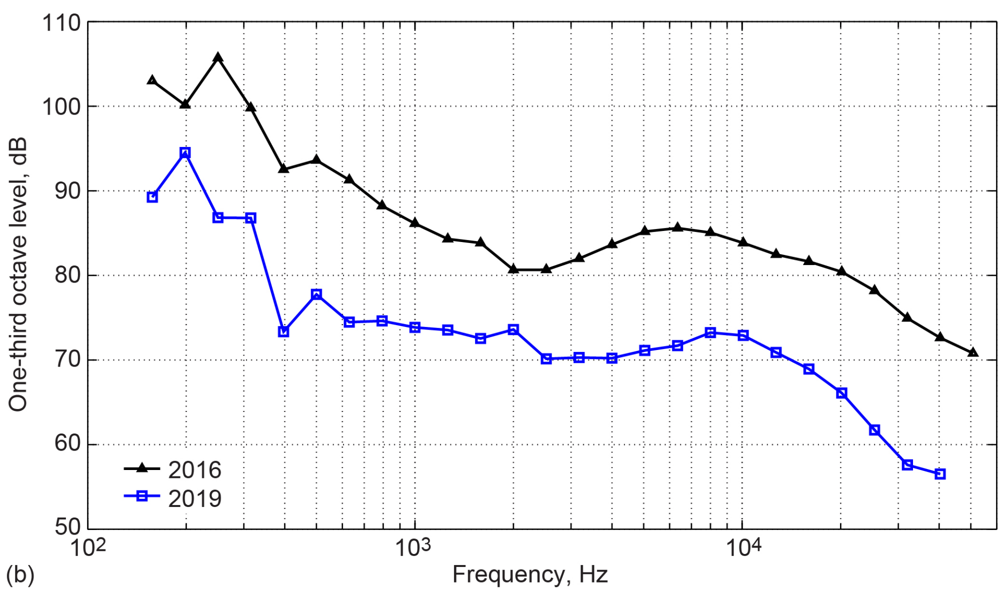

Figure 19.—Background noise measurements at Mach 0.20 before and after construction project, middle microphone location. (a) Narrowband. (b) One-third octave.

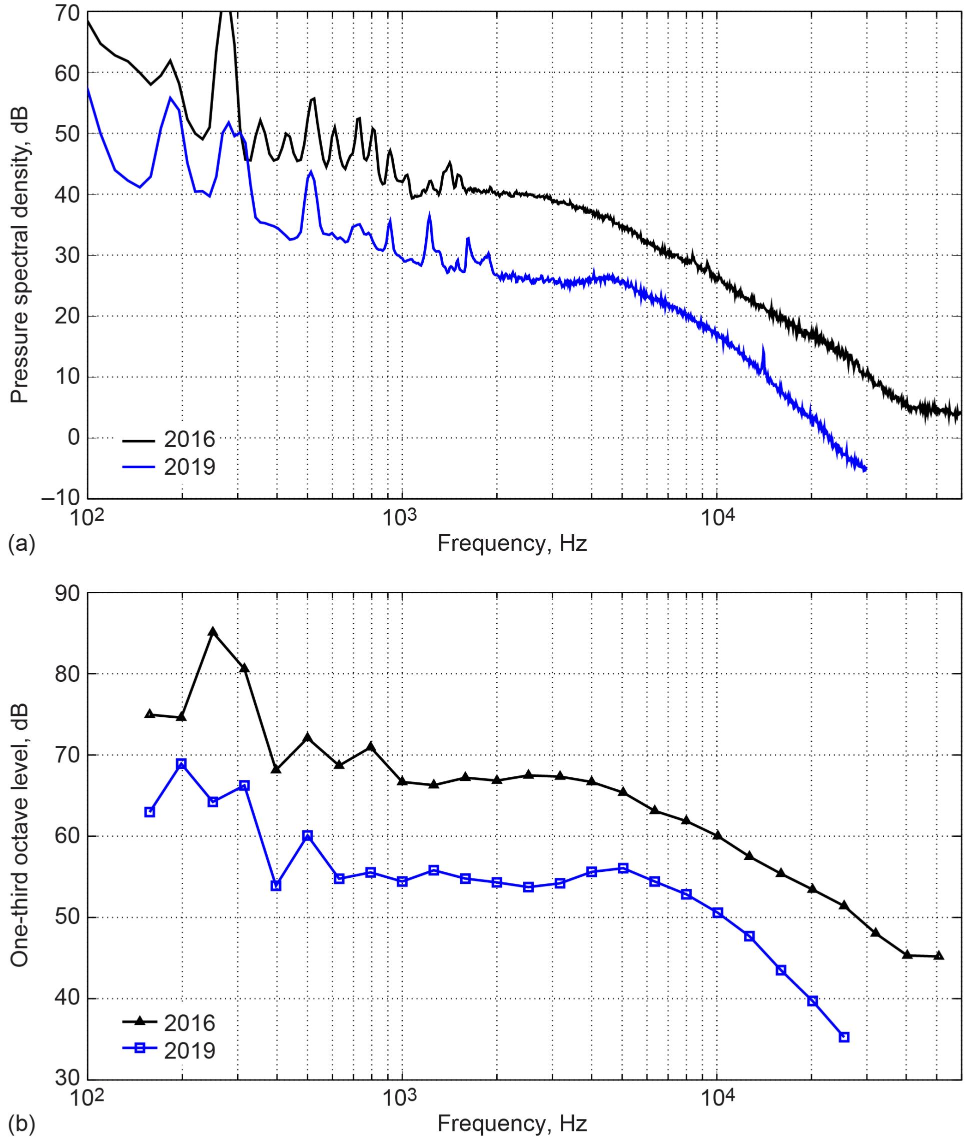

Figure 20.—Background noise measurements at Mach 0.10 before and after construction project, middle microphone location. (a) Narrowband. (b) One-third octave.

4.1.2 Background Noise Reduction

Narrowband and one-third octave band noise reduction amounts are given in Figure 21. It can be seen that some noise reduction is at a constant frequency for both Mach numbers, for example, between 1 and 2 kHz. Other noise reduction moves in frequency in tunnel speed, specifically noise above 2 kHz. A pinch point in the noise reduction is observed right around 2 kHz, where only about 5 dB of reduction was obtained. This frequency was previously a local minimum at Mach 0.20, but is now a local maximum.

The main noise reduction came from the replacement of the flow surface, as previously discussed in Section 3.3. The perforate hole size has increased slightly from 3.2 mm (1/8 in.) to 4 mm (5/32 in.). The percent open area was increased from 40 to 63 percent, and most importantly a micronic wire cloth was bonded to the perforate panels. As discussed in Reference 1 for this improvement project, extensive noise measurements were made due to flow over various panels. Some remaining noise from the flow surface was expected, and the overall trends scaled well between the component level tests and the final implementation in the tunnel.

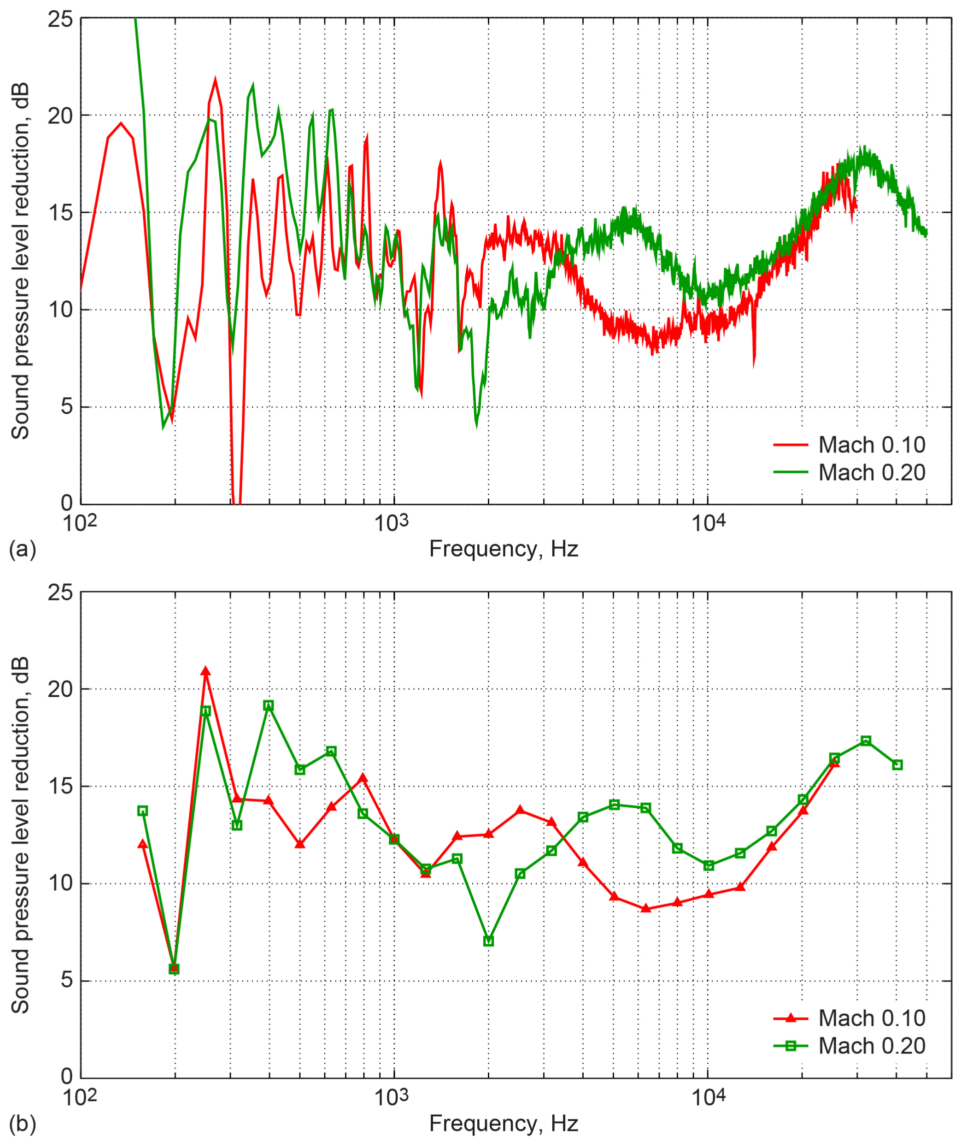

Figure 21.—Background noise reduction. (a) Narrowband. (b) One-third octave.

4.1.3 Effect of Mach

The variation of background noise with tunnel Mach number is shown in Figure 22 for four tunnel Mach numbers. By examining different Mach numbers, spectral features can be separated into those dependent on flow speed and those dependent on geometry. Flow speed features would correlate with the nondimensional Strouhal number $St = fL/U$ and geometry features would correlate with the nondimensional Helmholtz number $He = fL/c$, where L is a relevant length scale, U is the tunnel flow speed, and c is the speed of sound. The spectral features below about 2 kHz seem largely fixed in frequency as the tunnel speed changes, although the amplitude does increase. This suggests a spectral feature caused by resonance linked to geometry, such as the streamlined strut holding the microphone, or perhaps the plate holding it to the floor. New plates with a streamlined fairing were used for the 2019 test as seen in Figure 17. However, the effort does not seem to have resulted in a completely clean measurement at these frequencies. Above 2 kHz, the spectral shape changes significantly with flow speed and is likely dominated by flow over the test section surface, both in 2016 and 2019.

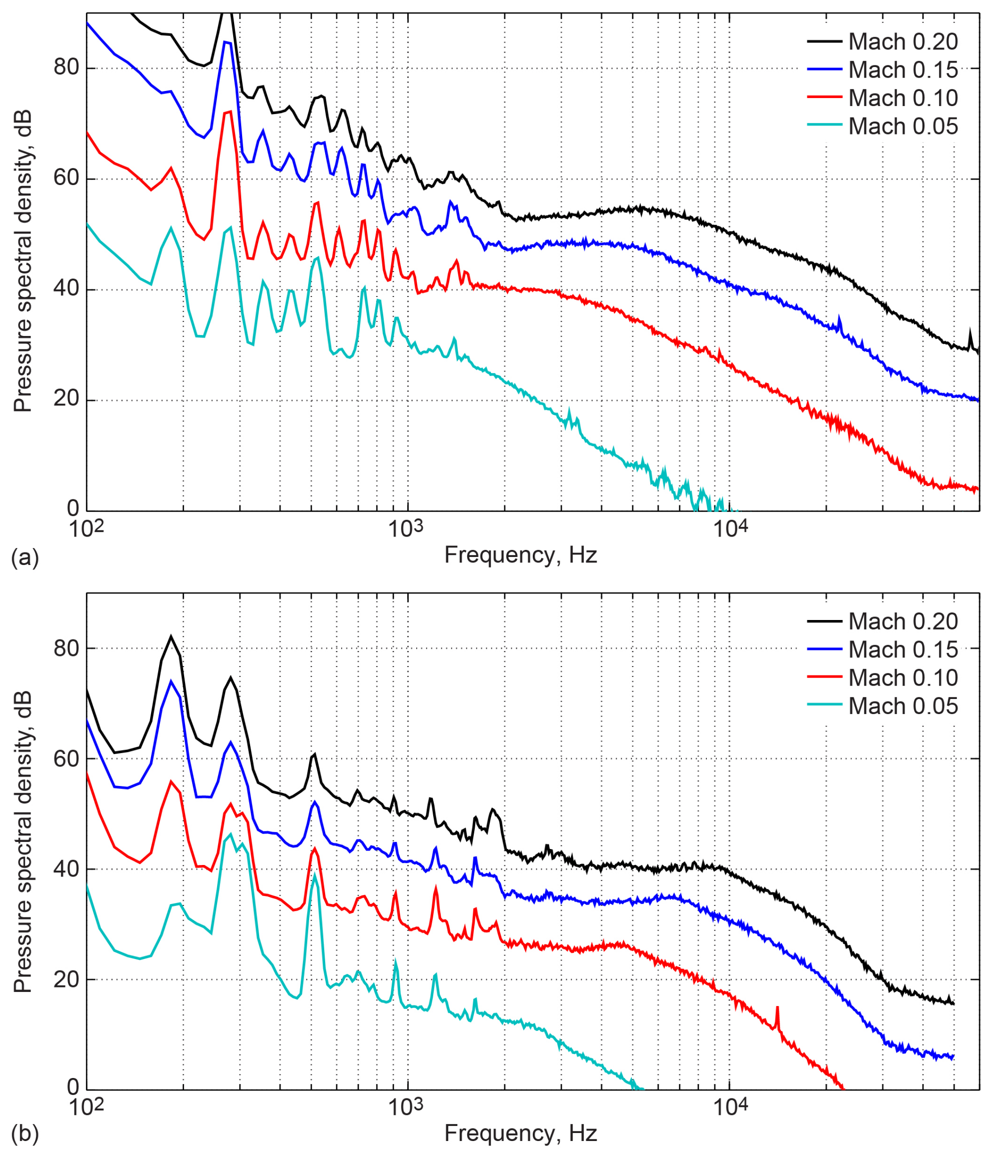

Figure 22.—Background noise versus Mach. (a) 2016. (b) 2019.

4.1.4 Effect of Location in Test Section

The variation of background noise with streamwise location within the test section is shown in Figure 23. The use of three measurement locations can help give some idea of noise sources, with higher amplitude perhaps implying the microphone is closer to the source. In Figure 23(a), it can be seen that the noise above 2 kHz is louder upstream, while below 2 kHz, the noise is louder to the aft of the test section. After the improvement project, the spectra shown in Figure 23(b) shows the noise is louder upstream everywhere. With the hypothesis that the measured noise is primarily caused by flow over the rough surface, it is concluded that this source is louder near the front of the test section. Presumably this is because the boundary layers on the tunnel are thinner at the front, and the flow surface is exposed to higher speed air. The effect is quite small however and likely has minimal implication for testing specific models in the facility.

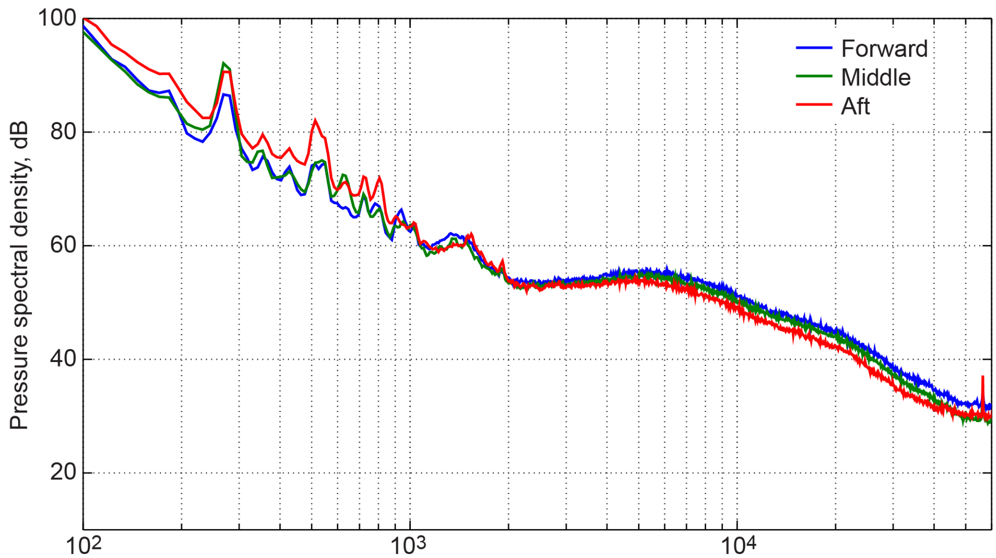

(a)

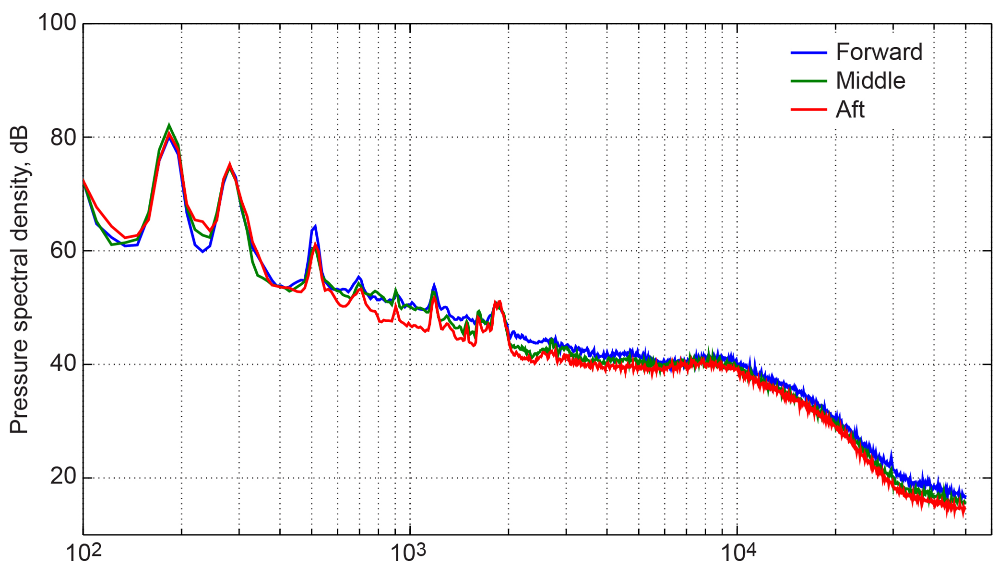

(b)

Figure 23.—Background noise versus location at Mach 0.20. (a) 2016. (b) 2019.

The tones at low frequencies show some variation with location in the test section. In both 2016 and 2019 tests, the mounting plate had to be removed and reinstalled between tunnel runs, so there is the possibility that the installation was slightly different between tests. A better assessment is expected once the traversing microphone is available.

4.2 Implications for Fan Testing

The purpose of reducing the noise in the 9×15 LSWT test section is to enable better signal-to-noise ratio testing of quiet models. The NASA Glenn Acoustics Branch is part of the Propulsion Division and typically is involved in testing of aircraft propulsor models in the wind tunnel.

Figure 24 shows data from a test of the Advanced Ducted Propulsor Fan 1 test (Ref. 20) recorded Oct. 29, 1996. On this test date, the model was configured with double-degree-of-freedom liners in all three bays in the model. The data shown is from reading 382, with the fan at a low-power setting of 4,950 rpm corrected. This dataset is thus a good surrogate for a low-noise fan model with acoustic liners. The tunnel was operated at Mach 0.10 for this reading, as it was known that the background noise would be too high to make the measurement at Mach 0.20. The fan model has a long inlet, and thus, is relatively insensitive to external flight speed. Modern fans are expected to utilize short inlets, and thus, need to operate at more realistic free-stream speeds to get the expected inlet flow profile. This figure shows that this measurement could be made at Mach 0.20 with good signal-to-noise at most frequencies of interest, except for upstream measurements below 2 kHz where the sideline microphone is near the front of the test section and geometrically far from the fan model. Future fan designs may incorporate more effective liners or other low-noise technology designs. Perspective users of the facility will need to consider the background noise level of the facility while planning their test matrix.

4.3 Implications for Open Rotor Testing

The background noise level in the 9×15 LSWT was a known contaminant for some of the data acquired in the open rotor test campaign that began in 2009. During these tests, the tunnel was typically operated at Mach 0.20, as this was required to get the proper inflow into the counterrotating propeller model. The noise from the open rotor propulsor is dominated by strong tones, but broadband levels were also of interest as a noise contribution. When the rotor was tested at low power levels, the background noise of the facility dominated the broadband spectral content of the model. An example of this is from the F31/A31 dataset (Ref. 21), reading 462, which is a low-power condition with the blades at the takeoff pitch angles acquired on Aug. 4, 2010. As shown in Figure 25, the empty tunnel noise at Mach 0.20 prior to 2016 is essentially equal to the broadband noise from the rig. The improved tunnel background noise would likely allow a measurement of the broadband noise caused by the open rotor operating at this condition.

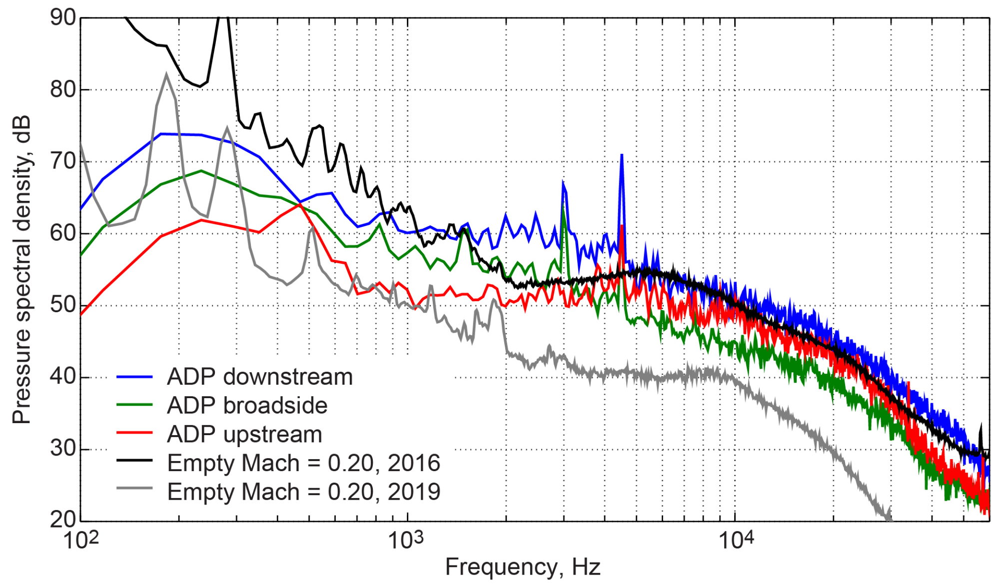

Figure 24.—Tunnel background noise compared with noise of low-speed fan model. Advanced Duct Propulsor (ADP).

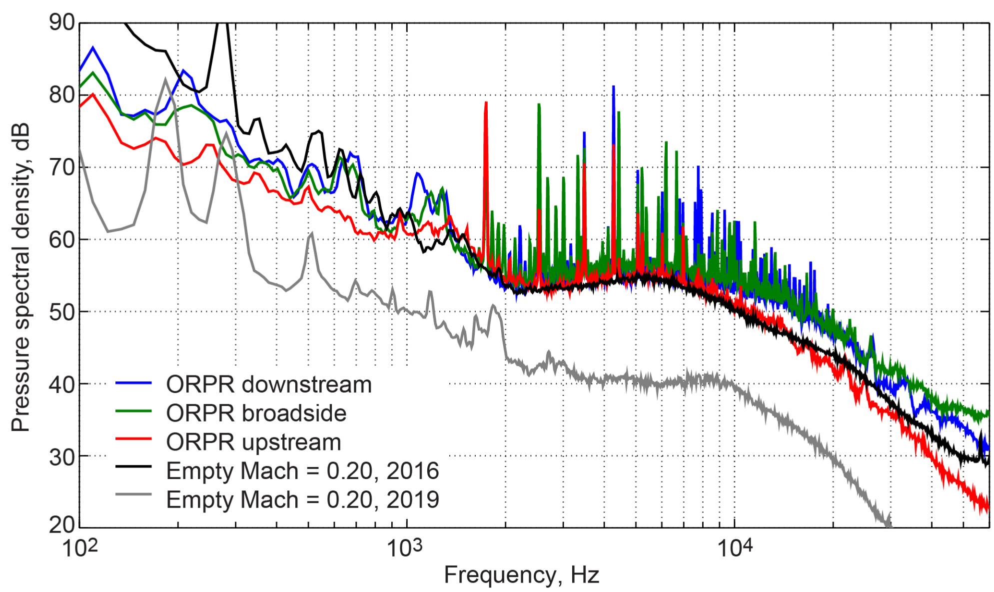

Figure 25.—Tunnel background noise compared with noise of open rotor propulsor model at low speed. Open Rotor Propulsion Rig (ORPR).

4.4 Tabulated Noise Data

One-third octave sound pressure levels observed in the preconstruction and postconstruction validation testing are tabulated in Table 1.

TABLE 1.—SOUND PRESSURE LEVEL BACKGROUND NOISE MEASUREMENTS IN 9- BY 15-FOOT LOW-SPEED WIND TUNNEL

Frequency, Hz	2016		2019	
	Mach 0.10	Mach 0.20	Mach 0.10	Mach 0.20
157	75.0	103.0	63.0	89.3
198	74.6	100.1	68.9	94.5
250	85.1	105.7	64.2	86.8
315	80.6	99.8	66.3	86.8
397	68.1	92.5	53.9	73.4
500	72.1	93.6	60.1	77.8
630	68.7	91.3	54.8	74.5
794	70.9	88.2	55.5	74.6
1,000	66.7	86.1	54.4	73.9
1,260	66.3	84.3	55.8	73.5
1,587	67.2	83.8	54.8	72.5
2,000	66.8	80.7	54.3	73.6
2,520	67.5	80.7	53.7	70.1
3,175	67.3	82.0	54.2	70.3
4,000	66.7	83.6	55.6	70.2
5,040	65.4	85.2	56.1	71.1
6,350	63.1	85.6	54.4	71.7
8,000	61.9	85.1	52.8	73.2
10,079	60.0	83.8	50.6	72.9
12,699	57.5	82.5	47.7	70.9
16,000	55.4	81.6	43.5	68.9
20,159	53.4	80.4	39.7	66.1
25,398	51.4	78.2	35.3	61.7
32,000	48.0	74.9	NA	57.6
40,317	45.3	72.6	NA	56.5
50,797	45.2	70.8	NA	NA

5.0 Impulse Response

A relatively common technique for evaluating the acoustic properties of an interior volume is an impulse response test. The method is fast and easy with modest equipment requirements and may give very useful qualitative information. The resulting measurements are not a substitute for a draw-away measurement using a tone source to give a quantifiable uncertainty for measurement accuracy, but the approach is a good complement to other test methods. The impulse response of the 9×15 LSWT was investigated some 20 years previously by Woodward et al. (Ref. 10). The results from that test were found to be very consistent with results presented here for the preconstruction facility. The main purpose of this section is to describe the test method used and compare the impulse response of the 9×15 LSWT before and after the construction project.

5.1 Test Method

The impulse for the test was generated using a hand-held starter pistol operated in the usual manner. Three test configurations were used, each with two microphones on tripods, oriented vertically to be roughly omnidirectional to sounds reverberating in the horizontal plane. The microphones and pistol were all positioned at the middle of the test section height. This test was conducted without using the facility steady-state data acquisition system (Escort) as no aerodynamic data was to be acquired. The usual 9×15 LSWT acoustics system (Ref. 19) composed of Brüel and Kjaer 4939 microphones, Brüel and Kjaer Nexus units, and an RC Electronics, Inc., DataMAX recorder set to 200 kHz were used. The typical microphone gridcaps were used as there was no airflow in the test section during these tests.

Three configurations of microphones and source were used, as shown in Figure 26 to Figure 28. Configurations 1 and 2 had the source and both microphones positioned approximately on tunnel centerline. For configuration 1, the pistol was pointed downstream, with the operator standing at the end of the contraction just upstream of the test section. For configuration 2, the pistol was pointed upstream with the operator standing at the start of the diffuser. These orientations were intended to measure the sound impulse reverberating around the tunnel loop, in the downstream and upstream directions, respectively. The use of two microphones with a spacing of 3 m (10 ft) gives a noticeable arrival time difference, so the direction of propagation can be determined. These configurations were reproduced relatively accurately before and after the construction task. Configuration 3 roughly replicates the typical orientation of fan tests in the facility. In 2016, the source was located at the fan stacking axis, while in 2019, the source was at the center of the turntable used for the fan drive rig. In both cases, the two microphones were positioned at the upstream and downstream ends of a typical traverse path, although the 2019 test section is about 137 cm (54 in.) longer, so the downstream microphone was further aft. A new traversing microphone system was still being developed at the time of the 2019 test.

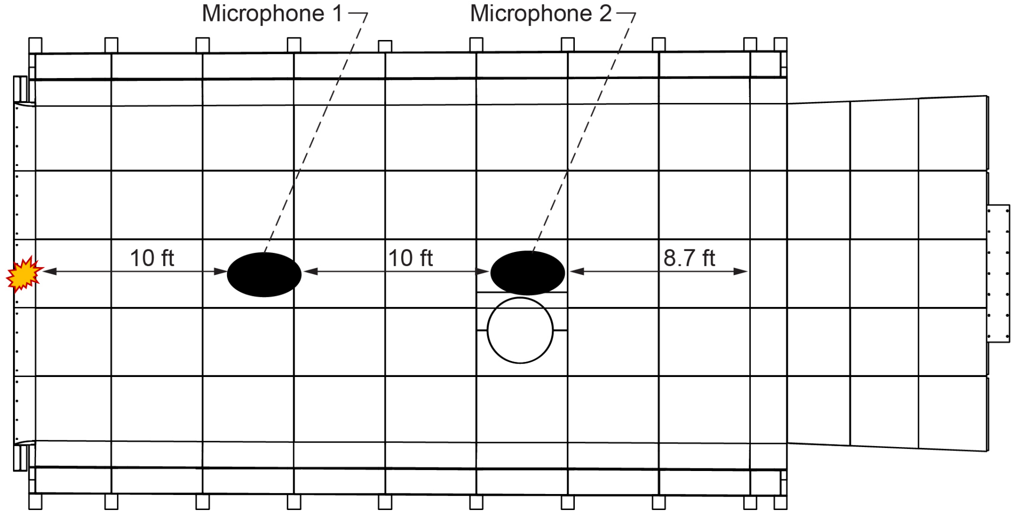

Figure 26.—Impulse response configuration 1, view from above.

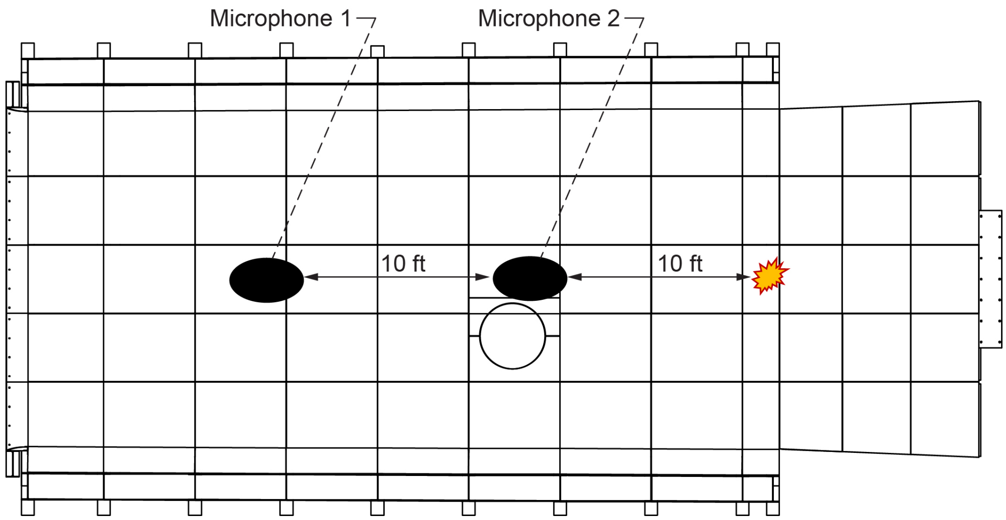

Figure 27.—Impulse response configuration 2, view from above.

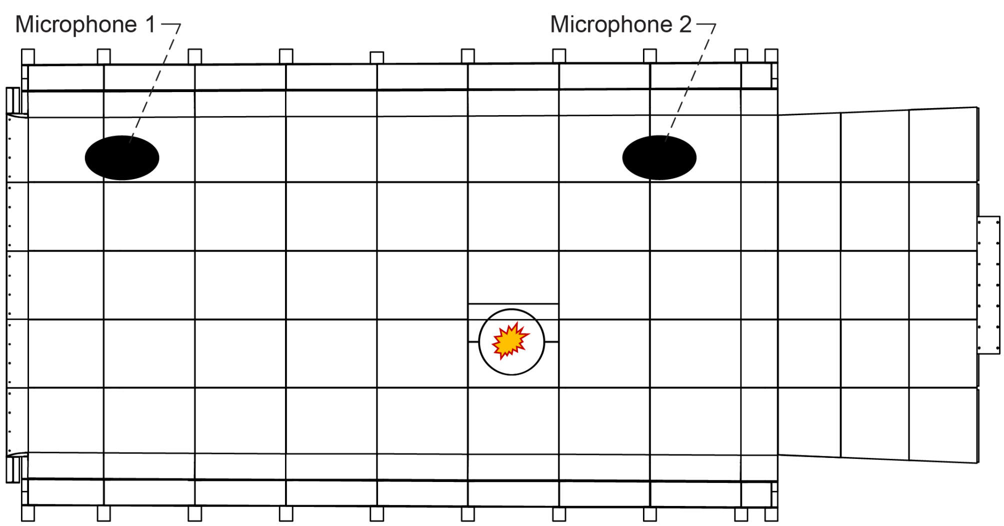

Figure 28.—Impulse response configuration 3, view from above.

For these tests, the wind tunnel was in the usual configuration for running the 9×15 LSWT leg, with doors 1 and 2 (in turn 2) and 4 and 5 (in turn 3) all closed, and door 3 (at the upstream edge of the 9×15 LSWT test section) open. The tunnel drive was off and minimal airflow was present in the tunnel leg. The personnel doors into the test section were closed. In the postconstruction tunnel, the starter pistol operator stood on a small piece of plastic panel to protect the floor from damage due to man load and shoes. Photographs of the test are shown in Figure 29.

Figure 29.—Experimental setup for impulse response measurements. (a) Impulse response test conducted July 22, 2016. View from upstream south camera, photograph of video monitor is of poor quality. (b) Impulse response test conducted June 17, 2019. View from north tunnel door, direct camera photograph. Door was closed and hearing protection applied before testing commenced.

5.2 Signal Processing

Three recordings were made in each test condition, with approximately a minute of time between each test to let long reverberations decay. The peaks of the three recordings were aligned and a mean time series was computed. The measurements were recorded at 200 kHz, and the mean signal was processed using a moving standard deviation window of 1,000 samples length or 5 ms. This was converted to decibels using 20 μPa reference pressure. The two microphones were sometimes operated with different amplifier gain settings, which caused the noise floor to change between channels and tests.

5.3 Results

Figure 30 shows the results for configuration 1, both before and after the construction project. The 16-bit resolution of the data system was stretched during these experiments, and the limit of maximum to minimum signal resolution is apparent as the level on the left-hand side of the graph. A study of the dimensions of the wind tunnel and the time delay for the various signals gives insight into the source of the reflections evident in the time history plots. A set of scale drawings showing the preconstruction and postconstruction 9×15 LSWT drawings is given in Figure 8. These drawings were interrogated as the impulse response measurements were reviewed.

In the preconstruction results, configuration 1 produced the clearest impulse response. These are shown in Figure 30(a), where a few major features are identified. “A” denotes the direct impulse, which is traveling downstream. “B” denotes the slope of the decay of reverberations within the test section. “C” is an upstream traveling reflection from the end of the upstream diffuser, where the expansion ratio changes suddenly. “D” is a downstream traveling echo from the vicinity of the upstream cooler. “E” identifies an upstream traveling reflection from the dump into turn 3. “F” is the biggest reflection of them all, and with a time delay of nearly half a second, it is clearly from the wall at the end of turn 3. This wall was treated from floor to ceiling with 20 cm (4 in.) of vinyl-coated foam. While this no doubt helped, a clap in the test section produced a very clear echo from this wall, so this result is not a surprise. Additionally, there was no acoustic treatment downstream of the test section except for this wall and the column in the middle of turn 3, which was treated similarly to the wall. For time delay higher than 0.5 s, the reflections become muddled as sound reverberated around the tunnel leg. Nearly all of these distinct echoes are gone from the postconstruction measurements, as seen in Figure 30(b). The only remaining echo seems to be E, although the amplitude is reduced approximately 15 dB.

After the construction project, configuration 2 produced the clearest impulse response, suggesting the principal reflections are now from upstream of the test section rather than downstream. In Figure 31(b), a set of reflections denoted “G” is readily seen, propagating from upstream. The time delay corresponds to the vicinity of the flow conditioner, the screens, honeycomb, and, probably, the trailing edges of the new serpentine baffles. The amplitude of these reflections is such that they would have been obscured in the 2016 preconstruction measurements. An upstream traveling reflection denoted “H” is from either the end of the treated part of the new diffuser or the upstream edges of the downstream turning vanes. The timing corresponds rather closely with reflection E in Figure 30(a), although the amplitude is reduced by around 25 dB. This is reasonable, as the entire diffuser is now lined with acoustic treatment, except for the access ramp in the center of the floor. Results from configuration 3 are presented in Figure 32 for completeness.

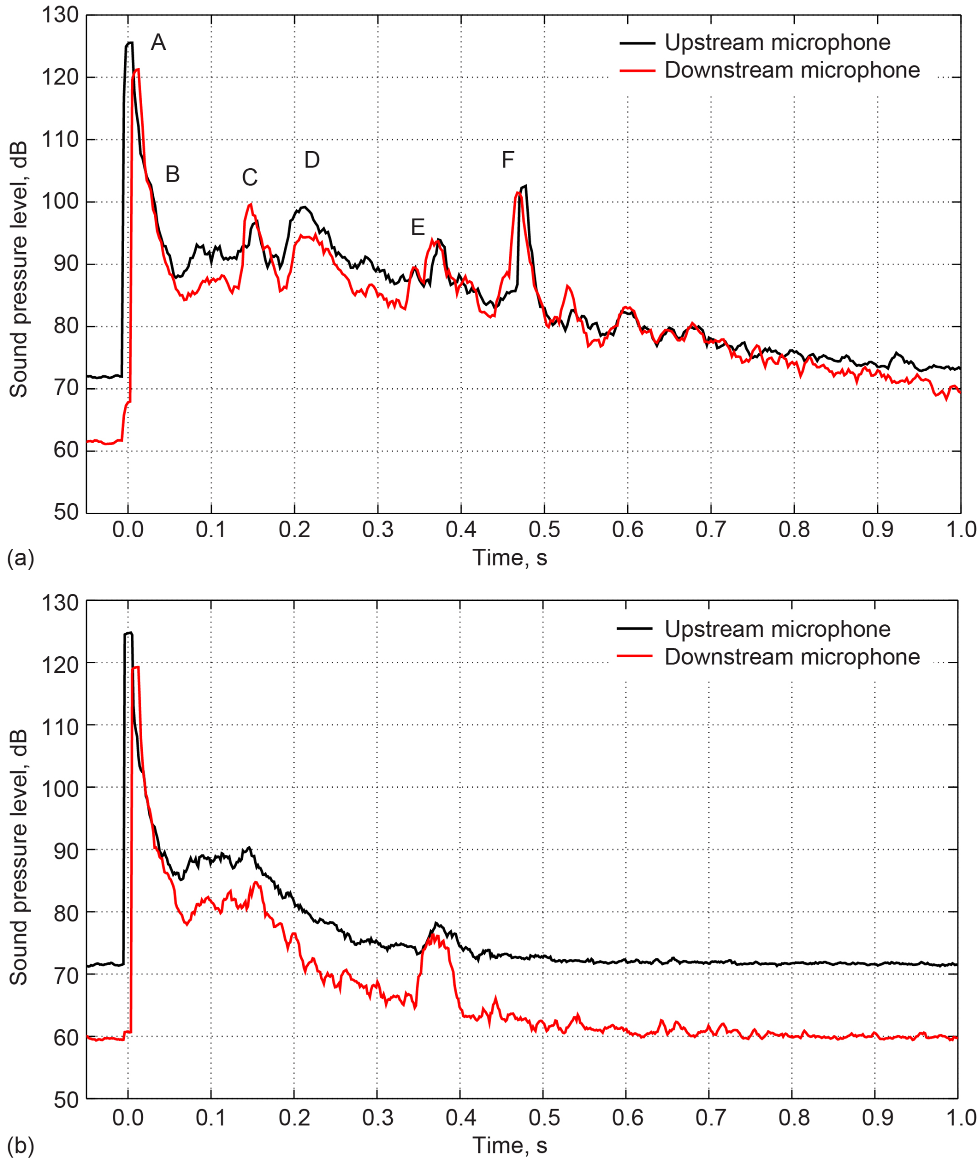

Figure 30.—Impulse response measurements for configuration 1. (a) 2016. (b) 2019.

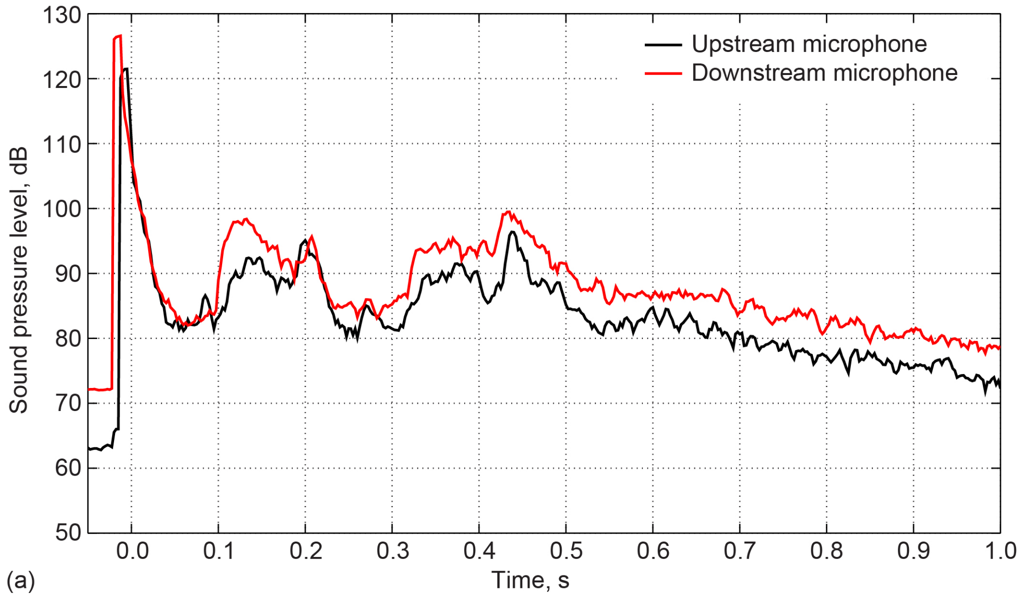

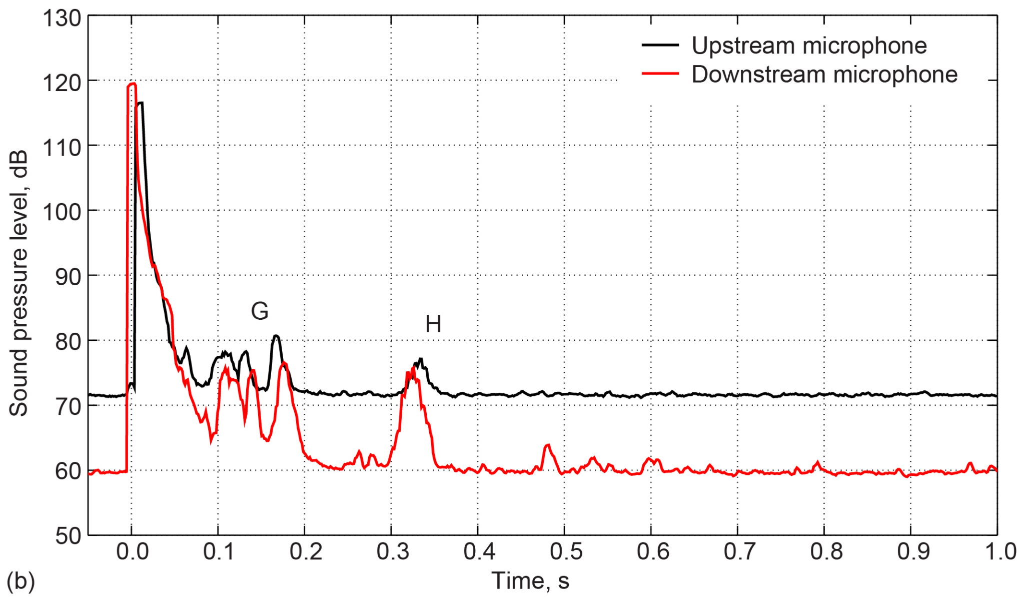

Figure 31.—Impulse response measurements for configuration 2. (a) 2016. (b) 2019.

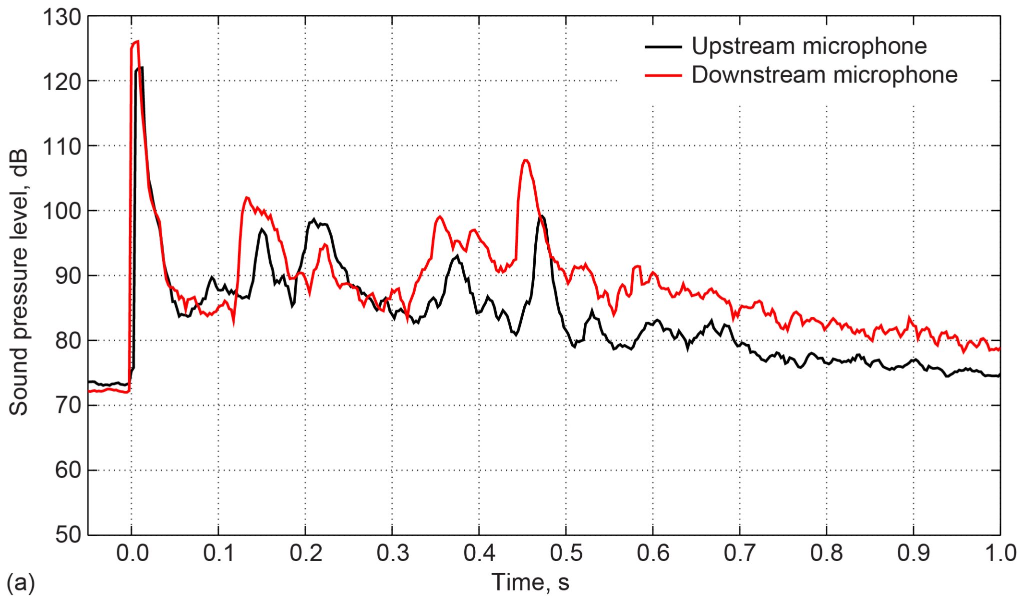

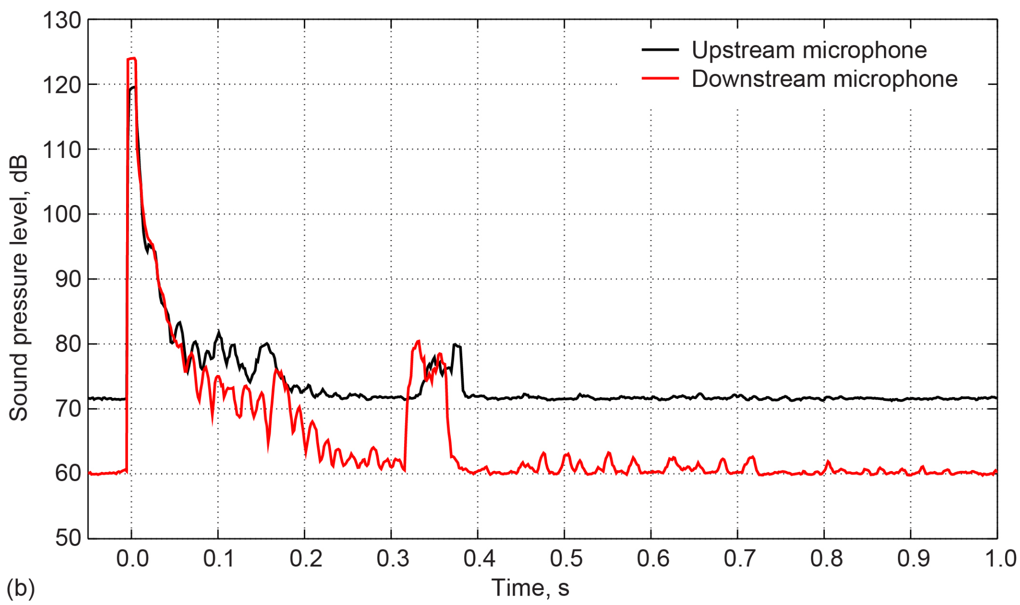

Figure 32.—Impulse response measurements for configuration 3. (a) 2016. (b) 2019.

5.4 Summary

A summary of the impulse response measurements, preconstruction and postconstruction is given in Figure 33. This visually illustrates the improvements in the impulse response, and the reader is reminded that the ideal response is a delta function to mimic what would be recorded in free space. A few quantifiable metrics can be pulled from this result. As seen in Figure 33(a), with a peak signal level of about 120 dB, it can be readily seen that secondary reflections are reduced from –20 to –34 dB. Figure 33(b) shows data from configuration 3 processed using a 0.25-ms (50 sample) moving window. This allows looking at short time reflections, such as those within the test section. The initial peak shows the direct sound reflections from the floor and ceiling are delayed by about 1 ms, and reflections from the sidewall are delayed by about 2.5 ms. It can be seen that the secondary reflections are reduced by approximately 9 dB in the 2019 test section.

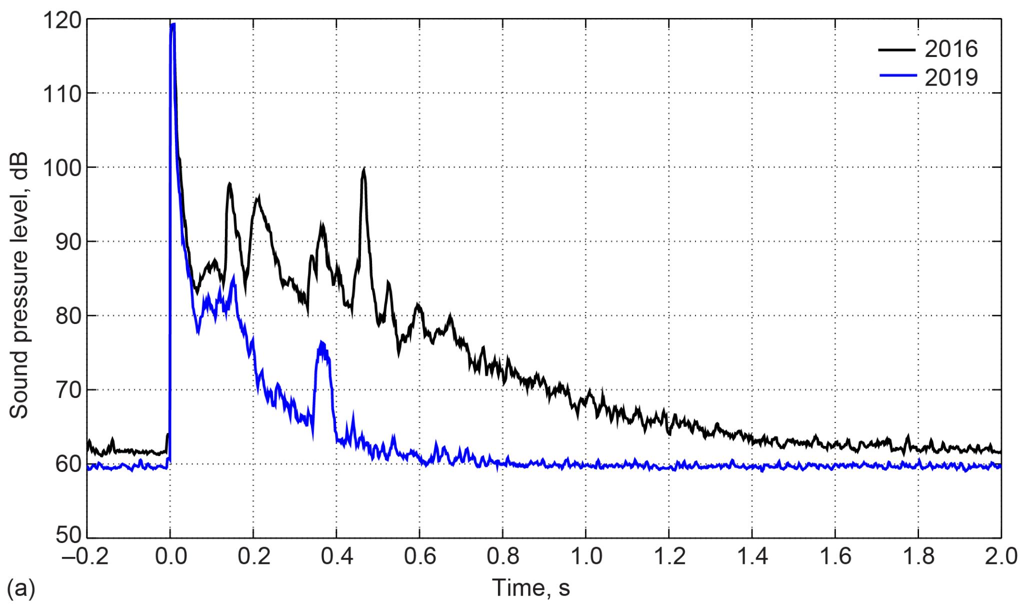

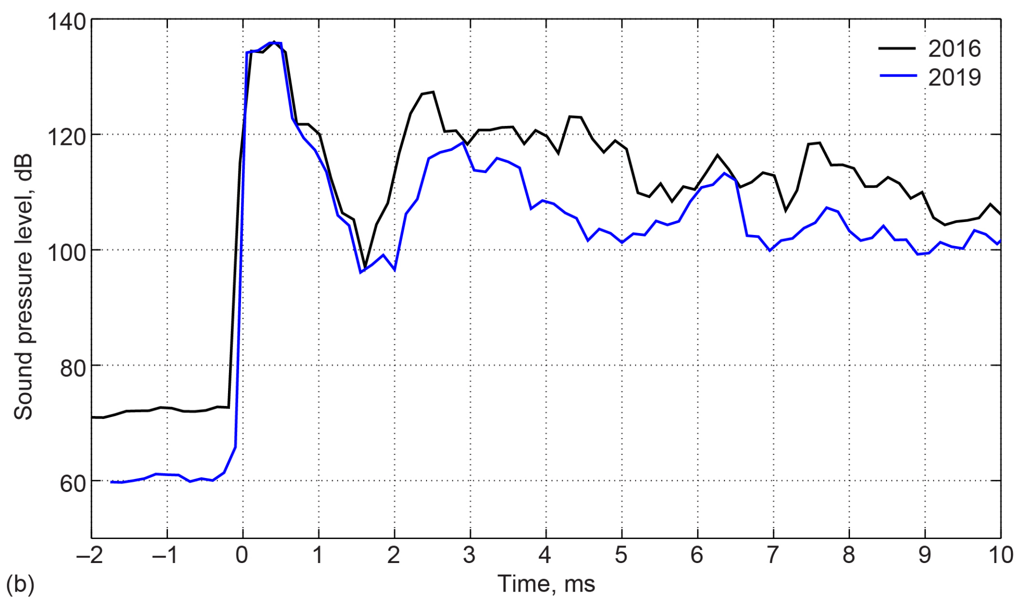

Figure 33.—Impulse response, 2016 versus 2019. (a) Configuration 1, microphone 2, 5-ms window. (b) Configuration 3, microphone 2, 0.25-ms window.

Additionally, the metric L_{eq} captures levels of time-varying signals. This metric is given in Equation (1),

$$L_{eq} = 10\log_{10}\left(\frac{1}{T}\int_0^T \frac{p^2(t)}{p_o^2}dt\right) \tag{1}$$

where T is the measurement duration, $p(t)$ is the sound pressure signal, and p_0 is the reference pressure of 20 µPa. The amplitude L_{eq} was calculated twice for each curve, using an integration time of 14 ms and then 1 s. The duration T of 14 ms was chosen as representing about 20 dB down from the main peak, while the duration 1 s was chosen as capturing most of the large reverberations in the record. In this way, an error can be calculated for each measurement as $L_{eq,1000ms} - L_{eq,14ms}$. According to this metric, the error in L_{eq} has been reduced from 0.8 to 0.2 dB.

6.0 Reverberation Time

A common metric for speech intelligibility in a room is the reverberation time. This is commonly used in architectural acoustics but is a quick and effective test to perform and gives a quantitative metric for the acoustic quality of a room. This section describes a set of tests performed using an interrupted noise method to determine the reverberation time in the 9×15 LSWT test section.

6.1 Experimental Method

Measurements of the reverberation time in the 9×15 LSWT were made using a CESVA Instruments SLU FP121 dodecagon speaker system, including a model AP601 power amplifier and BP012 12-element speaker. Preconstruction testing was conducted on Feb. 21, 2012, while postconstruction testing was performed on June 17 and 18, 2019. The testing method largely followed the specifications for interrupted noise testing described in ISO 354 (Ref. 22). The speaker was kept at the typical model mounting location, as shown in Figure 34. The traversing microphone (not shown in Figure 34 but previously pictured in Figure 4) was already installed in the test section so it was utilized as the acoustic instrumentation. It could be easily and remotely positioned along the length of the test section.

In 2012, a Stanford Research Systems DS360 function generator was used to provide a white noise signal to the AP601 amplifier, controlled from the Auxiliary Control Room. In 2019, the AP601 built-in noise generator was used instead of the DS360. This is believed to be responsible for the higher sound level recorded in 2019. The timing of the signal termination and data recording was handled manually. When the speaker was turned on, the test section was “ensonified” (filled with sound). The microphones were recorded on the usual RC Electronics DataMAX system. While the recording was active, the sound source was abruptly shut off and the sound field decayed. This was repeated 10 times for improved statistics. Triggering was done by hand, from a location outside the test section. The test section was in an “empty” configuration with the personnel doors closed as though ready for airflow.

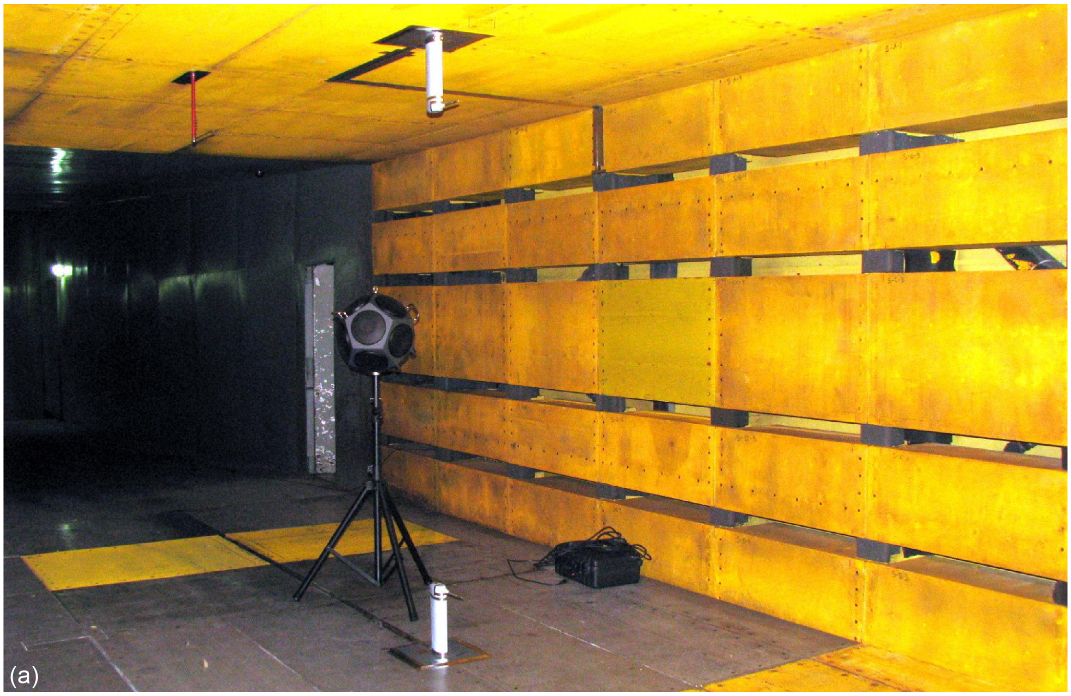

(a)

(b)

Figure 34.—Experimental setup of dodecagon speaker in 9- by 15-Foot Low-Speed Wind Tunnel test section at location of typical fan model. (a) Test conducted Feb. 21, 2012. Looking downstream towards south wall side door. (b) Test conducted June 17 and 18, 2019. Looking upstream from diffuser ramp.

6.2 Signal Processing

The recorded acoustic time histories were digitally filtered on a one-third octave band basis into 30 bins ranging from 100 Hz to 80 kHz. The speaker produced usable signal levels (at least 15 dB above the background) between approximately 250 Hz and 15 kHz. These filtered signals were then converted to sound levels using a moving window standard deviation computation with window length of 10,000 points, or 50 ms, at the 200-kHz sample rate of the recording. This gives noise level as a function of time. The speaker shutoff time was determined from the measured sound level, but this precise value is not necessary for the subsequent data processing. The time histories of pressure standard deviation for each one-third octave band were then down-sampled by a factor of 100, giving a new sample rate of 2,000 Hz. This was convenient for data storage and graphing and had no significant impact on the results since it was done after all the frequency-dependent signal processing was completed. Finally, each of the 10 individual measurements were averaged before being converted to decibels.

6.3 Postprocessing

A selection of results from testing is given in Figure 35. The center frequency bands of 630 Hz, 5,040 Hz, and 12.7 kHz were chosen as spanning the frequency range expected for model scale testing. Examining the 2012 result in Figure 35, it can be seen that the different frequencies show a varied and complicated response. At 630 Hz, both early and late reflections are observed. The early reflections quickly decay to about 12 dB below the starting sound level while the sound termination is observed in the late reflections to occur at about 0.4 s. This corresponds to a round trip distance of around 140 m, roughly the distance from the test section to the downstream wall of turn 3. A more gradual rolloff is observed at 5,040 Hz, suggesting multiple reflection paths. At 12.7 kHz, the late reflections were not observed down to the microphone system noise floor of more than 25 dB below the initial noise level.

As described in ISO 354, the reverberation time is typically given as RT60, the time required for the sound to decay 60 decibels. Directly measuring this would require a source that could produce more than 60 dB of noise above the noise floor of the room and measurement system. Since this is not always possible, a smaller decay is measured, and the RT60 is extrapolated from that. Using this method, RT60 was calculated and is shown in Figure 36. These numbers suggest that prior to the improvement project, the 9×15 LSWT test section is too reverberant to use as a lecture room.

Based on the suggestion by Spalt et al. (Ref. 23), who conducted an acoustic calibration in the NASA Langley 14- by 22-Foot Subsonic Tunnel, the interrupted noise results were used to calculate the effective signal-to-noise ratio (ESNR), as shown in Figure 37 for the one-third octave band frequency around 1 kHz. This is the measured level difference in decibels between the starting noise level and the start of rolloff due to reflections. This should be the difference in sound level between the incident sound and the reflected sound. The difference between the starting noise level and the background noise level is denoted as the reverberation time signal-to-noise ratio (RTSNR) for convenience.

The resulting values are plotted in Figure 38. When the ESNR is not measurably less than the RTSNR, the ESNR cannot be determined accurately. This happens both at low frequencies, where the sound source produced only a very weak signal, and at high frequencies, where the reflections are too weak to measure. If the ESNR and RTSNR are essentially the same, the RTSNR can be considered to set a lower bound for the ESNR. Figure 38 shows that reflections in the 9×15 LSWT test section can be expected to be at least 15 dB below the incident signal between 200 Hz and 20 kHz.

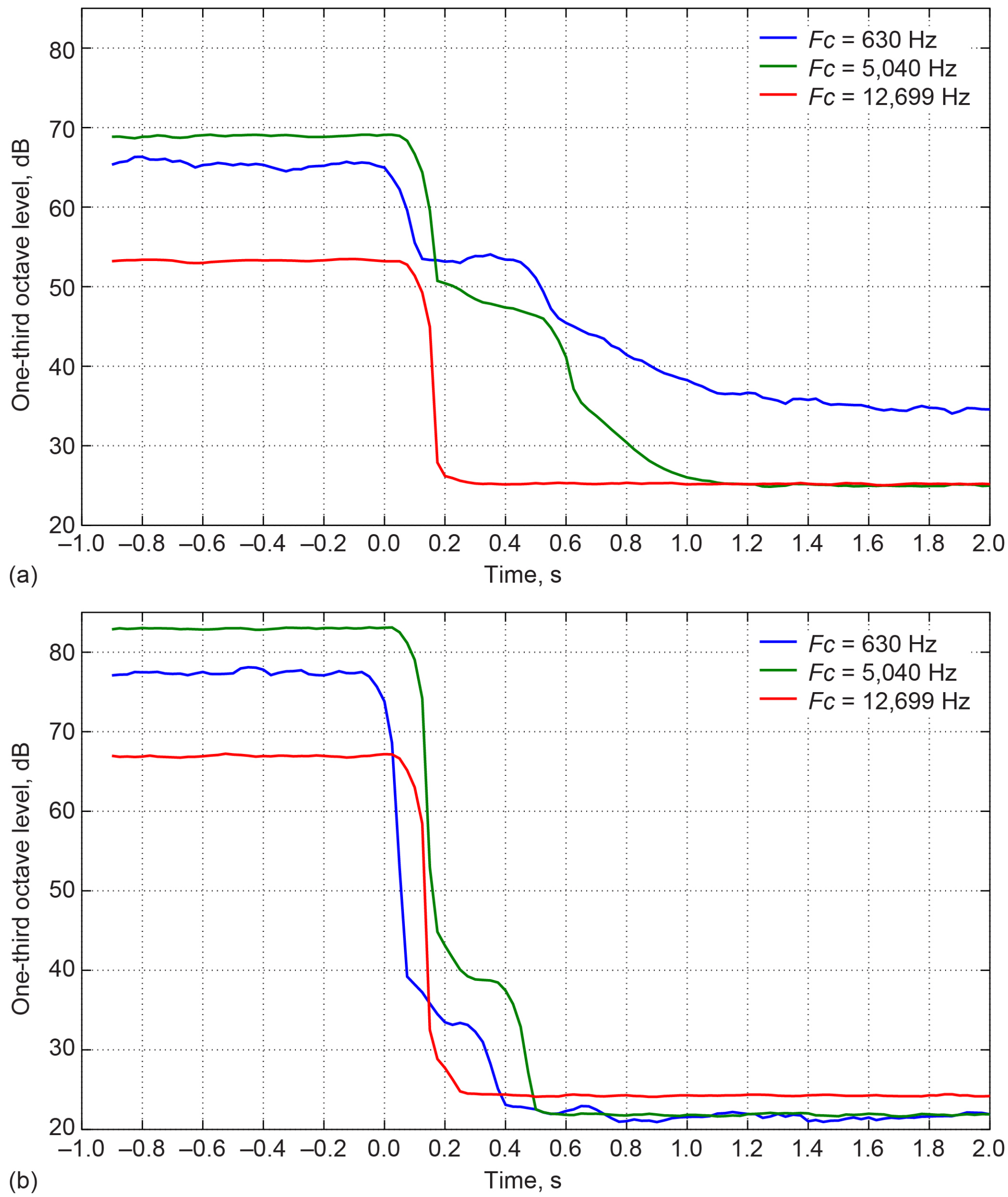

Figure 35.—Example reverberation time measurements. (a) 2012. (b) 2019.

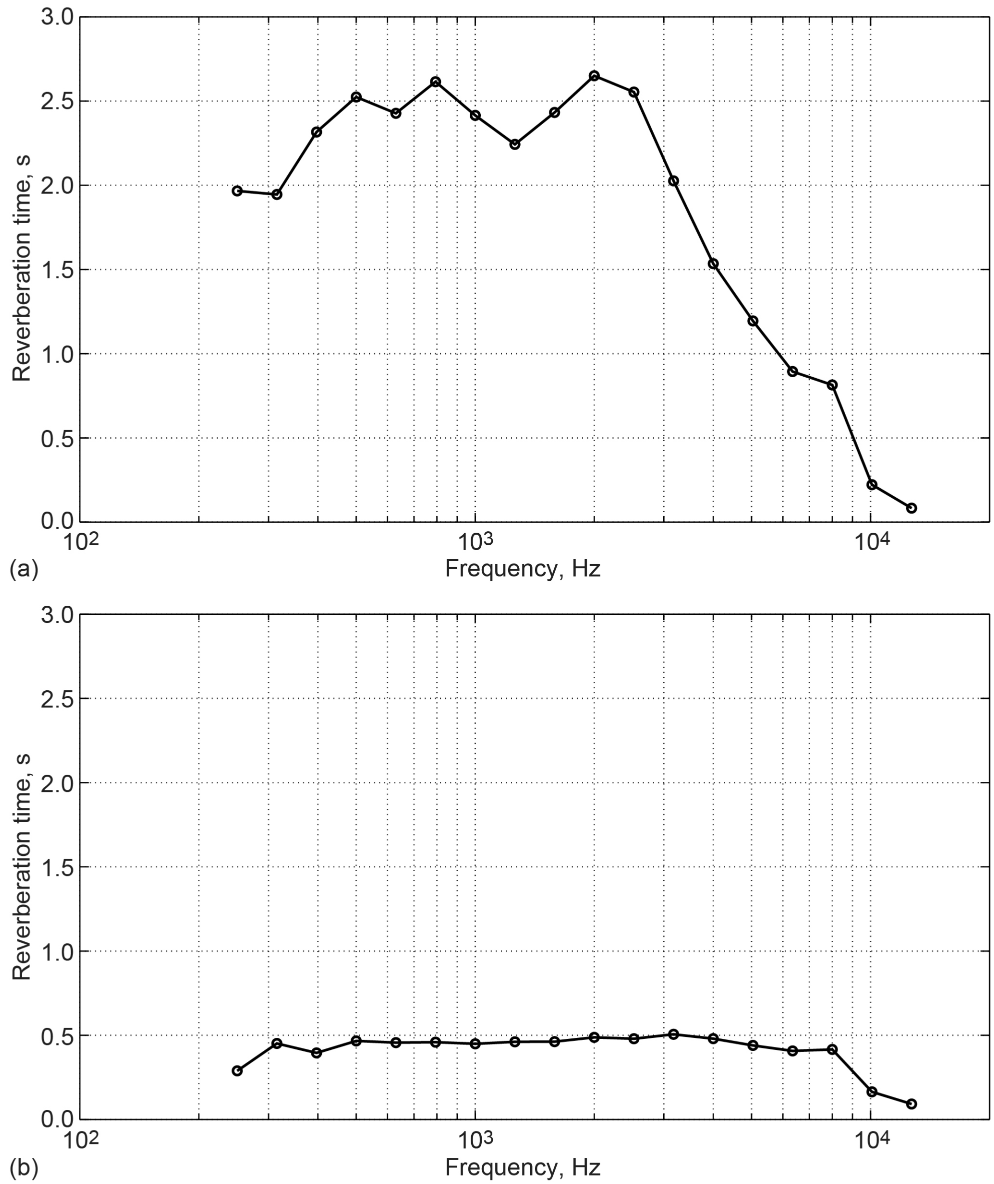

Figure 36.—Reverberation time (RT60) measurements. (a) 2012. (b) 2019.

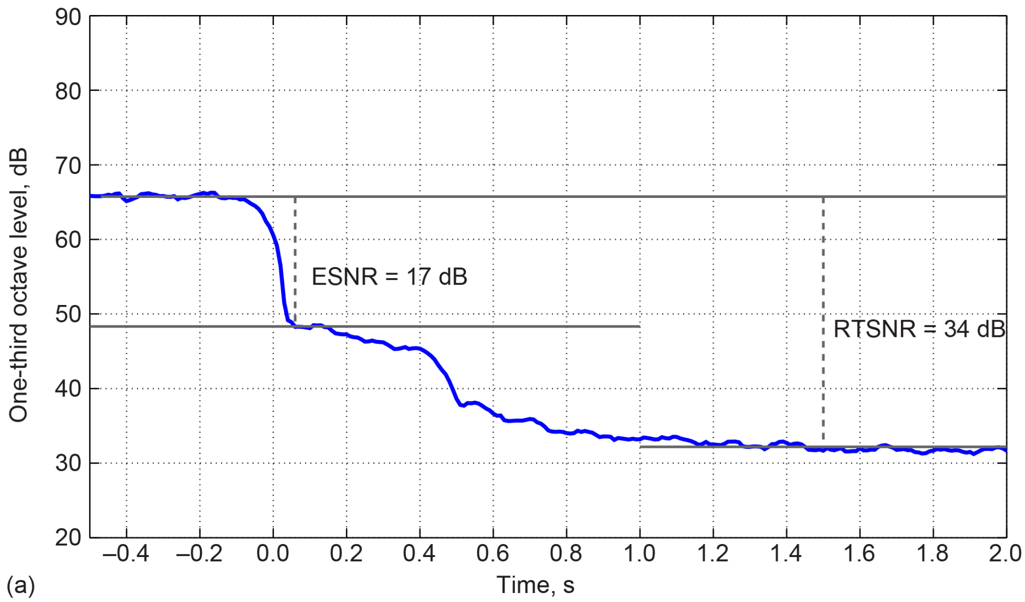

(a)

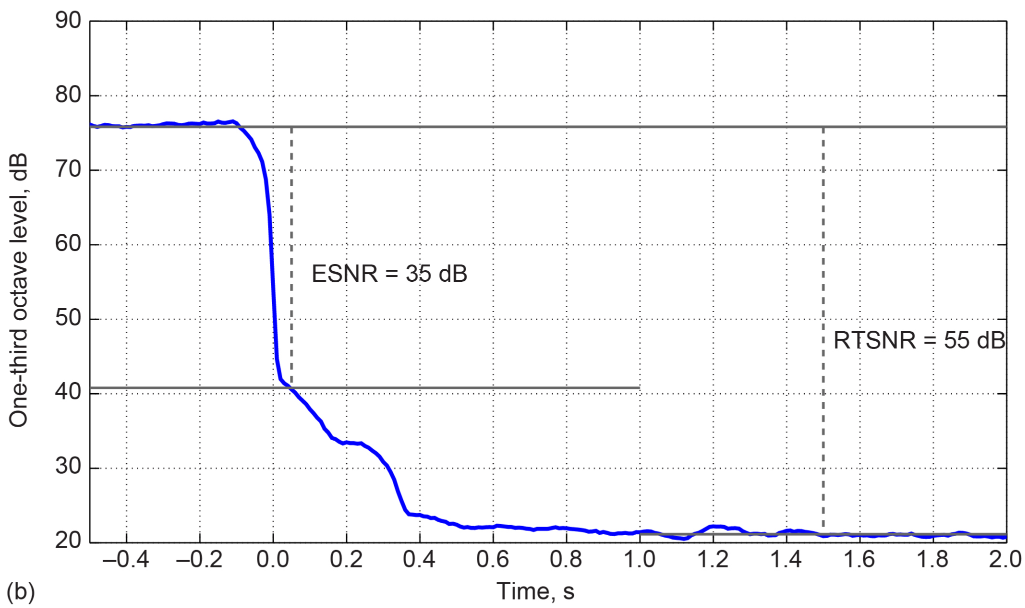

(b)

Figure 37.—Example effective signal-to-noise ratio (ESNR) and reverberation time signal-to-noise ratio (RTSNR) for 1,000 Hz. (a) 2012 measurements. (b) 2019 measurements.

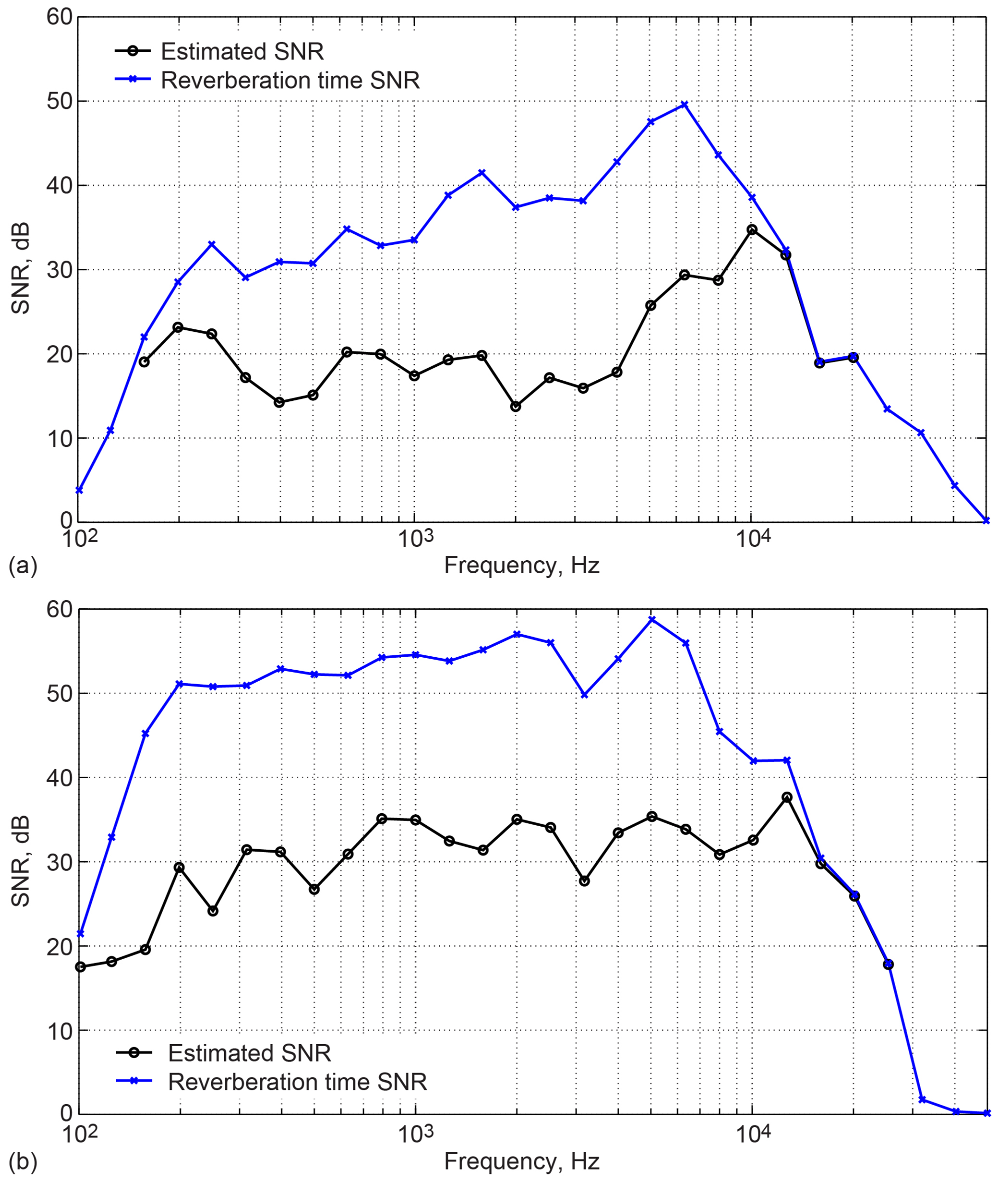

Figure 38.—Resulting signal-to-noise ratios (SNRs) for all frequencies measured. (a) 2012 measurements. (b) 2019 measurements.

7.0 Draw Away

The most elaborate and sensitive test that was used to quantify the anechoic quality of the test section is the draw-away test. An omnidirectional sound source is placed at a location of interest in the test section. While the speaker is continuously producing a tone, a microphone measures the sound level at different locations in the test section. This is typically along a ray passing through the center of the speaker, as described by ISO 26101 (Ref. 24), but it could be another path of interest such as the traverse sideline. The expected "decay with distance" of the noise is an inverse square of distance r, $1/r^2$, and deviations from this are assumed to be due to reflections from the tunnel walls, which cause constructive and destructive interference. This test is extremely sensitive, but time consuming and requires specialized equipment. A simulation result showing the sound field generated by a tone source with partially reflecting walls is shown in Figure 39. Traversing a microphone through this sound field will reveal the oscillations in amplitude, even as the source emits a constant noise level.

7.1 NASA Assessment

Spherical spreading tests were previously conducted in the 9×15 LSWT by Dahl and Woodward (Ref. 9). Following this example, along with the ISO 26101 standard and other papers discussing the topic (Refs. 24 to 27), we decided to build a rig for measuring spherical spreading. The source was a JBL 2426H horn driver plumbed with pipe fittings into a 6-mm (1/4-in.) tube. The tube has a right-angle bend about 8 cm (3 in.) from the end, such that the height of the effective source is at tunnel centerline. The tube was wrapped with pipe insulation, and the driver was encased in a conical metal shell and covered with a dense vinyl. A lightweight traverse was built using extruded aluminum to move a single hanging microphone through the sound field. The combined system is shown in Figure 40.

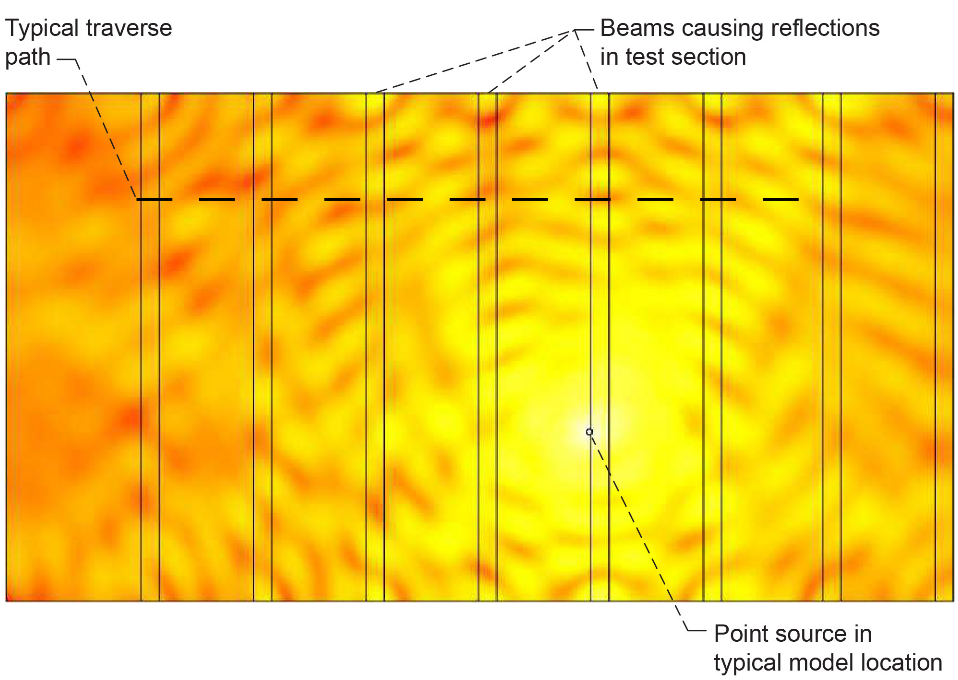

Figure 39.—Simulation illustrating standing waves in 1986 test section, with strong reflections off structural beams. Figure is intended to be qualitative.

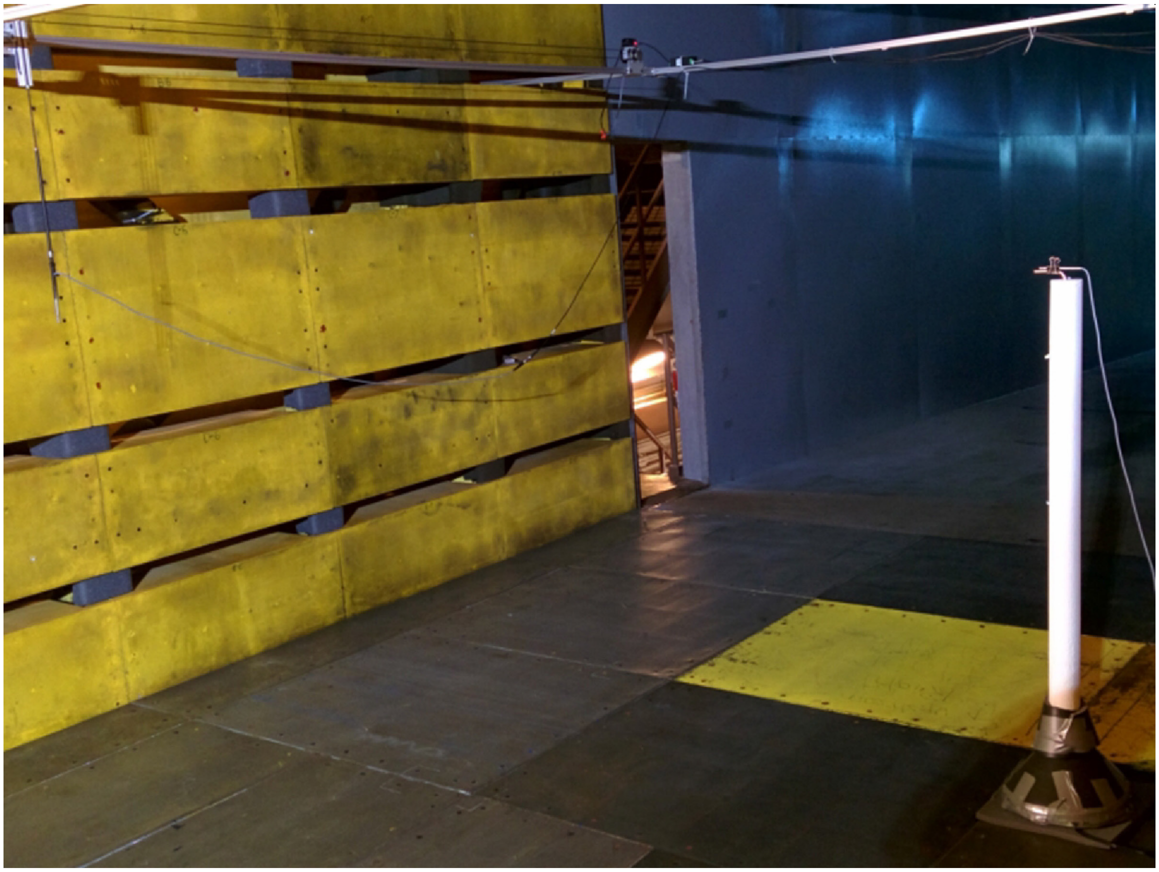

Figure 40.—NASA-developed draw-away test equipment in 9- by 15-Foot Low-Speed Wind Tunnel (9×15 LSWT) preconstruction. Utilizing this equipment, we investigated sound field in preconstruction 9×15 LSWT.

We became convinced that the structural beams in the original design caused standing waves in the test section and motivated us to advocate for a new test section with uniform deep acoustic treatment. Additionally, we decided to contract with an established acoustics firm with experience qualifying anechoic chambers to the ISO 26101 standard. The contractor would perform a more thorough investigation of the facility, and hopefully, provide clearer insight into the potential for improvements.

Figure 41 shows one example of data we collected. For this example, the sound source emits a steady tone at 1,000 Hz, and a microphone makes measurements of the tone amplitude at various distances away. The measured tone amplitude is then corrected for spherical spreading to give a "distance-corrected tone level." When the microphone is close to the source, the reflections are a minor effect, and the amplitude is near 0 dB. The further the microphone is from the sound source, the reflections cause larger deviations in the tone amplitude.

The 1988 data in blue dots was extracted from the previous assessment by Dahl and Woodward (Ref. 9). Their spherical spreading assessment was developed independently before the ISO standard (Ref. 24). A horn is a highly directional sound source and might be preferable for focusing on only a single reflection. They are also very efficient radiators. Plumbing a compression driver into a small tube gives a much better omnidirectional source but loses a lot of sound amplitude and may give an undesirable frequency response. In any case, the measurements shown in Figure 41 indicate that for small errors, measurements should be taken close to the model and at the typical 88-in. sideline. The tone measurement uncertainty at 1,000 Hz might be several decibels. More study was warranted.

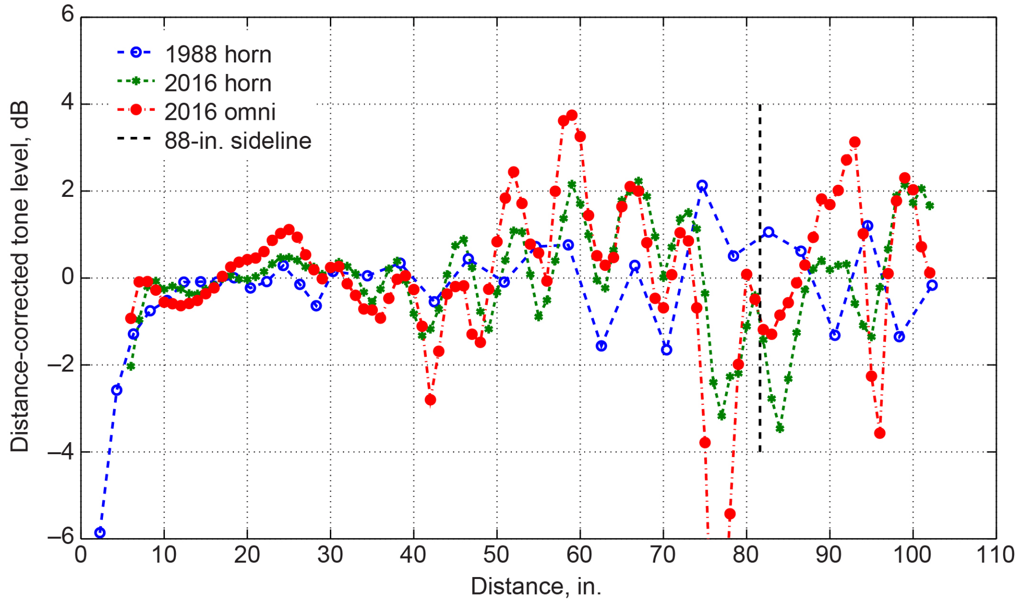

Figure 41.—Measurement of spherical spreading at 90° across test section and 1,000 Hz.

7.2 Contractor Assessment

Anechoic chamber evaluation specialists ViAcoustics and ETS-Lindgren were contracted to perform a draw-away test based on ISO 26101, both before and after the construction project. The two test configurations are shown in Figure 42.

The equipment used for these draw-away tests was mounted on tripods and could be arranged in a number of orientations. For all tests, the sound source was located in the middle of the test section height. In 2016, the source was approximately at the location that the hub of a fan model would be at when installed on the NASA fan model drive rig. In 2019, the sound source was placed above the center of the turntable installation location. This location is approximately 160 cm (63 in.) downstream of the fan hub. The entire tunnel frame was removed during the construction project and rebuilt to new external dimensions, and the test section was lengthened by 137 cm (54 in.). Ultimately, it was decided that repeating the test setup precisely was not required. Qualitative sketches showing the draw-away test paths are given in Figure 43.

The complete results from both test campaigns are given in a pair of reports (Refs. 28 and 29), so only a summary of the improvement will be included here. As reported by Schmitt in Reference 29, the maximum deviation from the inverse square law along the three horizontal traverse paths intersecting the typical NASA survey locations was reduced at all frequencies above 500 Hz and by an average of 2.5 dB.

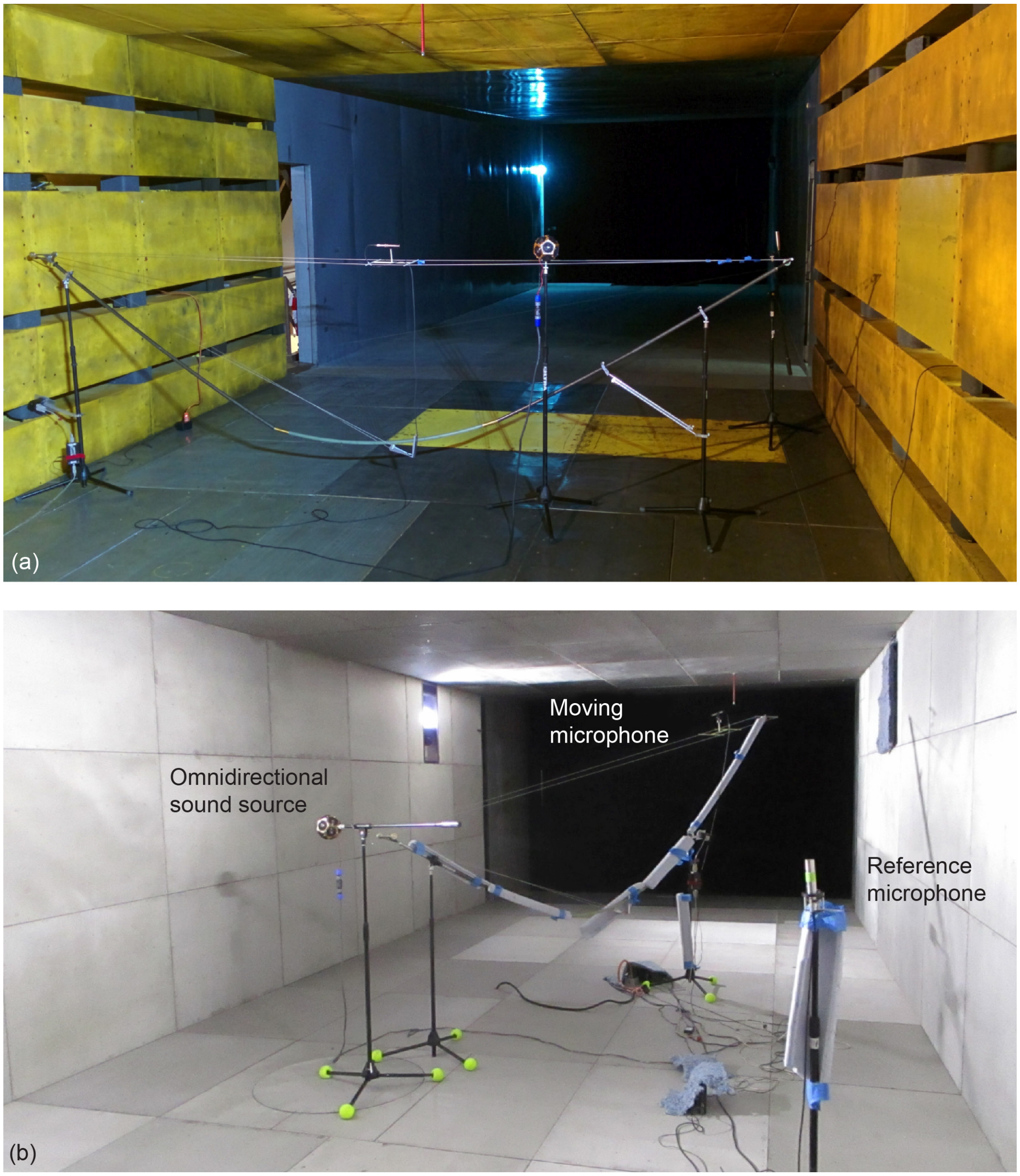

Figure 42.—Experimental setup for draw-away testing measurements. (a) Draw-away test conducted July 22, 2016. Looking downstream. (b) Draw-away test conducted June 25, 2019. View from north tunnel door. Door was closed before testing commenced.

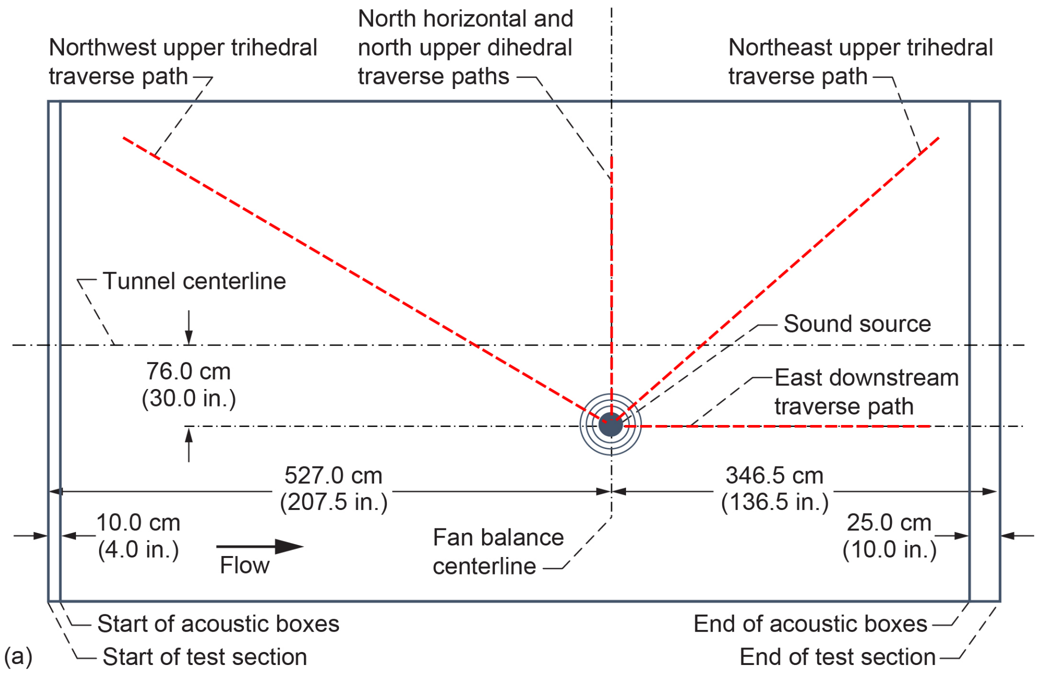

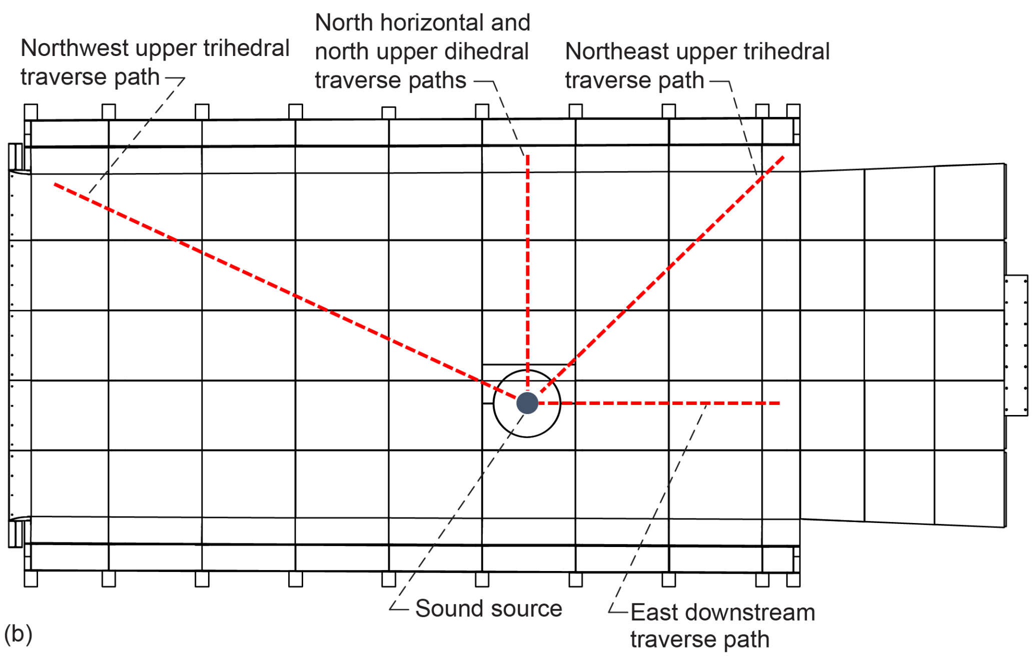

Figure 43.—Draw-away paths used in contractor assessment of test section anechoic quality. (a) 2016. (b) 2019.

8.0 Acoustic Box Testing

The walls, floor, and ceiling of the 9×15 LSWT are built of individual acoustic boxes, most are approximately 90 by 120 cm (3 by 4 ft). As described in Reference 1, the design of these boxes was developed in part by extensive testing in the NASA Glenn Acoustical Testing Laboratory (ATL) (Ref. 30). The test method used is a variation of the one described in the 40- by 80-Foot Wind Tunnel improvement project publications (see Figure 18 of Ref. 31 and supporting text). That publication cites a series of reports by Wilby and White and Wilby. These reports were not available, but Reference 31 contains sufficient description and diagrams of the method such that a similar experiment could be developed. The technique is related to the impedance tube methods for measuring absorption coefficient and impedance (Ref. 32) but has the advantages of being able to test larger samples and at a much wider frequency range.

The concept is to measure the acoustic reflection from an isolated acoustic box or subassembly made of panels and absorber materials. A speaker emits a short time chirp, which reflects off of the sample and is measured by a microphone. The chirp is short enough that time windowing gives the reflected sound separately from the incident sound. To serve as a reference, the same measurement is repeated with a steel sheet covering the test panel. The steel sheet is assumed to be perfectly reflective. The principal assumption is that the complex reflection coefficient is the transfer function between the sound reflecting off a treated panel and the solid steel sheet.

8.1 Experimental Setup

Since the experiment uses short time pulses, an anechoic environment is not strictly required for this measurement. A low background noise level is very helpful, because the short time signal from a speaker will not have very much energy and could be easily contaminated by ambient noise. Any sufficiently large and quiet space would be usable. These tests were all performed at the NASA Glenn ATL. In theory, a small and portable unit could be used to make similar measurements in the 9×15 LSWT test section.

The implementation of the method used for this report is described briefly. A speaker is pointed at the panel to be tested, with the largest practical distance between them. This distance should be chosen such that sound reflections from other surfaces (walls, floor, and ceiling) do not impact the measurement. A microphone is positioned between the speaker and the panel, approximately 2/3 of the way from the speaker to the panel and pointed at the panel. The speaker is used to emit a short time sound signal, on the order of 2 ms but dependent on the amount of space available. This sound would then pass over a microphone positioned between the speaker and the panel being tested, reflect off the panel, and then back to the microphone. The key is that the geometry of the room and the shortness of the time signal ensure that during the few milliseconds the reflected signal is received by the microphone, it is the only signal received by the microphone. Also, during a series of tests, the positions and overall geometric relationship between the components must be maintained. One of the panels in the test series must be a solid plate, assumed to give a perfect reflection. The panels should be flat, which is not always the case when dealing with sheet metal.

The signal sent to the speaker was a white noise burst, and a different signal was sent as the process was repeated many times, typically 100. The same seeding was used for the random number generator, so the 100 white noise signals were identical between tests. Even though the signal output from the data system had a flat frequency response, the amplifier, 80-Hz high-pass crossover, horn driver, and horn all modify the signal before it is converted to a pressure wave in the test chamber. These effects should all cancel out in the data processing, as discussed in the following section. A virtual instrument was created in National Instruments™ LabVIEW software to conduct the experiment and record the data. A screen capture of the software is shown in Figure 44.

As part of the data processing, a test with a solid steel panel is always conducted to give a reference “absorption coefficient = 0” measurement. This is assumed to account for the finite size of the test panel, atmospheric conditions, microphone directivity response, and other practical concerns. The test with the solid panel must be conducted in the exact same geometric setup configuration as the treated panels being tested and as close in time as practical. This reflection from a solid panel also lets the experimenter determine the exact time window when the reflection is arriving, as it might be difficult with a highly absorptive panel and corresponding small return signal.

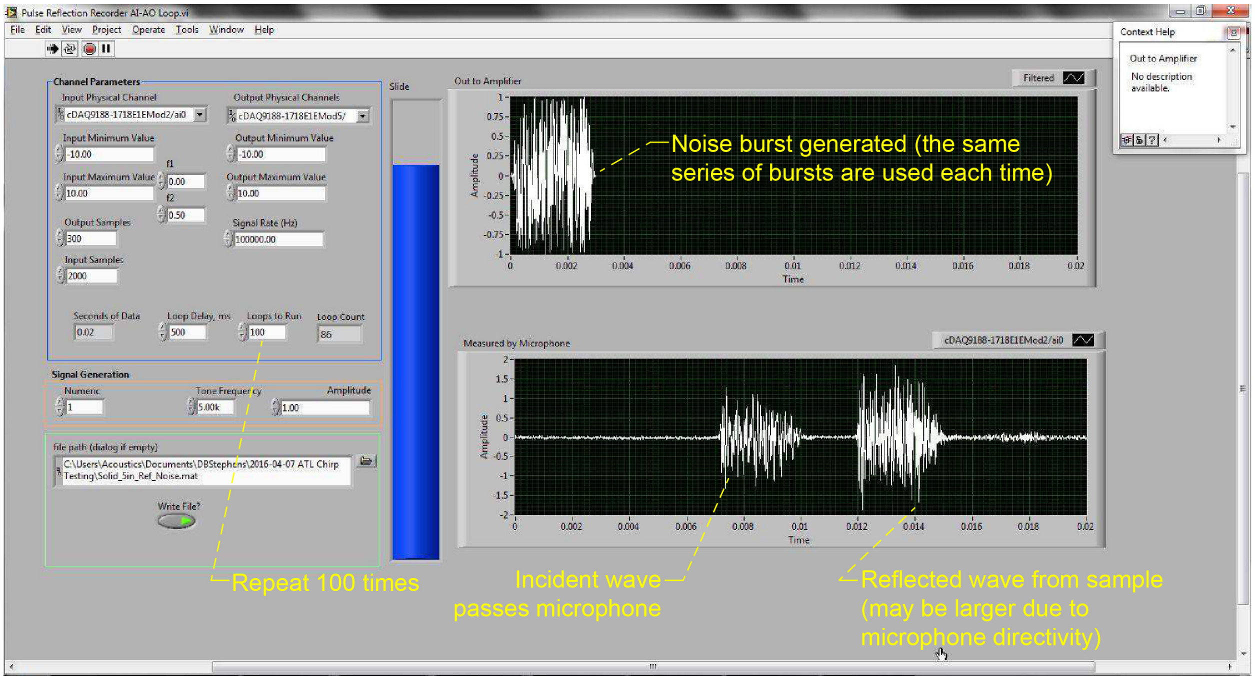

Figure 44.—National Instruments™ LabVIEW program used for sound burst testing, one channel version.

An improvement to the setup was to use three microphones positioned at different heights above the sample. The intention was to reduce sensitivity to the microphone placement; thus, three different locations could be measured at once. A photograph of the experimental setup including the three microphones, an acoustic box, and the solid steel sheet are shown in Figure 45. The microphones are roughly 20, 30 and 40 in. above the top of the sample.

The equipment used for this testing included a Yamaha P7000S power amplifier, JBL 2426H horn driver with a Selenium HL14–25 horn, and National Instruments™ NI–9222 DAQ chassis with a cDAQ–9188 analog input card and cDAQ–9269 analog output card. The microphone system was Brüel & Kjaer 4939 microphones with Falcon Range 2670 preamplifier. Microphones were calibrated using a GRAS Sound & Vibration 42AP pistonphone. The D/A and A/D sampling rates were both 100 kHz.

8.2 Absorption Coefficient Calculation

Sample time history recordings from the three microphones are shown in Figure 46. Only the reflected sound signal is used for the analysis described here. The example measurements are from new 9×15 LSWT acoustic box C27, which is one of the best boxes tested to date.

The short signal pulses that were reflected off the panel and recorded by the microphone were processed in order to get a frequency dependent spectral density function. The best practice for doing this was found to be Welch's method with a Hamming window of the same length as the pulse, and with zero overlap, in order to calculate $\overline{p^2(f)}$. This gives the sound pressure spectral density of the reflected sound. Since the signal chirp was 200 samples at 100 kHz, the frequency resolution available using this method is 500 Hz up to 50 kHz. The pressure spectral density of the reflected sound from the solid and treated sample are shown in Figure 47. The sound level of the reflection from box C27 is shown to be reduced by 5 to 15 dB compared to the solid reflection.

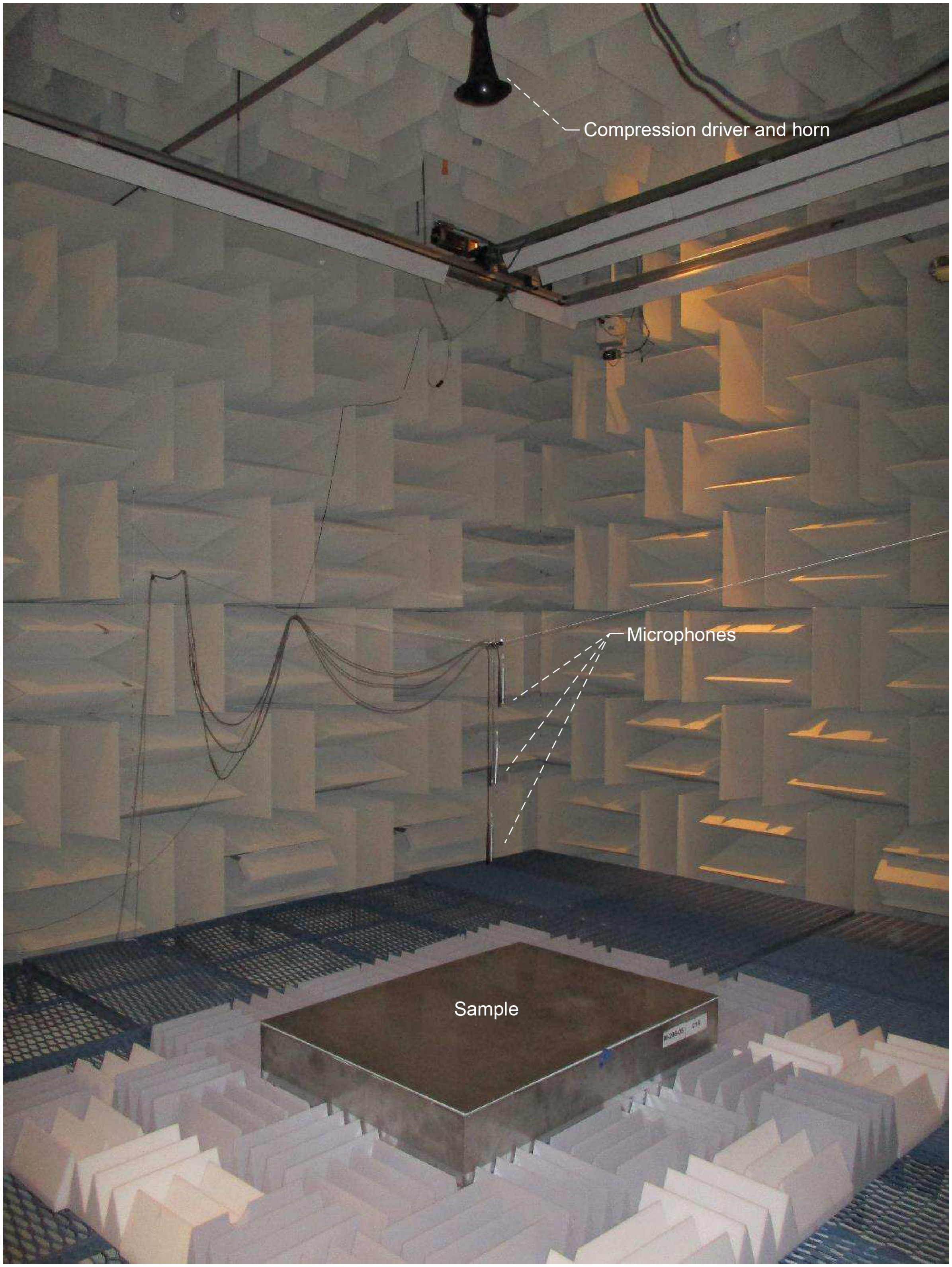

Figure 45.—Setup for testing acoustic boxes at NASA Glenn Research Center Acoustical Testing Laboratory. Sample is shown covered by solid (not perforated) steel sheet.

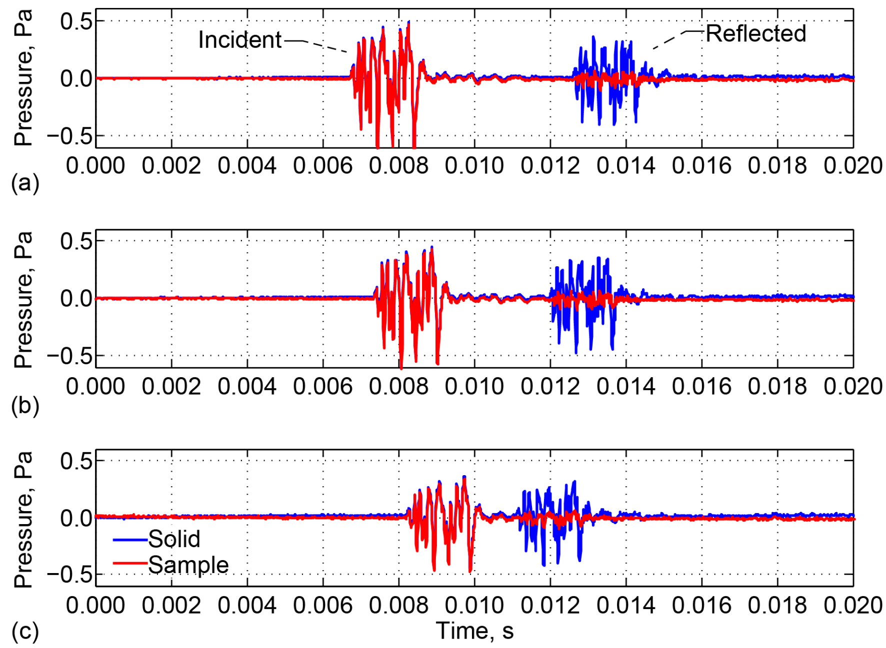

Figure 46.—Time history of three microphone reflection. Downward propagating sound is on left, curves overlap. Upward propagating sound on right. Reflection off of treated sample is visibly attenuated. (a) Top microphone. (b) Middle microphone. (c) Lower microphone.

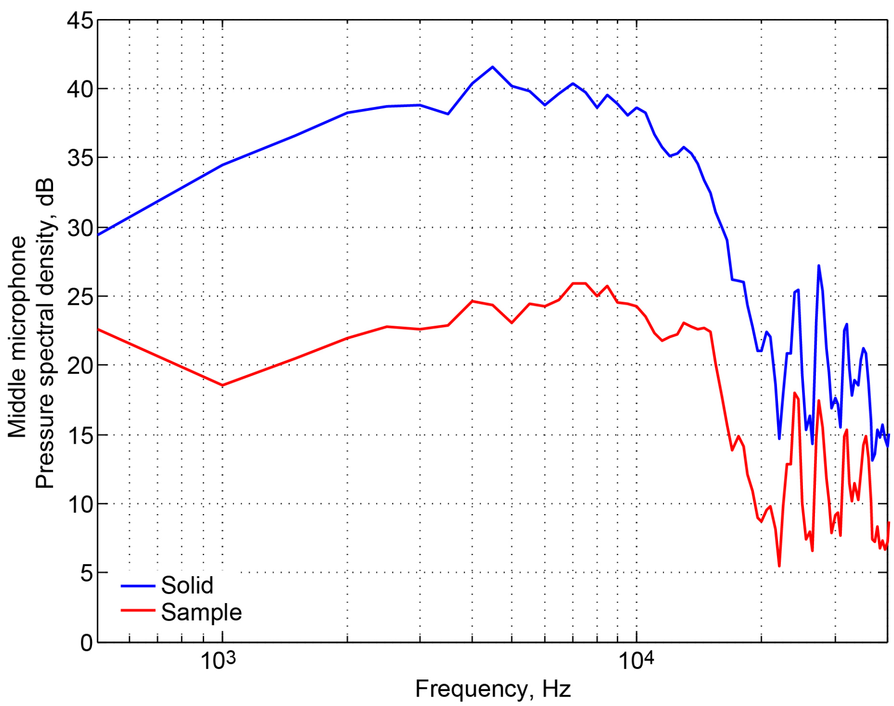

Figure 47.—Spectral content of sound reflected off of solid and treated samples.

To get absorption coefficient, the reflection off of a 16-ga solid (nonperforated) steel panel was also measured. This allows us to compute the absorption coefficient of the panel being tested as

$$a(f) = 1 - \frac{\overline{p^2(f)_{\text{Sample}}}}{\overline{p^2(f)_{\text{Solid}}}} \tag{2}$$

The absorption coefficient was calculated for each microphone, and a median was taken as the best result. This was done to reduce apparent amplification or attenuation in the measurement due to the specific location a microphone might be placed. For example, edge effects due to the finite size of the sample might create nodes or antinodes in the sound field above the sample. By taking the median, these could be reduced. All four curves are shown in Figure 48.

8.3 Impedance Calculation

Similarly, the "solid" and "treated" reflection signals can be used to calculate a transfer function, again using Welch's method. The typical definition of "reflection coefficient" is given by Pierce (Ref. 33, p.108),

$$R(f) = \frac{\hat{g}}{\hat{f}} \tag{3}$$

where $\hat{f}$ is the Fourier transform of the incident waveform and $\hat{g}$ is the Fourier transform of the reflected waveform. For the purposes of this experiment, $\hat{f}$ is measured as the reflection off of the steel panel, where $R(f)$ is assumed to be 1. The reflection coefficient was calculated for all three microphones and is shown in Figure 49.

The reflection coefficient is related to the absorption coefficient as

$$a(f) = 1 - |R(f)|^2 \tag{4}$$

The absorption coefficient calculated using both methods is shown in Figure 50. The short time burst (2 ms) means there is very little sound below 1 kHz, so the test is ambiguous at these frequencies. Similarly, the horn driver is poor at replicating sound above 25 kHz.

The relationship between R and the complex impedance Z is

$$Z(f) = \frac{1 + R(f)}{1 - R(f)} \tag{5}$$

The resistance and reactance are the real and imaginary parts of $Z(f)$, respectively. These are shown in Figure 51.

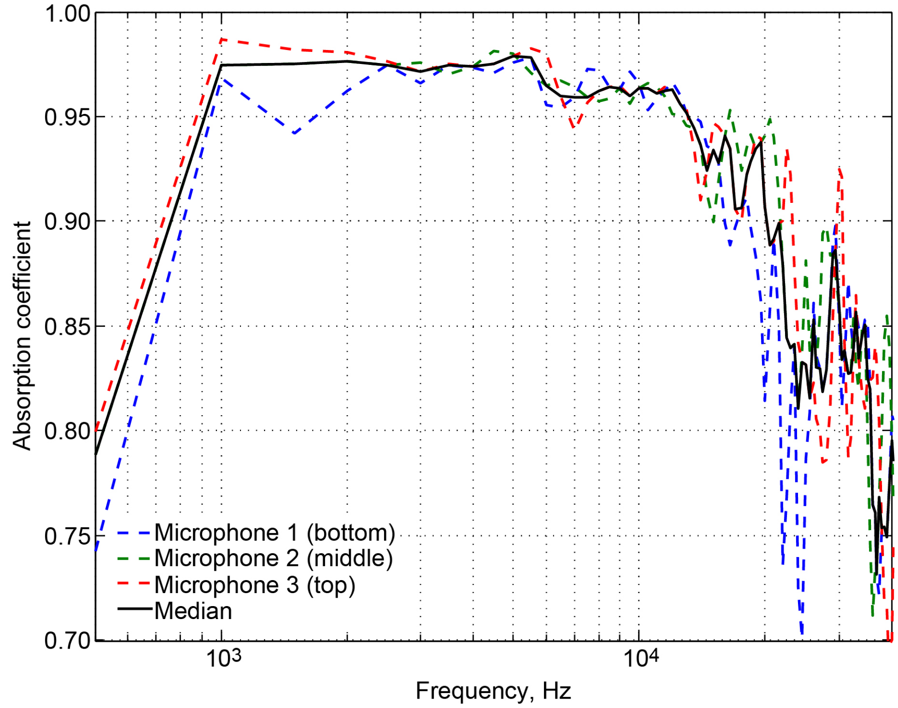

Figure 48.—Absorption coefficient from each of the three microphones.

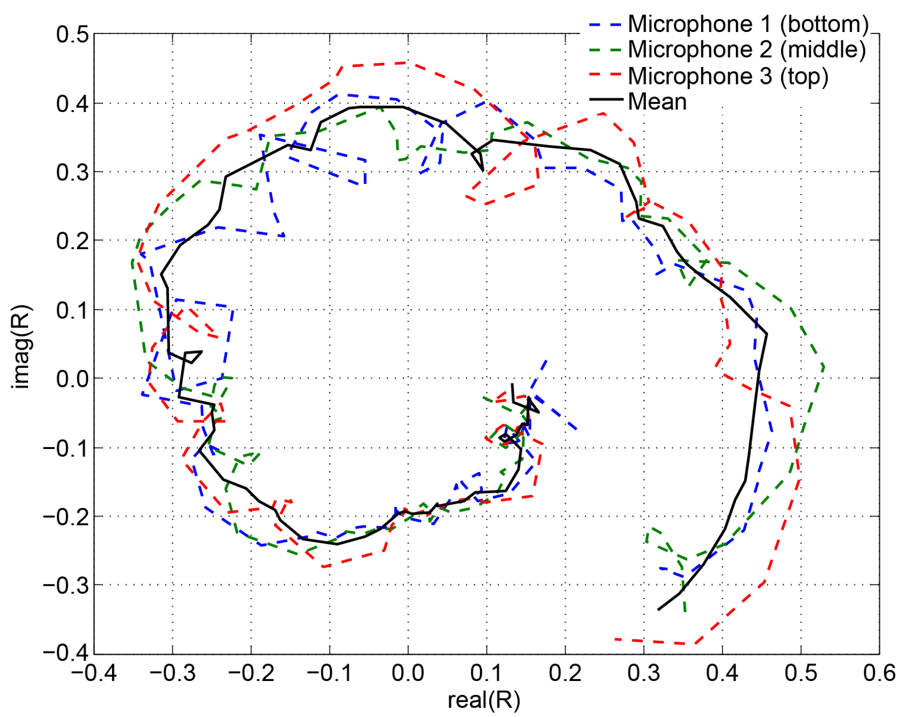

Figure 49.—Complex reflection from each of the three microphones.

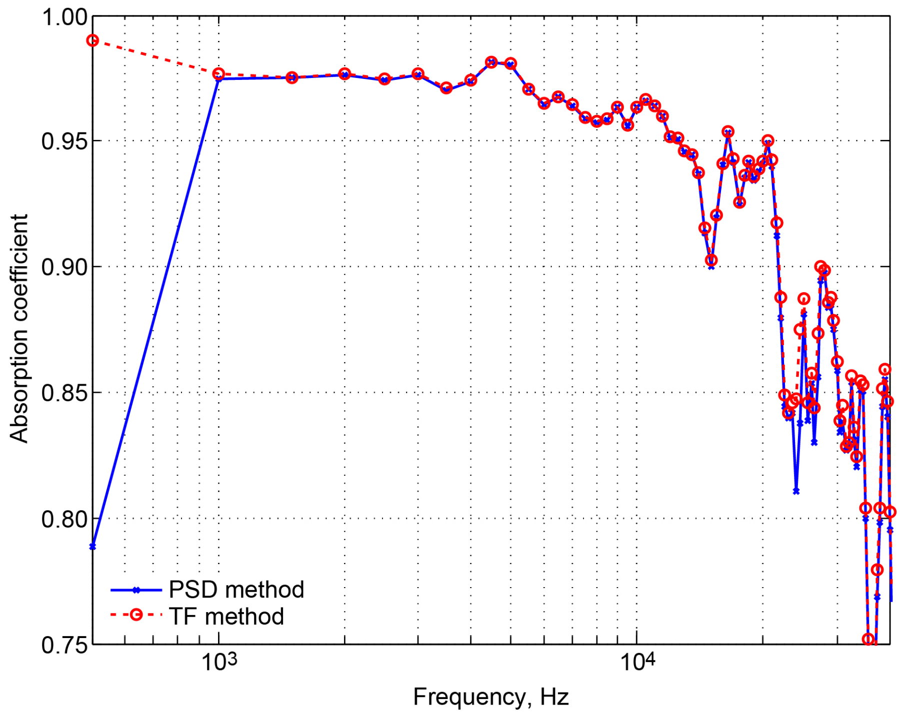

Figure 50.—Absorption coefficient calculated using both pressure spectral density (PSD) and reflection coefficient (TF) methods.

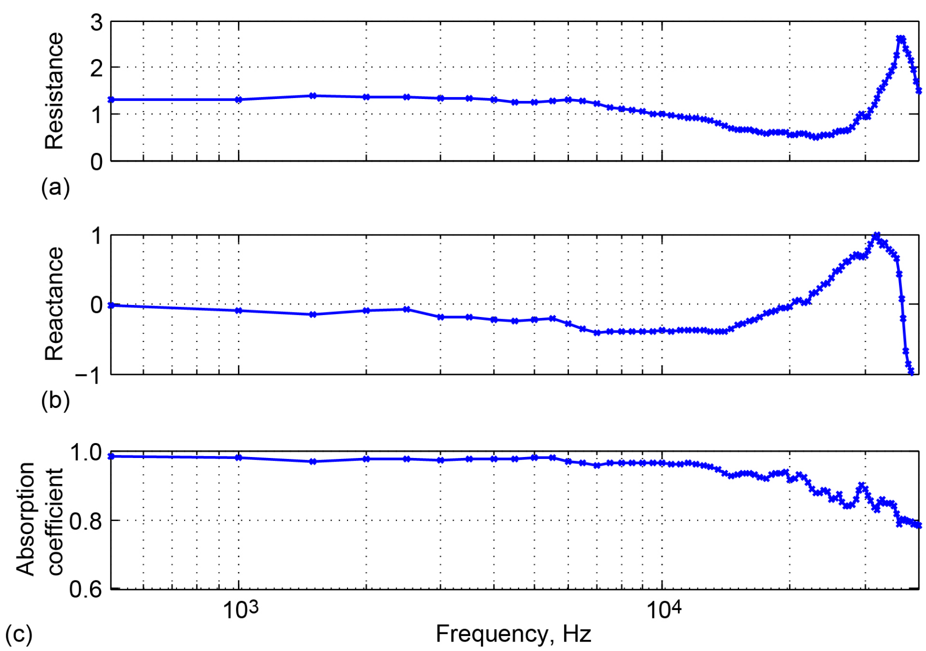

Figure 51.—Normalized specific resistance and reactance, plus absorption coefficient calculated using transfer function method. Sample is 9- by 15-Foot Low-Speed Wind Tunnel box C27. (a) Resistance. (b) Reactance. (c) Absorption coefficient.

8.4 Recommendations

For measurements of absorption coefficient very close to 1.0 (say, above 0.95), background noise corrections might be appropriate. For example, even with no reflective sample present, the microphone may measure some ambient noise or residual noise from the speaker module. For much of the present data, we used a compression driver with a horn, and there may have been some reverberations inside the horn for several milliseconds that caused the signal to be longer than intended, resulting in extra noise on the microphone. The compression driver and horn combination was selected as it had a wide frequency range capability and considerable sound power output. Future testing would include investigating other candidate speakers.

9.0 Computational Analysis

A series of computational acoustic predictions were used to guide design decisions during the early stages of the acoustic improvement project. Later analysis evaluated instrumentation options as the inflow traversing microphone assembly was being redesigned. Finally, this section presents the impact from the primary deviations from a uniform acoustic treatment and ends with an assessment of the expected as-built configuration.

9.1 Background

The 1986 acoustic configuration of the 9×15 LSWT consisted of 33-cm- (13-in.-) deep treatment over most of the wall surface and 4-cm- (~2-in.-) deep treatment over the support beams. Offset behind the flow relief slots was a second set of deep acoustic treatment so that flow could escape into the tunnel shell and sound would be absorbed. A gray thin foam was bonded to the steel beams that crossed the flow relief slots. This prior-to-upgrade test section is shown in Figure 52.

In the upgrade from the 1986 configuration, the 1986 support frame, Figure 53, was rebuilt to be entirely outside the acoustic treatment. This change allowed for a uniform 33 cm (13 in.) of treatment on all wall surfaces. In addition, the test section length was increased by 152 cm (5 ft) with acoustic treatment added to the new downstream diffuser. Figure 54 shows the 1986 configuration dimensions with positions of the model and microphones. When the test section was lengthened, the contraction was kept in place while the downstream end changed position.

The following COMSOL Multiphysics® (Ref. 34) analyses were covered in Reference 1, where the intent was to evaluate major test section design options prior to selection. Content in that report includes

- Description of the test section geometry
- Description of the COMSOL modeling (two-dimensional (2D) and three-dimensional (3D)) using the no-flow acoustic pressure frequency domain physics (acpr)
- Boundary conditions, perfectly matched layer versus cylindrical or spherical radiation
- Selection of uniform wall treatment over retrofit options
- Improved aft measurement uncertainty as a side effect of the test section extension
- Impact of diffuser acoustic treatment

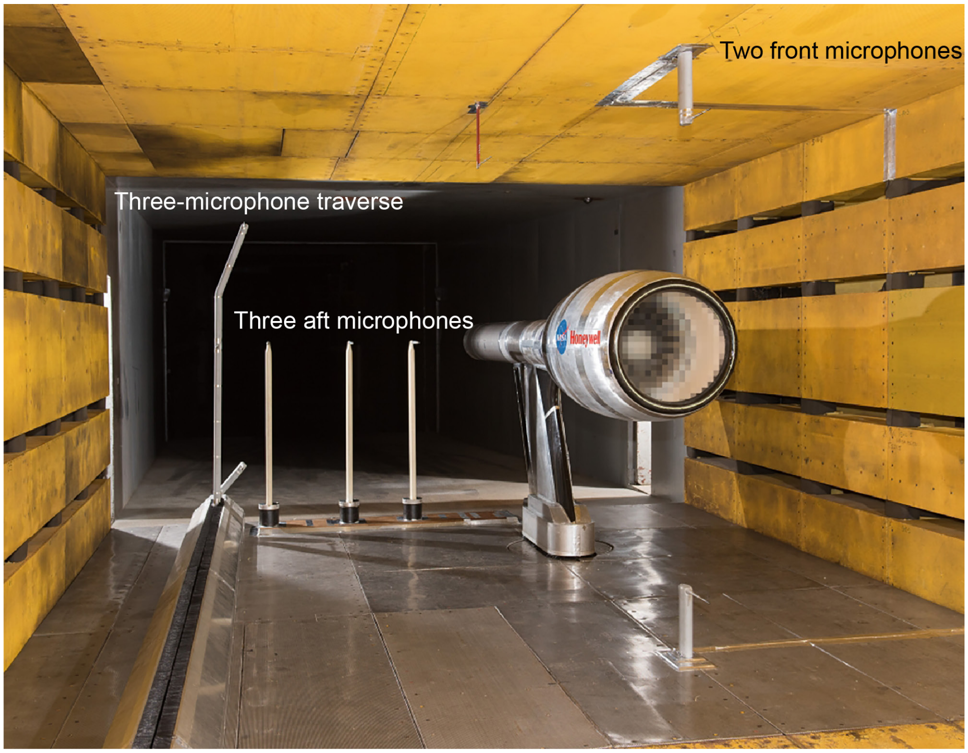

Figure 52.—Forward looking aft at 9- by 15-Foot Low-Speed Wind Tunnel test section with representative model and microphones, 1986 configuration. Test section support frame is visible in horizontal slots: vertical beams covered with gray foam. Hard-wall diffuser, painted gray, is behind and downstream of yellow treatment boxes. Visible floor treatment boxes are stainless steel and not painted.

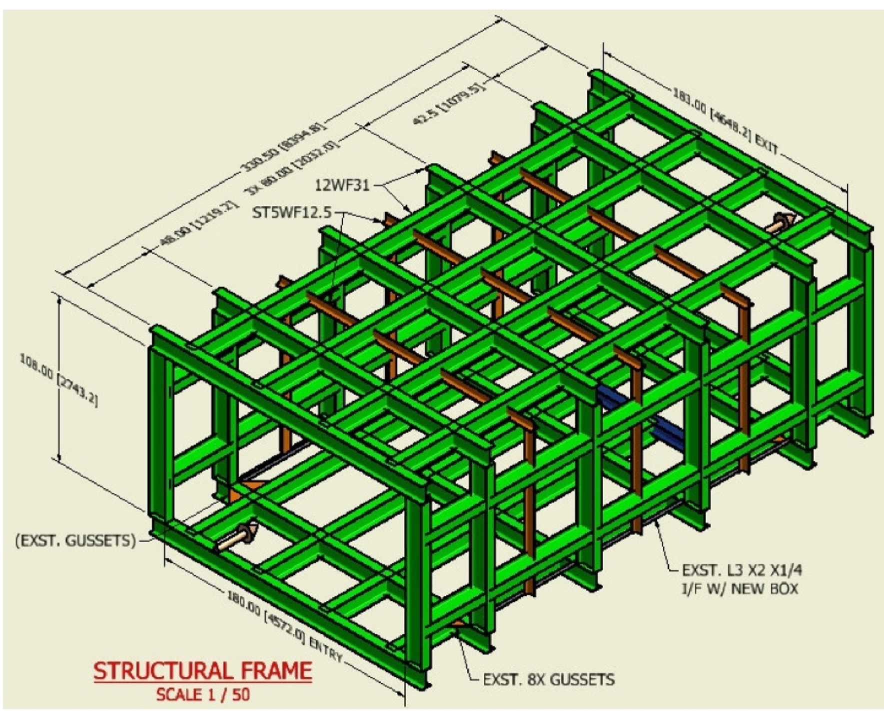

Figure 53.—Oblique view of original test section structural support beams. All dimensions are in inches (millimeter). Note: change in width over length to mitigate boundary layer blockage.

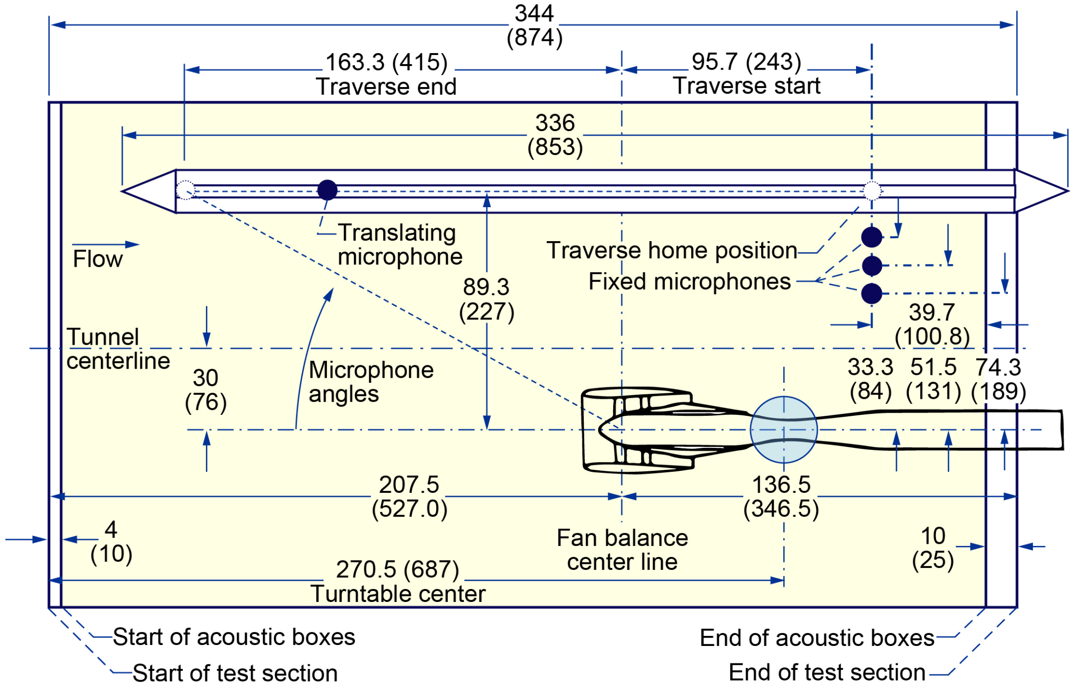

Figure 54.—Select dimensions of standard acoustic measurement locations in 9- by 15-Foot Low-Speed Wind Tunnel, in 1986 configuration. Not to scale, locations are approximate. All dimensions are in inches (centimeters).

9.2 Report Outline

This report describes further analyses and assessment of the new acoustic traverse, wall penetration options, hard-wall windows for lights and cameras, and a walkway proposed to reduce model change over time. Again, COMSOL Multiphysics® (Ref. 34) was used for the numerical analyses. All assessments were to estimate the impact on the measurement uncertainty from reflections due to the item being assessed. For the analyses, the COMSOL names for the model physics are noted in parentheses below.

- Modeling: comparison of with flow (hmnf+lnsf) versus no-flow (acpr).
- Impact of the brush seals size and location on measurement uncertainty (pabe)
- Impact of the hard-wall windows for the light and camera boxes by location on measurement uncertainty (pabe)
- Impact of the proposed walkway in the south floor at the corner (pabe)
- Impact of the new traverse armature and microphone stand-off distance

9.3 Analysis With and Without Flow

To evaluate the impact of flow on the acoustic field in the test section, two 2D (midheight cross plane) COMSOL analyses were compared:

1. No flow: solving for acoustic pressure in the frequency domain (acpr)
2. With flow: solving first for the flow using the high Mach number flow (hmnf) physics with the $k - \varepsilon$ turbulence model, then using that as the background flow field for the linearized Navier-Stokes analysis in the frequency domain (lnsf).

The sound source for all the acoustic assessments is a spherical (or circular for 2D) monopole located on the fan rotation axis, at the axial position of the center of the fan rotating force balance. This is the position noted in Figure 54 as “Fan balance centerline.” The source sphere radius is 15 cm (6 in.) for all the assessments except the final near-term configuration, “Impact of the Armature,” where the source sphere radius is 2.5 cm (1 in.).

For the flow field solution, the mesh generation used the COMSOL “Normal” mesh density setting, with eight layers in the boundary layer. For the acoustic solutions, the mesh used a maximum element size to yield 10 points per shortened wavelength of waves running upstream against the mean flow. This (very conservative) large number of points per wavelength was chosen for the initial assessment to guarantee sufficient wave resolution in unexpected regions of higher than tunnel speed velocity.

The analysis approach was applied to three cases:

1. For the best-case condition, all wall boundary conditions are set to cylindrical wave radiation to infinity to achieve no reflections. This case is labeled “no walls.”
2. For the best practical case, the full 33-cm (13-in.) depth treatment is applied to the sidewalls, as well as the inlet and diffuser. This case is labeled “13-13”
3. The most likely case has full-depth treatment on the test section sidewalls, and hard walls on the inlet and diffuser. This case is labeled “13-hw.”

These analyses quantified the reduction in reflection based uncertainty in measurements along the traverse attainable by treating the inlet and diffuser, as well as the changes due to tunnel mean flow.

The no walls case at Mach 0.0 also quantifies the numerical uncertainty for the given mesh and topology. The ripples in the COMSOL model apparently result from the mesh and overall topology. Not shown is a repeat analysis with a perfectly matched layer on all outer boundaries. The resulting pattern of acoustic reflections in the test section was virtually identical to the result when using the cylindrical wave radiation. Because of the lower resource requirements, cylindrical or spherical wave radiation was used in all following analyses.

In the comparison discussion and plots to follow, the sound pressure levels are the difference between the computed and the expected sound pressure levels from a monopole source in free air.

Figure 55 is a representative result, comparing the 500 Hz “1-ft” (30.5-cm) lossless delta sound pressure level along the 227-cm (89.3-in.) sideline traverse, for two wall treatment conditions and two tunnel mean flow Mach numbers.

The axial position of the interference pattern peaks and valleys through the test section shift with flow, but the amplitudes stay about the same. This indicates that the no-flow (acpr) analysis is suitable for determining the level of interference due to reflections from various test section hardware changes, and the lower memory requirements when using acpr allows for running to higher frequencies.

Comparing the “Mach 0.2, 13-13” with “Mach 0.2, 13-hw,” shows that treatment on the inlet contraction would reduce reflections in the first 1.5 m (5 ft) of the test section from ±1 dB down to ±0.5 dB. At 1,000 Hz, not shown, the benefit is less, and the benefit drops with increasing frequency.

Similarly, treatment on the diffuser would reduce reflections seen in the last 2 m (6.6 ft) with the same fall off of benefit with frequency as was seen for the treated inlet. This analysis supported the decision to include treatment on the new diffuser. Treatment on the inlet diffuser, because of the complex shape, was not feasible.

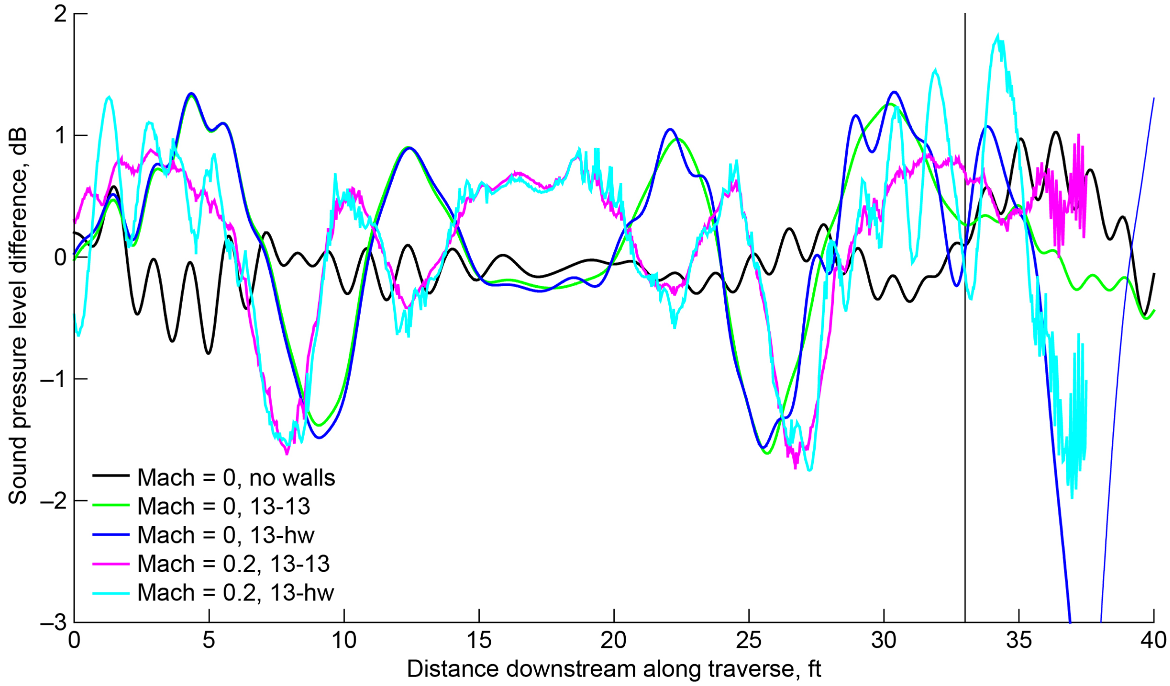

Figure 55.—Delta sideline sound pressure level with and without flow, and each flow with and without diffuser treatment. Mach 0 "no wall" curve shows numerical uncertainty in what should be zero difference from acoustic radiation from spherical source in free air. Test section flow, Mach 0.0 versus Mach 0.2, shifts 500-Hz standing wave pattern, but the reflection magnitude is consistent. Impact of diffuser treatment, 13-hw versus 13-13, on reducing aft reflections is similar with and without flow. Extended test section ends at 10 m (33 ft).

9.4 Impact of Brush Seals

In the 1986 configuration, the sideline microphone traversing mechanism was located on the floor where it was exposed to the flow and the model acoustic field, as shown in Figure 52. As a result, acoustic reflections from the traverse cover reach the sideline microphones. To reduce these reflections, it was proposed to move the traversing mechanism outside the test section, into the outside corners, which are not used for acoustic treatment. This is the space above and below the sidewall acoustic treatment and to the side of the ceiling and floor treatment. To access this unused space, the sidewall acoustic boxes nearest the corners were reduced in height to leave a gap through which the microphone support armature would pass into the test section through the sidewall. The gap would be closed to the test section flow using a brush seal.

For the assessment of the treatment penetration options, several assumptions were made:

- The sidewall treatment performance would be the same for all options.
- The strength of the reflection from the slot option is small, and any further reflection off a treated surface can be ignored.
- Relative levels of reflection are sufficient for design choices.
- Absolute levels of reflection, and hence measurement uncertainty, can be determined later.

Based on those assumptions, the boundary element method (pabe) was suitable for the assessment.

Several configurations of the gap and brush seal placement were evaluated to allow for trades on other design requirements. Initially, a 5-cm (2-in.) gap was thought to be sufficient, with the brush seal flush to the flow surface face of the acoustic treatment. This configuration is referred to below as the

“I-corner.” To allow for an additional sideline traverse on the opposite sidewall, the evaluation included slots and seals on all four side corners. The I-corner configuration was ultimately selected.

A second design considered the same vertical gap, but with the brush seal recessed into the gap, and again the brush seal is parallel to the tunnel sidewall flow surface. This configuration, shown in Figure 56, is referred to as the “L-corner.” For all designs, the floor and ceiling treatment boxes were a constant width, matching the downstream end, resulting in the wall boxes overlapping the floor or ceiling treatment for 7.6 cm (3 in.) at the front, down to 0 cm at the aft end of the test section. With the gap exposed and the brush seal aligned with the recessed edge of the floor or ceiling treatment box, one side of the gap slot is exposed to the adjacent ceiling or floor treatment while the other is the hard-wall side of a treatment box creating a lined duct. This second configuration with the exposed slot reduced the reflection from the brush seal onto the sideline measurement surface, but likely has additional flow noise. The L-corner design was not selected.

The COMSOL analyses for the impact of the brush seals used the boundary element acoustic physics (pabe), with elements sized for six points per wavelength. A check using eight points per wavelength found no appreciable difference in the solution, so the coarser meshing was used to enable runs at higher frequencies. The brush seals were modeled as hard-wall surfaces to get the worst-case estimate for, or upper bound on, the reflection effect. The physical brush seals have some porosity and a slight edge-to-edge gap between them and are, therefore, a soft wall of undetermined acoustic character. All other settings for the COMSOL solution sequence were the default.

Figure 57 shows the components in the initial boundary element analysis of the test section: brush seals in all four corners (to consider an additional future traverse), the eight commonly used hard-wall window locations, and the source sphere. For the assessment of the brush seals alone, the computational domain is simplified to the upper half of the test section with all windows removed, with the reflections assessed on the 227-cm (89.3-in.) sideline measurement surface of the traversing microphone, as shown in Figure 58.

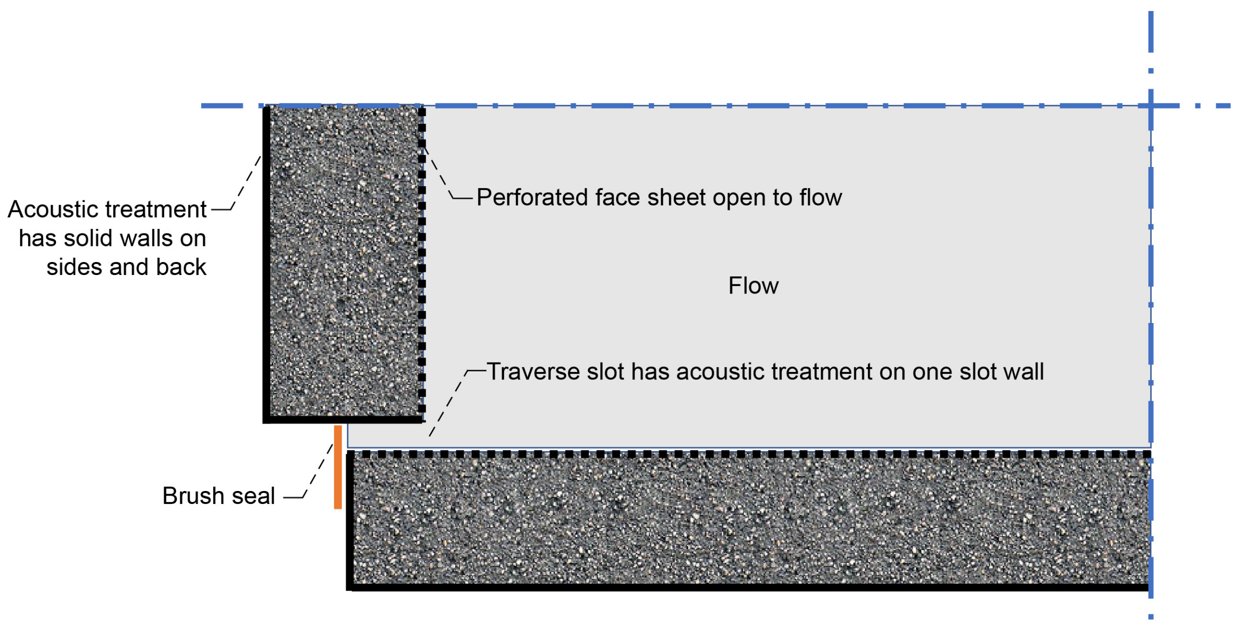

Figure 56.—Test section corner geometry for “L-corner” configuration. Brush seal is mounted on side of floor treatment, creating slot with treatment on one side.

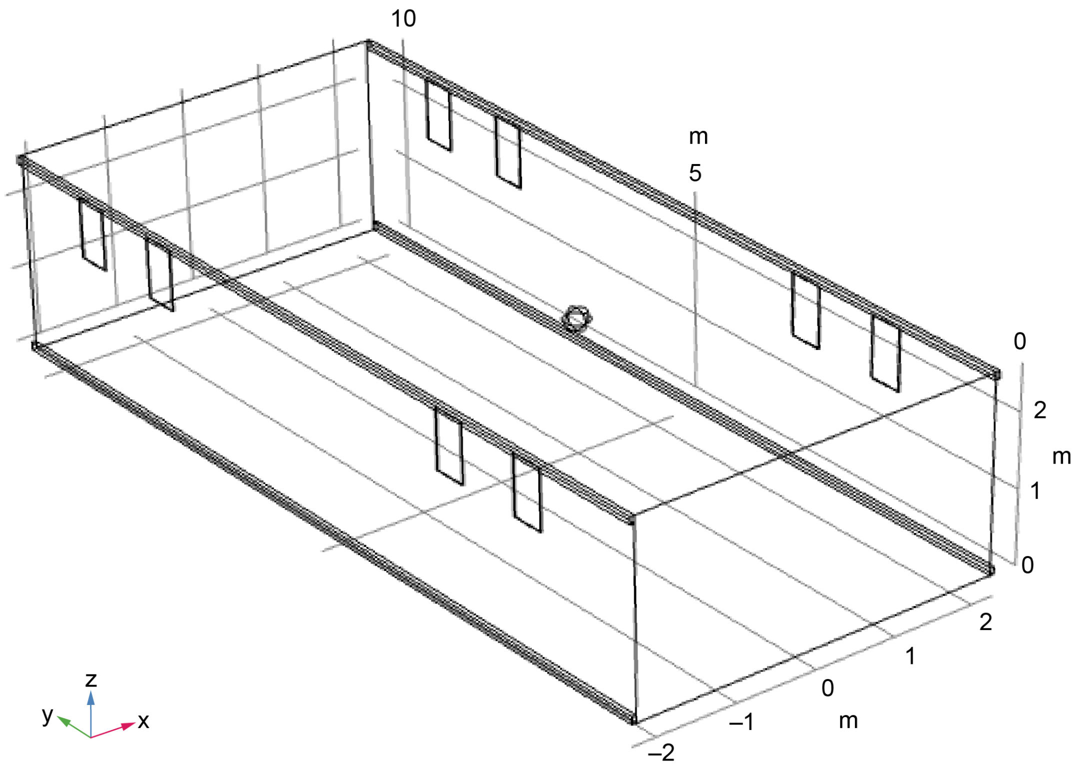

Figure 57.—Test section model for boundary element analysis (pabe), with spherical source, axial brush seals in all four corners, and rectangular panels where hard-wall windows can be placed for lights and cameras. There are no wall treatment boxes in this model as it is used to determine relative levels of reflection from design choices (e.g., if A or B is required, which is better).

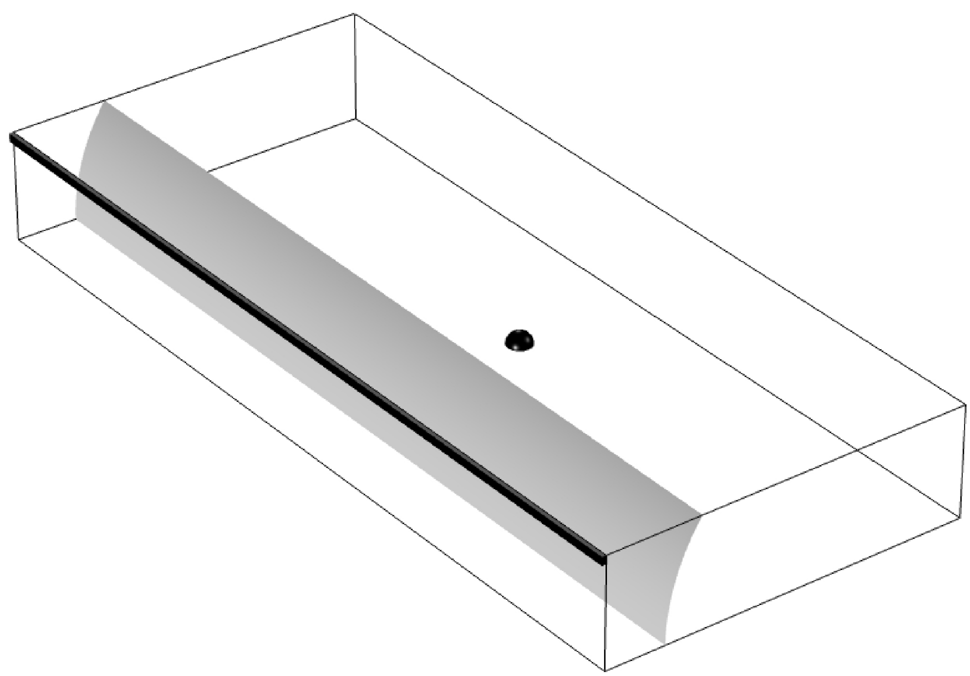

Figure 58.—Reduced domain for 10-cm (4-in.) “I-corner” analysis, sampled along 227-cm (89.3-in.) sideline traverse arc (gray cylindrical surface). For analysis of brush seals alone, symmetry can be used to reduce computational domain to upper half of test section.

The configuration with the brush seal at the tunnel flow surface was selected for the tunnel upgrade. The gap was increased to 10 cm (4 in.) to allow for ease of installation and maintenance, additional tolerance to alignment precision, and to accommodate the final larger thickness of the microphone support armature. An assessment of this wider brush seal is shown in Figure 59 for 2,000 Hz, showing a ±2.5 dB estimate in lossless sound pressure level for perturbations from a hard-wall brush seal at the 227-cm (89.3-in.) sideline measurement arc. The perturbations are highest near the ceiling (or floor) where the reflections from the hard-wall brush seal are more direct and towards the inlet and exit. Perturbation magnitudes for a range of source frequencies from 100 to 8,000 Hz are shown in Figure 60 with the data in Table 2.

To summarize: reflections from the brush seals alone introduce up to a ±2.5 dB (at 2 kHz) uncertainty in measurements of 1-ft lossless sound pressure level on the 227-cm (89.3-in.) sideline arc.

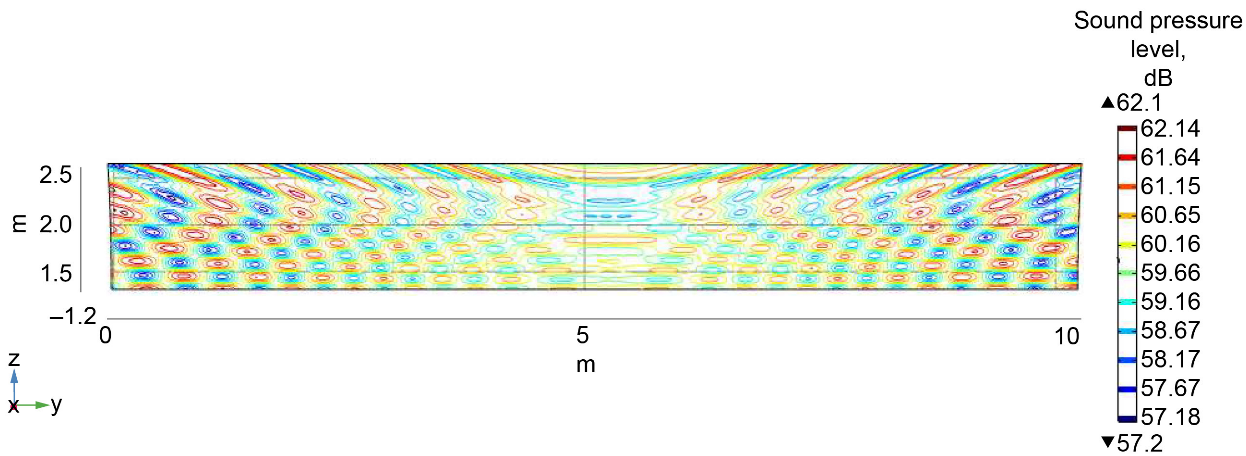

Figure 59.—One-foot lossless sound pressure level for 10-cm (4-in.) “I-corner” brush seal configuration (assuming hard-wall seals), sampled on 227-cm (89.3-in.) sideline traverse arc. Symmetry was used to reduce computational domain to upper half of test section, as shown. Reflections from brush seals alone contribute up to ±2.5 dB uncertainty near inlet and exit of test section.

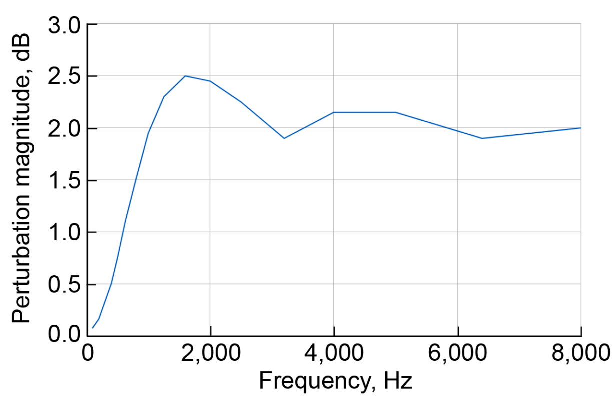

Figure 60.—Estimated upper bound on 1-ft lossless sound pressure level perturbation, as measured on 227-cm (89.3-in.) sideline traverse arc from brush seals on traverse side.

TABLE 2.—PERTURBATION UPPER BOUND FOR LOSSLESS SOUND PRESSURE LEVEL ON 227-cm (89.3-in.) SIDELINE MEASUREMENT SURFACE DUE TO REFLECTIONS FROM HARD-WALL BRUSH SEALS ON TRAVERSE SIDE

Frequency, Hz	Maximum uncertainty, dB
100	0.1
200	0.2
400	0.5
500	0.8
630	1.1
800	1.5
1,000	2.0
1,250	2.3
1,600	2.5
2,000	2.5
2,500	2.3
3,200	1.9
4,000	2.2
5,000	2.2
6,400	1.9
8,000	2.0

9.5 Impact of Light Box Locations

Cameras and lights are used during model buildup and are required for observing the model and instrumentation during a tunnel run. These cameras and lights are placed in a “light box,” which replaces one or more of the acoustic treatment boxes in the sidewalls. The window on the light box is transparent, but acoustically hard, and can reflect model acoustics to the sideline measurement cylindrical surface, depending on the window location.

These light boxes can be placed on either sidewall by removing appropriate treatment boxes. There are multiple possible axial and vertical locations. Eight of the commonly used locations are shown in Figure 57. In the analyses, the light box positions (rectangles) were referred to as “inner” (towards the test section center, and hence the model) and “outer” (further from the test section center and closer to either the inlet or exit), on either the traverse side or the model side. All light box locations were assessed for the level of reflection to the sideline traverse location, to guide the selection of a minimally intrusive set.

Figure 61 shows a representative result for all four hard-wall light boxes installed on the model-side sidewall. Reflections from the light boxes closest to the inlet or exit, the outer boxes, are angled into the inlet or exit space and miss the sideline traverse. Reflections from the light boxes closest to the source, the inner boxes, are angled towards the inlet and exit end of the sideline traverse. The reflections from these inner boxes have reflections that contribute up to ±6 dB uncertainty at the sideline measurement surface (not shown).

In these figures, the y-z data plane slices are located at the source (right plane, 76-cm (30-in.) right of center), and at the 227-cm (89.3-in.) sideline distance of the traversing microphone (left plane). The x-z plane slices are positioned on inner window center lines. The horizontal data plane goes through the source center.

Placing the light boxes on centerline, in the inner locations on either wall, particularly on the model side, provides the best view of the model. Unfortunately, these locations also provide the most reflection to the 227-cm (89.3-in.) sideline measurement surface.

As shown in Figure 62, reflections and scattering from these locations still reach the measurement surface, adding up to ±7 dB to the measurement uncertainty. In summary, the inner locations on either wall are to be avoided.

Placing the light boxes in the upper row, away from the centerline in the outer positions on either the traverse- or model-side walls significantly reduces the direct reflection to the 227-cm (89.3-in.) sideline location.

Figure 63 shows the reflections from outer light boxes in the upper row on both sidewalls. While a very small amount of light box edge scattering from the model-side boxes reaches the measurement surface, it appears to be much less than the reflection from the traverse-side light boxes. The light boxes on the traverse side will reflect onto the measurement surface, up to ±3 dB at 500 Hz. So light boxes on the traverse side should be avoided.

The outer windows on the model side do not have a ray-like bounce to the sideline measurement surface and seem to have essentially no perturbation effect. The recommendation from these analyses is to use the upper row outer locations on the model side only.

The assessments so far have included extra components (e.g., a traverse on both sidewalls) to evaluate options. Assuming that the near-term configuration will include only brush seals and a traverse on one wall and light box windows only on the model side in the upper row outer locations, the next assessment is of that simplified geometry, as shown in Figure 64 and results summarized in Table 3.

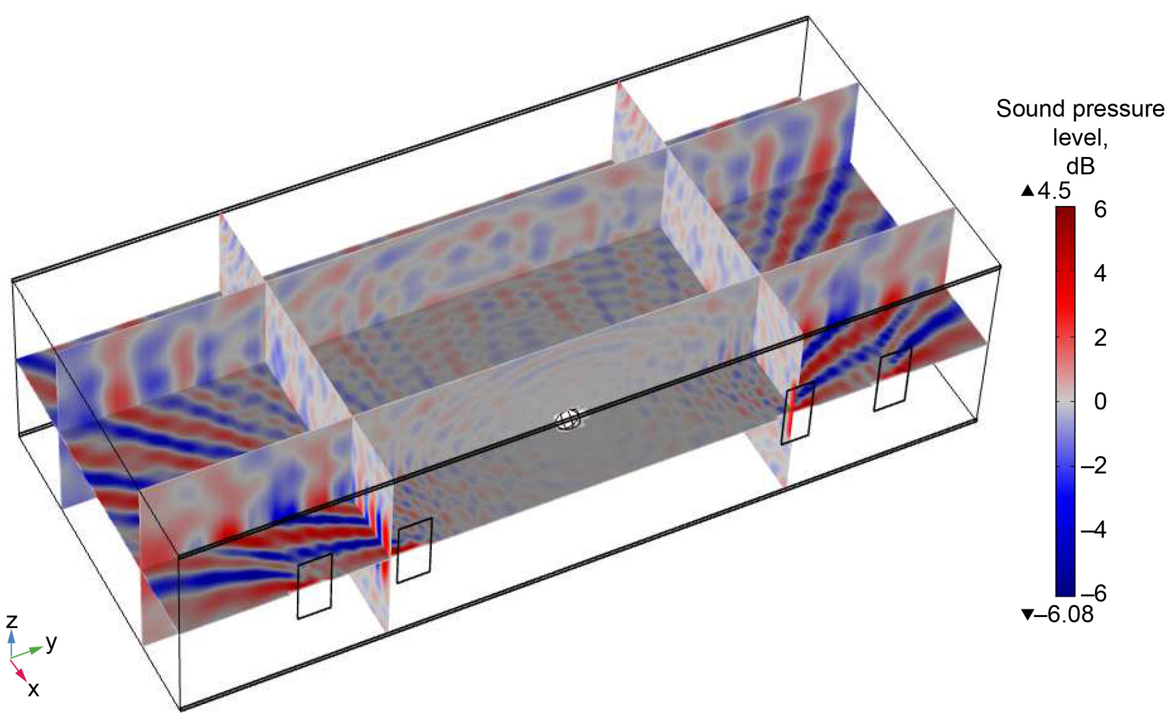

Figure 61.—Perturbations in lossless sound pressure level from both “inner” and “outer” light box locations in vertical center row on model side at 1,000 Hz.

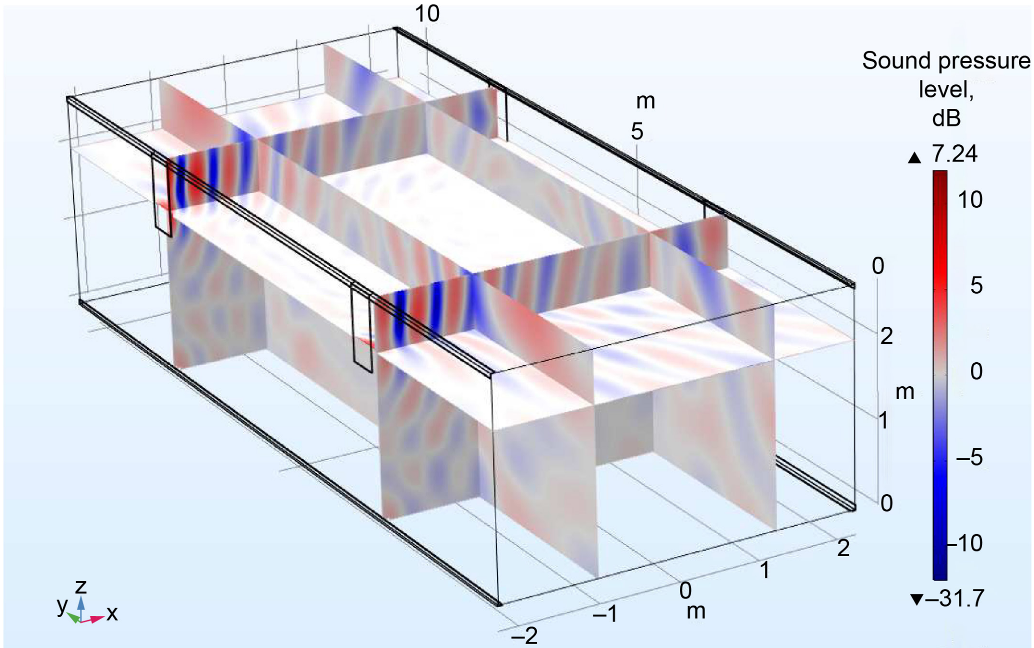

Figure 62.—Traverse side “inner” window location perturbations in lossless sound pressure level at 500 Hz from boundary element analysis. Reflections from traverse slot brush seals in corners are minor but included in this analysis. Perturbations from light box windows at inner position on traverse (left) sidewall are up to ±7 dB. Reflections from source side (right) angle forward and aft and essentially do not intersect sideline measurement surface. Tunnel flow is lower right to upper left.

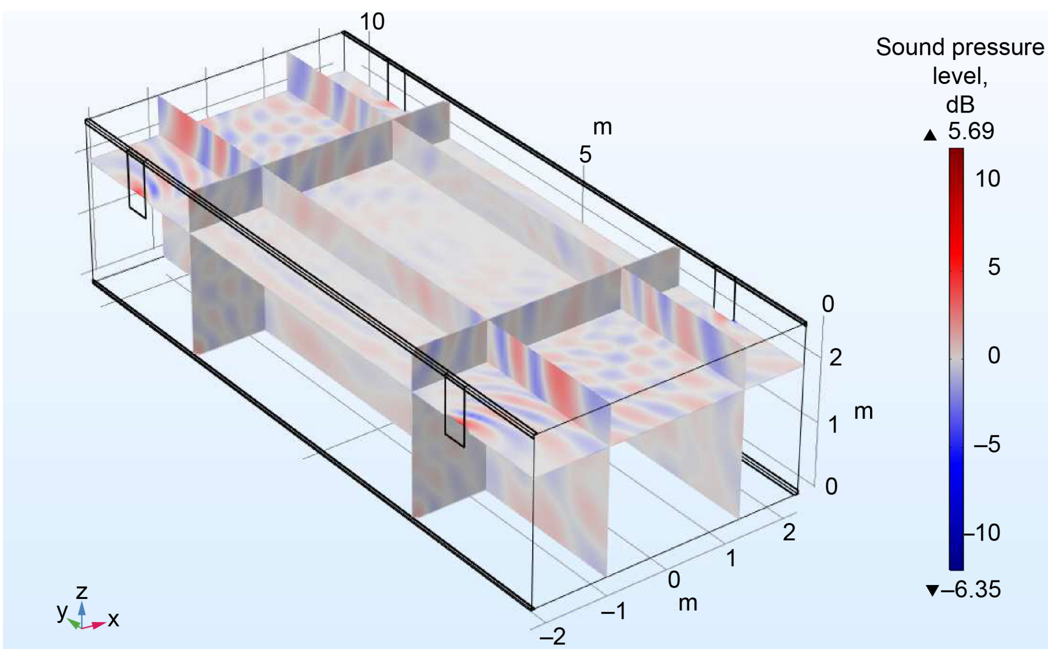

Figure 63.—Traverse side, “outer” window location perturbations in lossless sound pressure level at 500 Hz from boundary element analysis. Reflections from traverse slot brush seals in corners are minor but included in this analysis. Reflections from light box windows at outer position on traverse-side (left) wall are up to ±3 dB. Reflections from source or model side (right) angle forward and aft, and do not intersect sideline measurement surface. Tunnel flow would be from lower right to upper left. Vertical y-z solution planes are located at source (right) and at roughly 227-cm (89.3-in.) sideline distance of traversing microphone.

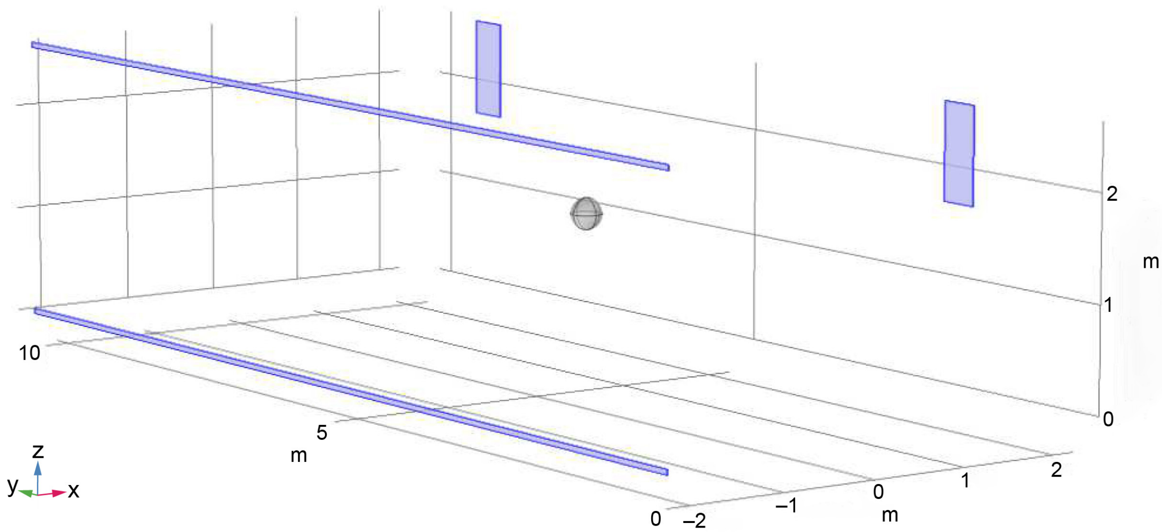

Figure 64.—Geometry for analysis of brush seals on traverse side and hard-wall light box panels on model side.

TABLE 3.—SIDELINE MEASUREMENT SURFACE PERTURBATIONS IN LOSSLESS SOUND PRESSURE LEVEL (SPL) FROM TRAVERSE-SIDE BRUSH SEALS AND UPPER ROW "OUTER" LIGHT BOXES ON MODEL SIDE

Frequency, Hz	Maximum SPL uncertainty, dB
500	0.65
1,000	1.1
2,000	1.7
4,000	2.6
6,000	2.3
8,000	2.4

Figure 65 to Figure 70 present the magnitude of the lossless sound pressure level perturbation, that is, abs(Lp_{lossless}) − mean(Lp_{lossless}), for a sequence of frequencies, presented on the 227-cm (89.3-in.) sideline surface, as viewed from the model side. In this view, the test section entrance is on the left.

In Figure 65, for 500 Hz, the light box reflection is evident at the test section entrance (left) and exit (right). Over most of the test section, the perturbations are less than 0.3 dB. But near the ceiling, and particularly near the test section entrance, the perturbations can be up to 0.65 dB.

At higher frequencies, the general level of perturbation through the test section rises, as does the peak levels near the entrance and exit at the ceiling and floor. Up through 1,000 Hz, the peak perturbation appears to come from the light boxes. At higher frequencies, the peak perturbation is more uniformly along the floor and ceiling, see Figure 67 for example, which indicates reflections from the brush seals. At the higher frequencies, the peak perturbation magnitude is roughly 2.5 dB in lossless sound pressure level on the 227-cm (89.3-in.) sideline surface.

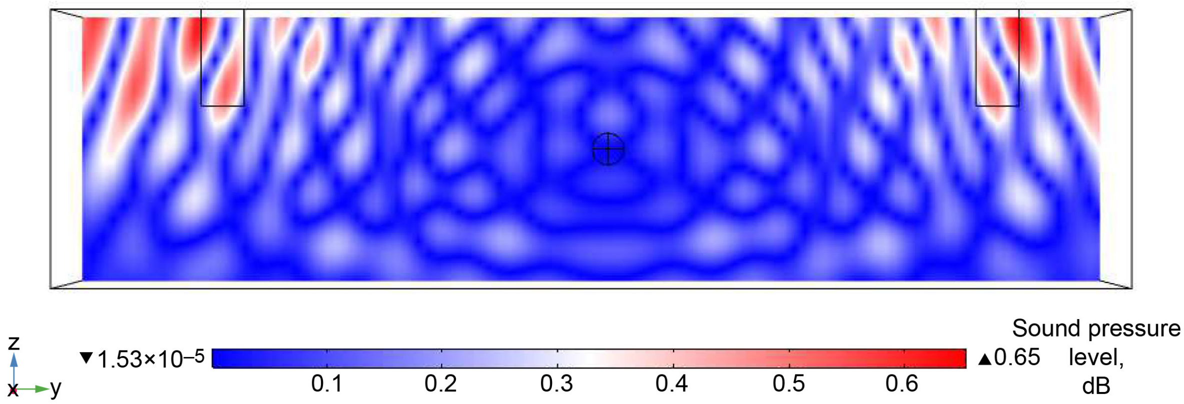

Figure 65.—Magnitude of lossless sound pressure level on 227-cm (89.3-in.) sideline measurement surface at 500 Hz.

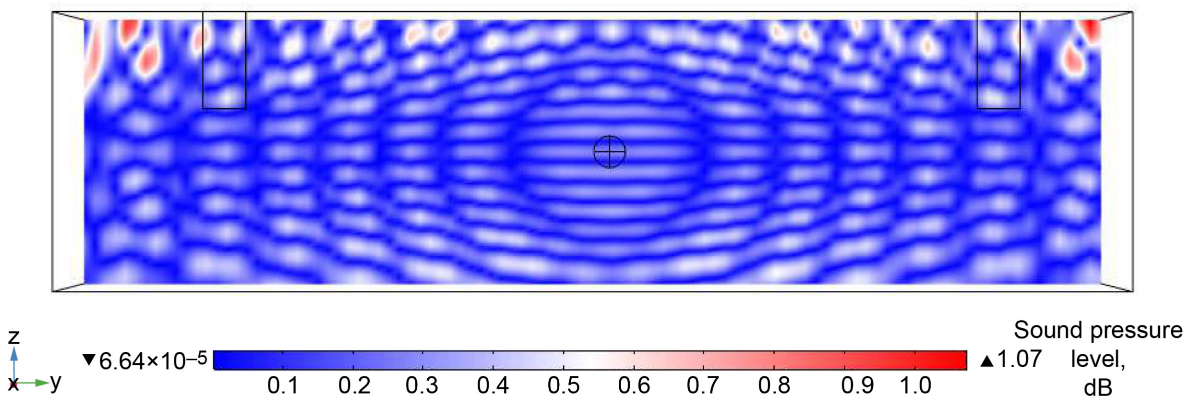

Figure 66.—Magnitude of lossless sound pressure level on 227-cm (89.3-in.) sideline measurement surface at 1,000 Hz.

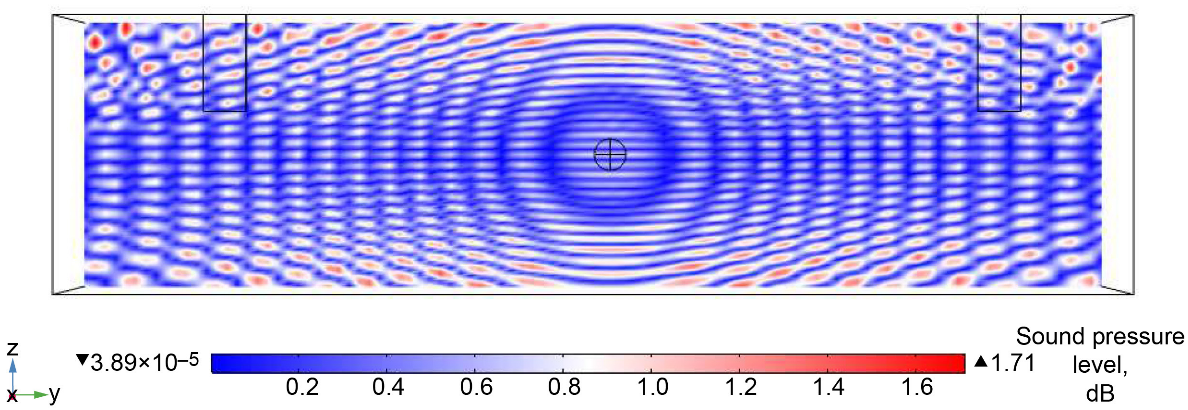

Figure 67.—Magnitude of lossless sound pressure level on 227-cm (89.3-in.) sideline measurement surface at 2,000 Hz.

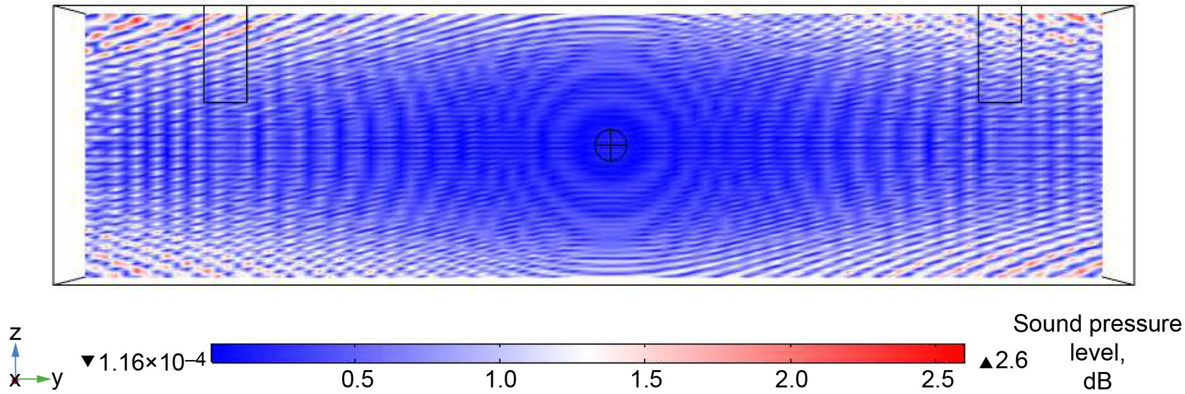

Figure 68.—Magnitude of lossless sound pressure level on 227-cm (89.3-in.) sideline measurement surface at 4,000 Hz.

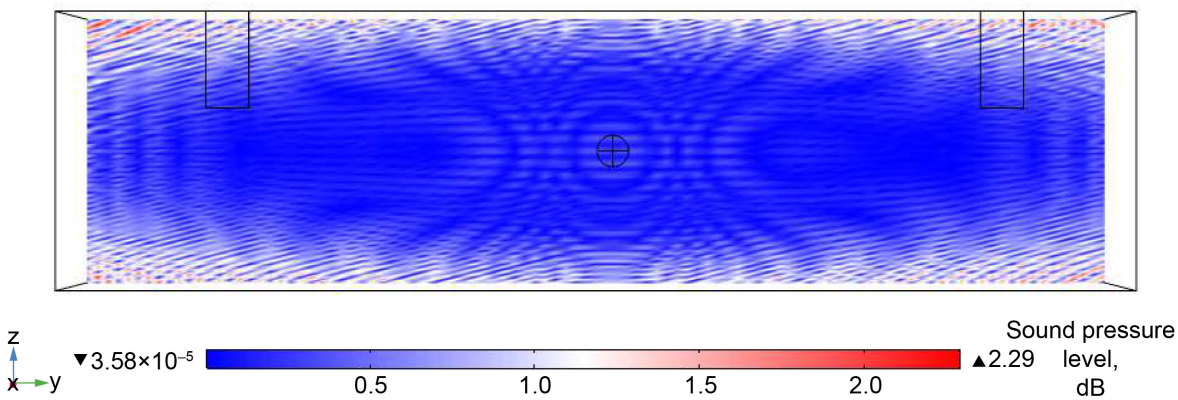

Figure 69.—Magnitude of lossless sound pressure level on 227-cm (89.3-in.) sideline measurement surface at 6,000 Hz.

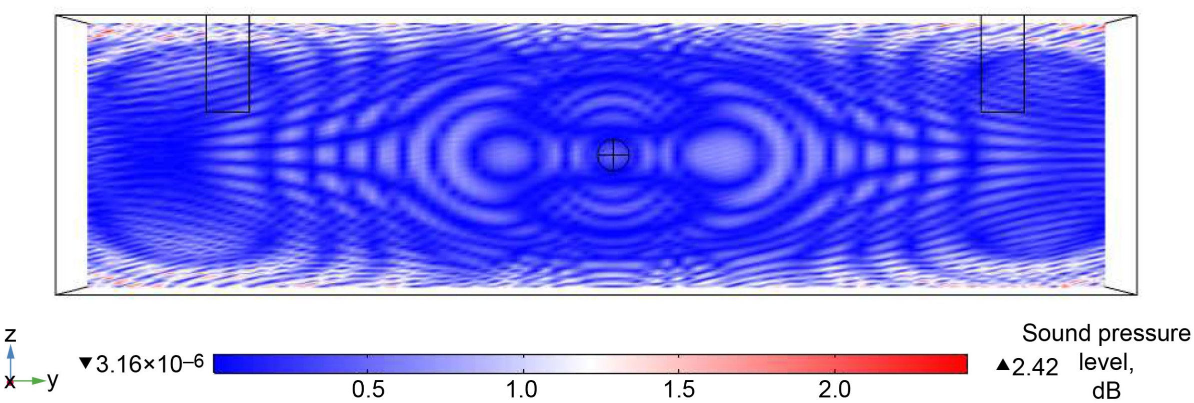

Figure 70.—Magnitude of lossless sound pressure level on 227-cm (89.3-in.) sideline measurement surface at 8,000 Hz.

9.6 Impact of Hard Walkway

Having a permanent hard-surface walkway along the wall next to the model would significantly reduce model change time and increase productivity. Normally, temporary work surfaces are installed prior to a model change, then removed for testing. The impact of such a walkway was assessed to quantify the perturbations to the traverse sideline measurements. Customers can then weigh the impact on measurements versus the productivity improvement.

Two configurations were evaluated, where one or two axial rows of acoustic boxes were replaced with hard flooring. These configurations are shown in Figure 71 for one row and Figure 72 for two rows.

The one-row results are shown for a series of frequencies in Figure 73 for 500 Hz to Figure 76 for 2,000 Hz. At 500 Hz, there is a general perturbation of about 1 dB over the 227-cm (89.3-in.) sideline, with a few regions of about 1.5 dB.

At 1,000 Hz, Figure 74, there are some regions of up to 1-dB perturbation and a few small regions of 2 dB.

At 2,000 Hz, Figure 75, the field has a general pattern of 1- to 2-dB perturbation with a couple of small regions of 3 and 4 dB.

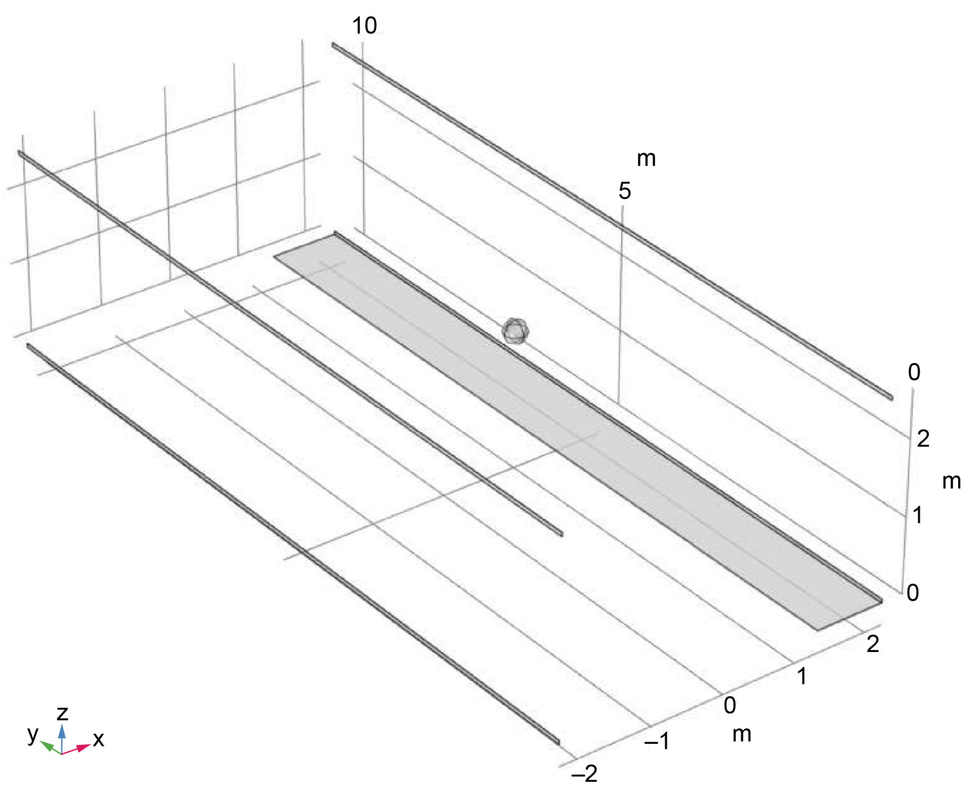

Figure 71.—Geometry for test section with brush seals in corners and single row of acoustic floor boxes replaced with hard-surface walkway.

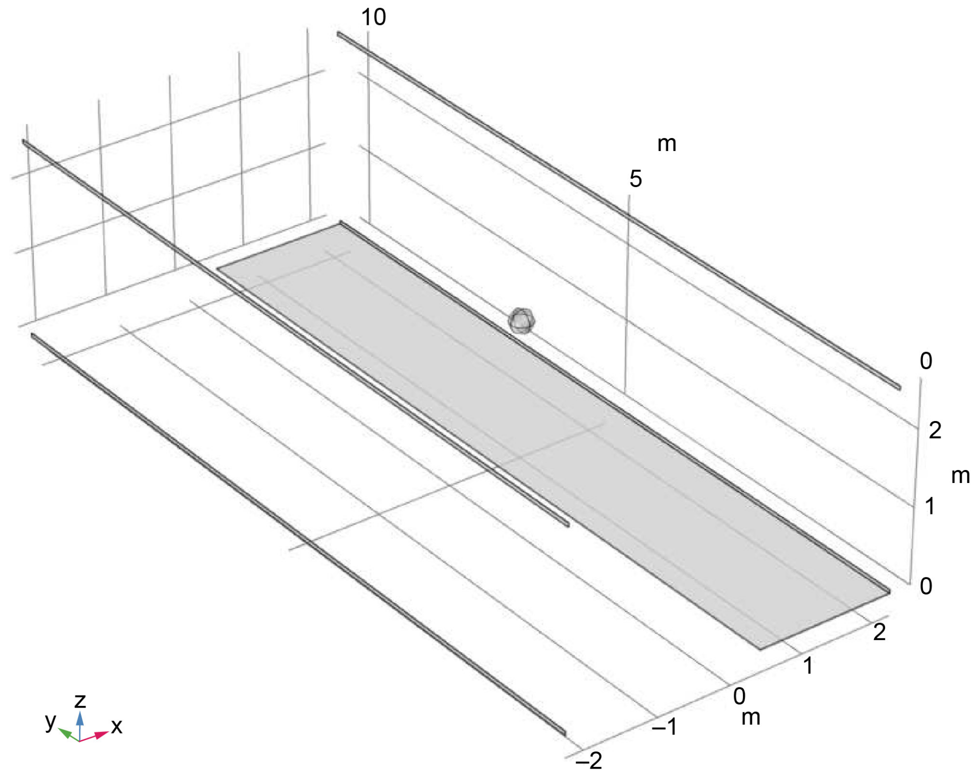

Figure 72.—Geometry for test section with brush seals in corners and two rows of acoustic floor boxes replaced with hard-surface walkway.

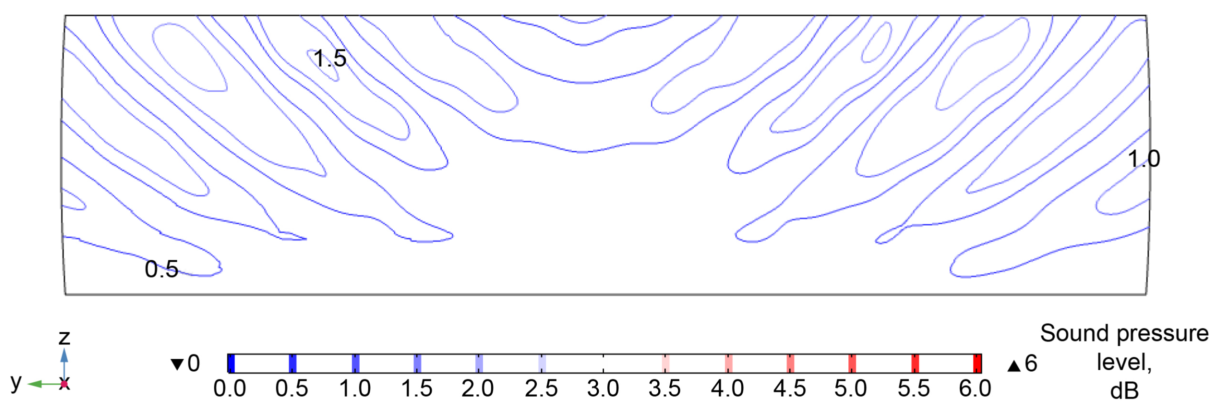

Figure 73.—Lossless sound pressure level perturbation magnitude on 227-cm (89.3-in.) sideline measurement surface at 500 Hz for one-row walkway.

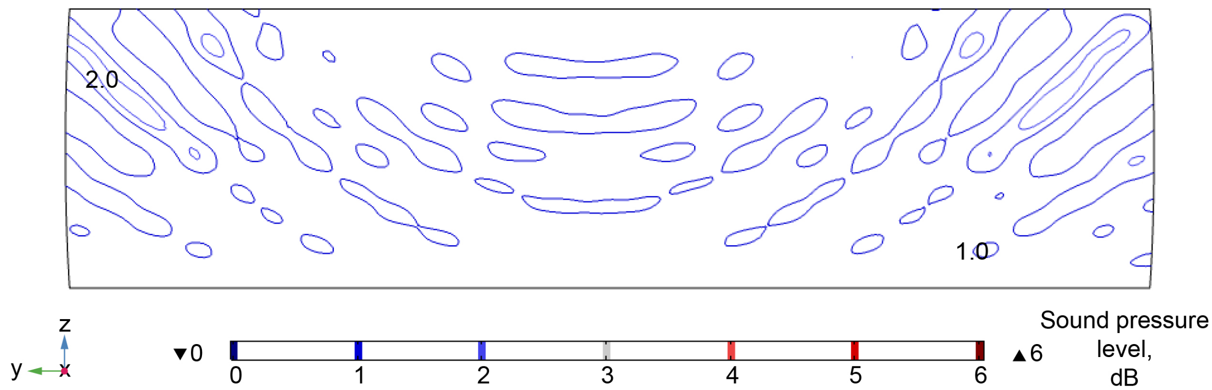

Figure 74.—Lossless sound pressure level perturbation magnitude on 227-cm (89.3-in.) sideline measurement surface at 1,000 Hz for one-row walkway.

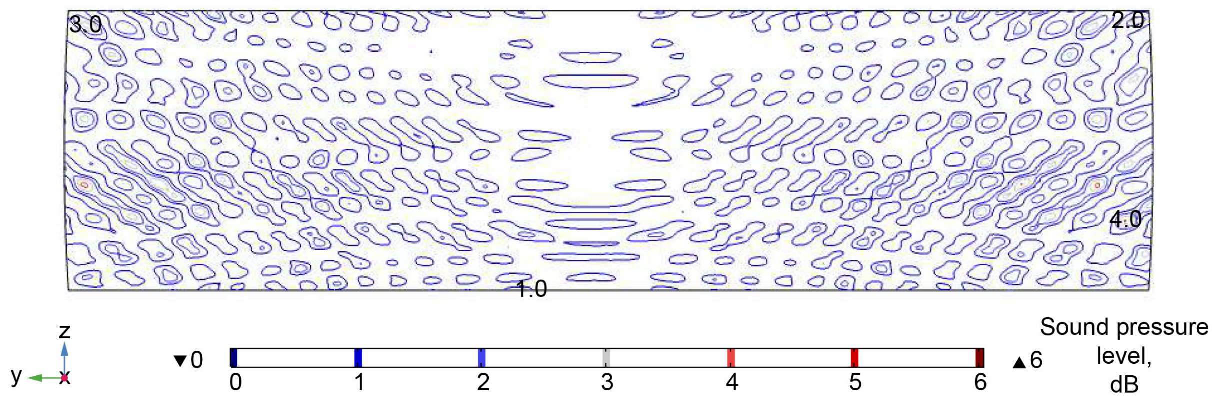

Figure 75.—Lossless sound pressure level perturbation magnitude on 227-cm (89.3-in.) sideline measurement surface at 2,000 Hz for one-row walkway.

Finally, at 4,000 Hz, Figure 76 shows that the predicted perturbations are similar in magnitude to those at 2,000 Hz, but with a finer scale to the pattern due to the higher frequency.

The second walkway configuration has two rows of acoustic boxes removed. This provides a hard surface from the wall to the model, but also significantly increases the reflection area and moves the impedance jump closer to the source. As expected, Figure 77 to Figure 79 show significantly larger perturbations on the 227-cm (89.3-in.) sideline.

At 500 Hz, Figure 77, the peak perturbation is over 6 dB, while it was only 1.5 dB for the one-row configuration. At 1,000 and 2,000 Hz, the peak perturbation is also well over 6 dB. The two-row walkway is not feasible, and the one-row walkway introduces a noticeable level of additional uncertainty.

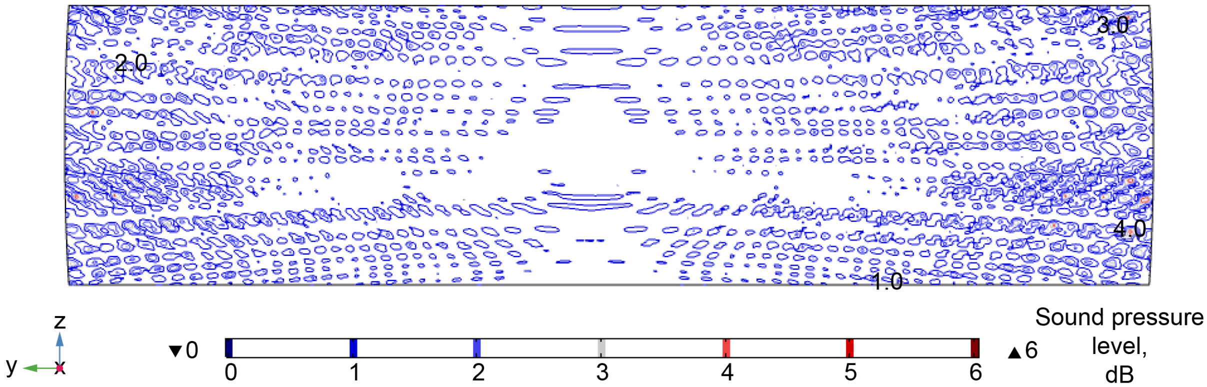

Figure 76.—Lossless sound pressure level perturbation magnitude on 227-cm (89.3-in.) sideline measurement surface at 4,000 Hz for one-row walkway.

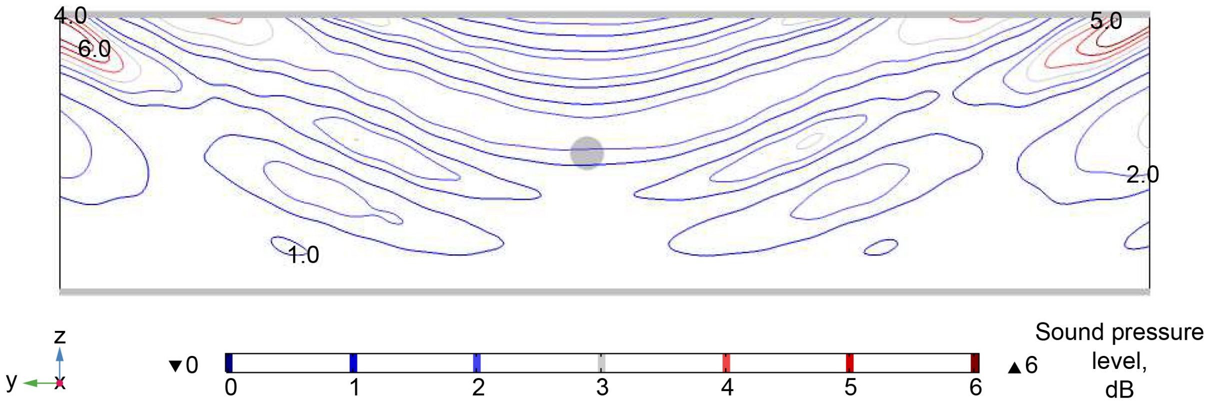

Figure 77.—Lossless sound pressure level perturbation magnitude on 227-cm (89.3-in.) sideline measurement surface at 500 Hz for two-row walkway.

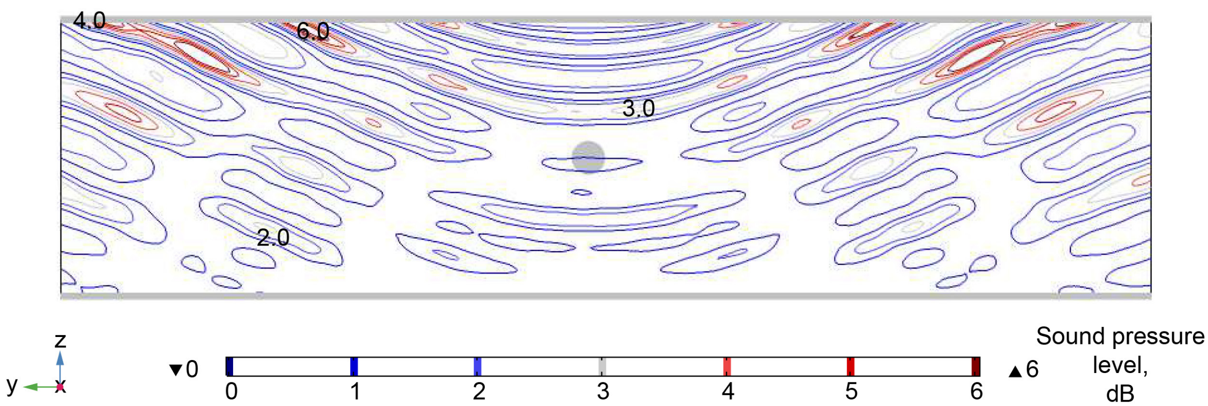

Figure 78.—Lossless sound pressure level perturbation magnitude on 227-cm (89.3-in.) sideline measurement surface at 1,000 Hz for two-row walkway.

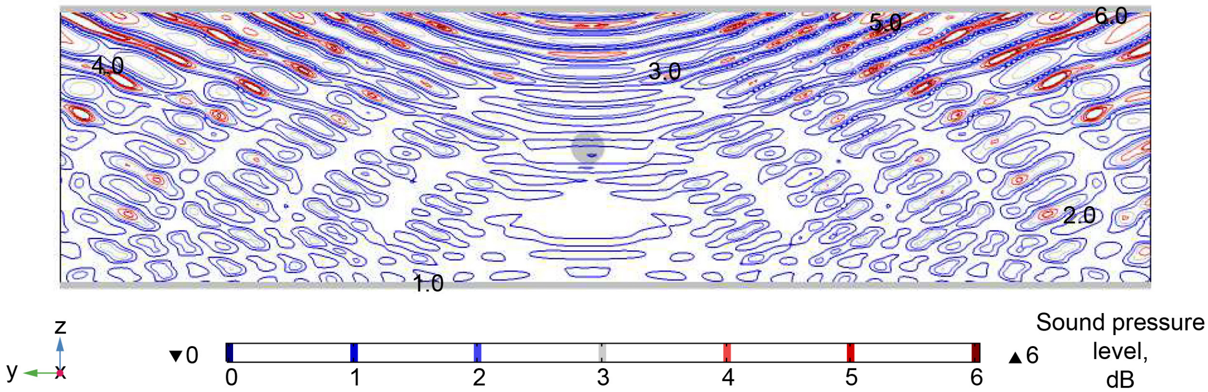

Figure 79.—Lossless sound pressure level perturbation magnitude on 227-cm (89.3-in.) sideline measurement surface at 2,000 Hz for two-row walkway.

9.7 Impact of Armature

The final analysis to be presented is an assessment of the traversing microphone armature in the presence of the hard-wall inlet contraction, brush seals on the traverse side, and the light boxes on the model side in the upper row outer locations.

COMSOL boundary element analyses, pabe physics, were run with the traverse at a sequence of positions starting near the test section entrance, 51 cm (20 in.), in increments of 127 cm (50 in.), to the aft most position 940 cm (370 in.). The sideline traverse armature holds five microphones, with microphone number 1 at the bottom and number 3 in the center. The microphone positions relative to the model shaft axis are nominally –25°, –15°, 0°, 15°, or 25° from horizontal. The microphone cartridge would be approximately 26 cm (10 in.) ahead of the armature leading edge, but the microphones and support tubes ahead of the armature are not in this model. Lossless sound pressure level perturbations are predicted on the 227-cm (89.3-in.) sideline measurement surface from the entrance to an axial position 15 cm (6 in.) behind the microphone position or 9 cm (3.5 in.) ahead of the armature leading edge. Note that the monopole source now has a 2.5-cm (1-in.) radius.

Figure 80 shows this near-term full operational configuration.

Figure 81 shows the results for 400 Hz. Reflections and scattering from the armature show up as local differences near the armature. The character away from the armature is independent of armature position, being the reflections from the inlet, brush seals, and light boxes. Through most of the test section, the resulting lossless sound pressure level uncertainty is less than ±0.5 dB at 400 Hz. The perturbation that follows the armature varies with armature position due to presenting different portions of the armature to the incoming wave. From the test section inlet to about the 2-m position, there is little armature perturbation. The largest perturbation is seen for the x = ~6.9-m position (yellow curve) where the reflections from the armature introduce up to ±0.2-dB changes in the standing pattern. Positioning the microphone further upstream of the microphone would reduce the armature-related perturbations, but the offset would need to be an additional 0.5 m to remove the effect near x = 6.5 m. At 400 Hz, reducing the armature-related perturbation is unnecessary as it is much smaller than the ±1-dB variation in the standing pattern.

Figure 82 presents the same analysis at 800 Hz. The lossless sound pressure level perturbations are less than ±1 dB through most of the test section, although near the inlet the uncertainty is ±1.5 dB.

At 1,600 Hz, Figure 83, the uncertainty on microphone 3 is roughly ±1.5 dB throughout the test section. At 2,400 Hz, Figure 84, the character of the uncertainty has changed: higher at the test section inlet and exit at roughly ±2.5 dB, reducing to ±1 dB in the center. The axial position of the source is at about 5 m where the perturbations are minimum.

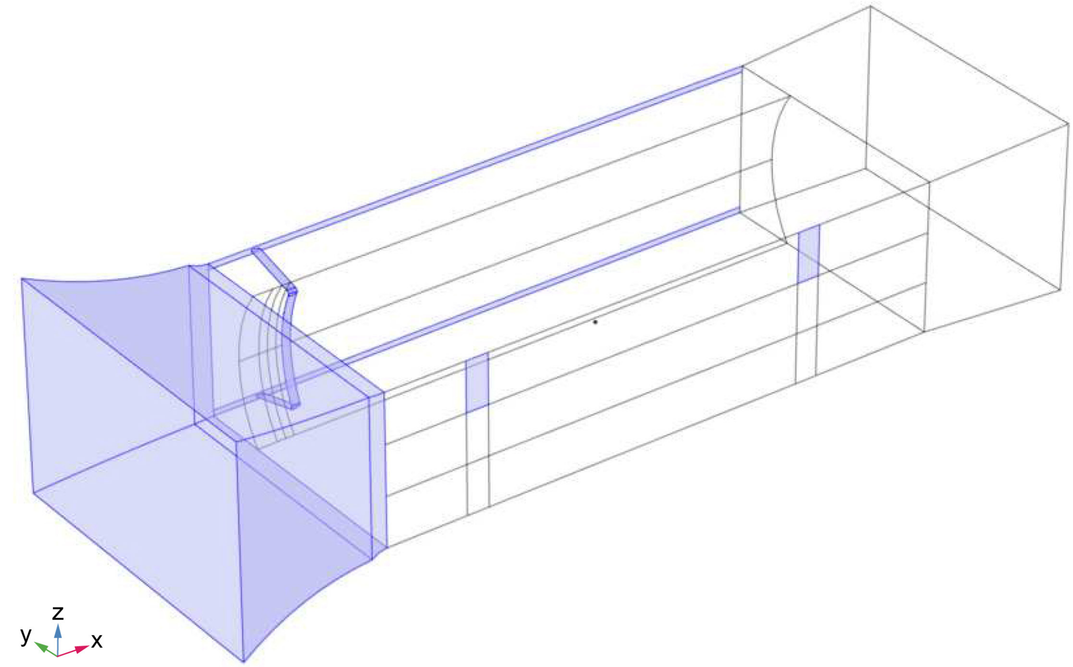

Figure 80.—Boundary element model (pabe) for 9- by 15-Foot Low-Speed Wind Tunnel with hard-wall (blue shade) contraction, two light boxes on traverse sidewall, 10-cm (4-in.) brush seals in both traverse- and model-side wall upper and lower corners, and traversing microphone armature in position near test section entrance. Flow would be from left to right. Monopole spherical source is 1-in. diameter (dot in center of figure).

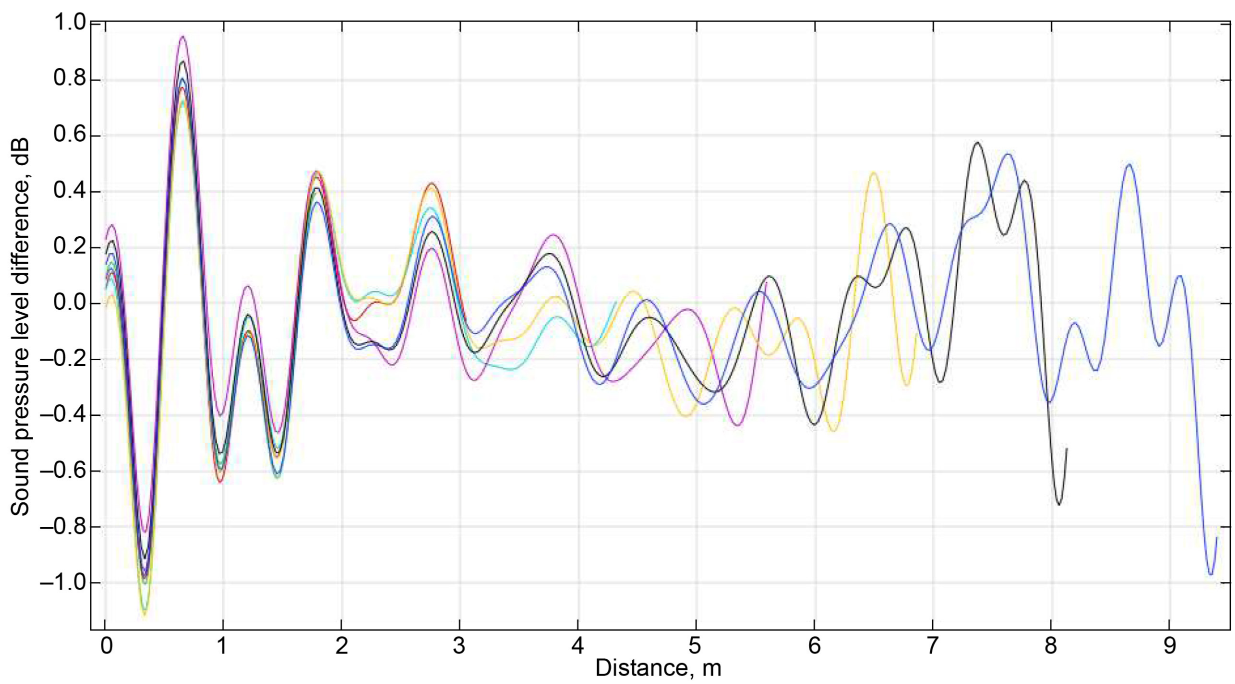

Figure 81.—Lossless sound pressure level (SPL) perturbation at 400 Hz on 227-cm (89.3-in.) sideline surface along path for microphone 3 (on center). For sequence of armature positions, delta SPL is shown from inlet to armature position.

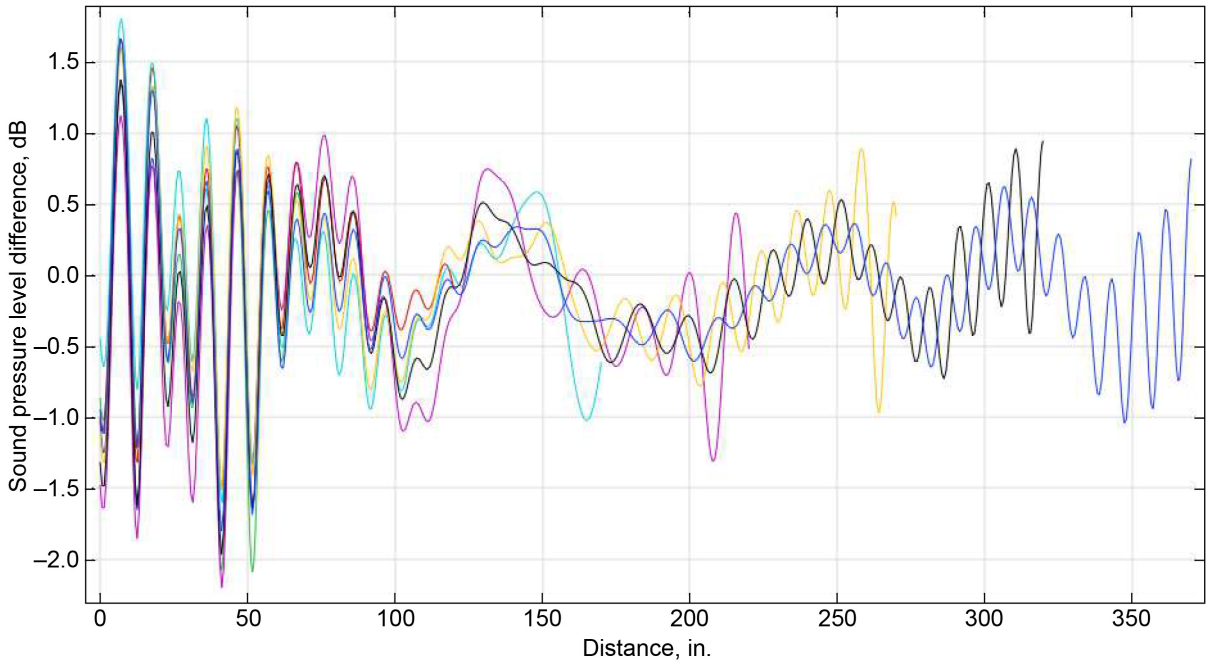

Figure 82.—Lossless sound pressure level perturbations on 227-cm (89.3-in.) sideline for microphone 3 at 800 Hz. Results are plotted for sequence of armature positions.

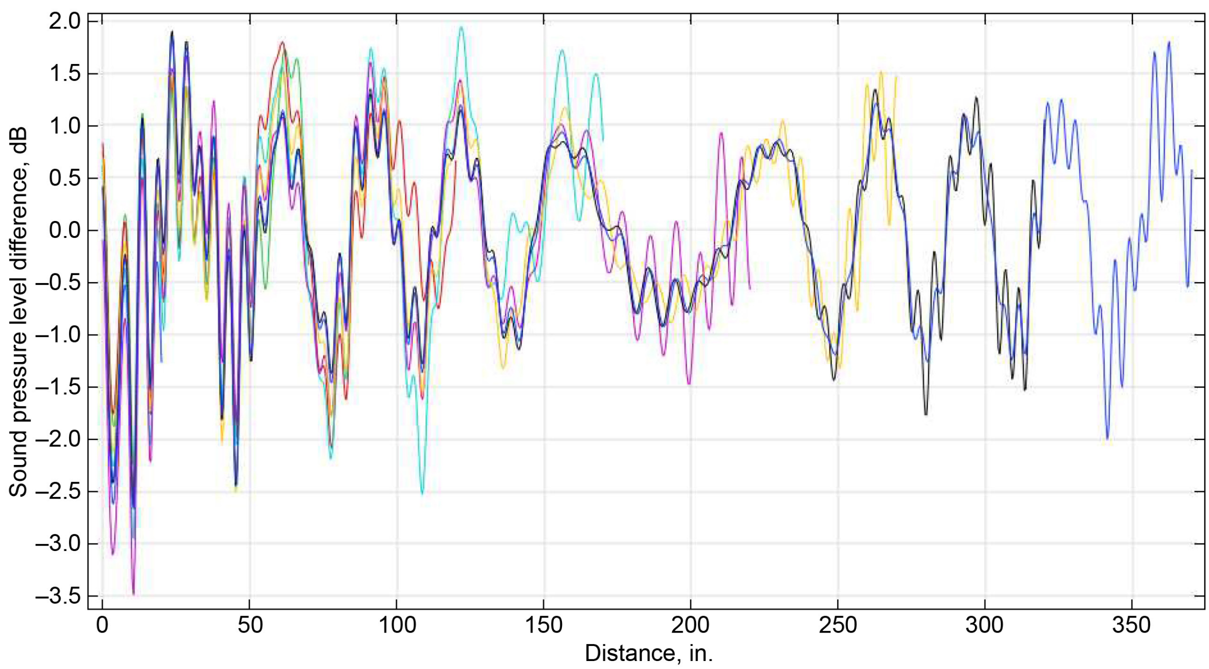

Figure 83.—Lossless sound pressure level perturbation at 1,600 Hz on 227-cm (89.3-in.) sideline surface along path for microphone 3 (on center). Results are plotted for sequence of armature positions.

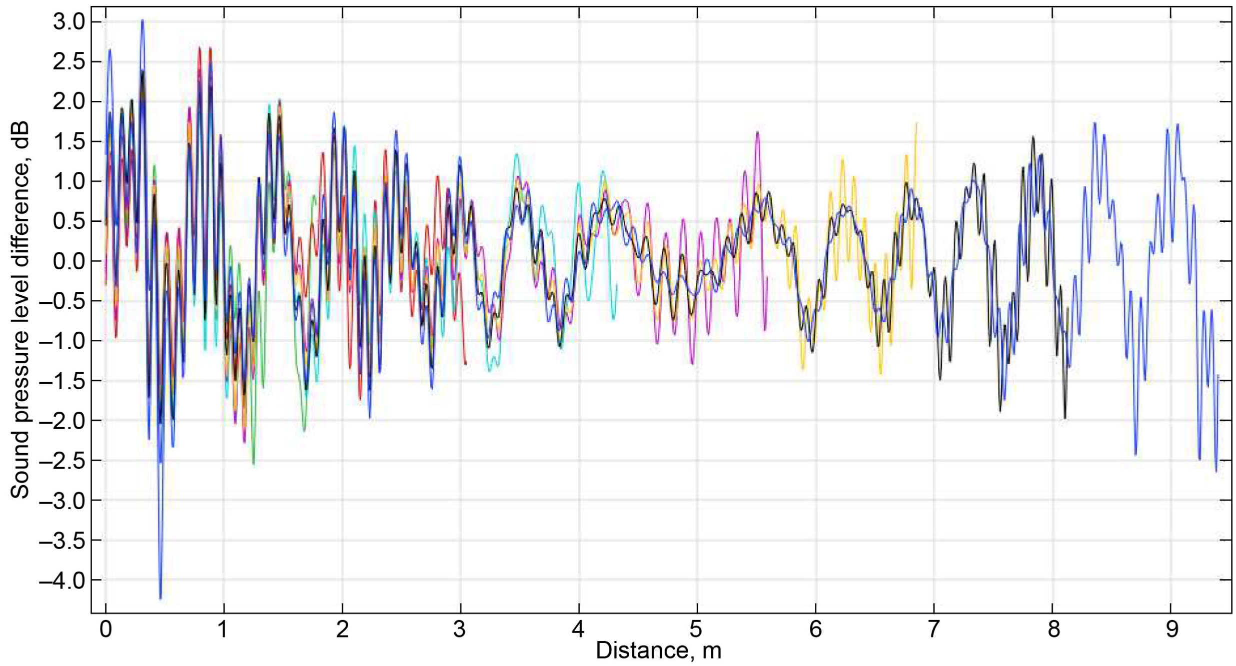

Figure 84.—Lossless sound pressure level perturbation at 2,400 Hz on 227-cm (89.3-in.) sideline surface along path for microphone 3 (on center). Results are plotted for sequence of armature positions.

At 4,800 Hz, Figure 85, the perturbations are similar to those at 2,400 Hz: ±2.5 dB at the inlet and exit, tapering to ±1 dB in the middle. Again, reflections and scattering from the armature show up as local differences near the armature. Consider the microphone near 7 m, downstream of the source location at 5.27 m. The yellow curve shows axial oscillations range from –2 to 1.5 dB near the armature. At this axial location, for armature positions further downstream, the oscillations are reduced, ranging from –1 to 0.75 dB.

Figure 86 to Figure 94 present views of the magnitude of the lossless sound pressure level perturbations across the entire 227-cm (89.3-in.) sideline surface, computed with the traverse at the furthest downstream position.

At 400 Hz, Figure 86, the largest perturbations, just over ±1 dB, are not on the centerline (seen by microphone 3) but are nearer the floor and ceiling at the inlet to the test section. Most of the sampling surface is under ±0.5 dB.

At 800 Hz, Figure 87, the perturbations are larger. Near the inlet are a couple of small regions just over ±2.0 dB. The middle of the test section is less than ±1.0 dB, and usually less than ±0.5 dB.

At 1,600 Hz, Figure 88, there are peaks of ±2 dB near the inlet, and a few very small regions at ±3 dB. At this frequency and higher, the perturbation pattern has a vertical symmetry.

Figure 89, for 2,400 Hz, shows essentially the same result as for 1,600 Hz: mostly below ±1 dB, some regions above ±2 dB, and a few small regions above ±3 dB. The higher uncertainty regions will affect microphones near the floor (1 and 2) and near the ceiling (4 and 5).

Figure 90, for 3,200 Hz, is again similar to the 1,600 and 2,400 Hz results but has larger regions near the inlet with uncertainty above ±3 dB. This frequency has the largest, but still small, regions above ±3 dB for all the frequencies examined.

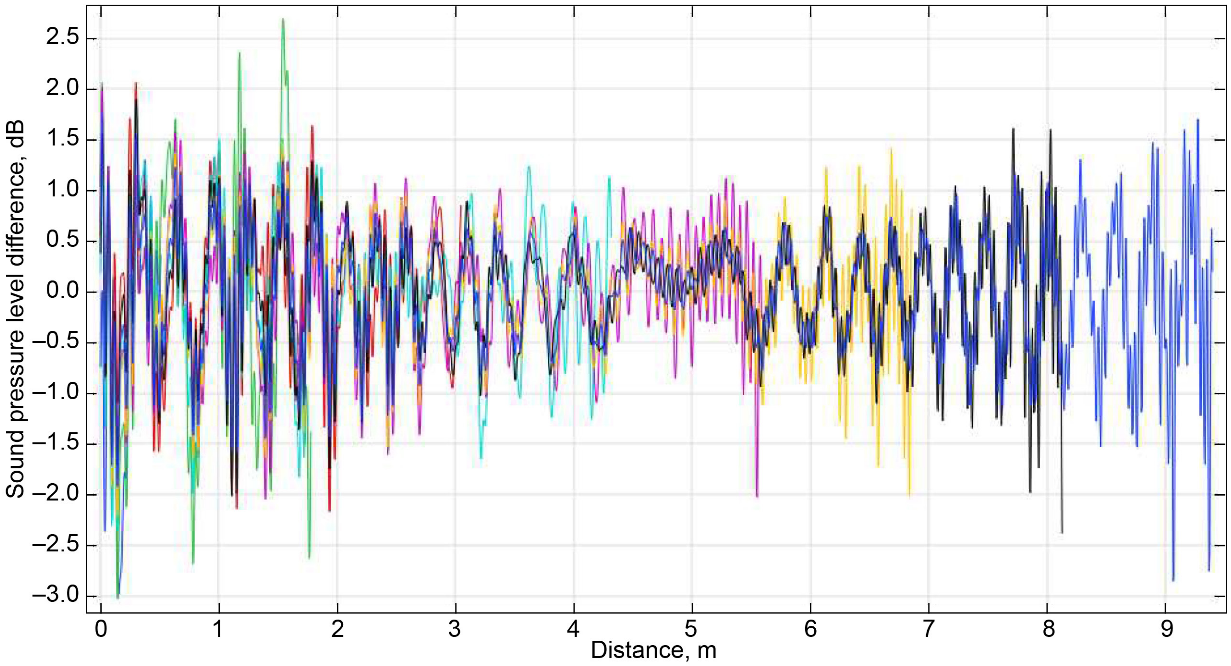

Figure 85.—Lossless sound pressure level perturbation at 4,800 Hz on 227-cm (89.3-in.) sideline surface along path for microphone 3 (on center). Results are plotted for sequence of armature positions.

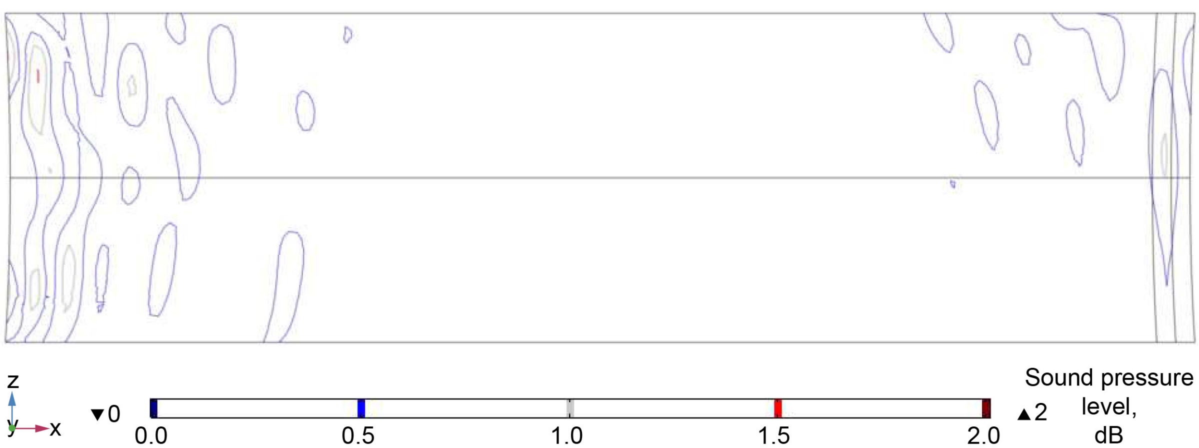

Figure 86.—Lossless sound pressure level perturbation magnitude at 400 Hz on 227-cm (89.3-in.) sideline surface axially from inlet to 940 cm (370 in.) downstream.

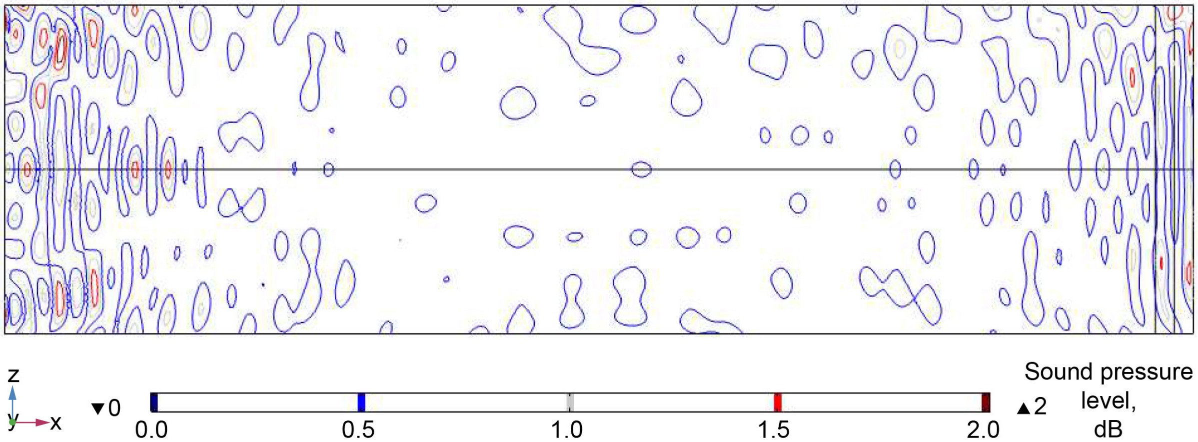

Figure 87.—Lossless sound pressure level perturbation magnitude at 800 Hz on 227-cm (89.3-in.) sideline surface axially from inlet to 940 cm (370 in.) downstream.

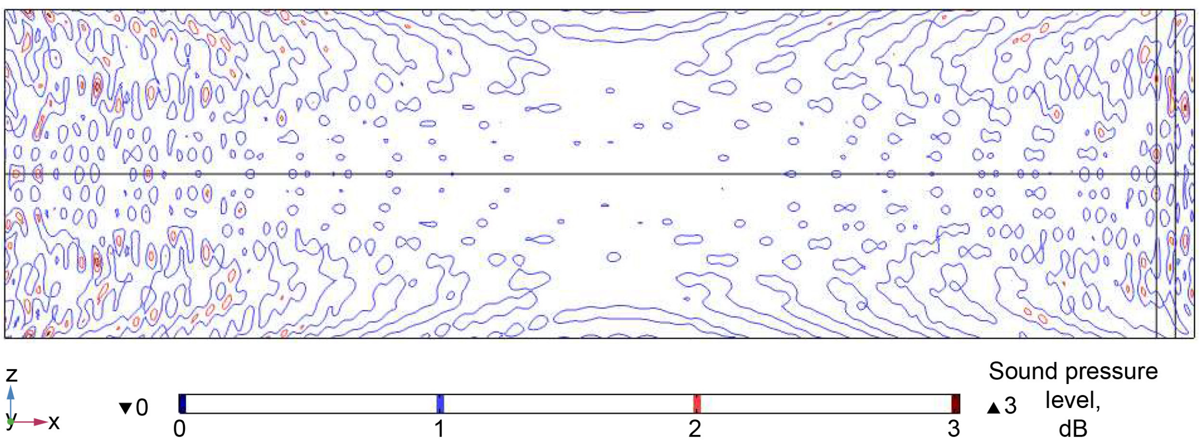

Figure 88.—Lossless sound pressure level perturbation magnitude at 1,600 Hz on 227-cm (89.3-in.) sideline surface axially from inlet to 940 cm (370 in.) downstream.

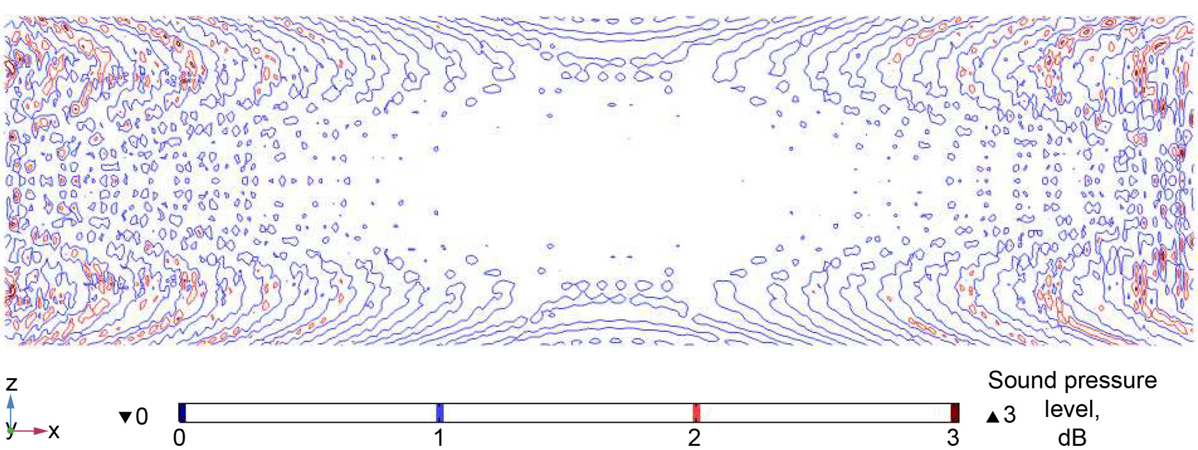

Figure 89.—Lossless sound pressure level perturbation magnitude at 2,400 Hz on 227-cm (89.3-in.) sideline surface axially from inlet to 940 cm (370 in.) downstream.

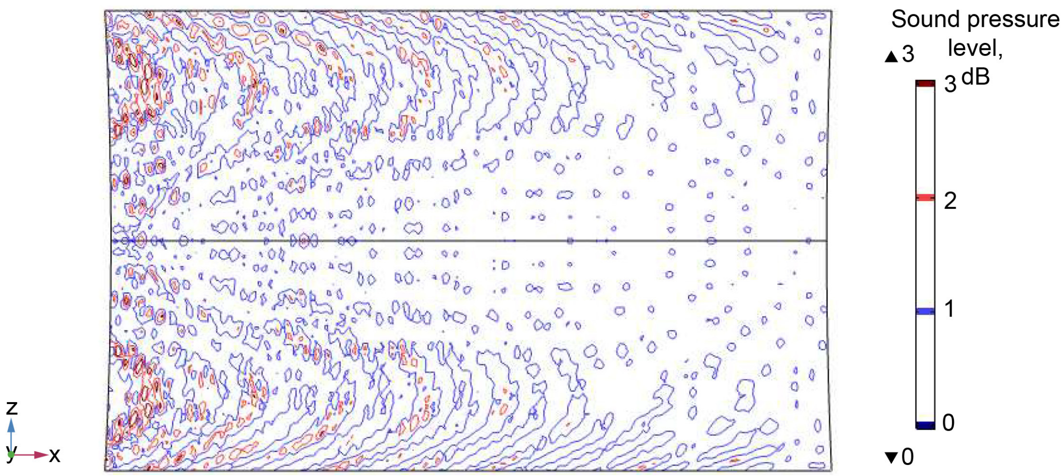

Figure 90.—Lossless sound pressure level perturbation magnitude at 3,200 Hz on 227-cm (89.3-in.) sideline surface axially from inlet to 432 cm (170 in.) downstream.

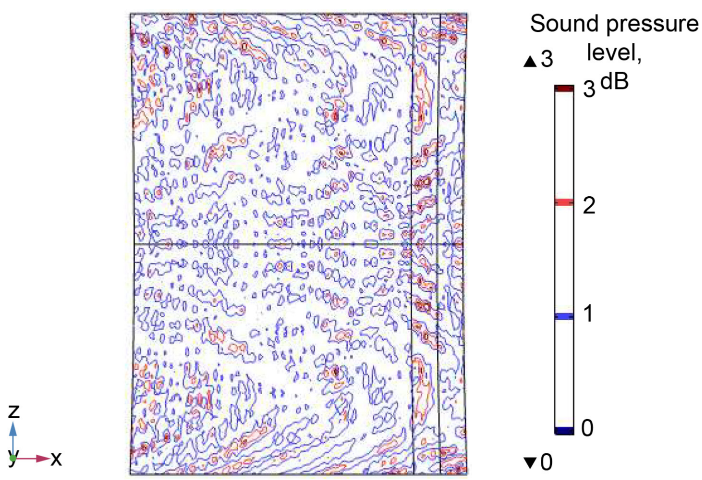

Figure 91.—Lossless sound pressure level perturbation magnitude at 4,000 Hz on 227-cm (89.3-in.) sideline surface axially from inlet to 178 cm (70 in.) downstream.

Figure 91, for 4,000 Hz, shows the regions near the inlet of higher uncertainty are decreasing in size. By plotting the results for an armature position near the inlet, where the armature is upstream of the source, the scattering from the armature has a significant effect at the microphone location (the vertical black line nearest the right edge of the plot).

Figure 92, for 4,800 Hz, shows that even more of the sideline measurement surface has a maximum uncertainty below ±1 dB. The reflections and diffractions at the inlet and exit are reducing in magnitude.

Figure 93 has a magnified view of the inlet-ceiling corner, which is usually the region of highest uncertainty. The regions above ±3 dB are almost gone. Figure 94 for 5,400 Hz is similar.

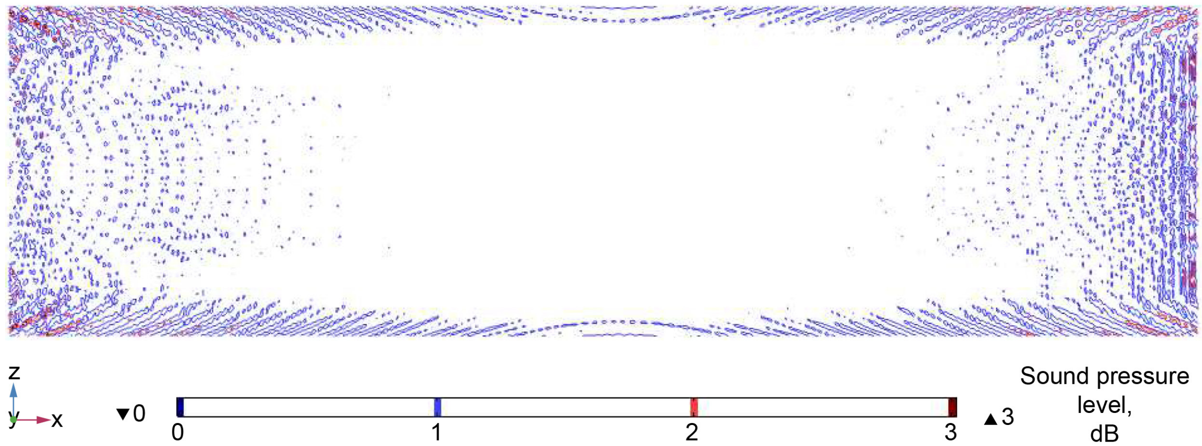

Figure 92.—Lossless sound pressure level perturbation magnitude at 4,800 Hz on 227-cm (89.3-in.) sideline surface axially from inlet to 940 cm (370 in.) downstream.

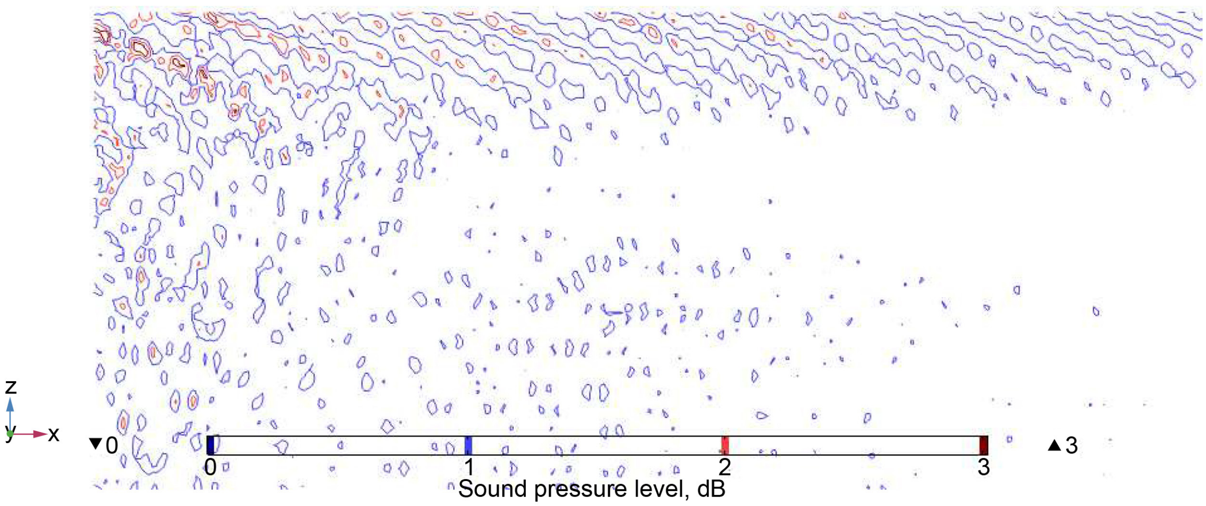

Figure 93.—Lossless sound pressure level perturbation magnitude at 4,800 Hz on upper half of 227-cm (89.3-in.) sideline surface axially from inlet to approximately 381 cm (150 in.) downstream.

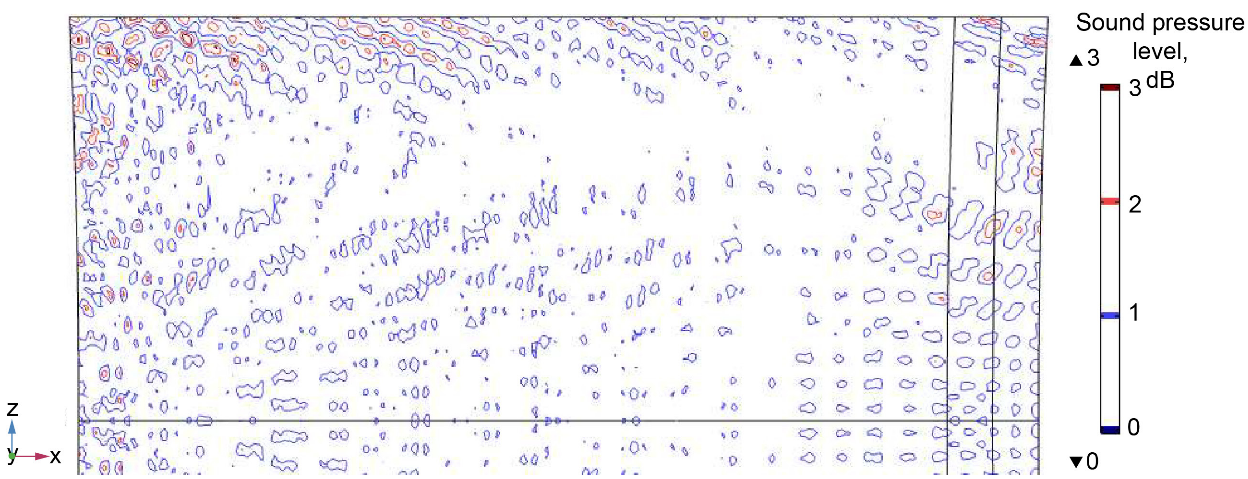

Figure 94.—Lossless sound pressure level perturbation magnitude at 5,400 Hz on upper half of 227-cm (89.3-in.) sideline surface axially from inlet to 305 cm (120 in.) downstream.

In summary, this boundary element analysis for the upper bound on measurement uncertainty has found that over most of the 227-cm (89.3-in.) sideline surface swept out by the traversing microphone, the uncertainty due to reflections from the camera boxes, traverse arm, and hard-wall inlet is less than ±1 dB. There are regions where the upper bound on uncertainty can be as much as ±3 dB, but these regions are small. Computational resource limitations prevented running the better computational estimate including reflections from the acoustic treatment boxes.

10.0 Conclusions

In summary, this analysis for the upper bound on measurement uncertainty has found that over most of the 227-cm (89.3-in.) sideline surface swept out by the traversing microphone, the uncertainty due to reflections from the camera boxes, traverse arm, and hard-wall inlet, but not including reflections from the acoustic treatment boxes, is less at ±1 dB. There are regions where the upper bound on uncertainty can be as much as ±3 dB, but these regions are small. The reverberation time measurements discussed in Section 6.3 were carried out with the hard-wall inlet and light boxes, but without the brush seals and traversing armature. That analysis determined that reflections from the treatment boxes would be 15 dB below the incident signal. This very low level of reflection supports the boundary element modeling approach. The draw-away test discussed in Section 7.2 found a measurement uncertainty of 2.5 dB. Again, this was done with the hard-wall inlet and light boxes (on the south, or model side, but not on the traverse side), and without the brush seals and traversing microphone armature. While the COMSOL results for the upper bound on measurement uncertainty are consistent with the experimental measurements, the COMSOL modeling did not include the configurations tested, so there is no direct comparison with test data. Another test, a traversing microphone sweep with the known source, would provide the best comparison with the computational assessment, and the best assessment of the as-built new test section measurement uncertainty.

Appendix A.—Preconstruction Testing

This appendix documents the background noise measurements that motivated and enabled the acoustic improvement project, as discussed in Section 2.0. The open rotor program for nonproprietary data, Escort program D069, was used for these measurements. Runs 204 to 209 were acquired with test dates between Feb. 23 and Mar. 12, 2012. Not all of the data turned out to be useful, but all runs and readings are reported here for completeness sake. The runs are summarized in Table A.1. Configurations for each run are documented in Table A.2 to Table A.4. Logs for individual runs are provided in Table A.5 to Table A.10.

- Run 204: This test was a first attempt at measuring the noise through the 9- by 15-Foot Low-Speed Wind Tunnel (9×15 LSWT) leg of the tunnel loop. The microphone locations are given in a schematic in Figure A.1 and in Table A.2. The data from this measurement came out well except for channel 11, which was in the diffuser. After attempting to make even more measurements of the noise in the diffuser during runs 207 to 209, we realized that the flow separation in the diffuser must lead to turbulence that impinges on the microphones, swamping the acoustic pressures of interest.
- Run 205: The results from run 204 were briefly examined, and the microphones were moved to capture the noise elsewhere in the tunnel loop, including the 8- by 6-Foot Supersonic Wind Tunnel (8×6 SWT) portion of the tunnel loop. Figure A.2 shows the microphone locations for runs 205 and 206.
- Run 206: Same as run 205 but with some slight clean up in the test section: vertical door in test section cleaned up, door slot taped, floor microphone realigned with floor, and center traverse microphone realigned with flow.
- Run 207: Traverse removed along with all microphones except the ceiling microphone. Remaining microphones include three upstream (either side of parallel baffles, plus front of cooler) and three downstream (two on original diffuser and one in front of doors 4 and 5). Figure A.3 is a schematic of the microphone locations for runs 207 to 209.
- Run 208: Same as 207 but the tunnel aerodynamic rakes were removed. The test section conditions were set using motor revolutions per minute and door positions as recorded in run 207. Run ended in questionable data as a microphone cable was damaged by doors 1 and 2 motion.
- Run 209: Repeat runs 207 and 208.

TABLE A.1.—D069 EMPTY TUNNEL ACOUSTICS RUN LOG

Run number	Reading number	Date	Comment
204	2011 to 2028	2/23/2012	Microphones in 9- by 15-Foot Low-Speed Wind Tunnel leg of tunnel loop
205	2029 to 2042	2/29/2012	Microphones in 8- by 6-Foot Supersonic Wind Tunnel leg of tunnel loop
206	2043 to 2056	3/2/2012	Same as 205 but with clean up in test section
207	2057 to 2063	3/9/2012	Vary shock doors, vary doors 1 and 2, record motor revolutions per minute
208	2064 to 2071	3/9/2012	Repeat 207 but with tunnel rakes removed
209	2072 to 2090	3/12/2012	Repeat of runs 207 and 208

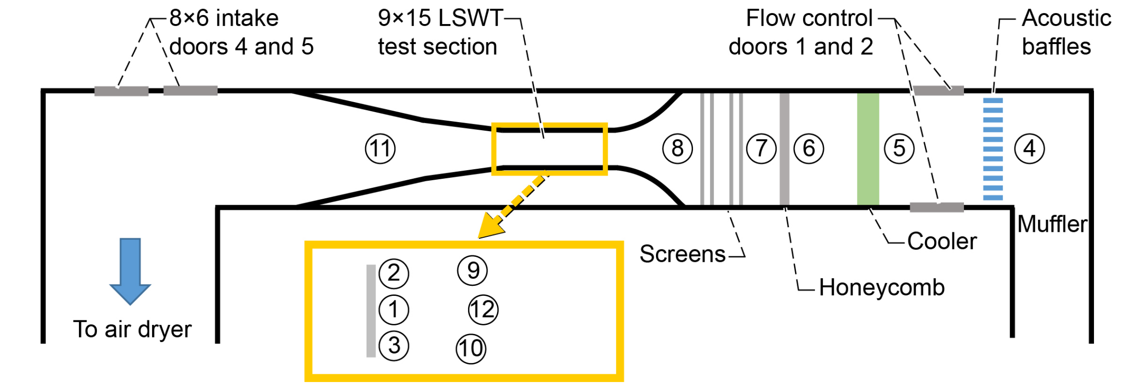

Figure A.1.—Sketch showing microphone locations used for run 204. Not to scale. Low-speed wind tunnel (LSWT).

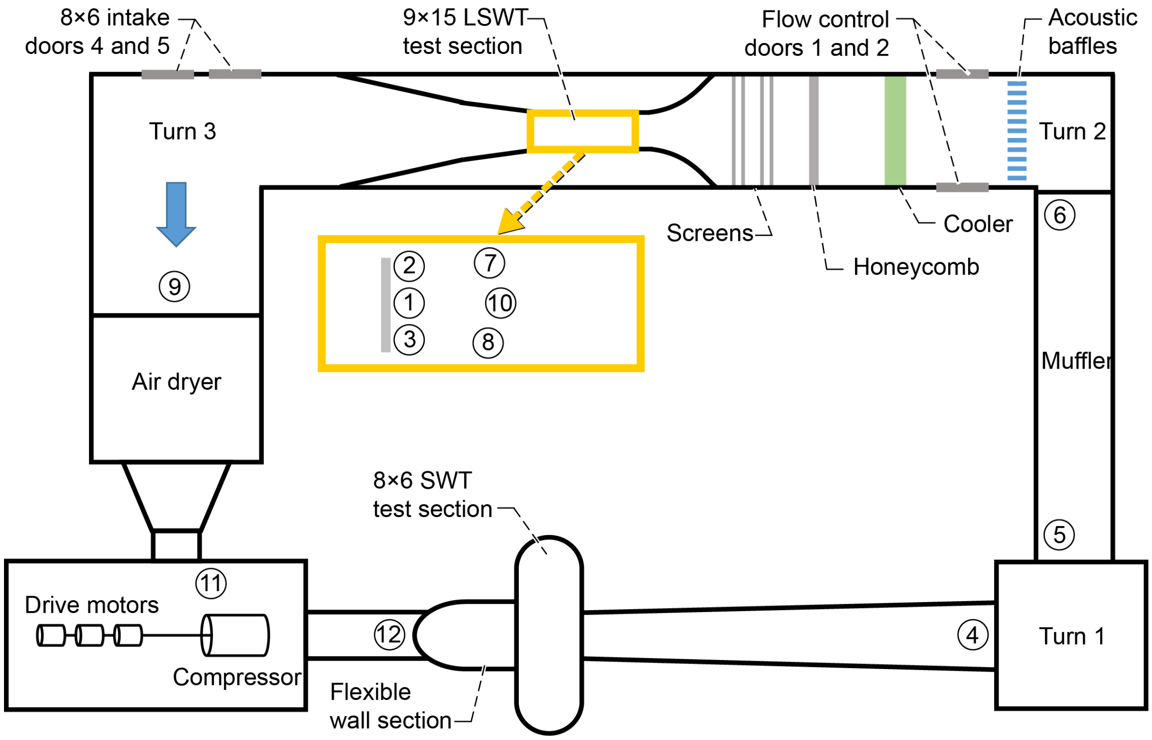

Figure A.2.—Sketch showing microphone locations used for runs 205 and 206. Not to scale. Gray bar represents three-microphone traversing probe. Low-speed wind tunnel (LSWT).

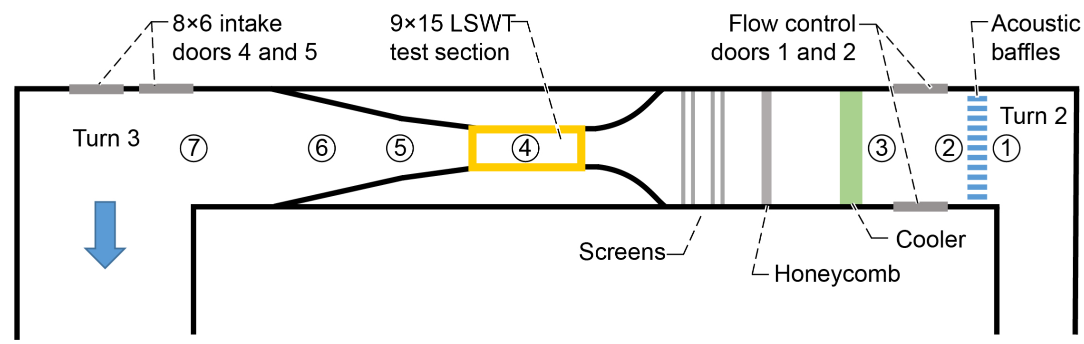

Figure A.3.—Sketch showing microphone locations used for runs 207 to 209. Not to scale. Low-speed wind tunnel (LSWT).

A.1 Photographs

This section includes pictures (Figure A.4 to Figure A.18) of the instrumentation used in the preconstruction noise testing.

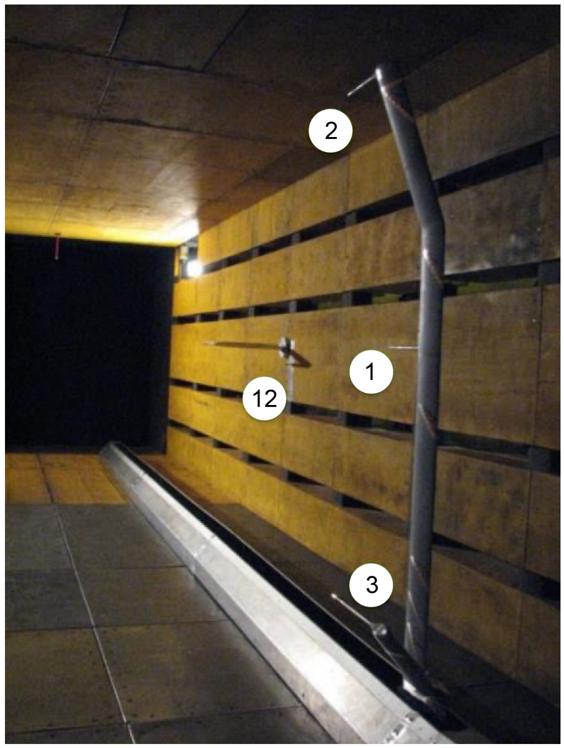

Figure A.4.—Microphones 1, 2, 3, and 12 in test section during run 204.

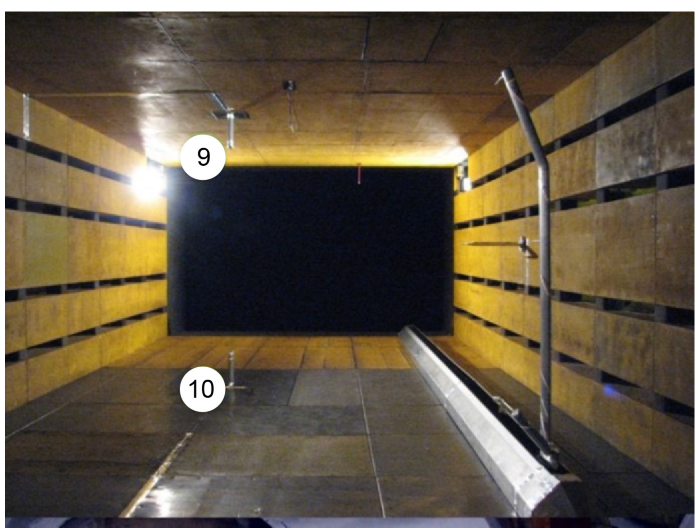

Figure A.5.—Microphones 9 and 10 in test section during run 204.

Figure A.6.—Microphone channel 4 used in run 204. Location is turn 2 plenum, just upstream of parallel baffles.

Figure A.7.—Microphone channel 5 used in run 204. Location is upstream of cooler and downstream of doors 1 and 2.

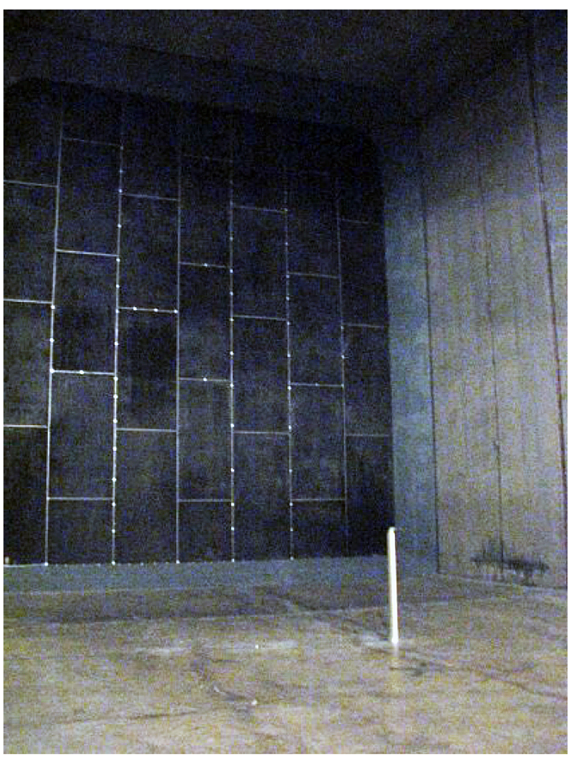

Figure A.8.—Microphone channel 6 used in run 204. Location is upstream of honeycomb and downstream of cooler.

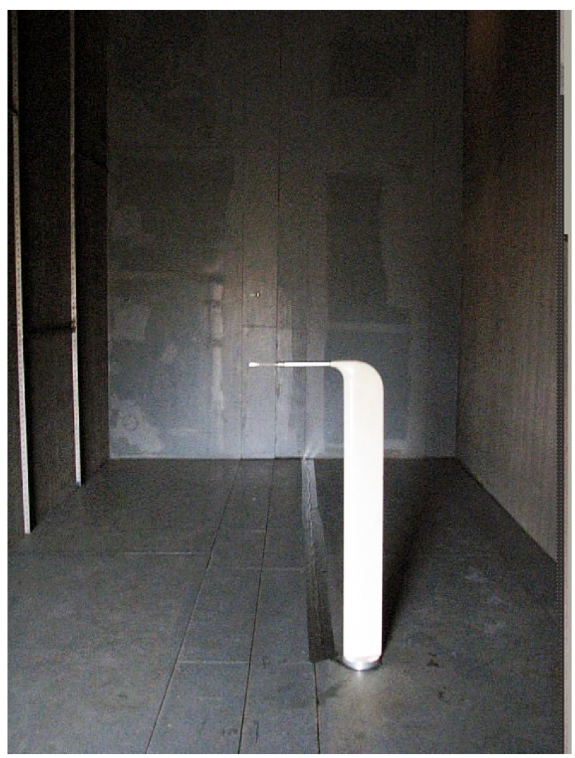

Figure A.9.—Microphone channel 7 used in run 204. Location is upstream of first screen and downstream of honeycomb.

Figure A.10.—Microphone channel 8 used in run 204. Location is upstream of contraction and downstream of last screen.

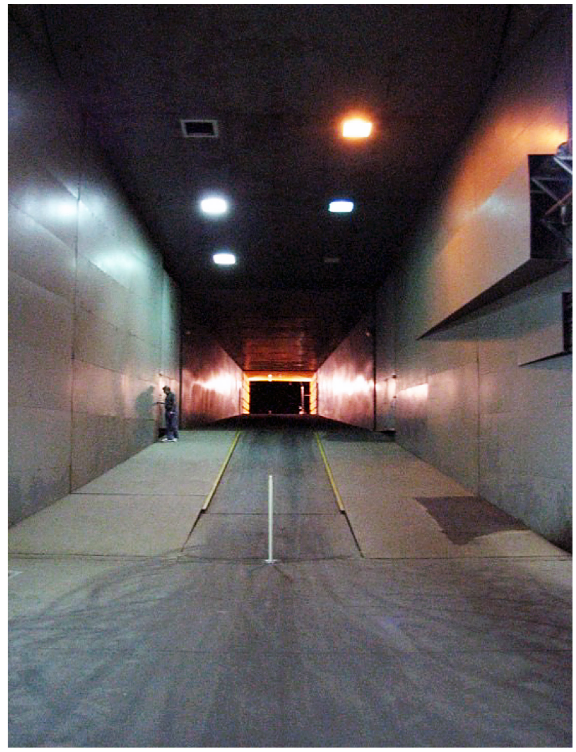

Figure A.11.—Microphone channel 11 used in run 204. Location is end of downstream diffuser.

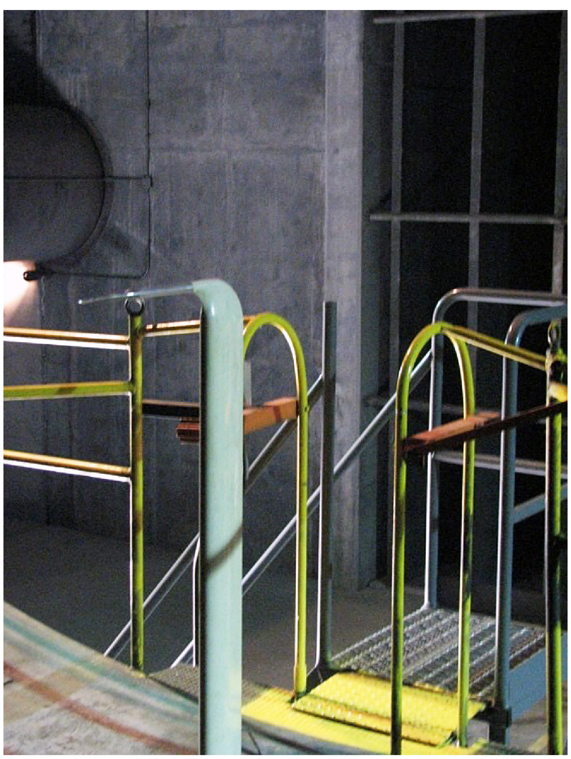

Figure A.12.—Microphone channel 4 used in run 205. Location is exit of 8- by 6-Foot Supersonic Wind Tunnel diffuser, just upstream of stairs.

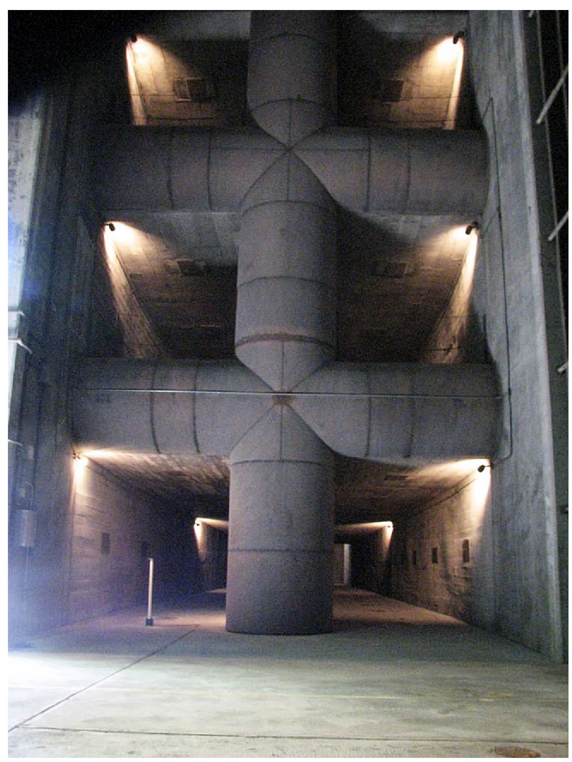

Figure A.13.—Microphone channel 5 used in run 205. Location is entrance to muffler.

Figure A.14.—Microphone channel 6 used in run 205. Location is exit of muffler.

Figure A.15.—Microphone channel 9 used in run 205. Location is upstream of air dryer filters in turn 3.

Figure A.16.—Microphone channel 11 used in run 205. Location is compressor plenum. Recorded on separate recorder than channels 1 to 10.

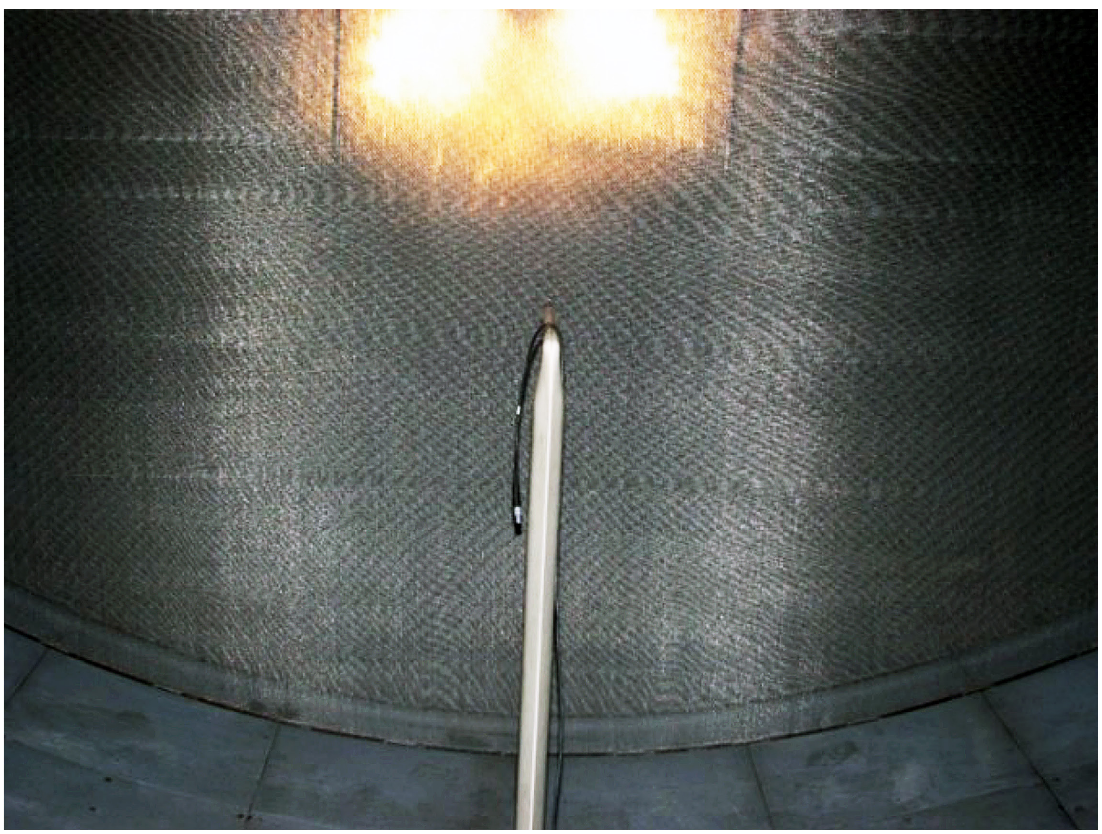

Figure A.17.—Microphone channel 12 used in run 205. Location is downstream of 8- by 6-Foot Supersonic Wind Tunnel screens. Recorded on separate recorder than channels 1 to 10.

Figure A.18.—Microphone channels 5 to 7 for runs 207 to 209. Locations are in 9- by 15-Foot Low-Speed Wind Tunnel diffuser and in front of doors 4 and 5 as shown in Figure A.3.

A.2 Tunnel Operation Observations

As part of the tunnel background noise observations, we manipulated the various control mechanisms at the disposal of the tunnel operators. There are four control mechanisms:

- Doors 1 and 2: These doors are at the upstream edge of the 9×15 LSWT leg. From the point of view of the 8×6 SWT, these are outlet doors, which could be opened to exhaust combustion products.
- Compressor speed: The wind tunnel is driven by a seven-stage axial compressor designed and built in the late 1940s. The compressor speed is varied using a liquid rheostat system (Ref. 35).
- Doors 4 and 5: These doors are at the downstream end of the 9×15 LSWT leg. The 9×15 LSWT test section can be isolated by closing door 3 (at the upstream edge of the test section) and doors 6 and 7 (at the downstream end of the high-speed diffuser). The various doors are indicated in Figure 1. The 9×15 LSWT test section can be isolated to facilitate model installation during cold weather or while testing is occurring in the 8×6 SWT test section. When the 8×6 SWT is operating in this “open loop” configuration, 100 percent of the air running through the compressor is exhausted out of doors 1 and 2 and outside air is pulled in through doors 4 and 5. When the tunnel is operating “closed loop,” then it is expected that there is very little flow through these doors. A vent also exists in turn 3, ensuring that this point in the tunnel loop is always at atmospheric pressure.
- Shock doors: When the 8×6 SWT is in supersonic operation, the pressure in the test section is maintained by a set of very stout hydraulically actuated doors. These doors hold the normal shock that occurs before the flow decelerates into the diffuser. They can be used to maintain the backpressure on the compressor during 9×15 LSWT operation.

The flow control doors 1 and 2 are shown in Figure A.19. In order to achieve a test section speed of Mach 0.20, the compressor is operated at a speed of around 685 rpm when the doors are completely closed. With the doors 10 percent open, a compressor speed of 800 rpm is required to reach Mach 0.20 in the test section. At 14 percent open, a compressor speed of 865 rpm is required. The noise generated at these three operating conditions is shown in Figure A.19 and Figure A.20. Figure A.19 shows that in the vicinity of doors 1 and 2, the noise absolutely changes with door position. The loudest case is that of the doors completely closed, with a noticeable local maximum at around 1,300 Hz. It may be that whatever leakage velocity occurs, it is highest with the doors closed. Either way, Figure A.20 shows that the noise in the test section does not change, although there does seem to be a remnant of the noise at 1,300 Hz, manifesting as a local maximum.

Further evidence that the 1,300-Hz local maximum is propagating from upstream into the test section comes from measuring the noise at different places in the test section. As shown in Figure A.21, this spectral feature is loudest near the front of the test section and quietest in the aft. The rest of the sound spectra is essentially unchanged, although slightly louder upstream above 2 kHz. It is currently believed that this is due to “roughness noise” from flow over the acoustic boxes. The noise is louder upstream because the boundary layer is thinner and more high-speed flow interacts with the tunnel walls.

Slightly different conclusions were found during the 2011 survey, with results shown in Figure A.22. During this survey, additional low-frequency noise was found to be propagating into the tunnel from downstream. It creates the peculiar condition that below 1 kHz, the tunnel noise is louder aft, while above 1 kHz, the noise is louder upstream. The source of the downstream low-frequency noise has not been identified, but it did reappear in the 2016 survey discussed in Section 2.1.

The noise due to rakes in the test section was investigated. Run 209 was conducted with only one test section rake installed, in the aft position. The tunnel was operated at Mach numbers of 0.10, 0.15, and 0.20. The tunnel operations parameters (compressor speed and door positions) were recorded. The rake was removed, and the slot for the rake was covered with aluminum tape. The tunnel was brought up to speed again, then driven blindly to the same set of operating conditions. As shown in Figure A.23, the rake was apparently responsible for a quite narrow tone at 23 kHz.

This tone should not be confused with the self-induced pressure fluctuations sometimes generated by inflow microphone windscreens operating above their designed flow speed.

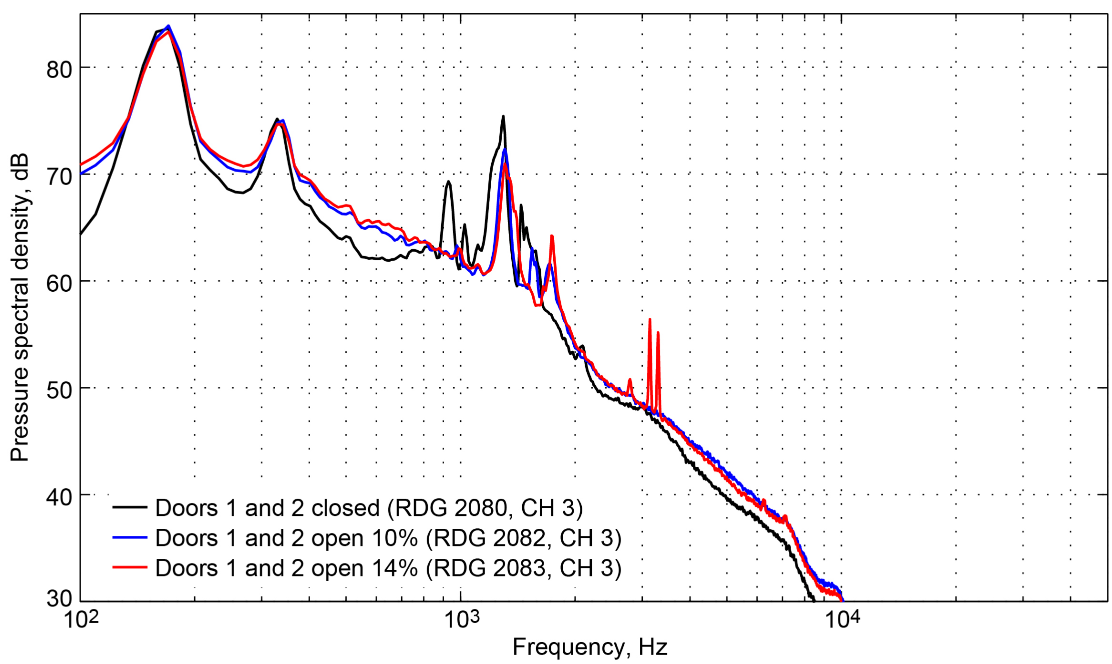

Figure A.19.—Measured sound spectra upstream of cooler showing effect of door position. Tunnel speed at Mach 0.20. Reading number (RDG). Channel (CH).

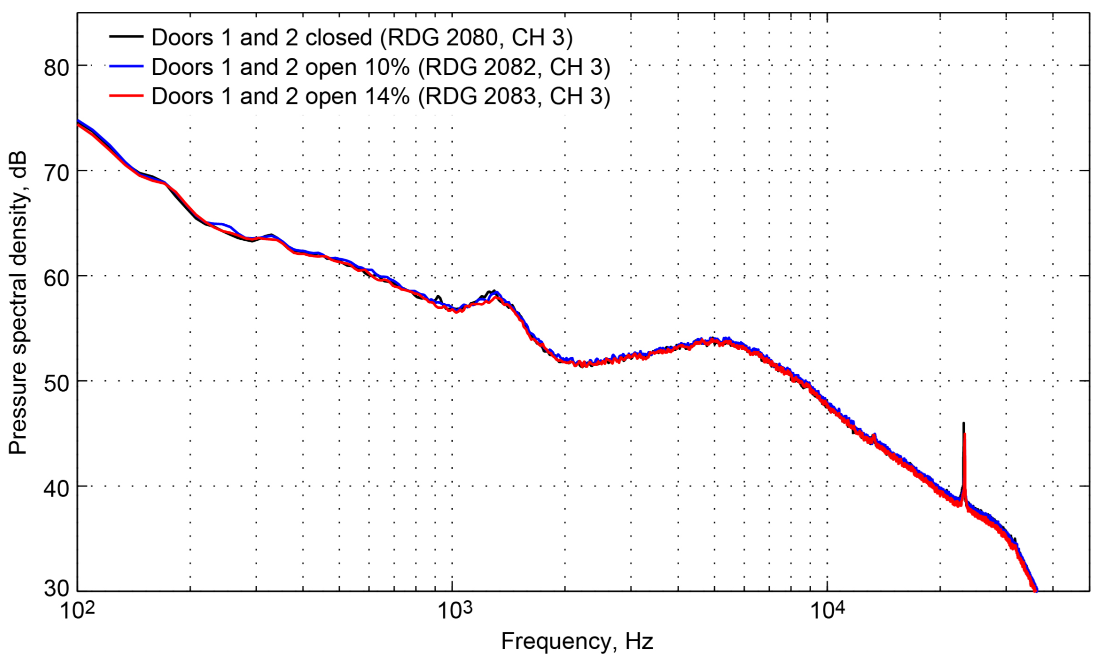

Figure A.20.—Measured sound spectra in 9- by 15-Foot Low-Speed Wind Tunnel test section as it varies with doors 1 and 2 positions. Tunnel speed at Mach 0.20. Reading number (RDG). Channel (CH).

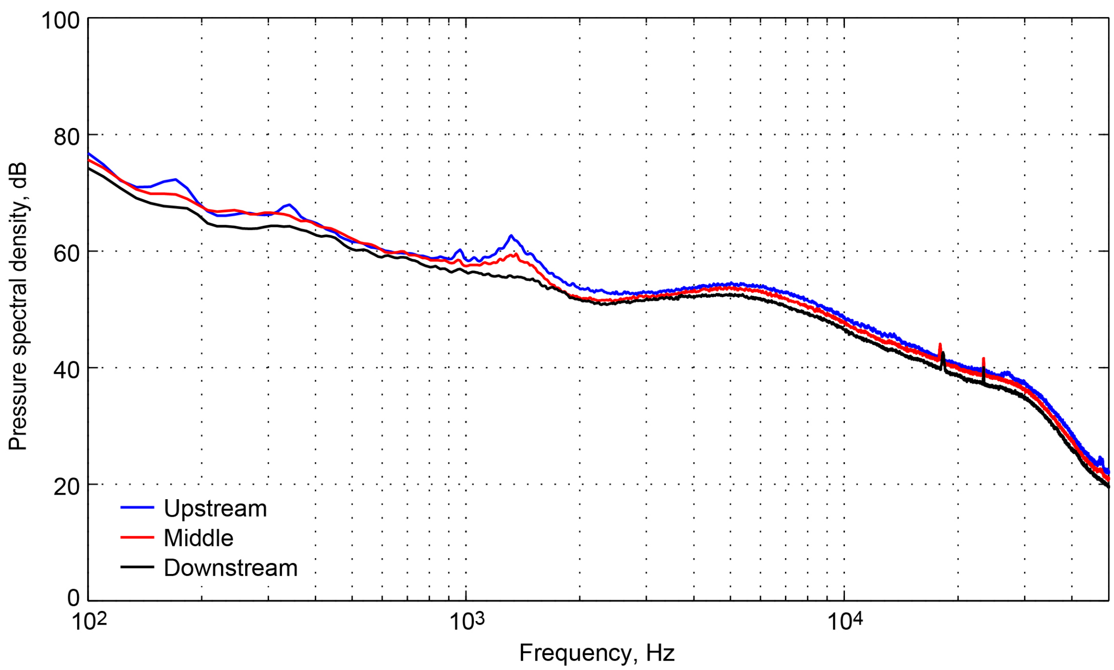

Figure A.21.—Measured sound spectra in 9- by 15-Foot Low-Speed Wind Tunnel test section with position inside test section. Tunnel speed at Mach 0.20. Top traverse microphone. Run 204, channel 2, reading numbers 2021, 2022, and 2023.

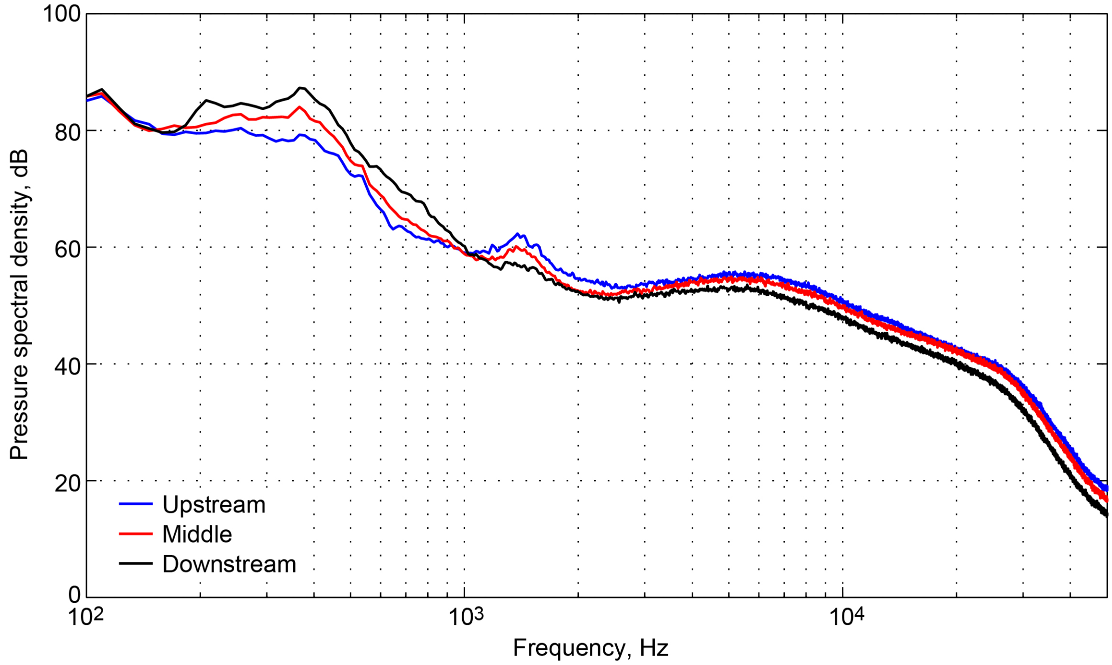

Figure A.22.—Measured sound spectra in 9- by 15-Foot Low-Speed Wind Tunnel test section. Tunnel speed at Mach 0.20. Single microphone on NASA Ames Research Center-style fiberglass holder. 2011 empty tunnel test, reading number 1932.

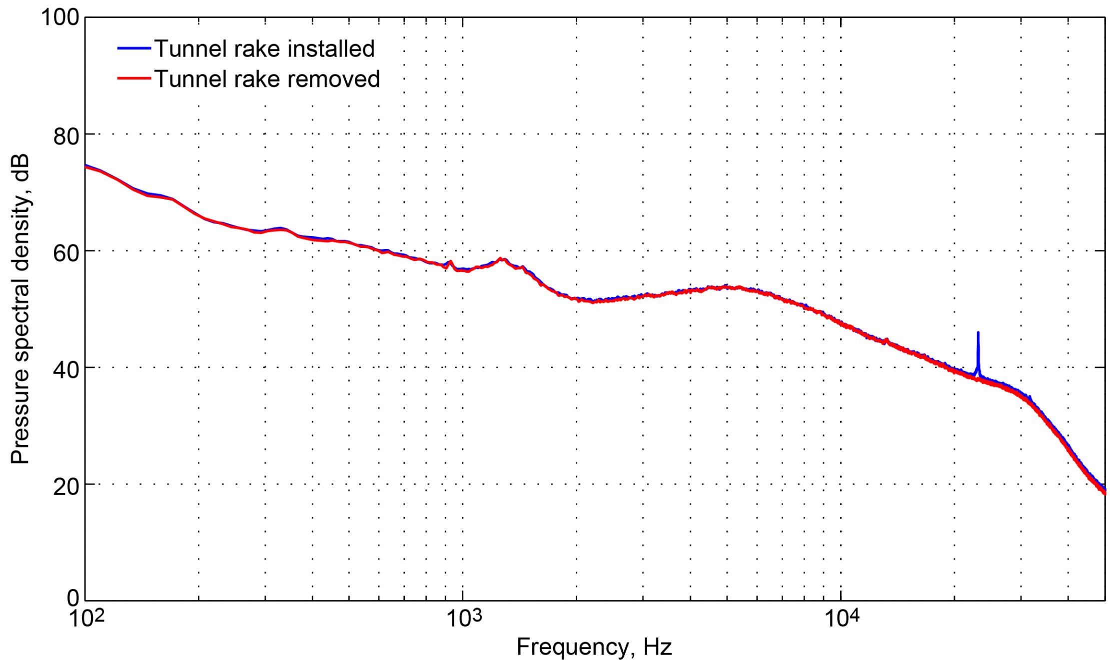

Figure A.23.—Measured sound spectra in 9- by 15-Foot Low-Speed Wind Tunnel test section. Tunnel speed at Mach 0.20. Ceiling microphone. Run 209, channel 4, reading numbers 2080 and 2088.

The effect of the microphone windscreen on the measured noise was studied in 2011, during a "piggyback" run during the portion of the open rotor test campaign taking place in the 8×6 SWT. The measurements shown in Figure A.24 were recorded on Feb. 15, 2011, as part of 9×15 LSWT Escort program D069. As discussed in more detail in Reference 19, the windscreens now used in the 9×15 LSWT are of the FITE. (Flow-Induced Tone Eliminator) design and do not demonstrate this self-noise.

The cooler is a major feature of the wind tunnel, designed to handle the heat load from a compressor driven by 87,000 hp. The water flow through the cooler is typically on, including times when the tunnel is not operating. The noise due to this water flow was measured by microphone channel 6 during run 204. Figure A.25 shows the result. The cooler flow does make noise, but far less than the airflow at Mach 0.10. No difference was measured in the test section noise.

The effect of doors 4 and 5 was also found to be negligible. Microphone channel 7 during run 209 was located just upstream of turn 3 and seems like a good candidate for making the measurement. However, during the process it was realized that the entire flow in the diffuser region is separated and turbulent, so all measurements made in these areas are somewhat suspect. Therefore, even though Figure A.26 shows some difference, it is believed to be largely aerodynamic, since opening the doors may change the flow field in the diffuser and turn 3. No change in the sound spectrum was measured in the test section when doors 4 and 5 were opened.

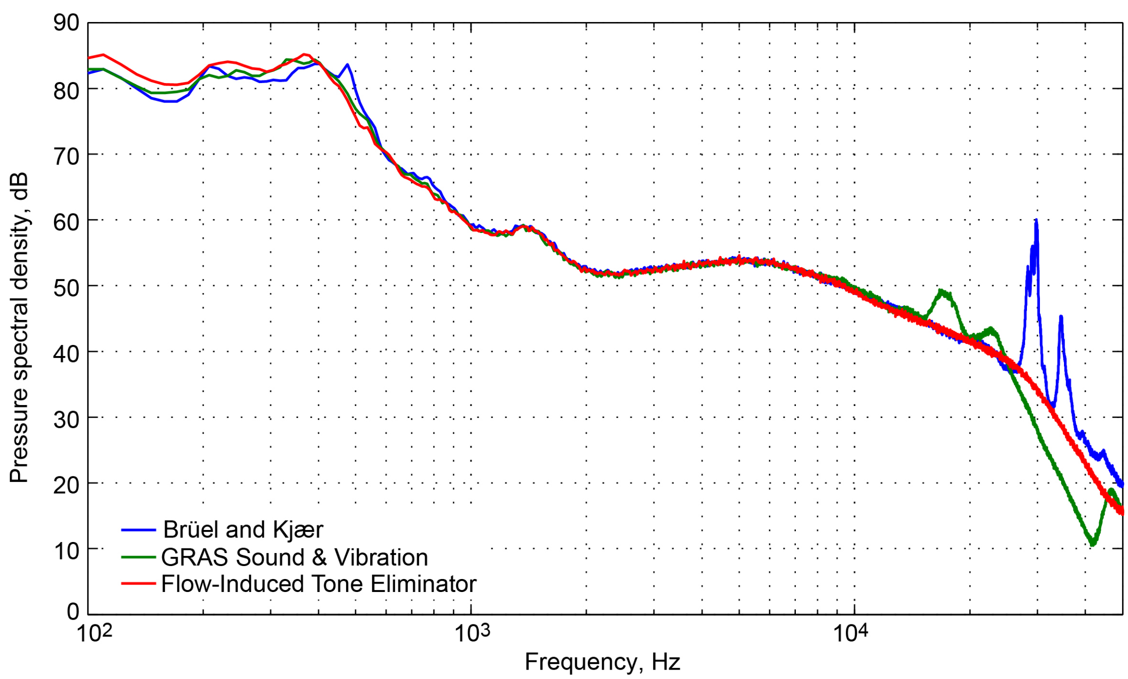

Figure A.24.—Effect of different microphone windscreens at Mach 0.20. Reading numbers 1924, 1928, and 1932.

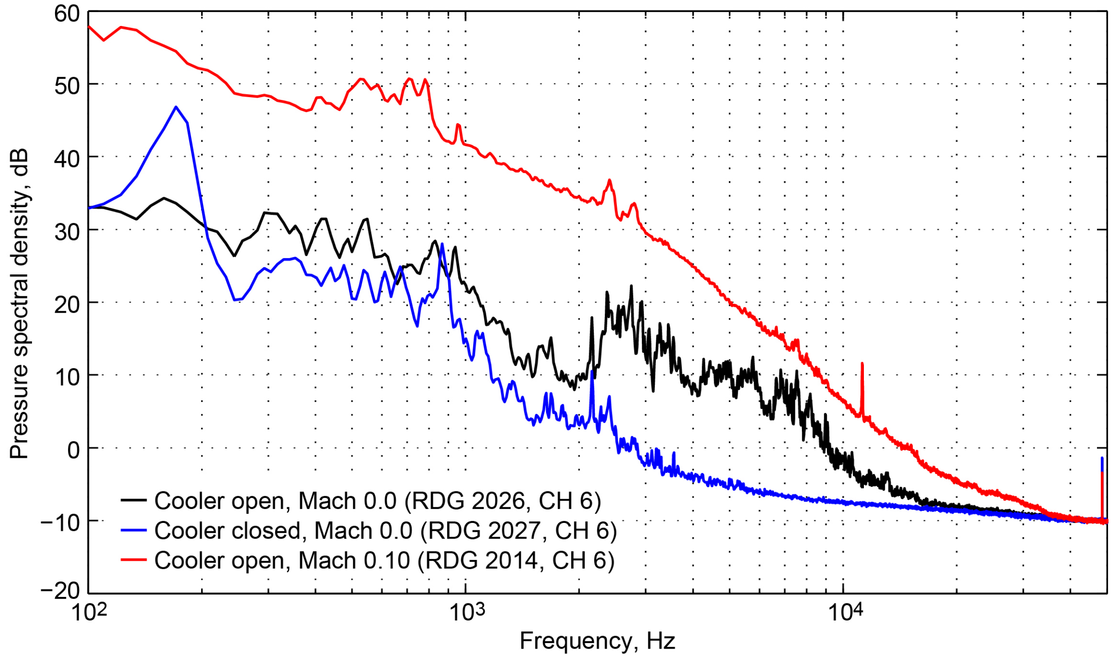

Figure A.25.—Measured sound spectra recorded by microphone channel (CH) 6, downstream of cooler. Noise due to flow through cooler is quantified when tunnel flow is off. Once tunnel is running, however, noise due to airflow overwhelms noise due to cooler. Reading number (RDG).

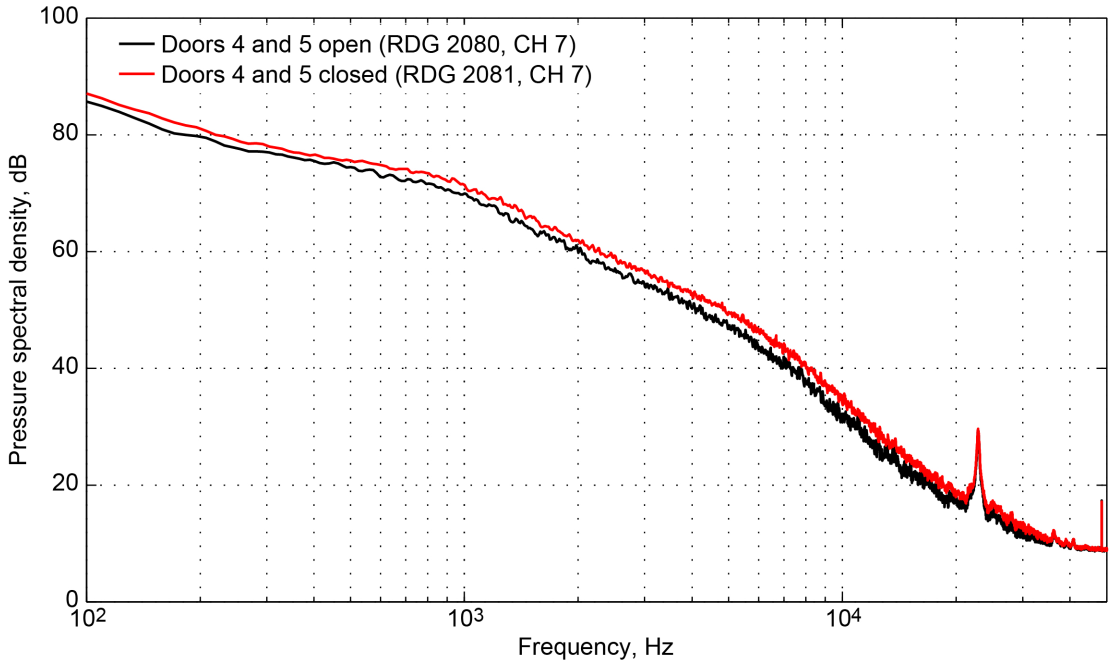

Figure A.26.—Measured pressure spectra in turn 3, run 207, channel (CH) 7, showing effect of doors 4 and 5. Note that flow in this area is very unsteady and measured pressure is likely mixture of acoustic and unsteady aerodynamic. Reading number (RDG).

A.3 Comprehensive Results

This section contains run logs from the empty tunnel testing conducted in February and March 2012. A set of figures showing the background noise in the tunnel loop is also included.

A.3.1 Noise Around Loop

Figure A.27 to Figure A.39 show the noise measured around the tunnel loop.

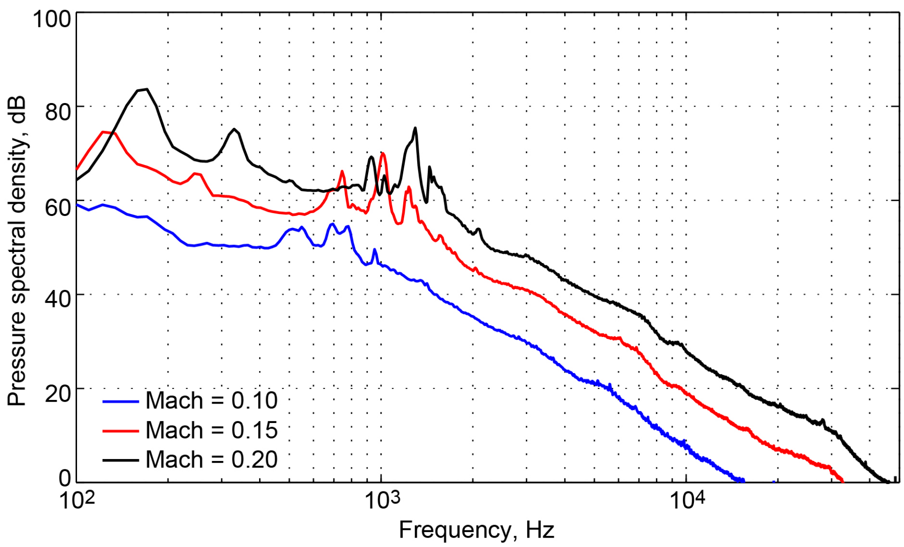

Figure A.27.—Noise measured upstream of cooler, downstream of doors 1 and 2. Run 209, channel 3, reading numbers 2078, 2079, and 2080. See Figure A.7.

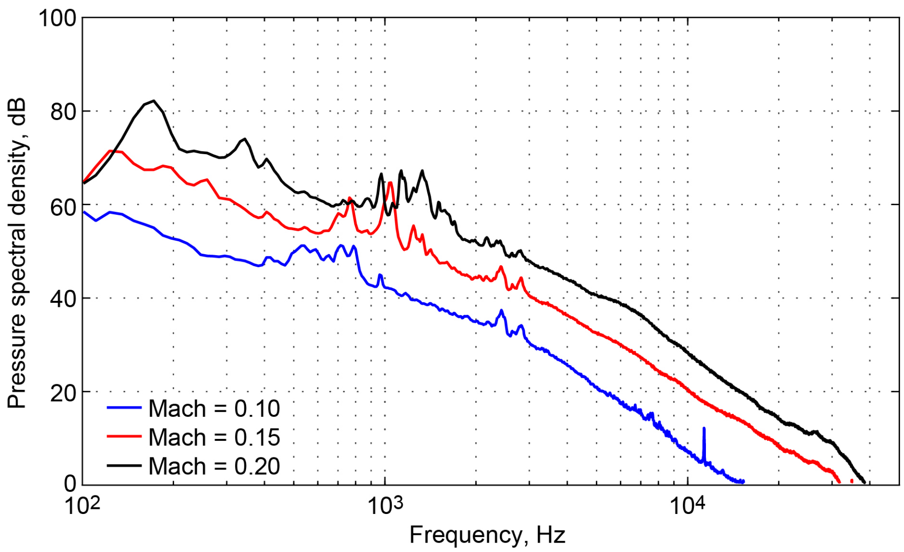

Figure A.28.—Noise measured between honeycomb and cooler in 9- by 15-Foot Low-Speed Wind Tunnel leg. Run 204, channel 6, reading numbers 2014, 2017, and 2023. See Figure A.8.

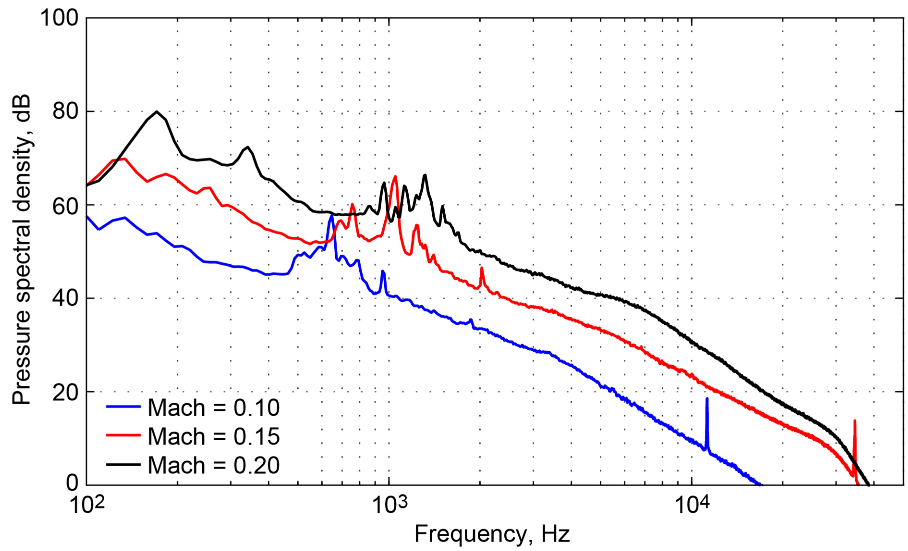

Figure A.29.—Noise measured between screens and honeycomb in 9- by 15-Foot Low-Speed Wind Tunnel leg. Run 204, channel 7, reading numbers 2014, 2017, and 2023. See Figure A.9.

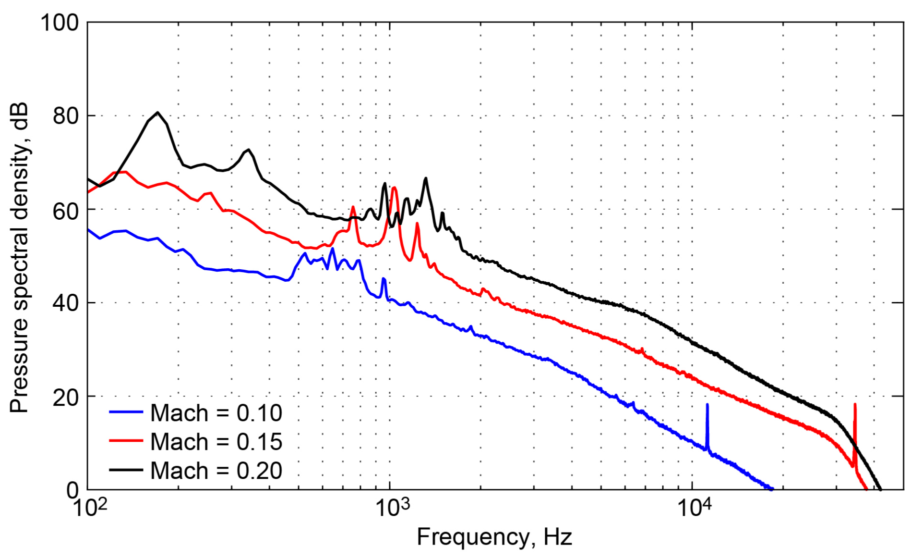

Figure A.30.—Noise measured at foot of 9- by 15-Foot Low-Speed Wind Tunnel contraction. Run 204, channel 8, reading numbers 2014, 2017, and 2023. See Figure A.10.

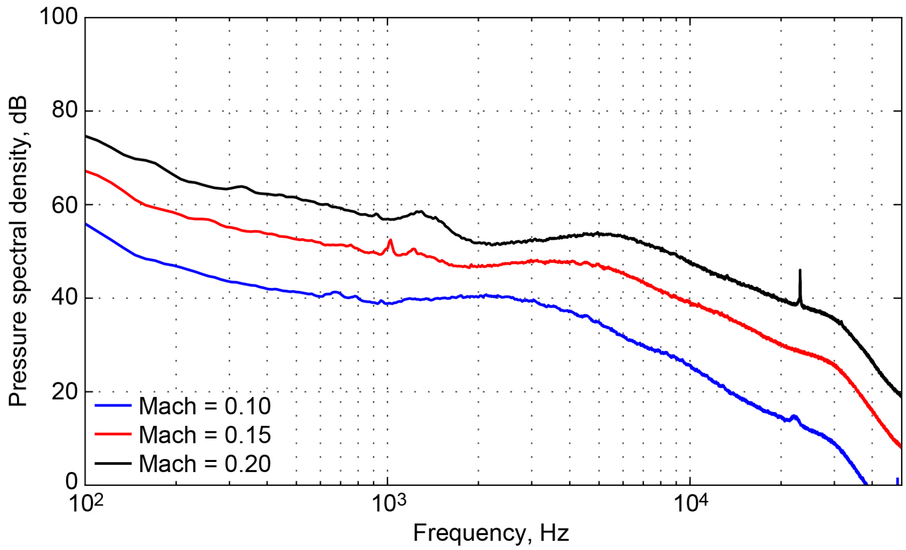

Figure A.31.—Noise measured in test section with only ceiling microphone installed. Run 209, channel 4, reading numbers 2078, 2079, and 2080.

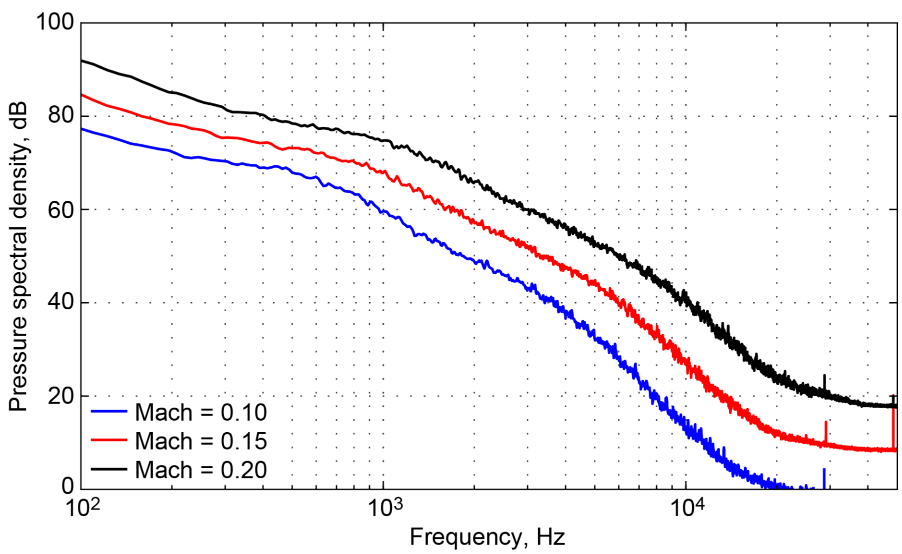

Figure A.32.—Noise and unsteady pressures measured in 9- by 15-Foot Low-Speed Wind Tunnel diffuser. Run 204, channel 11, reading numbers 2014, 2017, and 2023. See Figure A.11.

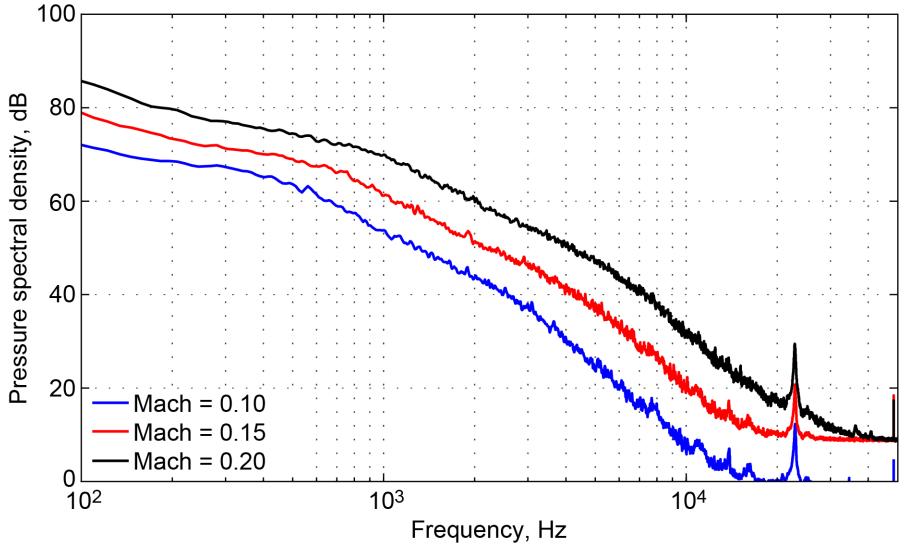

Figure A.33.—Noise measured upstream of doors 4 and 5 in 9- by 15-Foot Low-Speed Wind Tunnel diffuser leg. Run 209, channel 7, reading numbers 2078, 2079, and 2080. See Figure A.12.

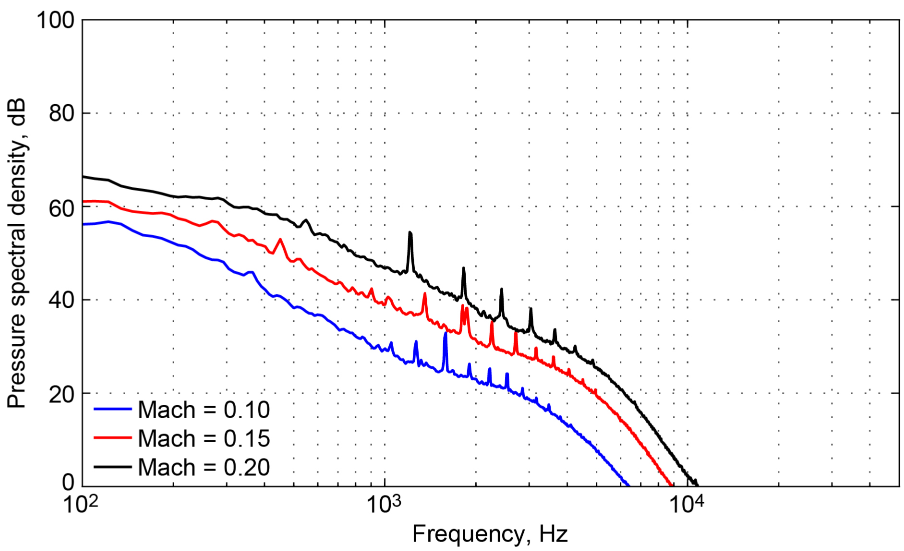

Figure A.34.—Noise measured upstream of air dryer filters in turn 3. Run 206, channel 9, reading numbers 2046, 2049, and 2052. See Figure A.15.

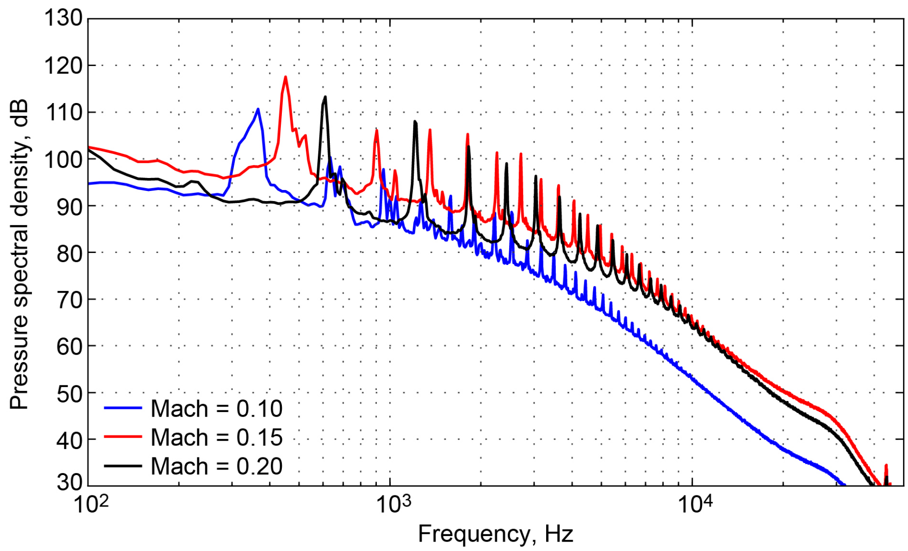

Figure A.35.—Noise measured in compressor plenum. Run 205, channel 11, reading numbers 2031, 2034, and 2037. See Figure A.16.

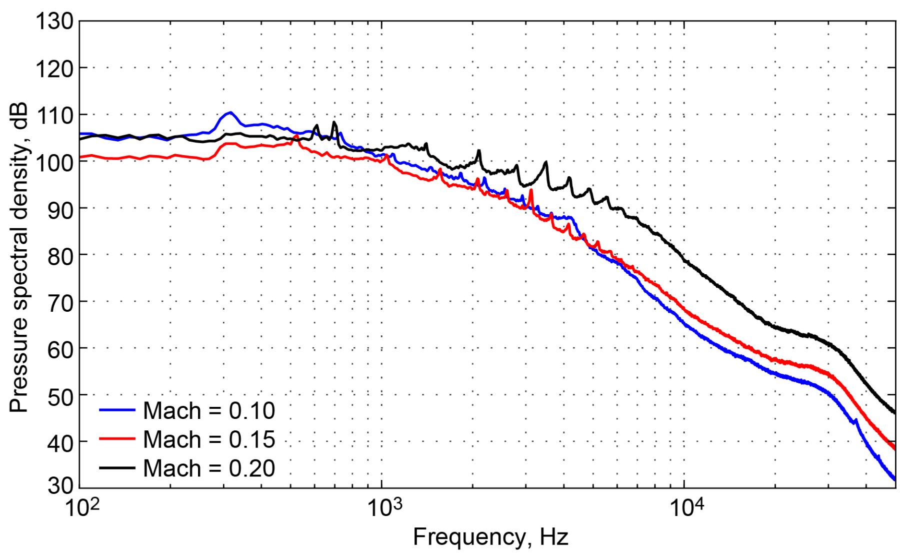

Figure A.36.—Noise measured in 8- by 6-Foot Supersonic Wind Tunnel contraction. Run 205, channel 12, reading numbers 2031, 2034, and 2037. See Figure A.17.

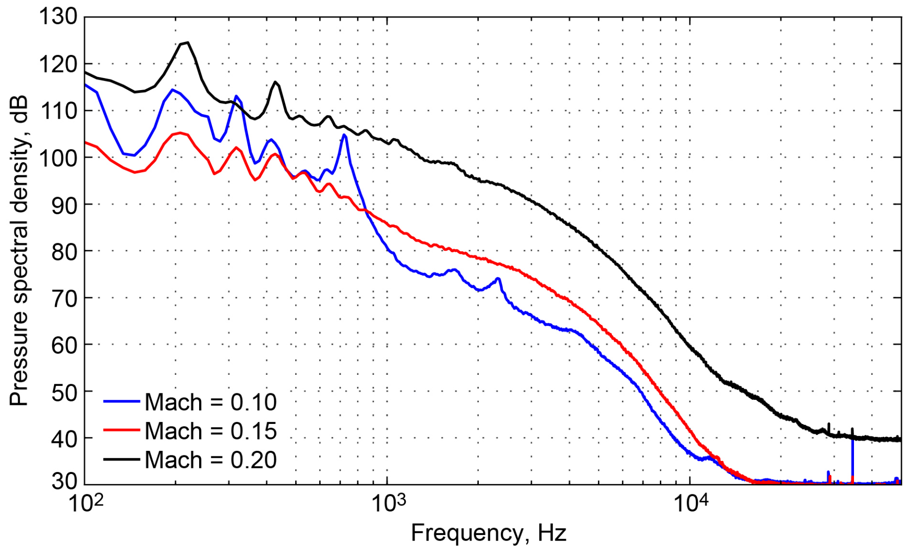

Figure A.37.—Noise measured in 8- by 6-Foot Supersonic Wind Tunnel diffuser, near exit to turn 2. Run 206, channel 4, reading numbers 2046, 2049, and 2052. See Figure A.12.

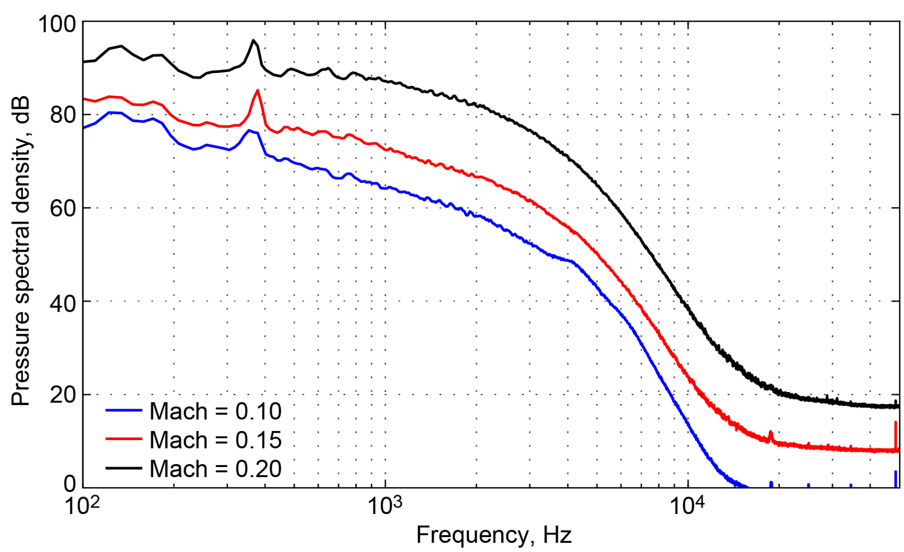

Figure A.38.—Noise measured in entrance to muffler. Run 206, channel 5, reading numbers 2046, 2049, and 2052. See Figure A.13.

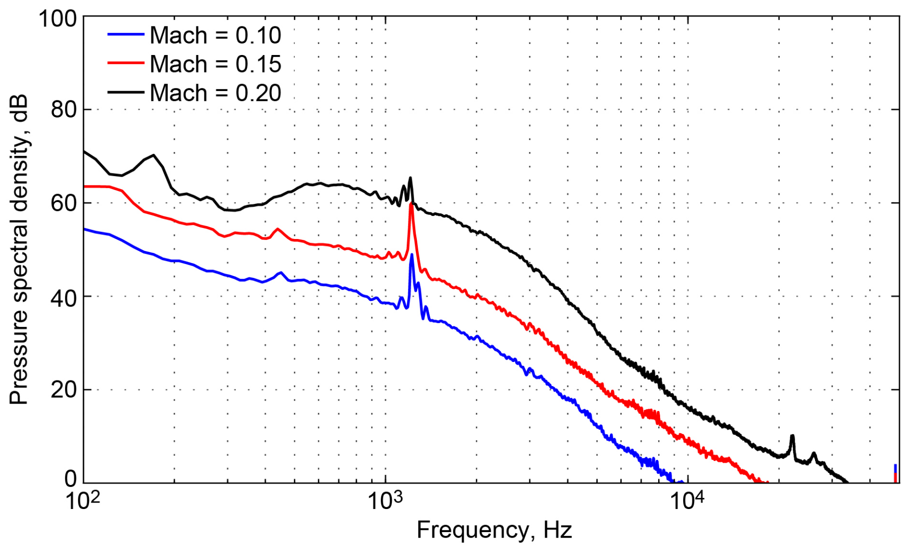

Figure A.39.—Noise measured in entrance to muffler. Run 206, channel 6, reading numbers 2046, 2049, and 2052. See Figure A.14.

A.3.2 Configuration Summaries

Configurations for the various runs are documented in Table A.2 to Table A.4.

TABLE A.2.—MICROPHONE LOCATIONS USED IN RUN 204

Channel	Description
1	Center traverse microphone
2	Top traverse microphone
3	Bottom traverse microphone
4	In turn 2 plenum, just upstream of parallel baffles
5	Between doors 1 and 2 and cooler
6	Between cooler and honeycomb
7	Between honeycomb and first screen
8	Between last screen and contraction
9	Ceiling microphone
10	Floor microphone
11	At base of ramp downstream of diffuser
12	Wall microphone at streamwise center of test section

TABLE A.3.—MICROPHONE LOCATIONS USED IN RUNS 205 AND 206
[Note that channels 11 and 12 were removed for run 206.]

Channel	Description
1	Center traverse microphone
2	Top traverse microphone
3	Bottom traverse microphone
4	8- by 6-Foot Supersonic Wind Tunnel (8×6 SWT) diffuser exit
5	Muffler entrance
6	Muffler exit
7	Ceiling microphone in 9- by 15-Foot Low-Speed Wind Tunnel (9×15 LSWT) test section
8	Floor microphone in 9×15 LSWT test section
9	Dryer inlet
10	Wall microphone in 9×15 LSWT test section
11	Compressor plenum (separate recorder)
12	8×6 SWT contraction (separate recorder)

TABLE A.4.—MICROPHONE LOCATIONS USED IN RUNS 207 THROUGH 209

Channel	Description
1	Upstream of baffles
2	Downstream of baffles
3	In front of cooler
4	Ceiling microphone in 9- by 15-Foot Low-Speed Wind Tunnel test section
5	1/3 way down from old diffuser
6	2/3 way down from old diffuser
7	Upstream of doors 4 and 5

A.3.3 Run Logs

Table A.5 to Table A.10 are the run logs for the preconstruction testing.

TABLE A.5.—RUN 204 LOG, FEB. 23, 2012, 9- BY 15-FOOT LOW-SPEED WIND TUNNEL (9×15 LSWT) ESCORT PROGRAM D069

[Configuration: Microphones in 9×15 LSWT leg of tunnel complex, see Figure A.1. Problem with drive motors between reading numbers (RDGs) 2025 and 2026 causes tunnel to be shut down for restart. Time: time of day in 24-h format. RDGs are steady-state readings. Tunnel compressor revolutions per minute (CSPEED). Wind off zero (WOZ) measurement. Dewpoint temperature (TDEW2). Cyclic are multiple steady-state records combined in one RDG.]

Time	RDG	Mach	CSPEED, rpm	Doors 1 and 2	Cooler valve	Number of motors	TDEW2, °F	Traverse location, in.
1,314	2011	0.0	-----	---------	---------	--	--------	----------
1,315	2012	WOZ	-----	---------	---------	--	---------	-----------
1,331	2013	0.10	365	Closed	Open	1	30.71	0
1,352	2014	0.10	365	Closed	Open	1	28.28	138
1,354	2015	0.10	365	Closed	Open	1	38.15	260
1,401	2016	0.15	520	Closed	Open	1	27.51	260
1,404	2017	0.15	520	Closed	Open	1	27.51	138
1,406	2018	0.15	520	Closed	Open	1	27.51	0
1,429	2019	0.15	520	Closed	Open	1	27.51	48 stop cyclic
1,457	2020	0.20	700	Closed	Open	3	24.85	48 stop cyclic
1,459	2021	0.20	700	Closed	Open	3	24.85	260
1,501	2022	0.20	700	Closed	Open	3	24.85	138
1,503	2023	0.20	700	Closed	Open	3	24.85	0
1,506	2024	0.20	700	Closed	Closed	3	24.57	0
1,518	2025	0.20	800	9% open	Open	3	24.57	0
1,532	2026	0.0	0	Closed	Open	0	---------	0
1,534	2027	0.0	0	Closed	Closed	0	---------	0
1,605	2028	0.10	365	Closed	Open	1	---------	48 stop cyclic

TABLE A.6.—LOG FOR RUN 205, FEB. 29, 2012, 9- BY 15-FOOT LOW-SPEED WIND TUNNEL ESCORT PROGRAM D069

[Reading numbers (RDGs) are steady-state readings. Tunnel compressor revolutions per minute (CSPEED). Wind off zero (WOZ) measurement. Dewpoint temperature (TDEW2).]

Time	RDG	Mach	CSPEED, rpm	Doors 1 and 2	Shock doors, percent	Number of motors	TDEW2, °F	Traverse location, in.
1,402	2029	0	0	Closed	---	0	------	-----
1,403	2030	WOZ	0	Closed	---	0	------	-----
1,438	2031	0.1	365	Closed	61	1	27.5	0
1,442	2032	0.1	365	Closed	61	1	27.5	138
1,444	2033	0.1	365	Closed	61	1	27.5	260
1,452	2034	0.15	520	Closed	40	1	26.95	260
1,455	2035	0.15	520	Closed	40	1	26.95	138
1,457	2036	0.15	520	Closed	40	1	26.95	0
1,510	2037	0.2	700	Closed	35	3	26.45	0
1,513	2038	0.2	700	Closed	35	3	26.45	138
1,516	2039	0.2	700	Closed	35	3	26.45	260
1,527	2040	0.2	790	9% open	22	3	26.16	260
1,529	2041	0.2	790	9% open	22	3	26.16	138
1,531	2042	0.2	790	9% open	22	3	26.16	0

TABLE A.7.—LOG FOR RUN 206, MAR. 2, 2012, 9- BY 15-FOOT LOW-SPEED WIND TUNNEL ESCORT PROGRAM D069

[Reading numbers (RDGs) are steady-state readings. Tunnel compressor revolutions per minute (CSPEED). Wind off zero (WOZ) measurement. Dewpoint temperature (TDEW2).]

Time	RDG	Mach	CSPEED, rpm	Doors 1 and 2	Shock doors, percent	Number of motors	TDEW2, °F	Traverse location, in.
1,152	2043	0	0	Closed	---	0	-------	-----
1,153	2044	WOZ	0	Closed	---	0	-------	-----
1,219	2045	0.1	365	Closed	60	1	31.83	0
1,222	2046	0.1	365	Closed	60	1	31.83	138
1,224	2047	0.1	365	Closed	60	1	31.83	260
1,232	2048	0.15	520	Closed	35	1	31.95	260
1,235	2049	0.15	520	Closed	35	1	31.95	138
1,237	2050	0.15	520	Closed	35	1	31.95	0
1,249	2051	0.2	700	Closed	35	3	31.95	0
1,251	2052	0.2	700	Closed	35	3	31.95	138
1,254	2053	0.2	700	Closed	35	3	31.95	260
1,302	2054	0.2	800	10% open	23	3	27.97	260
1,304	2055	0.2	800	10% open	23	3	27.97	138
1,306	2056	0.2	800	10% open	23	3	27.97	0

TABLE A.8.—LOG FOR RUN 207, MAR. 9, 2012, 9- BY 15-FOOT LOW-SPEED WIND TUNNEL ESCORT PROGRAM D069

[Reading numbers (RDGs) are steady-state readings. Tunnel compressor revolutions per minute (CSPEED). Wind off zero (WOZ) measurement. Dewpoint temperature (TDEW2).]

Time	RDG	Mach	CSPEED, rpm	Doors 1 and 2	Doors 4 and 5	Shock doors, percent	Number of motors	TDEW2, °F
1,250	2057	0	0	-------------	---------	---	0	-------
1,250	2058	WOZ	0	-------------	---------	---	0	-------
1,307	2059	0.1	362	Closed	Open	62	1	33.61
1,314	2060	0.15	515	Closed	Open	40	1	33.3
1,324	2061	0.2	680	Closed	Open	35	3	32.58
1,331	2062	0.2	800	11% open	Open	23	3	32.14
1,338	2063	0.2	683	Closed	Closed	35	3	31.56

TABLE A.9.—LOG FOR RUN 208, MAR. 9, 2012, 9- BY 15-FOOT LOW-SPEED WIND TUNNEL ESCORT PROGRAM D069

[Reading numbers (RDGs) are steady-state readings. Tunnel compressor revolutions per minute (CSPEED). Wind off zero (WOZ) measurement.]

Time	RDG	Mach	CSPEED, rpm	Doors 1 and 2	Shock doors extension, percent	Number of motors
1,454	2064	0	0	------------	---	--
1,455	2065	WOZ	0	------------	---	--
1,511	2066	0.10	362	Closed	62	1
1,519	2067	0.15	515	Closed	40	1
1,520	2068	0.15	515	Closed	40	1
1,531	2069	0.20	680	Closed	35	3
1,536	2070	0.20	800	11% open	23	3
1,345	2071	0	0	------------	---	--

TABLE A.10.—LOG FOR RUN 209, MAR. 12, 2012, 9- BY 15-FOOT LOW-SPEED WIND TUNNEL ESCORT PROGRAM D069
[Only aft test section tunnel rake used. This rake was removed after reading (RDG) 2083 to measure noise difference. RDGs are steady-state readings. Tunnel compressor revolutions per minute (CSPEED). Wind off zero (WOZ) measurement.]

Time	RDG	Mach	CSPEED, rpm	Doors 1 and 2	Doors 4 and 5	Shock doors, percent
1,347	2072	0	0	-------------	-------------	-----
1,348	2073	WOZ	0	-------------	-------------	-----
1,423	2075	0	0	-------------	-------------	-----
1,424	2076	WOZ	0	-------------	-------------	-----
1,425	2077	0	0	-------------	-------------	-----
1,439	2078	0.1	365	Closed	Open	60
1,446	2079	0.15	517	Closed	Open	40
1,458	2080	0.2	685	Closed	Open	35
1,500	2081	0.2	685	Closed	Closed	35
1,506	2082	0.2	800	10% open	Open	23
1,512	2083	0.2	865	14% open	Open	8
1,532	2084	0	0	-------------	-------------	-----
1,534	2085	WOZ	0	-------------	-------------	-----
1,548	2086	0.1	365	Closed	Open	60
1,555	2087	0.15	517	Closed	Open	40
1,605	2088	0.20	685	Closed	Open	35
1,610	2089	0.20	800	10% open	Open	23
1,619	2090	0	0	-------------	-------------	-----

Appendix B.—Postconstruction Testing

This appendix contains additional information regarding the background noise measurements made in the 9- by 15-Foot Low-Speed Wind Tunnel (9×15 LSWT) after the construction project. There were two main tests. In December 2018, a facility "checkout" was conducted, and microphone measurements were piggybacked onto this test. In June 2019, a postconstruction "validation" test was conducted, focused on making quality acoustic measurements in the test section. The present appendix contains information about the former test data, acquired as part of the checkout. The validation test data was presented in Section 4.0.

The eight-step tunnel checkout test sequence was run after the wind tunnel improvement project was completed. This included variously running the 8- by 6-Foot Supersonic Wind Tunnel (8×6 SWT) and 9×15 LSWT in all the expected configurations, activation of the air dryer, testing emergency stop switches, and other control scheme items. Microphone measurements in the tunnel leg were made during the 9×15 LSWT portion of the checkout test. The intent was to book end the pretest measurements described in Section 2.0 and Appendix A. This postconstruction test setup is illustrated in Figure B.1 to Figure B.12.

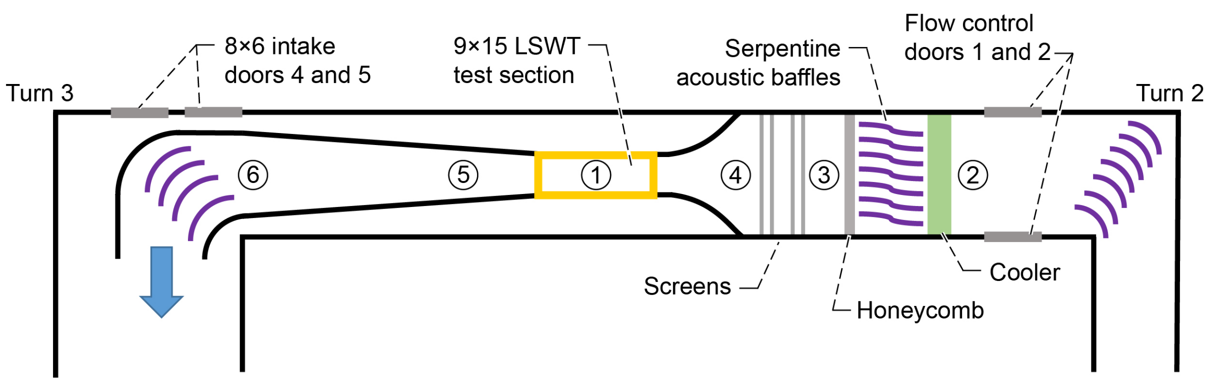

Figure B.1.—Sketch showing microphone locations used for postconstruction acoustic validation testing in December 2018. Not to scale. Low-speed wind tunnel (LSWT).

Figure B.2.—Microphone channel 1 in postconstruction validation test. See Figure B.1.

Figure B.3.—Microphone channel 2 in postconstruction validation test. See Figure B.1.

Figure B.4.—Microphone channel 3 in postconstruction validation test. See Figure B.1.

Figure B.5.—Microphone channel 4 in postconstruction validation test. See Figure B.1.

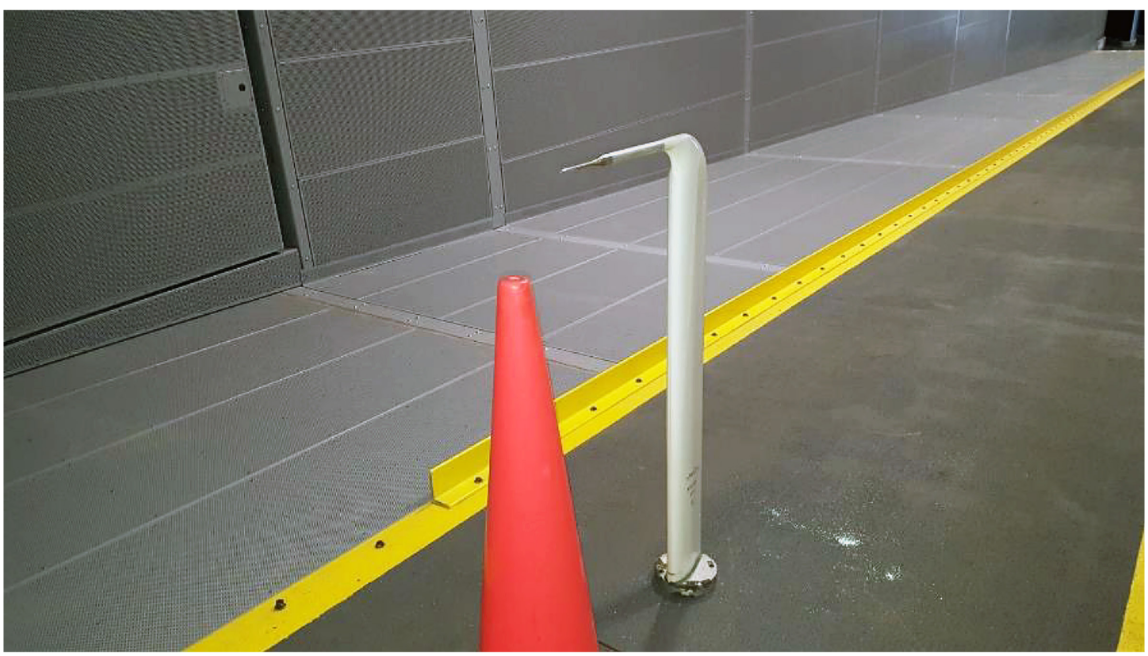

Figure B.6.—Microphone channel 5 in postconstruction validation test. See Figure B.1.

Figure B.7.—Microphone channel 6 in postconstruction validation test. See Figure B.1.

B.1 Noise Outside Test Section

As mentioned, a thorough survey of the noise through the entire wind tunnel complex was made in 2012, in order to support a comprehensive noise study and reduction effort. This included putting microphones in the airflow in both legs of the wind tunnel. A smaller study was repeated in 2018 as part of the postconstruction checkout and acceptance test. It was decided it would not be necessary to make measurements throughout the 8×6 SWT leg, for example, as no changes were made to that side of the facility that would affect the noise in the airflow.

It should be pointed out that locations outside the test section are not necessarily conducive to making inflow microphone measurements, due to reverberant walls and unknown turbulence levels.

B.1.1 Doors 1 and 2

Figure B.8 shows the noise in turn 2, before and after the construction project. The noise in this location is strongly affected by the position of the flow control doors, which were nominally closed in both test cases here. The aerodynamics of this corner is likely very different after the improvement project, with the addition of turning vanes and inboard fairing. Despite this, the noise in this location is largely unchanged. It is hard to say that the turn 2 turning vanes provided any noise reduction.

B.1.2 Upstream of Screens

Figure B.9 shows the noise downstream of the honeycomb and upstream of the screens, before and after the construction project.

B.1.3 Upstream of Contraction

Figure B.10 shows the noise downstream of the screen and upstream of the contraction, before and after the construction project.

B.1.4 Upper Diffuser

Figure B.11 shows the noise downstream of the test section in the upstream part of the diffuser, before and after the construction project.

B.1.5 Turn 3

Figure B.12 shows the noise downstream of the diffuser in turn 3, before and after the construction project.

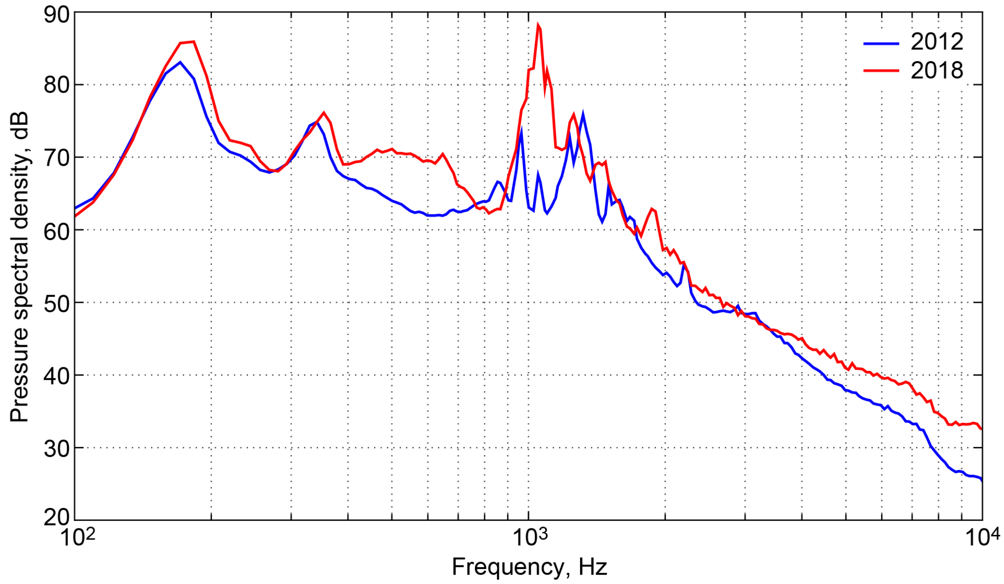

Figure B.8.—Noise measured in turn 2 upstream of heat exchanger during tunnel operation at Mach 0.20 in 9- by 15-Foot Low-Speed Wind Tunnel. Test data from Feb. 23, 2012, and Dec. 11, 2018.

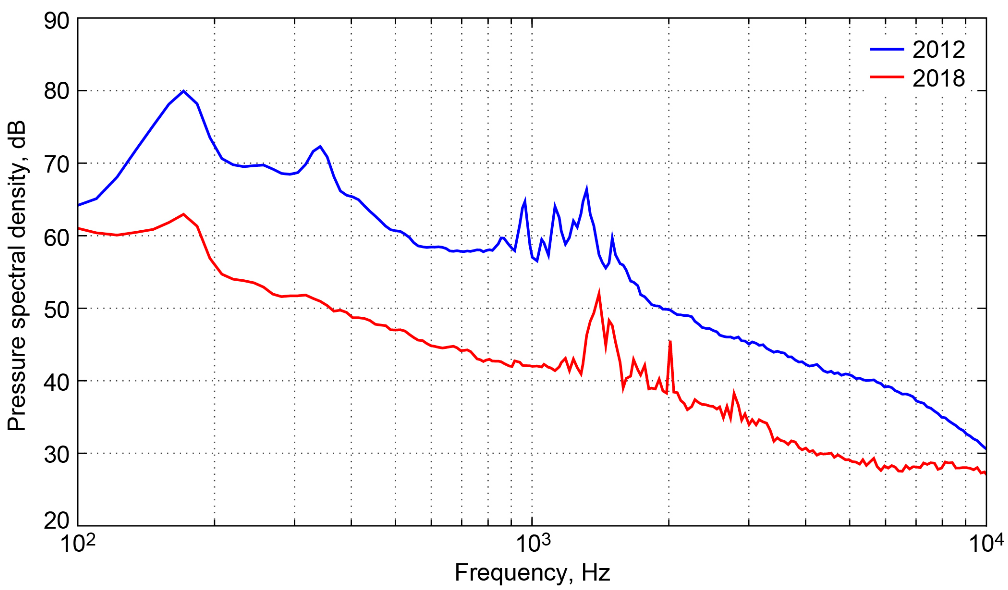

Figure B.9.—Noise measured upstream of screens during tunnel operation at Mach 0.20 in 9- by 15-Foot Low-Speed Wind Tunnel. Test data from Feb. 23, 2012, and Dec. 11, 2018.

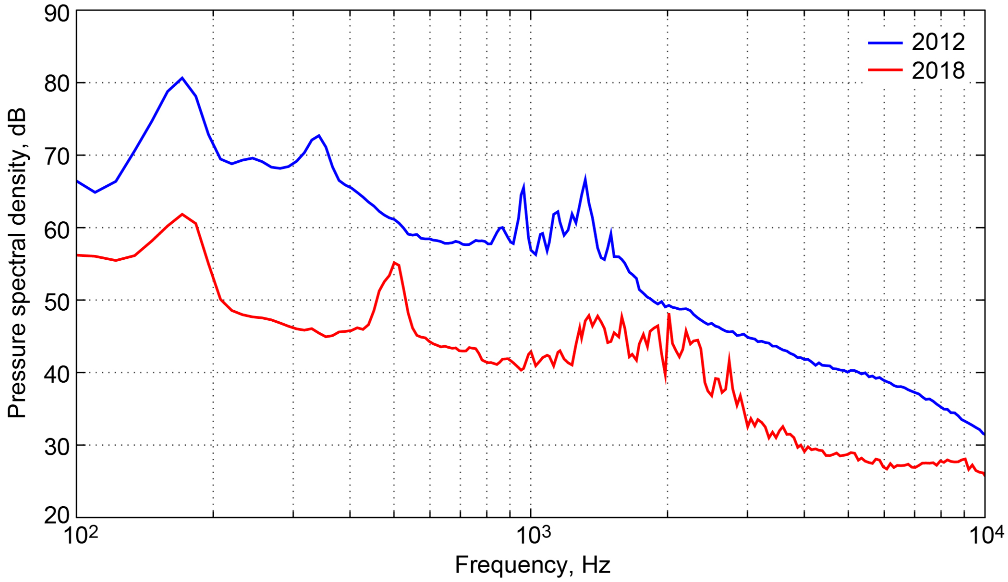

Figure B.10.—Noise measured upstream of contraction during tunnel operation at Mach 0.20 in 9- by 15-Foot Low-Speed Wind Tunnel. Test data from Feb. 23, 2012, and Dec. 11, 2018.

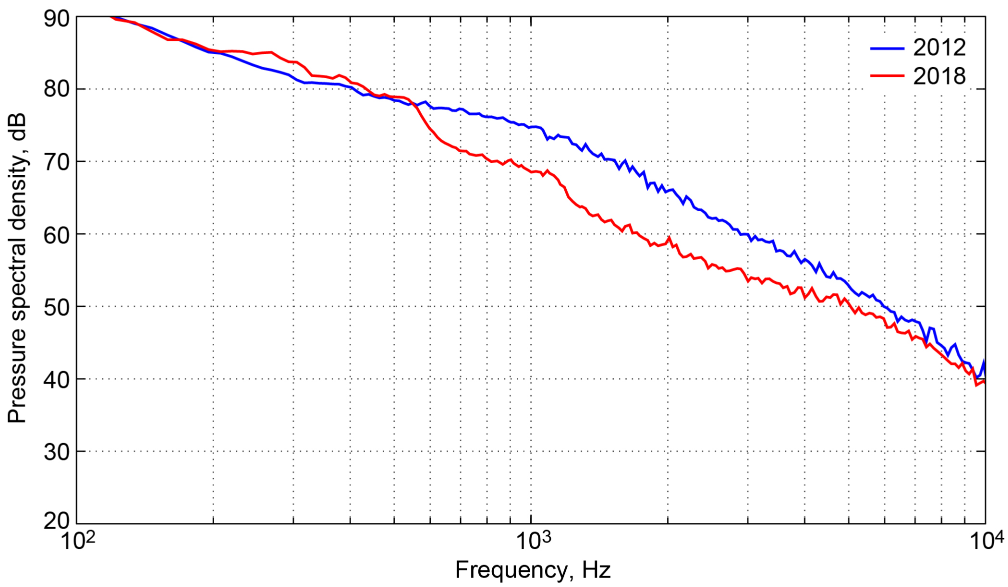

Figure B.11.—Noise measured downstream of test section during tunnel operation at Mach 0.20 in 9- by 15-Foot Low-Speed Wind Tunnel. Test data from Feb. 23, 2012, and Dec. 11, 2018.

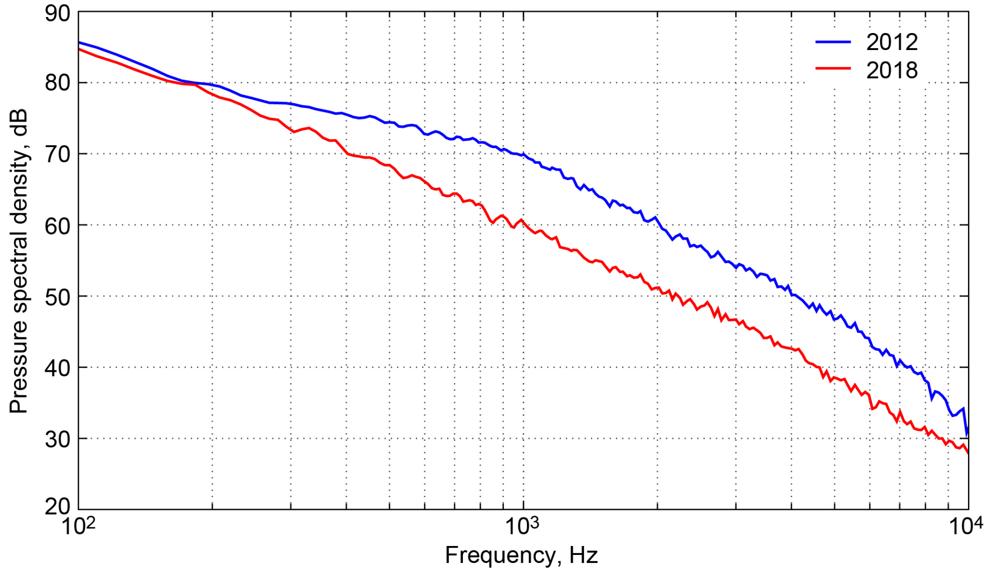

Figure B.12.—Noise measured in turn during tunnel operation at Mach 0.20 in 9- by 15-Foot Low-Speed Wind Tunnel. Test data from Mar. 12, 2012, and Dec. 11, 2018.

B.2 Modes of Operation

As part of the tunnel background noise observations, we manipulated the various control mechanisms at the disposal of the tunnel operators. There are four control mechanisms:

1. Doors 1 and 2: These doors are at the upstream edge of the 9×15 LSWT leg. From the point of view of the 8×6 SWT, these are outlet doors, which could be opened to exhaust combustion products.
2. Compressor speed: The wind tunnel is driven by a seven-stage axial compressor designed and built in the late 1940s. The compressor speed is varied using a liquid rheostat system (Ref. 35).
3. Doors 4 and 5: These doors are at the downstream end of the 9×15 LSWT leg. The 9×15 LSWT test section can be isolated by closing door 3 (at the upstream edge of the test section) and doors 6 and 7 (at the downstream end of the high-speed diffuser). The various doors are indicated in Figure 1. The 9×15 LSWT test section can be isolated to facilitate model installation during cold weather, or while testing is occurring in the 8×6 SWT test section. When the 8×6 SWT is operating in this "open loop" configuration, 100 percent of the air running through the compressor is exhausted out of doors 1 and 2 and outside air is pulled in through doors 4 and 5. When the tunnel is operating "closed loop," then it is expected that there is very little flow through these doors. A vent also exists in turn 3, ensuring that this point in the tunnel loop is always at atmospheric pressure.
4. Shock doors: When the 8×6 SWT is in supersonic operation, the pressure in the test section is maintained by a set of very stout hydraulically actuated doors. These doors hold the normal shock that occurs before the flow decelerates into the diffuser. They can be used to maintain the backpressure on the compressor during 9×15 LSWT operation.

The tunnel can be operated with the main drive at different revolutions per minute and doors used to vary the airflow. The blowers used to circulate flow through the air dryer can also be used to move air through the tunnel loop at low speed. Table B.1 shows the various conditions the tunnel was operated at while Figure B.13 shows the noise levels observed in the wind tunnel test section. The semitonal noise at frequencies of 540 Hz and below is believed to be due to whistling in the mounting mechanism holding the microphone probe. It can be observed that the noise is independent of the tunnel operation settings, and the noise is identical whether one- or three-drive motors are used.

B.2.1 Door Seals

The 8×6 SWT and 9×15 LSWT complex has a pair of flow control doors called doors 1 and 2. These doors were equipped with a pneumatic seal when the 9×15 LSWT leg of the wind tunnel was upgraded in 2017 and 2018. The purpose of the seals was to reduce air leakage through the gaps in the door and the associated noise. During checkout testing in December 2018, the seals were damaged and have not been used since. This section addresses whether the seals should be replaced.

The test points being considered are acoustic readings 7, 21, and 25, acquired on Dec. 6, 11, and 12, 2018, respectively. The 9×15 LSWT COBRA data acquisition system, replacing Escort, was not yet installed, so there are no associated COBRA readings for these conditions. All three readings were acquired at 9×15 LSWT speeds of Mach 0.15, based on tunnel rake measurements acquired into the Ovation tunnel control system. Acoustic readings 7 to 9 were acquired very early in the test campaign, when the door seals were in good condition, and thus, are the only measurements acquired with doors 1 and 2 closed and the seals inflated as intended. Reading 21 is with doors 1 and 2 open by 26 percent. The seals broke when the tunnel was first pushed to maximum 9×15 LSWT speed (Mach 0.23) during the run on Dec. 11, 2018 (reading 24). Acoustic reading 25 corresponds with 8×6 SWT COBRA program 001 reading 142.

TABLE B.1.—VARIOUS OPERATING CONDITIONS FOR
9- BY 15-FOOT LOW-SPEED WIND TUNNEL

Tunnel Mach	Compressor, rpm	Shock doors, percent	Doors 1 and 2
<0.05	0	0	Closed and sealed
0.05	400	40	50%
0.10	400	40	6%
0.15	594	30	6%
0.15	523	40	Closed and sealed
0.10	365	60	Closed and sealed

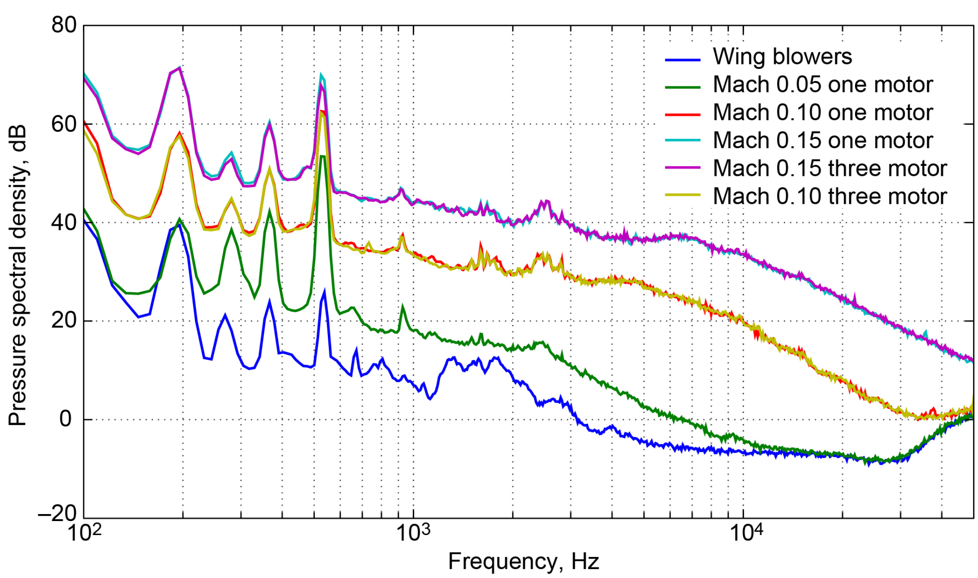

Figure B.13.—Noise measured in 9- by 15-Foot Low-Speed Wind Tunnel under various modes of tunnel operation. Test data from Dec. 4 and 6, 2018.

Figure B.14 shows noise measurements made by a microphone upstream of the cooler, just downstream of doors 1 and 2. Reading 7 with the doors closed and sealed is quietest, as expected. Figure B.15 shows noise measurements made by a microphone in the test section. Reading 25 (without the door seals) is quieter. Compared to reading 7, the door 3 slot has been taped, and the microphone mount was also taped up. The presence or absence of the door slots makes no difference to the noise level in the test section.

Air lost through the doors 1 and 2 leakage has a small but negative impact on tunnel operations. The drive system must push additional air to make up for the loss. If the air dryer is in use, the lost dry air must be made up with ambient air.

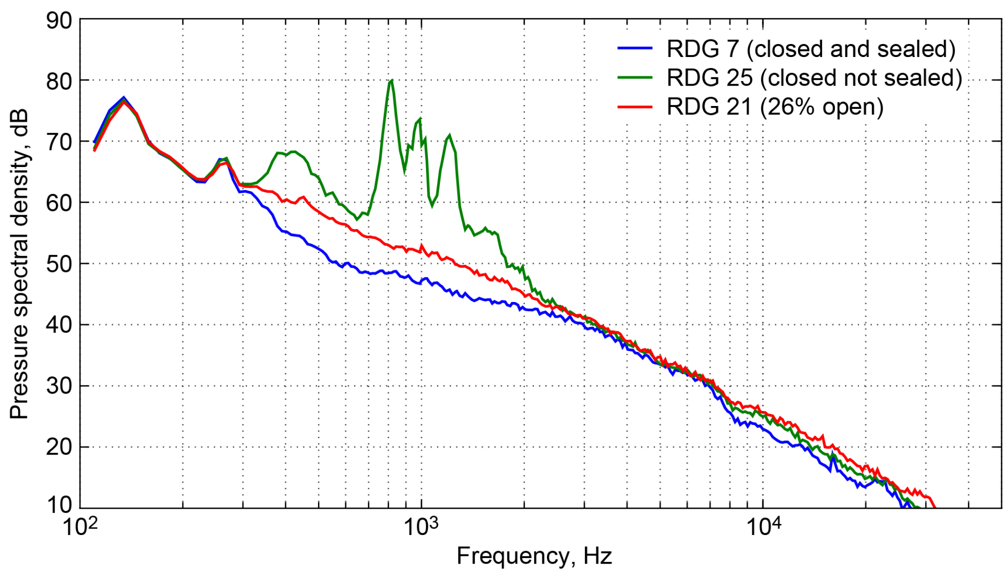

Figure B.14.—Upstream of cooler, Mach 0.15. Reading number (RDG).

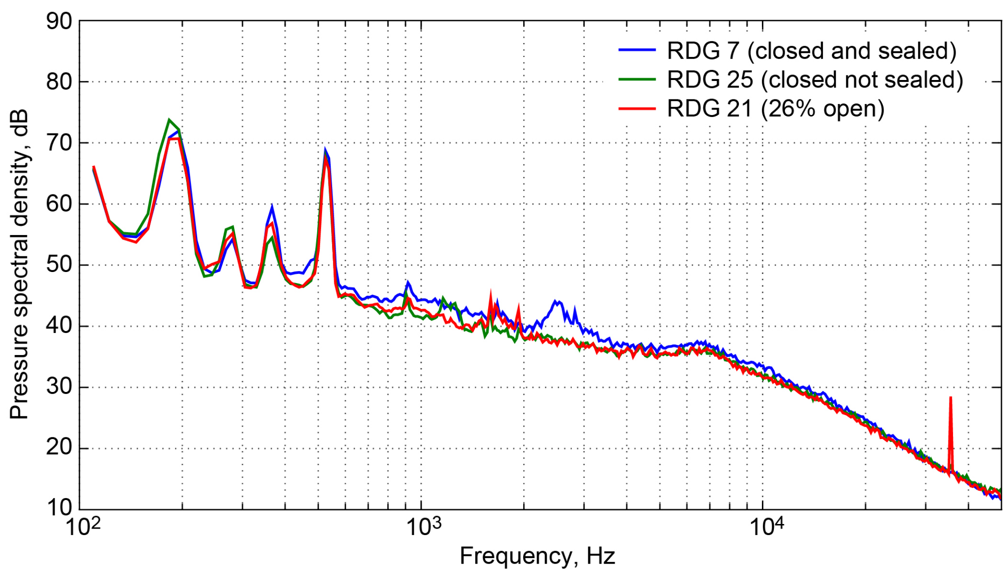

Figure B.15.—Test section, 9- by 15-foot, Mach 0.15. Reading number (RDG).

Appendix C.—Acoustic Box Database

As described in Section 8.0, many of the boxes installed in the 9- by 15-Foot Low-Speed Wind Tunnel (9×15 LSWT) were tested as a quality control procedure. The production, testing, and installation of acoustic boxes into the 9×15 LSWT started in August 2018. We considered it due diligence to compare a production box against a preproduction sample that we had tested in April 2018 and used to approve the design. The first available box was C53, and we identified that the acoustic performance was lower than was observed for the preproduction box, as shown in Figure C.1. Another production box, C32, was also available. As more boxes became available, we streamlined our process and expanded the scope of our quality assurance task. By the end of the project, we had tested 115 of the 140 acoustic boxes.

C.1 Tunnel Box Layout

Figure C.2 to Figure C.5 show the tunnel box layout and numbering scheme. The boxes were built and installed in "rings," from the front of the test section towards the diffuser. Thus, the oldest boxes have designations ending in "1," while the ones beginning with "DF" are the last ones built. As part of the testing discussed in Section 8.0, a deficiency of acoustic quality was first detected when testing box C53. Due to a perceived urgency in completing the construction, the first two rings of boxes were installed before we were able to test them.

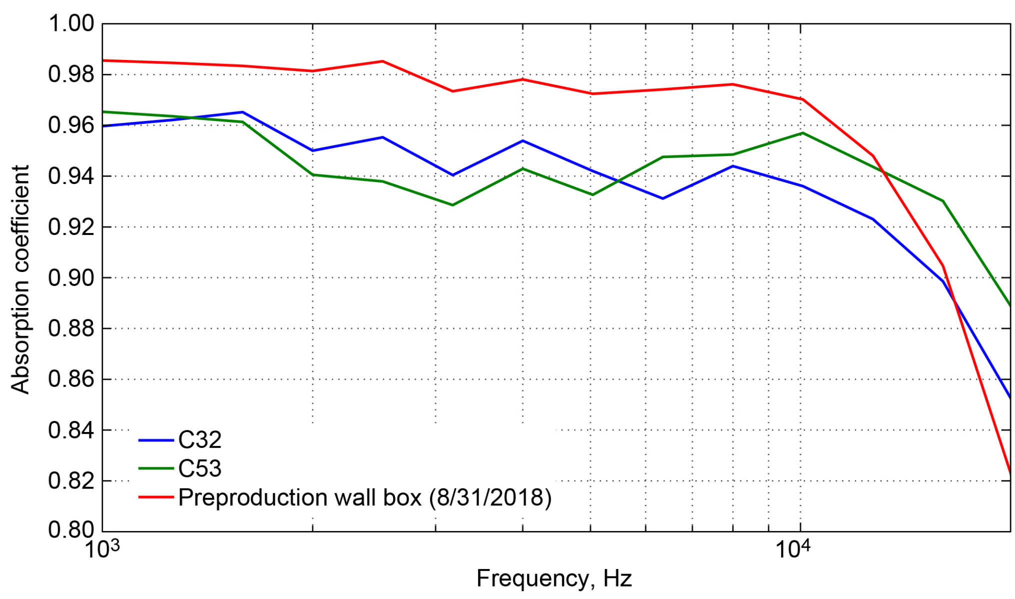

Figure C.1.—Absorption coefficient of acoustic boxes testing in NASA Glenn Research Center Acoustical Testing Laboratory.

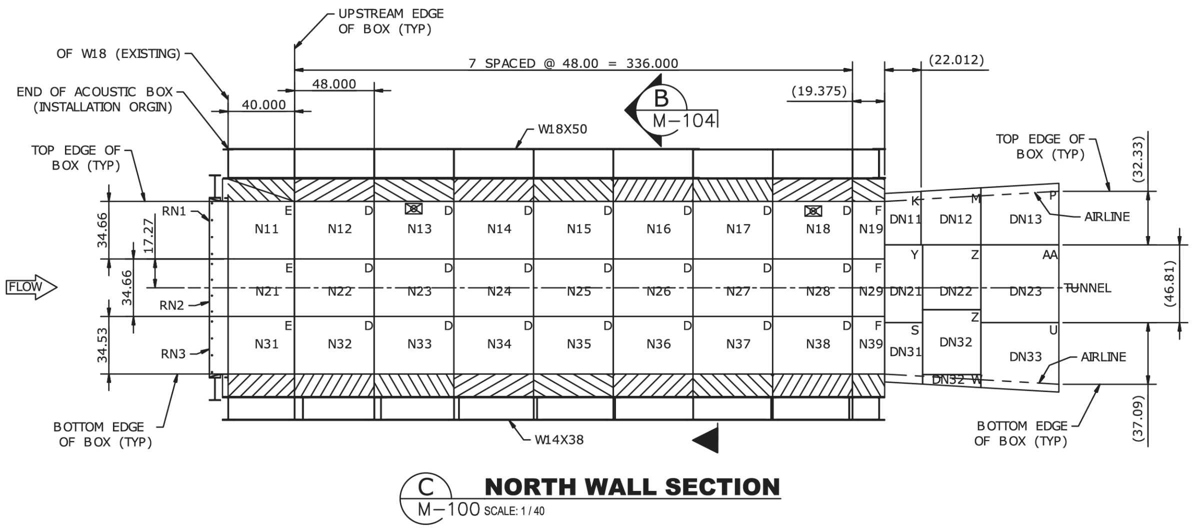

Figure C.2.—Tunnel box layout, north wall, view from inside, flow is from right to left.

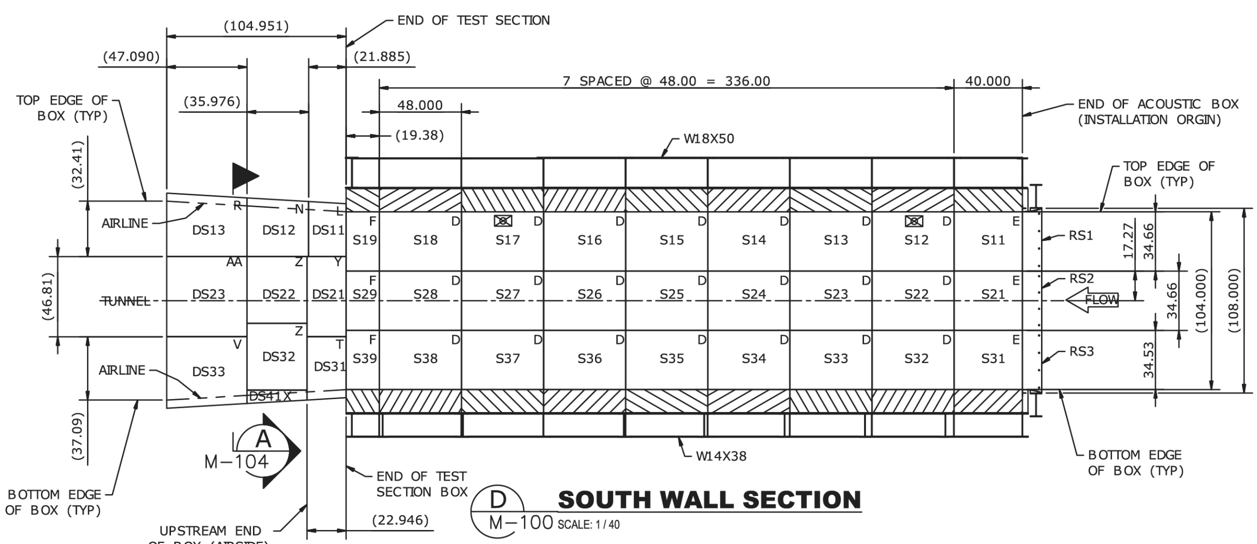

Figure C.3.—Tunnel box layout, south wall, view from inside, flow is from left to right.

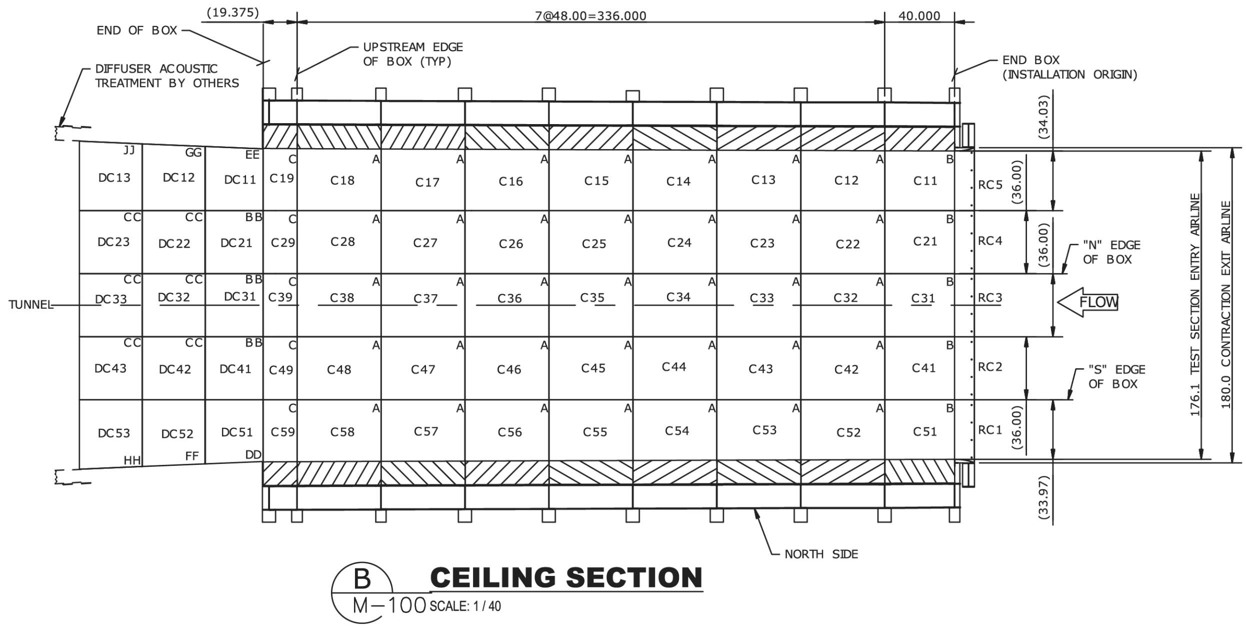

Figure C.4.—Tunnel box layout, ceiling, view from inside, flow is from right to left.

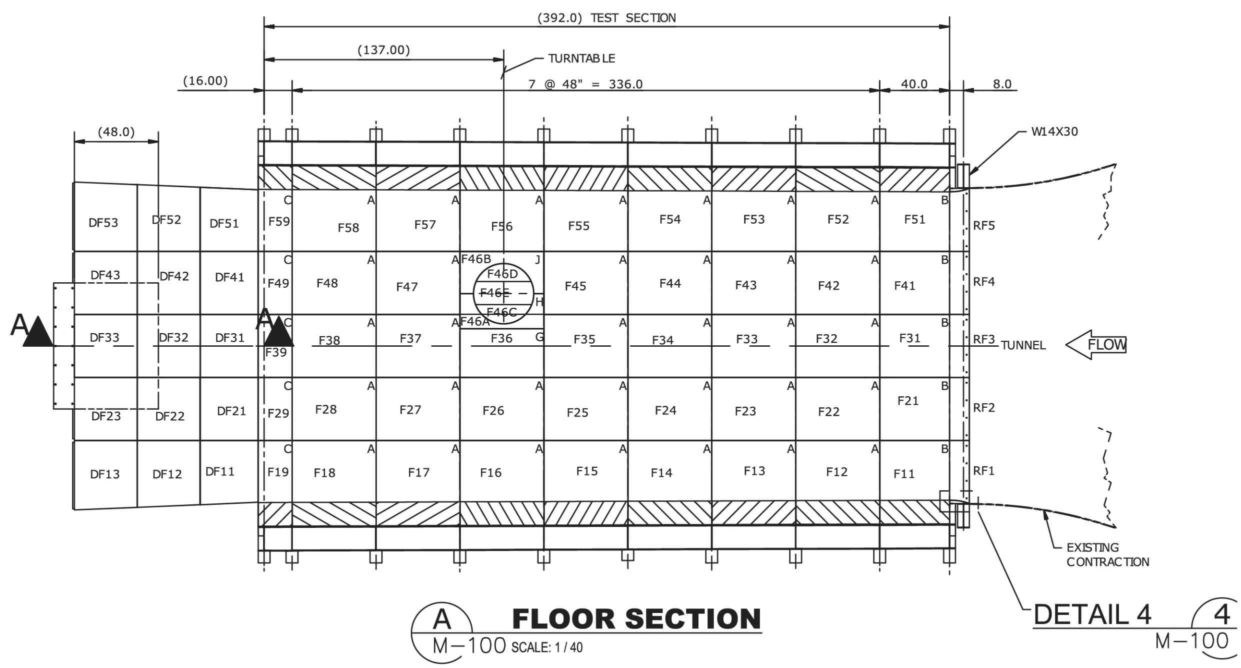

Figure C.5.—Tunnel box layout, floor, view from inside, flow is from right to left.

C.2 Sample Results

A few results from testing acoustic boxes will be shown. Figure C.6 shows all boxes versus the average, illustrating a range of results. Figure C.7 shows the average of the floor boxes, which are 16 ga, while the walls and ceiling are 20 ga and shown in Figure C.8. The diffuser boxes are shown in Figure C.9. Figure C.10 summarizes these results. Figure C.11 shows the best and worst boxes measured. Figure C.12 shows a histogram of mean absorption coefficient for all boxes tested.

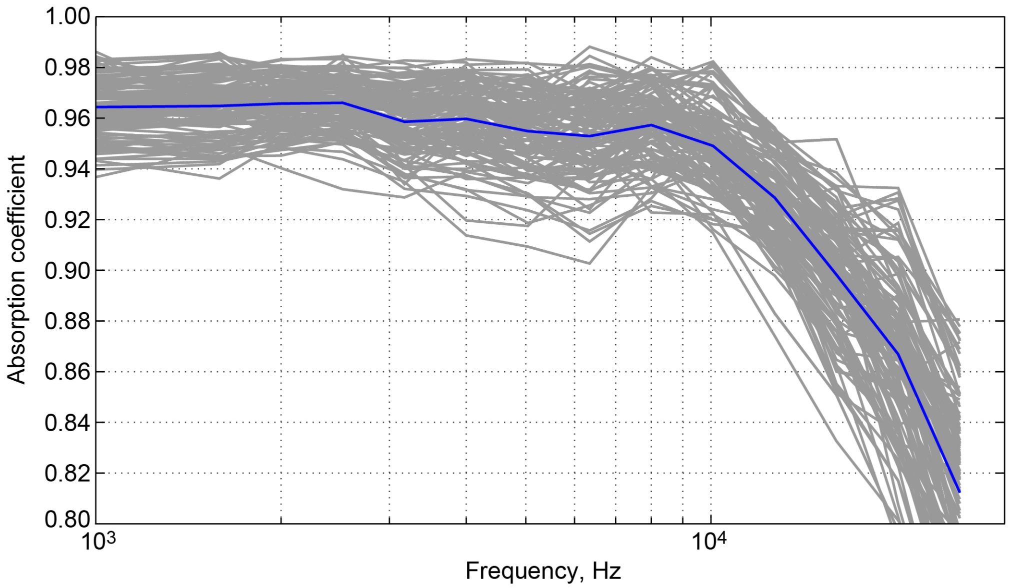

Figure C.6.—Absorption coefficient of all boxes versus average.

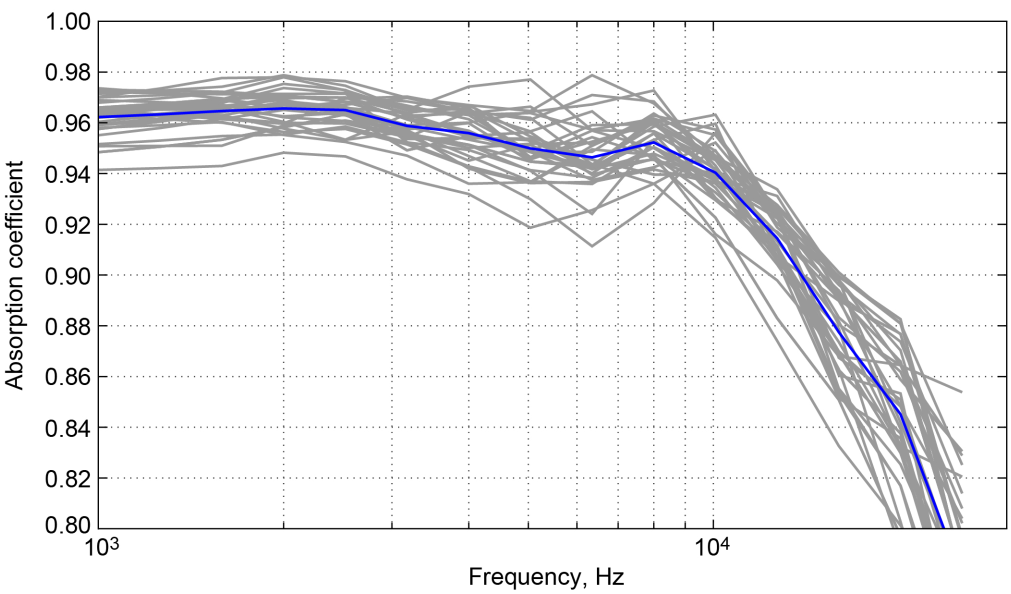

Figure C.7.—Absorption coefficient of floor boxes versus average of subset.

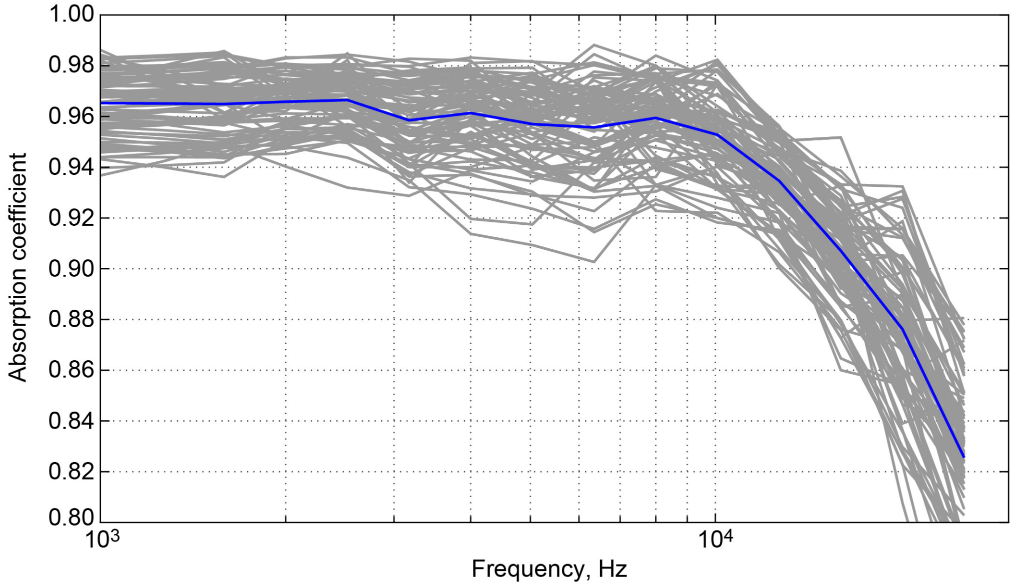

Figure C.8.—Absorption coefficient of wall and ceiling boxes versus average of subset.

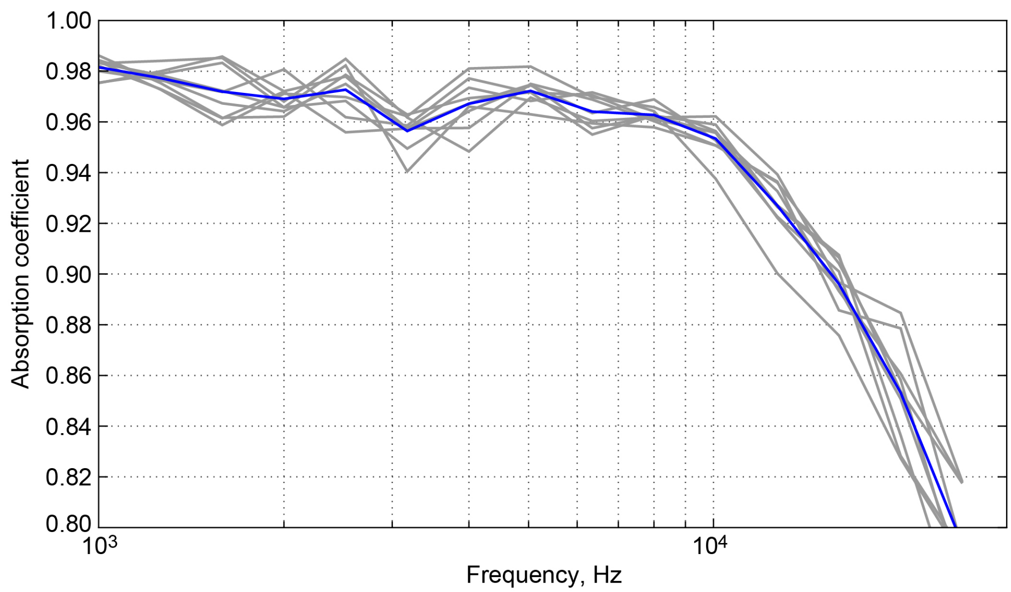

Figure C.9.—Absorption coefficient of diffuser floor boxes tested versus average of subset.

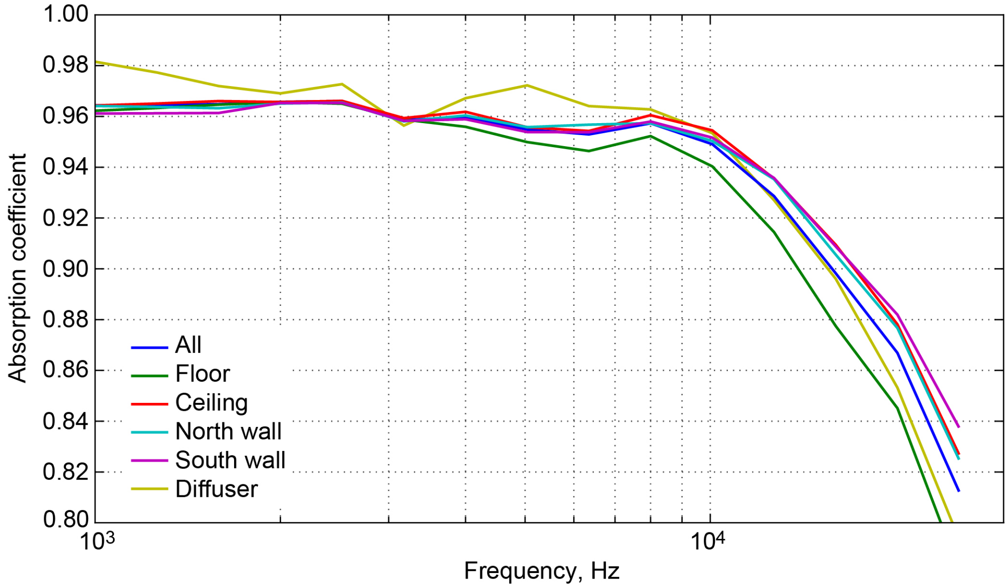

Figure C.10.—Absorption coefficient of various groups of boxes.

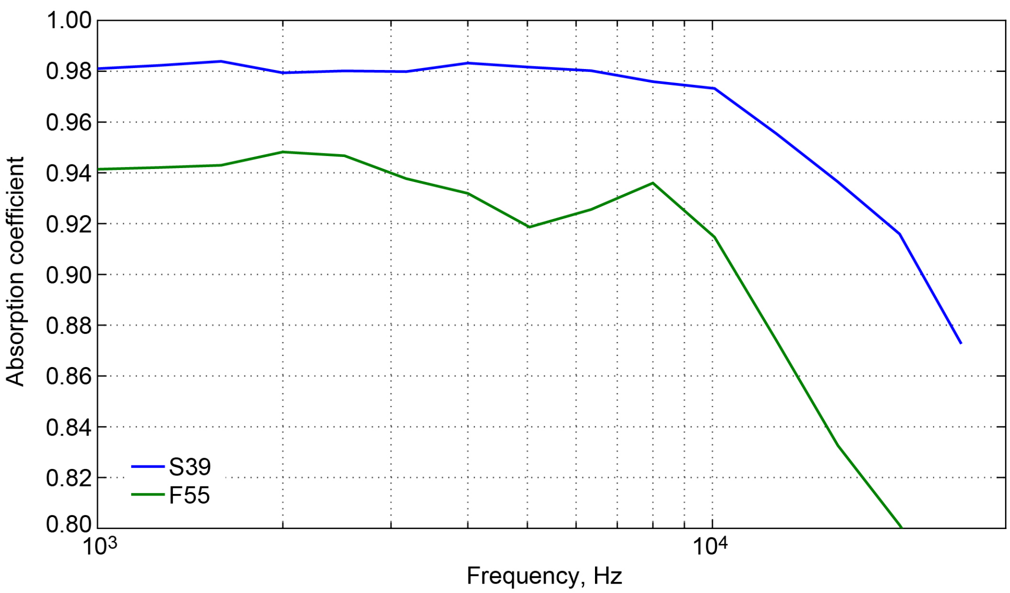

Figure C.11.—Overall best and worst boxes measured.

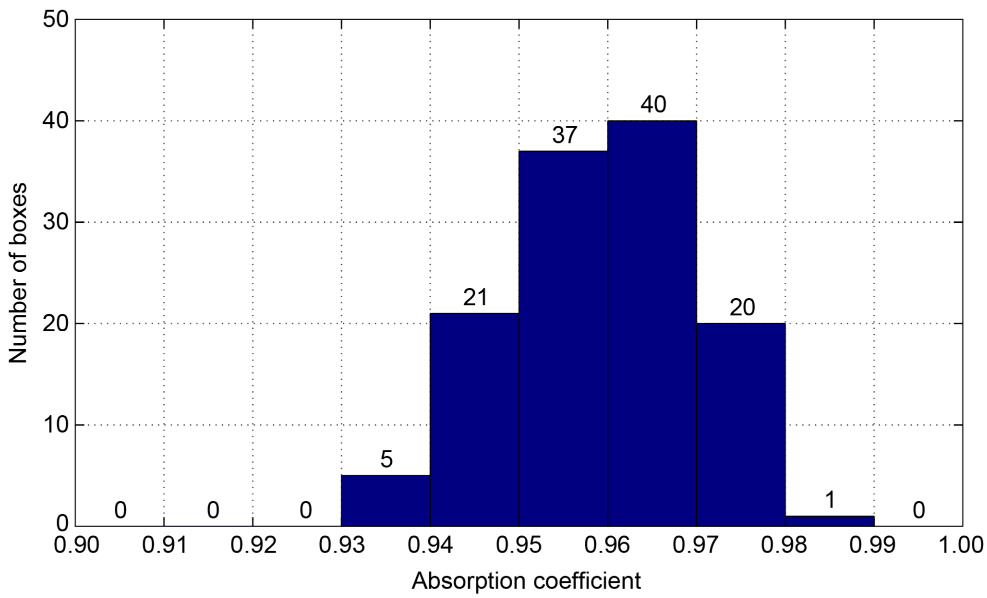

Figure C.12.—Histogram of mean absorption coefficient, 1 to 10 kHz.

References

1. Stephens, D.B.; et al.: 9x15 Acoustic Upgrade Part 1: Supporting Studies. NASA/TM-20210024786/Part 1, 2022.
2. Beranek, Leo L.; Labate, Samuel; and Ingard, Uno: Acoustical Treatment of the NACA 8- by 6-Foot Supersonic Propulsion Wind Tunnel. NACA TN–3378, 1955. https://ntrs.nasa.gov
3. Yuska, Joseph A.; Diedrich, James H.; and Clough, Nestor: Lewis 9- by 15-Foot V/STOL Wind Tunnel. NASA/TM X–2305, 1971. https://ntrs.nasa.gov
4. Soeder, Ronald H.: NASA Lewis 9- by 15-Foot Low-Speed Wind Tunnel User Manual. NASA TM–106247, 1993. https://ntrs.nasa.gov
5. Arrington, E. Allen; and Gonsalez, Jose C.: Calibration of the NASA Lewis Research Center 9- by 15-Foot Low Speed Wind Tunnel (1994 Test). NASA CR–195438, 1997. Available from the NASA STI Program.
6. Rentz, Peter E.: Hardwall Acoustical Characteristics and Measurement Capabilities of the NASA Lewis 9 x 15 Foot Low Speed Wind Tunnel. NASA CR–135025, 1976. https://ntrs.nasa.gov
7. Rentz, Peter E.: Softwall Acoustical Characteristics and Measurement Capabilities of the NASA Lewis 9 x 15 Foot Low Speed Wind Tunnel. NASA CR–135026, 1976. https://ntrs.nasa.gov
8. Dahl, Milo D.; and Woodward, Richard P.: Comparison Between Design and Installed Acoustic Characteristics of NASA Lewis 9- by 15-Foot Low-Speed Wind Tunnel Acoustic Treatment. NASA TP–2996, 1990. https://ntrs.nasa.gov
9. Dahl, Milo D.; and Woodward, Richard P.: Acoustical Evaluation of the NASA Lewis 9- by 15-Foot Low Speed Wind Tunnel. NASA TP–3274, 1992. https://ntrs.nasa.gov
10. Woodward, Richard P., et al.: Background Noise Levels Measured in the NASA Glenn 9- by 15-Foot Low-Speed Wind Tunnel. NASA TM–106817 (AIAA 95–0720), 1995. https://ntrs.nasa.gov
11. Stephens, David B.: The Acoustic Environment of the NASA Glenn 9- by 15-Foot Low-Speed Wind Tunnel. AIAA 2015–2684, 2015.
12. Woodward, Richard P.; Loeffler, Irvin J.; and Dittmar, James H.: Measured Far-Field Flight Noise of a Counterrotation Turboprop at Cruise Conditions. NASA TM–101383, 1989. https://ntrs.nasa.gov
13. Stephens, David B.; and Envia, Edmane: Acoustic Shielding for a Model Scale Counter-Rotation Open Rotor. AIAA 2011–2940, 2011.
14. Woodward, Richard P., et al.: Noise Source Diagnostic Test—Far-field Acoustic Results. AIAA 2002–2427, 2002.
15. Balan, Chellappa; and Hoff, Gregory E.: Propulsion Simulator for High Bypass Turbofan Performance Evaluation. SAE Technical Paper 931410, 1993.
16. Delaney, B.R., et al.: A Model Propulsion Simulator for Evaluating Counterrotating Blade Characteristics. SAE Technical Paper 861715, 1986.
17. Allen, Christopher S.; and Soderman, Paul T.: Aeroacoustic Probe Design for Microphone to Reduce Flow-Induced Self-Noise. AIAA 93–4343, 1993.
18. Allen, Christopher S., et al.: Aeroacoustic Measurements. Springer, Berlin, Heidelberg, 2002.
19. Brown, Clifford A.; and Stephens, David B.: Acoustic Methods Used in the NASA Glenn 9- by 15-Foot Low-Speed Wind Tunnel. NASA/TM—2018-218874, 2018. https://ntrs.nasa.gov
20. Dittmar, James H.; Elliott, David M.; and Bock, Lawrence A.: Some Acoustic Results From the Pratt and Whitney Advanced Ducted Propulsor: Fan 1. NASA/TM—1999-209049, 1999. https://ntrs.nasa.gov
21. Stephens, David B.: Data Summary Report for the Open Rotor Propulsion Rig Equipped With F31/A31 Rotor Blades. NASA/TM—2014-216676, 2014. https://ntrs.nasa.gov

22. International Organization for Standardization: Acoustics—Measurement of Sound Absorption in a Reverberation Room. ISO Standard 354:2003, 2003.
23. Spalt, Taylor B., et al.: Calibrations of the NASA Langley 14- by 22-Foot Subsonic Tunnel in Acoustic Configuration. AIAA 2014–2344, 2014.
24. International Organization for Standardization: Acoustics—Test Methods for the Qualification of Free-Field Environments. ISO Standard 26101:2012, 2012.
25. Schmitt, Jeff: A New Standard for the Qualification of Free Field Test Environments. Proceedings of the 38th International Congress and Exposition on Noise Control Engineering, Ottawa, Canada, 2009, p. 3288.
26. Winker, Douglas, et al.: A Precision Grade, Wide Bandwidth Source for the Qualification of Hemi-Anechoic Chambers. INTER-NOISE and NOISE-CON Congress and Conference Proceedings, Institute of Noise Control Engineering, vol. 2008, no. 1, 2008, pp. 779–787.
27. Winker, Douglas; Chadha, Ankit; and Ristroph, Einar: Source Design Considerations for Qualifying Hemianechoic Chamber in Compliance With ISO 3745. INTER-NOISE and NOISE-CON Congress and Conference Proceedings, Institute of Noise Control Engineering, vol. 2007, no. 1, 2007, pp. 585–595.
28. Schmitt, Jeff G.; and Stahnke, Brian: 9- by 15-Foot Low-Speed Wind Tunnel Acoustic Free Field Evaluation—Part 1: Qualification Report Summary. Part 2: Anechoic Environment Characterization Field Test Report. NASA/CR—2017-219509 (ARL–AQ6761), 2017. https://ntrs.nasa.gov
29. Schmitt, J.G.; and Ramirez, Z.: 9- by 15-Foot Low-Speed Wind Tunnel Acoustic Free Field Evaluation After Acoustic Improvement—Part 1: Qualification Report Summary. Part 2: Anechoic Environment Characterization Field Test Report. NASA Contractor Report to be published, 2022.
30. Cooper, Beth A.: Design and Construction of a Convertible Hemi/Anechoic Acoustical Laboratory for Testing Space Flight Hardware at the NASA Glenn Research Center. J. Acoust. Soc. Am., vol. 108, no. 5, 2000, pp. 2473–2473.
31. Soderman, Paul T., et al.: Design and Development of a Deep Acoustic Lining for the 40- by 80-Foot Wind Tunnel Test Section. NASA/TP—2002-211850, 2002. https://ntrs.nasa.gov
32. International Organization for Standardization: Acoustics—Determination of Sound Absorption Coefficient and Impedance in Impedance Tubes—Part 2: Transfer-Function Method. IOS Standard 10534-2:1998, 1998.
33. Pierce, Allan D.: Acoustics: An Introduction to Its Physical Principles and Applications. Phys. Today, vol. 34, no. 12, 1989.
34. COMSOL Multiphysics. Software Package, Stockholm, Sweden, 2022.
35. Becks, Edward A.; Bencic, Timothy J.; and Blumenthal, Philip Z.: Improved Speed Control System for an 87,000 HP Wind Tunnel Drive. NASA TM–106840, 1995. https://ntrs.nasa.gov